

REVEALING THE SECRETS OF WESTERLUND 2 - A YOUNG MASSIVE STAR
CLUSTER OBSERVED WITH THE HUBBLE SPACE TELESCOPE

PETER ZEIDLER

Dissertation
submitted to the
Combined Faculties of the Natural Sciences and Mathematics
of the Ruperto-Carola-University of Heidelberg, Germany
for the degree of
Doctor of Natural Sciences

Put forward by
Peter Zeidler
born in: Munich, Germany
Oral examination: 18 January 2017

ABSTRACT

We present a detailed study of the Galactic young massive star cluster Westerlund 2 (Wd2) using an optical and near-infrared high resolution multi-band survey observed with the *Hubble* Space Telescope. Images obtained in $H\alpha$ and $\text{Pa}\beta$ filters allowed us to derive a high-resolution pixel-to-pixel $E(B - V)_g$ gas extinction map. This map helped us to individually deredden the stellar photometry, to identify the cluster population, and to determine the properties of Wd2, such as distance ($d = 4.16$ kpc), total-to-selective extinction ($R_V = 3.95$), and age (1.04 ± 0.72 Myr). We identified 240 bona fide pre-main-sequence $H\alpha$ excess emitters indicating active disk accretion. A careful analysis of the radial dependence of the $H\alpha$ excess emission shows a 60% lower mass accretion rate in the cluster center, indicating a more rapid disk dispersal in close proximity to the massive OB-stars. We performed state-of-the-art artificial star tests to study the completeness-corrected spatial distribution of the stars. This revealed that Wd2 consists of two subclusters. Additionally, we determined the present-day mass function (PDMF) with a slope of $\Gamma = -1.53 \pm 0.05$, which translates to a total stellar cluster mass of $(3.6 \pm 0.3) \cdot 10^4 M_\odot$. The spatial analysis of the PDMF and the young age of Wd2 indicates that the cluster is, most likely primordial, mass segregated. A spatially uniformly distributed low-mass ($< 0.15 M_\odot$) population, extending into the gas and dust cloud, as well as a confined region of reddened stars, most likely caused by a foreground CO cloud, suggests that cloud-cloud collision might be the origin of the formation of Wd2.

ZUSAMMENFASSUNG

Wir stellen eine detaillierte Studie des galaktischen jungen massereichen Sternhaufens Westerlund 2 (Wd2) mit hochauflösenden optischen und nahinfraroten Multibandbeobachtungen des *Hubble* Weltraumteleskops vor. Aufnahmen in $H\alpha$ und $\text{Pa}\beta$ Filtern erlaubten uns eine hochaufgelöste Extinktionskarte des Gases zu erzeugen. Mit dieser konnten wir die stellare Photometrie individuell entröten, um so die Haufenpopulation zu identifizieren und die Eigenschaften von Wd2, wie Distanz ($d = 4.16$ kpc), Verhältniss von allgemeiner zu selektiver Absorption ($R_V = 3.95$) und Alter (1.04 ± 0.72 Myr) abzuleiten. Wir identifizierten 240 Vorhauptreihensterne mit $H\alpha$ Exzess, welche auf eine aktive Scheibenakkretion hindeuten. Eine sorgfältige Untersuchung der radialen Abhängigkeit der $H\alpha$ Exzessemission zeigt eine Reduzierung der Massenakkretionsrate um 60% im Haufenzentrum, welche auf eine schnellere Zerstörung der planetaren Scheiben in der Nähe der massereichen OB-Sterne hinweist. Tests mit künstlich eingesetzten Sternen zur Untersuchung der Vollständigkeit der Beobachtungen enthüllten, dass Wd2 aus zwei kleineren Haufen besteht. Zusätzlich konnten wir für die Massenfunktion eine Steigung von $\Gamma = -1.53 \pm 0.05$ herleiten und eine stellare Gesamtmasse des Haufens von $(3.6 \pm 0.3) \cdot 10^4 M_\odot$ bestimmen. Die räumliche Analyse der Massenfunktion in Zusammenhang mit dem jungen Alter von Wd2 legt nahe, dass Wd2 höchstwahrscheinlich primordial massensegregiert ist. Eine räumlich gleichförmig verteilte Population massearmer Sterne ($< 0.15 M_\odot$), die sich auch in die umliegenden Gas- und Staubwolken erstreckt, und eine räumlich begrenzte Region geröteter Sterne, die mit großer Wahrscheinlichkeit durch eine CO Wolke im Vordergrund erzeugt wird, deutet an, dass die Kollision von Gas- und Staubwolken der Grund für die Entstehung von Wd2 sein könnte.

ALLEIN DER VORTRAG MACHT DES REDNERS GLÜCK.

— JOHANN WOLFGANG VON GOETHE: FAUST, VERS 546

Contents

1	STAR- AND STAR CLUSTER FORMATION – AN OVERVIEW	1
1.1	An overview of star formation	1
1.1.1	The collapse of giant molecular clouds	1
1.1.2	The modes of cloud collapse and the onset of star formation	4
1.1.3	The pre-main sequence evolution	5
1.1.4	High-mass star formation	7
1.1.5	Observations of young stellar objects and determination of their physical properties	8
1.2	The formation and evolution of (massive) star clusters	10
1.2.1	Describing massive star clusters	10
1.2.2	The formation of young massive star clusters	12
1.2.3	The future of (young) massive star clusters	15
1.2.4	The connection of YMCs to globular clusters	17
1.2.5	What do we know about the most massive galactic YMCs?	17
2	THE YOUNG MASSIVE STAR CLUSTER WESTERLUND 2	25
2.1	The RCW 49 HII region - the birthplace of Wd2	26
2.2	Wd2 - A local laboratory for massive cluster evolution	27
2.2.1	The distance to Wd2	28
2.2.2	The reddening toward Wd2	29
2.2.3	The stellar content of Wd2	30
2.2.4	The age of Wd2	32
3	HST OBSERVATIONS AND DATA REDUCTION	35
3.1	Observations	35
3.2	Data reduction	36
3.2.1	The AstroDrizzle package	37

3.2.2	The ACS data	39
3.2.3	The WFC3/IR data	39
3.3	Quality check of the final images	40
4	THE PHOTOMETRIC CATALOG	43
4.1	Source detection and photometry	43
4.2	Improving the quality of the Photometric Catalogs	45
4.2.1	Object Type	45
4.2.2	Magnitude error	46
4.2.3	Sharpness	46
4.2.4	Crowding	47
4.3	Merging the different filters	48
4.4	Properties of the photometric catalog	49
4.5	The photometric improvement	50
5	THE ARTIFICIAL STAR TEST AND COMPLETENESS CORRECTIONS	55
5.1	The artificial star test	56
5.2	The global completeness limits of Wd2	57
5.3	The 2D completeness map of Wd2	57
5.3.1	The $F555W$ filter	60
5.3.2	The $F814W$ filter	60
5.3.3	The $F125W$ and $F160W$ filters	60
5.4	The true photometric uncertainties	60
6	A HIGH-RESOLUTION 2D MAP OF THE COLOR EXCESS	63
6.1	$H\alpha$ and $Pa\beta$ emission	63
6.2	The features of the color excess map	65
6.3	Uncertainties of the color excess map	69
6.3.1	Uncertainties due to the electron counts	69
6.3.2	Variations in the extinction law	70
6.3.3	Line emission contamination	70
6.4	Limitations of the color excess map	72
7	THE STELLAR REDDENING TOWARD THE DIRECTION OF Wd2	73
7.1	Transformation of the color excess between filter systems	73
7.2	Transformation of the gas excess map to the stellar excess map	76
7.3	The stellar color excess derived with UBV photometry	77

8	THE STELLAR POPULATION OF THE RCW 49 REGION	81
8.1	The separation of the cluster population from the field stars	81
8.2	The global, physical parameters of Wd2	83
8.2.1	The total-to-selective extinction toward the direction of Wd2	83
8.2.2	The extinction correction of our cluster CMD	84
8.2.3	The distance and age	85
8.3	The spatial distribution of the stellar population	86
8.3.1	The uniformly distributed low-mass stellar population	90
8.3.2	The red tail of the PMS population	90
8.4	A more detailed look at the stellar population	93
8.4.1	A closer look at the PMS ages	94
8.4.2	The individual regions in RCW 49	96
8.5	Summary and conclusions	97
9	THE MASS-ACCRETING PMS STARS	103
9.1	The <i>R</i> -band interpolation	104
9.2	The H α excess emission	106
9.3	The equivalent width	108
9.4	The Ae/Be star candidates	109
9.5	The accretion luminosity and mass accretion rate	111
9.5.1	Mass accretion rate as a function of stellar age	112
9.5.2	The spatial distribution of mass accreting PMS stars	112
9.6	Uncertainties in the H α luminosity and mass accretion rate	117
9.6.1	Observational uncertainties	117
9.6.2	The locus of the isochrones	118
9.6.3	The stellar metallicity	118
9.6.4	Geometrical alignment	118
9.7	Summary and conclusions	119
10	THE PRESENT-DAY STELLAR MASS FUNCTION OF WD2	123
10.1	The stellar masses	123
10.2	The slope of the present-day mass function	126
10.3	Uncertainties of the PDMF	127
10.4	The total stellar mass of Wd2	128
10.5	Mass segregation in Wd2	130
10.6	Discussion and Conclusions	132

11	SUMMARY AND FUTURE PLANS	135
11.1	Summary and Conclusions	135
11.2	Future Work	137
A	THE WEIGHTED MAPS	141
B	THE DRIZZLED FILTER MOSAICS	147
C	ADDITIONAL COMPLETENESS MAPS	155

List of figures

1.1.1	The pillars of creation and Gum 31	5
1.1.2	The PMS evolution stages	7
1.2.1	NGC 3603 and R136	18
2.1.1	The <i>Spitzer</i> color-composite image of RCW 49	27
2.2.1	The HST color-composite image of Westerlund 2	29
3.1.1	The field of view of the HST observations	37
3.2.1	The image cleaning	39
3.2.2	The pixel transformation of AstroDrizzle	40
3.2.3	The <i>F555W</i> weighted map	41
4.2.1	The object type distribution	46
4.2.2	The sharpness distribution	47
4.2.3	The crowding	48
4.4.1	The magnitude distribution the stars	50
4.4.2	The pipeline photometric uncertainties	51
5.2.1	The mean completeness distribution for the complete survey area	58
5.3.1	The 50% completeness map for all four wide-band filters	59
5.4.1	The measured photometric uncertainty	61
6.1.1	The pixel-to-pixel map of the color excess	66
6.2.1	The comparison between the color excess of the gas and the observations	67
6.2.2	The distribution of the color excess	68
6.2.3	The averaged radial distribution of the color excess	68
6.3.1	The throughputs of the HST filters	71
7.1.1	The different color-excess transformations for the <i>F555W</i> filter	76

7.1.2	The linear fit for the $F555W$ reddening correction	77
7.2.1	The transformation from the gas excess to a stellar excess	78
8.1.1	The $F814W$ vs. $(F814W - F160W)$ CMD of Wd2	82
8.2.1	The TCD to determine R_V	85
8.2.2	The reddened and dereddened $F814W$ vs. $(F814W - F160W)$ CMD . . .	86
8.2.3	The $F814W_0$ vs. $(F814W - F160W)_0$ CMD	87
8.3.1	The surface density map of the likely RCW 49 members	88
8.3.2	The three dimensional plot of the surface density of the likely RCW 49 mem- bers	89
8.3.3	The spatial location of the red tail stars	91
8.3.4	The $H\alpha$ emission and the <i>Spitzer</i> color-composite image	92
8.4.1	The $F814W_0$ vs. $(F555W - F814W)_0$ CMD of the RCW 49 members includ- ing the $H\alpha$ excess stars	95
8.4.2	The cumulative radial distribution	97
8.4.3	The $F814W_0$ vs. $(F814W - F160W)_0$ CMDs of the four different regions of RCW 49.	98
9.1.1	The $F555W - R$ vs. $F555W - F814W$ TCD	105
9.2.1	The $(F555W - F814W)_0$ vs. $(R - F658N)_0$ TCD of all cluster members. .	107
9.2.2	The histogram of the $H\alpha$ emission flux and accretion luminosity distribution of our 240 bona-fide PMS stars.	108
9.3.1	The $F814W_0$ vs. $(F814W - F160W)_0$ CMD of the RCW 49 members includ- ing the $H\alpha$ excess stars	109
9.3.2	The distribution of the EWs for the 240 bona fide $H\alpha$ emission PMS stars. .	110
9.5.1	Mass accretion rate vs. the stellar age	113
9.5.2	Mass accretion rate vs. the stellar age for different mass bins	114
9.5.3	The spatial distribution of the 240 $H\alpha$ excess stars	115
9.5.4	The mean mass accretion rate as a function of distance from the OB stars. .	116
10.1.1	The $F814W_0$ vs. $(F814W - F160W)_0$ CMD including the PARSEC 1.2S evolutionary tracks	124
10.1.2	The PDMF of the survey area	125
10.3.1	The comparison of stellar evolution models	128
10.5.1	The slope of the PDMF as function of distance	130
10.5.2	The slopes of the PDMF in the different annuli	131

11.2.1	The central region of Wd2, observed with MUSE	139
11.2.2	Different spectra obtained with MUSE	140
A.0.1	The <i>F658N</i> weighted map	142
A.0.2	The <i>F814W</i> weighted map	143
A.0.3	The <i>F125W</i> weighted map	144
A.0.4	The <i>F128N</i> weighted map	145
A.0.5	The <i>F160W</i> weighted map	146
B.0.1	The <i>F555W</i> mosaic	148
B.0.2	The <i>F658W</i> mosaic	149
B.0.3	The <i>F814W</i> mosaic	150
B.0.4	The <i>F125W</i> mosaic	151
B.0.5	The <i>F128N</i> mosaic	152
B.0.6	The <i>F160W</i> mosaic	153
C.0.1	The 25% completeness map for all four wide-band filters	156
C.0.2	The 75% completeness map for all four wide-band filters	157

List of tables

1.2.1	Overview over the most prominent young massive star clusters	19
2.2.1	Comparison to spectroscopic data	31
3.1.1	Overview over the observations	36
3.3.1	Summary of the weighted maps of the AstroDrizzle pipeline	42
3.3.2	The mean FWHM of the PSFs in the different filters	42
4.1.1	The parameters used to run the photometric routine	44
4.2.1	The thresholds for cleaning the catalogs	49
4.4.1	Properties of the final catalog	52
4.4.2	The final catalog	53
5.1.1	Artificial star test results	56
5.2.1	The completeness limits for different regions	57
5.4.1	The results of the photometric uncertainty fit	62
5.4.2	The photometric uncertainty	62
7.1.1	The transformation parameters	74
7.3.1	Comparison to spectroscopic data	79
8.4.1	The age distribution of the PMS and H α excess sources	96
8.4.2	The different areas of RCW 49	99
9.5.1	The mean mass-accretion rates	117
9.6.1	The sources of uncertainties	120
10.4.1	The integrated stellar masses	129
10.5.1	The slope of the MF relative to the cluster center	132

1

Star- and star cluster formation – an overview

As an introduction to my Thesis, I will give an overview of star formation and young massive star clusters (YMCs), to provide the reader with a general understanding of the main goals and drivers of this project. Much more detailed summaries can be found in the reviews of [Zinnecker and Yorke \(2007\)](#), [Portegies Zwart et al. \(2010\)](#), [Bodenheimer \(2011\)](#), [Preibisch \(2012\)](#), and [Dale \(2015\)](#), and references therein.

1.1 An overview of star formation

Star clusters, as the name tells us, are comprised of stars. In order to comprehend the processes and evolution of YMCs it is essential to understand the processes of star formation and stellar evolution on all scales – from the numerous population of low-mass stars up to the most massive O-stars.

1.1.1 The collapse of giant molecular clouds

Star formation begins with the collapse of giant molecular clouds (GMCs). Through a combination of processes, a low-density interstellar gas cloud is brought to a point where the force of gravity exceeds all other opposing forces, which finally results in the collapse of the cloud. Theoretical approaches to understand the basic conditions needed to start these collapsing processes were pioneered by Sir James Jeans in 1928 ([Jeans 1928](#)). One of the most important conditions needed for a molecular cloud to collapse is the so called Jeans length R_J . The radius of a (spherical) cloud must be smaller than the Jeans length, for a

given mass and temperature, to become unstable to gravitational collapse. The Jeans length is defined by the following expression:

$$R_J = \frac{0.4 \cdot GM\mu}{k_b T}, \quad (1.1)$$

where k_B is the Boltzmann constant, G is the gravitational constant, M the total cloud mass, T the temperature, and μ is the molecular weight of the gas in atomic gas units (≈ 2.37 for Solar composition with molecular hydrogen). Another common way to express this condition is to substitute the radius by the density ρ , assuming again that the gas cloud is approximately spherical. This results in the expression for the Jeans mass M_J , which is the minimum mass required for a given density and temperature, to become unstable:

$$M_J = \left(\frac{5 k_B T}{2 \mu G} \right)^{3/2} \left(\frac{4}{3} \pi \rho \right)^{-1/2}. \quad (1.2)$$

In the original definition to derive Eq. 1.1 and Eq. 1.2, Jeans took into account thermal and gravitational effects alone.

A simpler and more accurate way to describe the initial conditions for a collapse is to look at the total energy budget. The minimum requirement for a cloud to collapse is that the gravitational energy needs to exceed the sum of the thermal, rotational, turbulent, and magnetic energies:

$$|E_{\text{grav}}| > E_{\text{th}} + E_{\text{rot}} + E_{\text{turb}} + E_{\text{mag}}. \quad (1.3)$$

Most of the molecular gas is concentrated in giant molecular clouds (GMCs). These birthplaces for new stars are mainly built from molecular hydrogen H_2 and atomic helium He I. The first more complex molecules NH_3 and H_2CO were discovered by Cheung et al. (1968) and Snyder et al. (1969), respectively. Almost 200 molecules have been discovered in the inter-stellar medium (ISM) since (e.g., Belloche et al. 2014), such as HCN , CH_4 , HCL^+ , and much more complex ones e.g., $\text{CH}_3\text{OC(O)CH}_3$. For a full list see also <https://www.astro.uni-koeln.de/cdms/molecules>. These molecules form the dust, which is important for heating and cooling processes.

One of the most important molecules in GMCs is CO (mainly $^{12}\text{C}^{16}\text{O}$ and its isotopes $^{13}\text{C}^{16}\text{O}$, $^{12}\text{C}^{18}\text{O}$, etc). The importance of CO is that it is mostly used as tracer for H_2 and He I because observing these species directly via spectral lines is very difficult due to the insufficient conditions (mainly temperature) in a GMC to excite H_2 and He I. Also H_2 does not have a dipole moment, only a quadrupole moment with a transition line in the near-infrared at $28 \mu\text{m}$ in a wavelength regime where also dust radiates strongly.

With temperatures of 10–50 K, they are amongst the coldest places in the universe. Early molecular-line surveys using the molecule CO revealed an estimated molecular mass of the Galaxy of $2 \cdot 10^9 M_{\odot}$, of which most is concentrated in GMCs (e.g., [Clemens et al. 1988](#); [Lada 2005](#), and references therein). With masses between 10^4 – $10^6 M_{\odot}$ and sizes ranging from 20–100 pc, GMCs are the largest structures in the MW and rival globular clusters as the most massive objects in the Galaxy. These conditions correspond to a Jeans mass of $M_J \approx 20 M_{\odot}$, meaning that GMCs contain thousands of Jeans masses, are clearly gravitationally bound, and probably highly unstable, yet the magnetic field strength of the order of $10 \mu\text{G}$ leads to a magnetically critical mass (magnetically Jeans mass) of $M_{\text{mag}} \approx 5 \cdot 10^5 M_{\odot}$ ([McKee 1999](#)), which is the mass where magnetic forces are not able to prevent gravitational collapse.

The above treatment would suggest that a homogeneous GMC exceeding the Jeans limit would collapse to form a single star, which is obviously not the case. So the collapse of the GMC is needed with an associated fragmentation of the cloud into smaller and smaller bound clumps. Small-scale density fluctuations in the GMC are strongly amplified with time. This leads to one very important characteristic of these GMCs: they are highly structured, meaning they are extremely inhomogeneous with filaments, arcs, lobes, and embedded dense clumps. Although the mean density of GMCs is $\sim 10^4 \text{ cm}^{-3}$, the density can reach values up to 10^6 cm^{-3} and even 10^{10} cm^{-3} in their densest cores (e.g., [Lada et al. 1991](#); [Bodenheimer 2011](#)). Star formation and, especially, low-mass star formation is clearly favored by temperatures of around 10 K. This leads to the conclusion that these dense cores have to have mechanisms to maintain this temperature even under gravitational collapse. The heating and cooling are complicated mechanisms that are discussed at length in the literature (e.g., [Goldsmith and Langer 1978](#); [Spitzer 1978](#); [de Jong et al. 1980](#); [Boland and de Jong 1984](#); [Goldsmith 2001](#); [Stahler and Palla 2005](#); [Bodenheimer 2011](#)). At this point we will only summarize the dominant processes.

The heating processes:

- Photodissociation of H_2 by interstellar photons
- The photoionization of C-atoms by interstellar radiation
- Ionization of HI and H_2 by low-energetic cosmic rays
- Production of photoelectrons by interstellar UV photons interacting with dust grains

The cooling processes:

- Excitation of atoms, molecules, ions, and electrons, caused by collisions and followed by decay and the escape of a photon
- grain cooling

In addition to heating and cooling, there are several other important mechanisms that play a role during the cloud collapse and proto-star formation, such as the transfer of angular momentum¹, magnetic braking, the degree of ionization, magnetic diffusion, and turbulence. To describe all these processes in detail would exceed this introduction, therefore, I refer to a detailed overview by [Bodenheimer \(2011\)](#), and references therein).

¹Angular momentum problem: According to star formation models, stars should rotate faster than they actually do, meaning somehow they need to lose angular momentum in the early phases of star formation.

1.1.2 The modes of cloud collapse and the onset of star formation

The on-set of star formation in dense cloud cores releases energy that prevents the dense stellar cores from further fragmenting. Star formation shows different modes, taking place on different time scales, dependent on the physical processes. Generally one can distinguish between three main scenarios: magnetically-controlled star formation, turbulence-controlled star formation, and induced star formation.

Magnetically-controlled star formation takes place in low-mass cores that are magnetically sub-critical, meaning their mass is below the magnetic Jeans mass, and magnetic effects support the molecular cloud. Here the densest regions can evolve to the point of collapse through a process called ambipolar diffusion. Ambipolar diffusion causes neutral particles to drift inwards along magnetic field lines, since they are not stabilized against gravity by the magnetic field (e.g., [Spitzer 1978](#)). Therefore, ambipolar diffusion can increase the core's mass to the point where the gravitational forces are larger than the magnetic forces and the core begins to collapse even though the initial cloud mass is smaller than the magnetic Jeans mass. The time scale of this process is a few million to 10^7 yr ([Nakano 1984](#); [Lizano and Shu 1989](#); [Tomisaka et al. 1990](#); [Fiedler and Mouschovias 1993](#); [Basu and Mouschovias 1994](#)).

Turbulence-controlled star formation is nowadays thought to be the major effect driving star formation. In the molecular cloud, supersonic turbulence generates a complex shock pattern that can become unstable to collapse on local scales. It explains star formation on a time scale of 1 Myr, which is in agreement with many observations, yet, the observed star formation rate ($< 10\%$, e.g., [Evans et al. 2009](#)) is usually lower than the one in simulations (e.g., [Dale and Bonnell 2008](#); [Price and Bate 2009](#); [Clarke 2010](#), and references therein).

Induced star formation takes place in cores that are intrinsically stable against collapse. This means that star formation is not induced simply by gravitational collapse or turbulence, as described above, but triggered by an external event. For example, an external shock can compress molecular clouds less massive than their Jeans mass, and force them into collapse. These shocks can be generated by external events, such as mergers between galaxies (e.g., [Whitmore et al. 2010](#); [Hopkins et al. 2013](#)) and collisions between molecular clouds (cloud-cloud collision, e.g., [Furukawa et al. 2009](#)). Smaller scale feedback can also trigger star formation, e.g., supernova explosions (e.g., [Preibisch et al. 2002](#)), expanding H II regions around massive stars (e.g., Gum 31 in the Carina Nebula Complex, see right panel of Fig. 1.1.1, [Elmegreen and Lada 1977](#)), and highly-energetic fluxes from massive O-stars and Wolf-Rayet stars, compressing the surrounding material to pillar-like structures, at the tips of which gravitational collapse can be induced (e.g., the “Pillars of Creation” in M16 (Eagle Nebula), see left panel of Fig. 1.1.1).

Collapsing and rotating clouds are unstable to fragmentation. In the case of a low-mass core or a protostellar disk, fragmentation leads to the formation of binary and multiple systems, since the individual fragments are themselves unstable to collapse. The fragmentation of a higher mass cores can lead to the formation of a small cluster. The formation of multiple



Figure 1.1.1: **Left:** The “Pillars of Creation” in M16 (Eagle Nebula). *Image Credit: NASA, ESA, and The Hubble Heritage Team (STScI/AURA).* **Right:** Gum 31 (Gum 1955) in the Carina Nebula Complex observed with the 4m Visible and Infrared Survey Telescope for Astronomy (VISTA, Emerson et al. 2006) in the J , H , and K_s filter, shown in blue, green, and red, respectively, as part of the VISTA Carina Nebula Survey (ESO ID: 088.C-0117(A); PI: T. Preibisch, Preibisch et al. 2014).

system due to fragmentation has been shown in several simulations (e.g., Bate et al. 2002). Numerical simulation (Kroupa 1995; Bate et al. 2002; Delgado-Donate et al. 2004) indicate that the early formation of hierarchical multiple systems in clusters is caused by gradually braking up such multiple systems with time due to gravitational interactions and by captures of stars.

1.1.3 The pre-main sequence evolution

After a dense core in the GMC starts to collapse at the onset of star formation, it undergoes multiple evolutionary steps until it reaches the state of a zero-age-main-sequence (ZAMS) star². During these steps the cloud core undergoes a huge increase in density and temperature. A summary is also given in Preibisch (2012). These steps are shown in Fig. 1.1.2 and can be summarized as follows:

²A pre-main-sequence star reaches the ZAMS when it starts core hydrogen burning and reaches hydrostatic equilibrium.

- 1 **Pre-stellar core:** This stage follows the processes described above, immediately after the cloud core begins to collapse. Due to its own radiation the cloud core becomes optically thick, which can be used to define the timescale for stars to be born (e.g., [Wuchterl and Tscharnuter 2003](#)).
- 2 **Collapse Phase:** On timescales of a few thousand years, the gravitational collapse of the core leads to the formation of a central protostar. The dense envelope still absorbs any light emitted from the protostar, thus no stellar parameters can be determined (class 0 in Fig. 1.1.2).
- 3 **Protostar Phase:** In this phase the remaining circumstantial envelope starts to flatten out in a disk-like shape in order to conserve angular momentum. Within $\sim 10^5$ yr it evolves into a circumstellar disk, from which the protostar accretes mass. At this point the protostar becomes visible and can be detected at infrared wavelengths. Due to the absorption of most of the photons emitted by the central protostar, by the circumstellar disk and remaining envelope, and the reemission of this radiation by the same, the spectral energy distribution (SED) peaks in the far infrared and dominates the spectrum (similar to class I in Fig. 1.1.2).
- 4 **Classical T Tauri star:** The protostar has already reached $\sim 90\%$ of its final mass, yet it is still surrounded by an optically thick circumstellar disk, from which it actively accretes mass (similar to class II in Fig. 1.1.2). These accretion processes cause strong emission lines (especially $H\alpha$), which characterize the spectra of these objects. In the SED the star is now clearly visible and the luminosity and effective temperature can be determined, yet the active accretion causes strong infrared excess in the SED. Most of the circumstellar disk will be dispersed within a few Myr by either being accreted onto the star, accelerated outwards via jets, turned into protoplanets, or simply radiated away by stellar UV and X-ray radiation (e.g., [Ercolano et al. 2009](#)).
- 5 **Weak-line T Tauri star:** After further evolution (~ 10 Myr at most, e.g., [Briceño et al. 2007](#)) most of the surrounding gas and dust have been dispersed and the observed spectrum only shows weak infrared excess, caused by a thin remnant circumstellar disk. There is almost no accretion onto the central star (similar to class III in Fig. 1.1.2).
- 6 **Pre-main-sequence star:** After 5–10 Myr the protoplanetary disk is completely dispersed and only the pure photospheric stellar spectrum is observable. These young disk-less stars can be identified via strong coronal X-ray activity (e.g., [Casanova et al. 1995](#); [Preibisch et al. 1996](#)), chromospheric activity (e.g., [Herbig 1954, 1998](#)), the presence of lithium in the photosphere (e.g., [Walter et al. 1994](#)), a low surface gravity (e.g., [Slesnick et al. 2008](#)), or by strong variability (e.g., [Briceño et al. 2005](#)).

The typical strong variability of these young stars was first observed by [Hind \(1864\)](#) and this stellar class was later named “T Tauri” by [Joy \(1945\)](#) who discovered objects with similar characteristics (photometric variability, associated dark clouds, strong emission lines). These young low-mass stars have typical masses of $M \leq 2 M_{\odot}$. Their higher mass counterparts, Herbig Ae/Be stars, are defined by and named after George Howard Herbig, an American astronomer ([Herbig 1960](#)). They have a mass range of $1 M_{\odot} \leq M \leq 8 M_{\odot}$. The PMS stellar evolution of stars with masses $M \geq 8 M_{\odot}$ is so rapid that they cannot be observed in their PMS

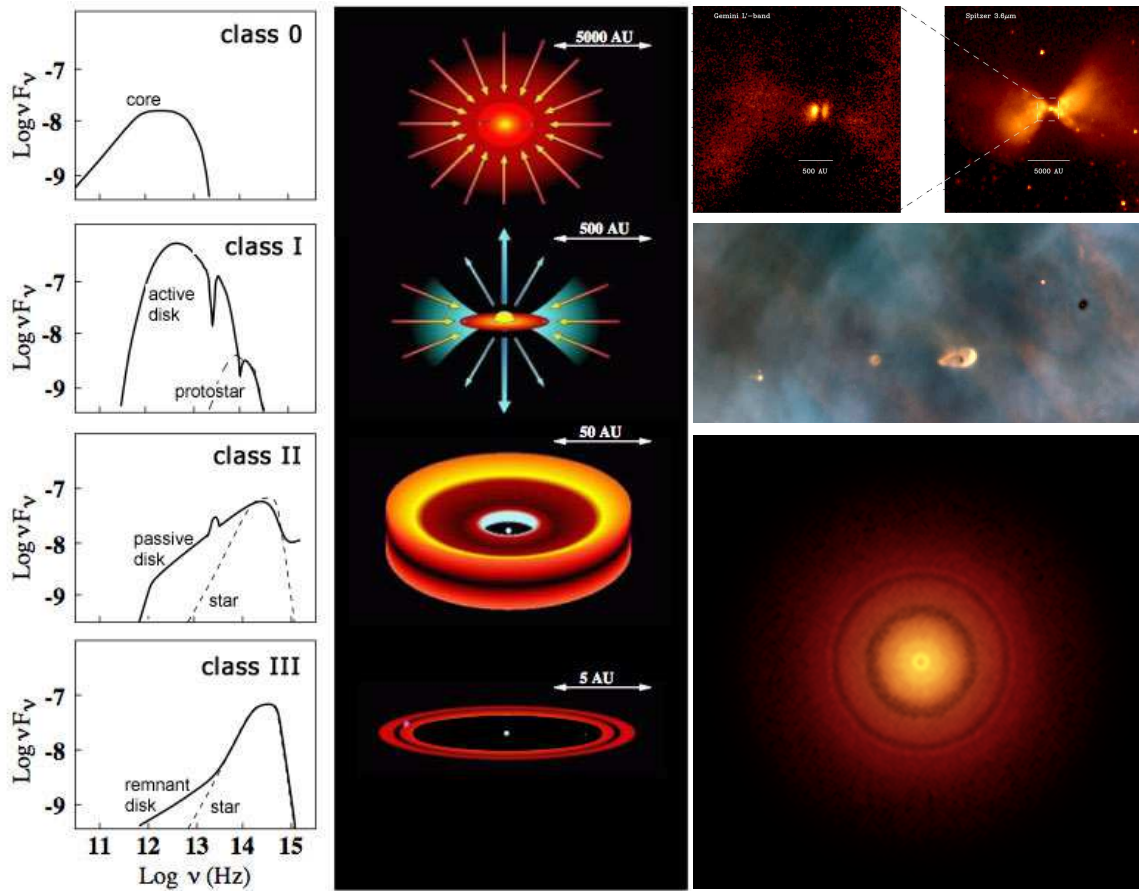


Figure 1.1.2: The different evolutionary stages of a PMS star. **Left:** SEDs of the four main stages of PMS evolution accompanied by sketches presenting the physical properties and spatial extents. *Image Credit:* A. Isella. **On the right** observations of (roughly) the different stages are shown. **Top, right:** Gemini NIRI image of L1527 taken in L' -band ($3.8 \mu\text{m}$) on the left and the *Spitzer* Space Telescope image taken at a similar wavelength of $3.6 \mu\text{m}$ (Tobin et al. 2010). **Mid, right:** A HST view of four stars that are surrounded by gas and dust being possibly protoplanetary disks that might evolve to agglomerate planets. *Credit:* C.R. O'Dell/Rice University; NASA. **Bottom, right:** ALMA image of the disk around the young star TW Hydrae, revealing the classic rings and gaps that are understood to signify that planets are in formation in this system. *Credit:* S. Andrews (Harvard-Smithsonian CfA); B. Saxton (NRAO/AUI/NSF); ALMA (ESO/NAOJ/NRAO).

phase, since as they become visible in the IR/optical wavelength regime, they are already in their main-sequence (MS) stage.

1.1.4 High-mass star formation

Although the high-mass stars are important for the galactic chemical evolution, since they enrich the interstellar medium (ISM) with heavy elements (supernovae type II) and their strong ultra-violet (UV) radiation erodes molecular clouds and creates H II regions (see Fig. 1.1.1), their formation has not yet been completely understood. One major difference to the low-

mass star formation is the evolutionary time scale. For example, due to their mass it can happen that the stellar core finishes with contraction, meaning it reaches the MS, while the envelope is still accreting mass. For low-mass stars the accretion time scale is always smaller than the contraction time scale.

One important question is whether there is an upper mass limit for massive stars. Two examples of the most massive stars observed and confirmed via spectroscopic orbital fitting are the double-lined binary Wolf-Rayet binary star WR20a with component masses of $83.0 \pm 5.0 M_{\odot}$ and $82.0 \pm 5.0 M_{\odot}$ (Bonanos et al. 2004; Rauw et al. 2004, 2005) and NGC 3603-A1 with $116 \pm 31 M_{\odot}$ and $89.0 \pm 16 M_{\odot}$ (Schnurr et al. 2008). Zinnecker and Yorke (2007, and references therein) have shown that there is an apparent upper mass limit around $150 M_{\odot}$. This is based on a discussion by Weidner and Kroupa (2004) and Figer (2005), who argued that the total mass of the R136 cluster in the Large Magellanic Cloud (LMC) is so massive that one would expect stars with masses of $500 M_{\odot}$ and even $750 M_{\odot}$, if the distribution follows a Salpeter (1955) initial mass function (IMF). This is not observed, meaning that either the IMF has a sharp cut-off at masses of about $150 M_{\odot}$ or there is a physical limit.

Physical limits of high-mass star formation may originate from the enormous radiation pressure. This means that stellar radiation increases with increasing mass to the point where the radiation pressure force exceeds gravity, the so-called Eddington limit (Eddington 1916). This is the limiting luminosity of a star at which point its outer layers begin to accelerate outwards and mass cannot be further accreted to increase the stellar mass (Zinnecker and Yorke 2007; Bodenheimer 2011; Kudritzki 2002, and references therein). If this limit is passed, the envelope will begin to lose mass through stellar winds. The mass flow onto the star can be continued if the accretion rate is high enough (high density of the parent cloud) in combination with a disk formation and bipolar outflows, which will channel the radiation in polar directions allowing further mass accretion through the disk. Also this mechanisms has its limitations causing an upper limit to the mass of the star, although these limits are not clear yet.

One way to reach higher masses would be high-mass star formation by hierarchical merging of lower mass stars. Bonnell and Bate (2002) considered this in their simulations and indeed, during their simulations 19 mergers occurred. This process is believed to mainly occur in the densest regions such as massive cluster cores, where the density is high enough and collisions become unavoidable. This is especially important for massive stars due to their short lifetimes of $\sim 2\text{--}5$ Myr (see Tab. 1.1, Sparke and Gallagher 2007).

Up to now there has already been a lot of effort and progress in understanding high-mass star formation, but a comprehensive picture of all relevant processes is still lacking.

1.1.5 Observations of young stellar objects and determination of their physical properties

During most of their early life, protostars or young stellar objects (YSOs) are only visible in the infrared (detectable via their IR-excess emission, e.g., Zeidler et al. 2016c) or even at longer wavelengths. For a long time, this made it difficult to properly detect them and

to study their properties. Only the development of large infrared and radio telescopes (see [Rieke 2009](#), for a detailed historical overview) over the last decades, such as the ESO 4 m Visible and Infrared Survey Telescope for Astronomy (VISTA, [Emerson et al. 2006](#)), HAWK-I at the ESO 8 m-VLT ([Pirard et al. 2004](#); [Kissler-Patig et al. 2008](#)), *Herschel* far-infrared observatory ([Pilbratt et al. 2010](#)), the *Spitzer* Space Telescope, the *Hubble* Space Telescope, or the Atacama Large Millimeter/Sub-millimeter Array (ALMA), made it possible to study these YSOs in greater detail. The development of space telescopes, such as the *Spitzer* Space Telescope, the *Herschel* far-infrared observatory, and in the near future the *James Webb* Space Telescope (JWST) has made it possible to observe in the mid- and far-infrared wavelengths at which the Earth's atmosphere is non-transparent.

Although we now have the tools to observe YSOs in large quantities with a reasonable integration time, scientifically it is still a challenge to interpret these data. As described above, the majority of these objects are still embedded in their cocoons and therefore not directly observable or obscured by circumstellar dust (see mid, right panel of Fig. 1.1.2).

To determine the stellar parameters it is crucial to know the luminosity of the star, which is, for PMS stars, highly variable with wavelength and on short time scales. The highly variable mass accretion rate from the surrounding envelope onto the star on an hourly or daily basis (e.g., [Smith et al. 1999](#)), caused by turbulences in the accretion disk, can produce considerable variation in the total luminosity. This accretion luminosity can constitute a substantial fraction of the total bolometric luminosity, which makes the star appear more luminous and, as a result, it appears to be more massive. Depending on whether one observes the stellar flux in the optical/near-IR, where the most of the flux originates in the stellar photosphere, or one observes the radiation coming from the disk in the mid- and far-infrared, one obtains totally different bolometric luminosities. Additionally the observed flux also depends on the viewing angle under which the disk is observed (face-on vs. edge-on, [Muzerolle et al. 2009](#)). T Tauri stars also contain a substantial fraction of dark star spots, which co-rotate with the stellar photosphere. The rotation of the stellar photosphere can therefore indirectly mimic a periodic dimming of the stellar optical and IR flux, mimicking additional variations of the stellar flux.

Most stellar parameters are determined by comparing the measured fluxes in the different wavelength regimes to evolutionary models, either fitting SEDs (for multi-filter observations over a wide wavelength range) or via fitting evolutionary tracks and isochrones to the Hertzsprung-Russel Diagram (HRD) or a color-magnitude diagram (CMD)³. While isochrones describe the luminosity and color of stars for a single age, the evolutionary tracks follow the evolution of a star with a specific initial mass. Both are the result of stellar evolution models, e.g., PARSEC 1.2S ([Bressan et al. 2012](#)), [Siess et al. \(2000\)](#), or [Baraffe et al. \(1998\)](#). In order to model the stellar evolution from core collapse until the star joins the MS, the parameter space for most physical parameters, such as stellar density, temperature, and radius, need to be modeled over many orders of magnitudes. Even with the fastest and

³The Hertzsprung-Russel Diagram is a graph showing the absolute stellar luminosity (in logarithmic scale) against the effective temperature (or spectral type), while the color-magnitude diagram shows the magnitude in one filter against the color (difference between the magnitudes of two filters).

most modern computers it is still impossible to model all parameters accurately, leading to a simplification of the models. As a consequence, the younger a star is the more uncertain the model becomes (see discussion in [Baraffe et al. 2002](#)).

Despite the huge progress during the last few decades in both modeling the stellar atmospheres and evolution, and on observing the youngest stars, the proper determination of stellar parameters for YSOs is still complicated and one needs to be very careful about the intrinsic uncertainties.

1.2 The formation and evolution of (massive) star clusters

Most stars form in clustered environments ([Lada and Lada 2003](#)). As [Lada and Lada \(2003\)](#) pointed out, most systems dissolve shortly after forming. They are building up the field population. These lower density systems are known as associations. Denser systems, known as open clusters ($\rho \leq 10^3 \text{ M}_\odot \text{ pc}^{-3}$), survive longer but they are loosely bound by gravitational interactions and are easily destroyed by close encounters such as other cluster or gas and dust clouds. The most massive and dense clusters, originated from YMCs ($\rho \geq 10^3 \text{ M}_\odot \text{ pc}^{-3}$), will remain gravitationally bound and are long-lived. Some of them potentially survive a significant fraction of a Hubble time and form globular clusters ([Brodie and Strader 2006](#)). As a result, YMCs are often referred to as young globular clusters or progenitors to globular clusters. Although the size distribution of YMCs show similarities to globular clusters ([Maíz-Apellániz 2002](#)) the physical properties of most YMCs are not so easily accessible due to the large distances. This makes the observations of the limited number of Galactic YMCs and the ones in the Magellanic Clouds so important. [Elmegreen and Efremov \(1997\)](#) and [Kruijssen \(2014\)](#) also suggested that the most massive of these YMCs may be the analogues to the old globular clusters. At the moment, about half of the Milky Way's star formation takes place in its 24 most massive GMC ([Lee et al. 2012](#)), yet it is unclear if the local star formation is typical.

1.2.1 Describing massive star clusters

Basic parameters

Most massive star clusters tend to have a spherical or ellipsoidal shape. To better define the size and stellar densities of clusters it is necessary to determine their spatial profile. The brightness profiles of globular clusters follow quite well the [King \(1962, 1966\)](#) model:

$$\Sigma(r) = \Sigma_0 \left(1 + \frac{r^2}{r_c^2} \right)^{-1}, \quad (1.4)$$

with the Σ_0 being the surface brightness in the center and r_c is the core radius, a scale parameter defining the cluster core. This profile does not hold for young clusters (e.g.,

Mackey and Gilmore 2003). They are much better represented by the profiles of Elson et al. (1987):

$$\Sigma(r) = \Sigma_0 \left(1 + \frac{r^2}{a^2}\right)^{\gamma/2}, \quad (1.5)$$

where a is a scale parameter and γ is a free fitting parameter. To connect the Elson et al. (1987) profile to the King (1966) core radius, the relation $r_c = a (2^{2/\gamma} - 1)^{1/2}$ is often adopted. Two other important parameters are the dynamical timescale (or crossing time) t_{cross} and the relaxation timescale t_{relax} . The crossing time t_{cross} is defined as the typical time a star needs to cross the system:

$$t_{\text{cross}} = 2 \cdot \left(\frac{GM}{r^3}\right)^{-1/2}, \quad (1.6)$$

where G is the gravitational constant and r and M are the total radius and mass of the cluster, respectively. The relaxation timescale t_{relax} is the time needed until the system reaches thermal equilibrium due to energy transfer by two body encounters. The relaxation time t_{relax} depends on the crossing time:

$$t_{\text{relax}} = \frac{N}{8 \ln N} \cdot t_{\text{cross}}, \quad (1.7)$$

where N is the number of stars in the cluster (e.g., Binney and Tremaine 1987). These basic equations already demonstrate how difficult it is to properly define the basic cluster parameters, which are crucial for the prediction (see Sec. 1.2.3) of the future survival of a young star cluster.

Mass Segregation

Analyzing the resolved stellar population and its underlying mass function (MF) shows that many of these massive star clusters are mass segregated, such as in the Orion Nebula Cluster (ONC, Hillenbrand and Hartmann 1998), the Arches cluster (Stolte et al. 2002), or NGC 3603 (Pang et al. 2013). Mass segregation means that many more high-mass stars are located in the center than in the outer regions compared to the low-mass stellar population. It is still a matter of debate whether mass segregation in such young clusters is primordial, meaning that the more massive stars formed originally in the central regions of the cluster, or whether it is dynamical, implying that they formed equally throughout the region and moved inwards due to interactions with the numerous low-mass stars.

For example Bonnell and Davies (1998) argued with the young age of the Trapezium cluster in the ONC that the massive stars did not yet have the time to move to the cluster

center but were born at their current location. The primordial mass segregation scenario is supported by the competitive accretion theory of [Bonnell et al. \(2001\)](#) and [Bonnell and Bate \(2006\)](#), which suggests that protostars can accrete more mass in the dense central regions of a young star cluster than in the outer regions.

On the other hand, [McMillan et al. \(2007\)](#) argue that young clusters showing mass segregation may be a result of mergers between small clumps that are already dynamically mass segregated.

[Krumholz et al. \(2009\)](#) and [Moeckel and Bonnell \(2009\)](#) argue that mass segregation can even occur on very short time scales so that the massive stars can be formed anywhere in the cluster.

[Haghi et al. \(2015\)](#) show that the scenarios of primordial mass segregation and mass segregation through evolution influences the shape of the present-day mass function (PDMF) slope in the low-mass regime ($m \leq 0.5 M_{\odot}$) differently. In their simulations [Haghi et al. \(2015\)](#) see a significant flattening of the mass function in the low-mass regime if primordial mass segregation is present. Yet this is still hard to confirm observationally, since the detection limits mostly cut off at higher masses and the mass determination of these low-mass PMS stars is still too uncertain (see Sect. 1.1.5).

Another theory by [McMillan et al. \(2007\)](#) and [Moeckel and Bonnell \(2009\)](#) is that the process of merging subclusters keeps the mass segregation imprint of these individual subclusters while [Allison et al. \(2010\)](#) argued that mass segregation can be introduced dynamically through violent relaxation much more rapidly than through two-body relaxation.

As one can see this is a very complicated topic, which will need a lot more data analyses. With the upcoming *James Webb* Space Telescope, for the first time, we will have the opportunity to sample the stars down to the lowest-masses in statistically significant numbers, to further investigate these scenarios.

1.2.2 The formation of young massive star clusters

So far we have discussed the general properties of YMCs. Another important aspect is their formation. In order to understand the formation processes of YMCs one needs to understand their progenitor clouds. So far only a few pre-star-forming clouds have been identified. These clouds need masses much higher than the total stellar mass of the final YMC ($M \geq 10^4 M_{\odot}$) and taking into account the star formation efficiency ϵ , the initial gas mass should be $M_{\text{gas}}^{\text{init}} = M_{\star}/\epsilon$.

In general there are two major theories on how cluster formation takes place:

Monolithic cluster formation: The stars form in a gravitationally bound centrally condensed population in one extremely compact parent giant molecular cloud. After the stars have begun to form, feedback processes expel the remaining gas and the reduced gravitational potential due to mass loss causes the cluster to expand to a final volume and its final, reduced density (e.g., [Lada et al. 1984](#); [Bastian and Goodwin 2006](#); [Banerjee and Kroupa 2015](#)).

Hierarchical cluster formation: In this scenario the stars form following the structure of the parental molecular cloud, which is known to be hierarchical and substructured (e.g., [Larson 1981](#); [Kruijssen 2012](#)). An increased star formation efficiency in the denser regions causes local removal of the gas and leading to a domination of the stellar dynamics and form subclusters (e.g., [Longmore et al. 2014](#); [Dale et al. 2015](#)). This is followed by a hierarchical merging of the subclusters, resulting in a centrally concentrated and bound cluster (e.g., [Parker et al. 2014](#)).

The discussion on monolithic versus hierarchical cluster formation is more relevant to the assembly of the cluster after the onset of star formation. Although the distribution of the gas and the stars are linked, this does not fully include the initial conditions of the gas (cloud) density at the very beginning of the formation of YMCs. This can be described in general by three different proposed initial conditions for massive star cluster formation (e.g., [Longmore et al. 2014](#); [Walker et al. 2016](#)):

Conveyor-belt: The initial density of the gas (and stars) is lower than the one of the final un-embedded YMC. The evolution is mainly defined by the collapse of the molecular cloud and on-going star formation.

In situ: The initial gas distribution is similar to the final star distribution. The YMC forms with little to no expansion or contraction.

Popping: The initial gas density is higher than the stellar density of the un-embedded cluster. After the stars have formed the remaining gas gets expelled and, due to its reduced mass, the cluster expands to its final density distribution.

A recent attempt to find such progenitor clouds was made by [Johnson et al. \(2015\)](#). Using ALMA CO and $870\ \mu\text{m}$ observations in the Antennae galaxy system, [Johnson et al. \(2015\)](#) have found one such cloud with properties of having a radius $< 24\ \text{pc}$ and a mass $> 5 \cdot 10^6\ M_{\odot}$. This cloud is dense enough to form stars and star clusters and the lack of thermal emission suggests that star formation has not yet altered the initial conditions. So far this is the only cloud capable of forming massive star clusters that has been found in the Antennae galaxy.

Finding these clouds in other galaxies is an important step forward in understanding the star cluster formation in different environments, but all these observations have a crucial problem, the extragalactic progenitor clouds cannot be spatially resolved to a level where YMC formation can be observed (at least not in the near future). Therefore, Galactic surveys (including SMC and LMC) are important to find these clouds. The major problem so far has been to find these progenitor clouds, where star formation has not yet begun. Only over the last years was it technically possible to carry out large Galactic plane surveys in the right wavelength range, in order to find these clouds, such as the NANTEN CO Galactic Plane Survey ([Mizuno and Fukui 2004](#)) or the Bolocam Galactic Plane Survey ([Aguirre et al. 2011](#)). A study of 18 clouds massive enough to form $> 10^4\ M_{\odot}$ star clusters within the first quadrant of the Galaxy outside the central kiloparsec by [Ginsburg et al. \(2012\)](#) using data from the Bolocam Galactic Plane Survey showed that all candidate clouds already show star formation. Nevertheless, [Ginsburg et al. \(2012\)](#) were able to use it to place an upper limit on the lifetime of clouds forming high-mass stars.

Another possible scenario for the formation of a massive star cluster is the cloud-cloud collision of giant molecular clouds. This can lead to a long-lasting, extended formation of a low-mass stellar population. Cloud-cloud collision is considered as one of the modes for high-mass star formation. Theoretical studies and hydrodynamical simulations for the scenario of cloud-cloud collision were made by [Habe and Ohta \(1992\)](#); [Anathpindika \(2010\)](#) and [Takahira et al. \(2014\)](#). This scenario has been suggested by [Nigra et al. \(2008\)](#) and [Cignoni et al. \(2009\)](#) for the star cluster NGC 602 in the SMC and is also debated for other star clusters such as NGC 3603 ([Fukui et al. 2014](#)) and RCW 38 ([Fukui et al. 2016](#)) in the MW.

One important question in massive star cluster formation is whether the environment of the progenitor cloud plays a role, especially if one wants to use the studies and observations in the MW to generalize the results for other galaxies. Extensive studies have been made to characterize the gas properties in the MW, and are found to be substantially different depending on the location (for an overview see the reviews and studies by [Morris and Serabyn 1996](#); [Ferrière et al. 2007](#); [Molinari et al. 2014](#); [Longmore et al. 2014](#), and references therein). In summary, the conditions in the Galactic center are very different from the ones in the disk. The gas in the center has much higher densities ([Longmore et al. 2013](#)), a larger velocity dispersion ([Shetty et al. 2012](#)), and a higher kinetic energy ([Ao et al. 2013](#)). Additionally, the metallicity varies within a factor of two of the Solar value ([Najarro et al. 2009](#)). Summarizing, one can say that the location within the MW matters. In the Galactic center the formation of YMCs is generally slow, meaning the gas is able to reach very high densities without forming stars. External events, such as cloud-cloud collisions, shocks, or tidal forces allow some of the gas to collapse under its own gravity and forming a YMC in the “in-situ” mode. On the other hand, so far, analyses have shown that the Galactic disk lacks starless $10^5 M_{\odot}$ clouds (e.g., [Ginsburg et al. 2012](#), and studies therein), leading to the conclusion that the preferred mode is the “Conveyor-belt” like mode, which may take place in the interaction zones of cloud-cloud collisions (e.g., [Furukawa et al. 2009](#); [Ohama et al. 2010](#); [Fukui et al. 2014](#)).

Independently of the differences of the modes and location of cluster formation the results are very similar, leading to a YMC. [Kruijssen and Longmore \(2013\)](#) showed that the properties in terms of their baryonic composition, kinematics, and densities, giant molecular clouds in the Solar neighborhood are similar to those in nearby galaxies and on the current observational uncertainty level the clouds in the Galactic Center are indistinguishable from those in high red-shift galaxies (e.g., [Bastian et al. 2010](#)). Following [Kruijssen \(2015\)](#), star formation in these high red-shift galaxies are the “natural” origin of globular clusters.

Summarizing the results shown above, to understand star cluster formation throughout the Universe and cosmological time scales (especially globular clusters), it is crucial to understand the formation of YMCs in the MW, since these results can be directly applied to the unresolved extragalactic observations.

1.2.3 The future of (young) massive star clusters

One of the most important key questions for the evolution of massive star clusters is, whether the YMC will survive, meaning staying gravitationally bound, or will it dissolve into the field population. The evolution of massive star clusters can be divided into three major steps:

The first few Myr: During this phase, stars are still forming and the cluster contains a significant fraction of gas.

<0.1–1 Gyr: This phase begins at the first supernovae explosion (~ 3 Myr after formation, [Eggleton 2006](#)). The cluster is mostly gas free but stellar mass loss plays an important role.

>0.1–1 Gyr: Stellar dynamical processes dominate the evolution of the cluster.

During the first phase (the first few Myr) the cluster evolution is dominated by a complex network of interactions between the conversion of gas into stars (within 10^5 Myr, see Sect. 1.1 and e.g., [Clarke 2010](#); [Elmegreen 2000](#)) and the feedback effect of the stars on the gas cloud (e.g., [Dale et al. 2005, 2012](#)). Unfortunately this phase of cluster evolution is not very well understood. To understand and to simulate long-term cluster survival these “initial” conditions set by the first phase are crucial but leave large uncertainties. Therefore, spatially resolved observations of massive star clusters during the early years of evolution, such as Westerlund 2 (this work) or NGC 3603 (e.g., [Pang et al. 2011](#)), are very important to better constrain the initial conditions for long-term cluster evolution simulations. These initial conditions, for which assumptions need to be made, are:

The stellar initial mass function: The distribution of stars in terms of their mass (e.g., [Salpeter 1955](#); [Scalo 1986](#); [Kroupa 2001](#); [Chabrier 2003b](#)), as well as the upper mass cut-off, i.e., the most massive stars. The high-mass population is important in the early years (feedback, etc.), while the low-mass stellar population contains most of the mass and so will be, later-on, the main driver of the cluster dynamics.

Multiplicity of stars: It has been shown that a non-negligible fraction of stars are components of binaries or higher-order multiples. Outside of the immediate Solar neighborhood these binaries and multiples are hard to detect. Therefore, the assumption of a certain binary fraction with a specific mass distribution influences the mass function (MF) and as a result the total stellar mass of the cluster.

Mass segregation: A concentrated high-mass stellar population in the center of a cluster can be much more destructive than an uniformly distributed population. The early mass loss due to high mass stellar evolution will lead to a stronger expansion in the mass-segregated case, increasing the chance of dissolving the cluster, than in unsegregated clusters ([Vesperini et al. 2009](#)).

Velocity and spatial distribution of the stars: Although for simplicity it is often assumed that the stellar distribution in a cluster is spherical (e.g., [Plummer 1911](#); [King 1966](#)), observations show this is not necessarily the case (see this study, Sect. 8.3).

Virial ratio: The ratio between the kinetic and potential energy after the gas has been expelled leaves the star cluster out of equilibrium, and therefore maybe unbound (e.g., [Hills 1980](#)).

Tidal field: Young star clusters are located within their host galaxy, meaning they feel its gravitational potential, which can lead to tidal stripping.

The first important step toward a long-term survival for a YMC is to overcome the “infant mortality” (Lada and Lada 2003). This describes the sudden decrease of the total number of YMCs after a few Myr. This is explained by the rapid (< 1 Myr, Seale et al. 2012) removal of the gas (due to the winds of the OB-star population and supernovae explosions) after the main star formation period. The gas expulsion time scale is meant to be short (a few dynamical time scales, see eq. 1.6) leaving the cluster in state far out of thermal equilibrium. This “sudden” decrease of mass leads to a shallower gravitational potential and results in the expansion of the cluster. This transition makes the star cluster vulnerable to dissolution which is, most likely, caused by a combination of tidal fields, the dynamical relaxation, and the interaction between the cluster and its surrounding GMCs (Gieles et al. 2006; Kruijssen et al. 2011).

Surviving phase 1, a YMC has made its first big step toward long-term survival. During phase 2 the cluster evolution is dominated by the high-mass stellar evolution and stellar mass loss. Most of the high-mass stars will leave the MS within a few Myr, and explode as supernovae and, depending on their mass, collapse into a black hole. The supernova explosions lead to a redistribution of the cluster’s mass and a significant mass loss of the cluster (10%–30% during the first 10–100 Myr for a Kroupa 2001, IMF between 0.1 – $100 M_{\odot}$), dominated by stellar mass loss. Some high velocity stars, exceeding the cluster’s escape velocity, will escape the cluster’s potential (e.g., Spitzer 1987; Heggie and Hut 2003). These are either stars of the high-velocity tail of the Maxwellian velocity distribution or high-velocity runaway stars accelerated by interactions with massive stars or by violent events such as supernova explosions. This will again cause an expansion of the cluster to adapt to the changing gravitational potential. Although this is not as violent as the rapid gas expulsion in phase 1, it can still lead to the cluster’s dispersal.

Phase 3 starts at the point when the stellar mass loss becomes minor as compared to the cluster evolution and the cluster stops to respond. Due to internal motions the cluster may keep expanding until it completely dissolves. In mass-segregated clusters however, this expansion will not be homologous. Due to a faster stellar evolution of the massive (segregated) core population, the cluster tends to lose relatively more mass in the center than in the lower mass halo stars. The result is a more dramatic expansion of the cluster core, with less severe effects farther out. If the cluster core is massive enough to overcome expansion and contracts again until it reaches thermal equilibrium. This would mean that the cluster is stable and will survive on a longer time frame.

Additionally during all the evolutionary stages external perturbations can also destroy the cluster, such as encounters with GMCs (Spitzer 1958). Due to the much higher mass of a GMC it is more likely that the cluster gets destroyed (Theuns 1991). Besides GMCs the cluster can encounter external tidal perturbations caused by passages through the galactic disk (e.g., Ostriker et al. 1972; Gnedin and Ostriker 1997), the bulge (e.g., Gnedin et al. 1999), or the spiral arms (e.g., Gieles et al. 2007).

1.2.4 The connection of YMCs to globular clusters

Observations in nearby galaxies have uncovered a large population of YMCs, mostly located in the disks of the galaxies, compared to globular clusters, which are located in the halos of galaxies. Globular clusters are found in all kind of galaxies including our own (Peng et al. 2008). The MW contains more than 150 old globular clusters with ages up to 13 Gyr and masses up to $10^6 M_{\odot}$ (e.g., Brodie and Strader 2006; Forbes and Bridges 2010). Yet the formation and origin of globular clusters is one of the major, still unsolved problems. Kruijssen (2015) argues that globular clusters are the “natural” outcome of high-redshift star formation yet an observational confirmation is still missing at these high redshifts ($z > 2$). One of the main questions remaining is, where do multiple populations in globular clusters come from.

In order to fully explain globular clusters and their formation, it is essential that we understand, in detail, the massive cluster formation and their evolution. This will give us the possibility to properly model the further evolution and to link it to the early evolution of the Universe. As long as we cannot spatially resolve YMCs in the more distant Universe, the only way to gain further insight into the physical processes of cluster formation and evolution is to observe the closest of these clusters (in the MW, LMC, and SMC) and to study them in detail.

1.2.5 What do we know about the most massive galactic YMCs?

The definition for YMCs, given in the review by Portegies Zwart et al. (2010) is also used later by Longmore et al. (2014) and gives a fair representation of the different kinds of clusters. They state that a cluster is young if $t \leq 100$ Myr, massive if $M > 10^4 M_{\odot}$ and it should be likely to survive for ~ 10 Gyr so it has the chance to become a globular cluster implying a density of $\rho \geq 10^3 M_{\odot} \text{pc}^{-3}$. This also indicates that their stellar density is so high that stellar collisions and interactions start to play an important role.

Applying these criteria to the known MW clusters and to the Magellanic Clouds, only a few fulfill these properties, of which the most prominent ones are listed in Tab. 1.2.1 including R136 in the Large Magellanic Cloud (LMC) and NGC 346 in the Small Magellanic Cloud (SMC). Although the Orion Nebula Cluster (ONC) is not massive enough to count as a massive star cluster, we decided to list it nevertheless, since it is, due to its close proximity, the best studied young star cluster. As examples for YMCs we show in Fig. 1.2.1 NGC 3603 and R136. Although these are not the most massive young star clusters known (which may have masses of several $10^5 M_{\odot}$ for super star clusters in M82 or NGC 1569, e.g., Westmoquette et al. 2014), their importance is clear due to the possibility of spatially resolving their stellar population spatially resolved (see Fig. 1.2.1).

To better compare the results of this work on Wd2 to other YMCs we will briefly discuss the known properties of each of the most prominent, resolved YMCs. A summary of these properties is given in Tab. 1.2.1. An introduction of Wd2 is given in Chapter 2. We limit ourselves to those YMCs that host a pronounced population of OB stars and are younger

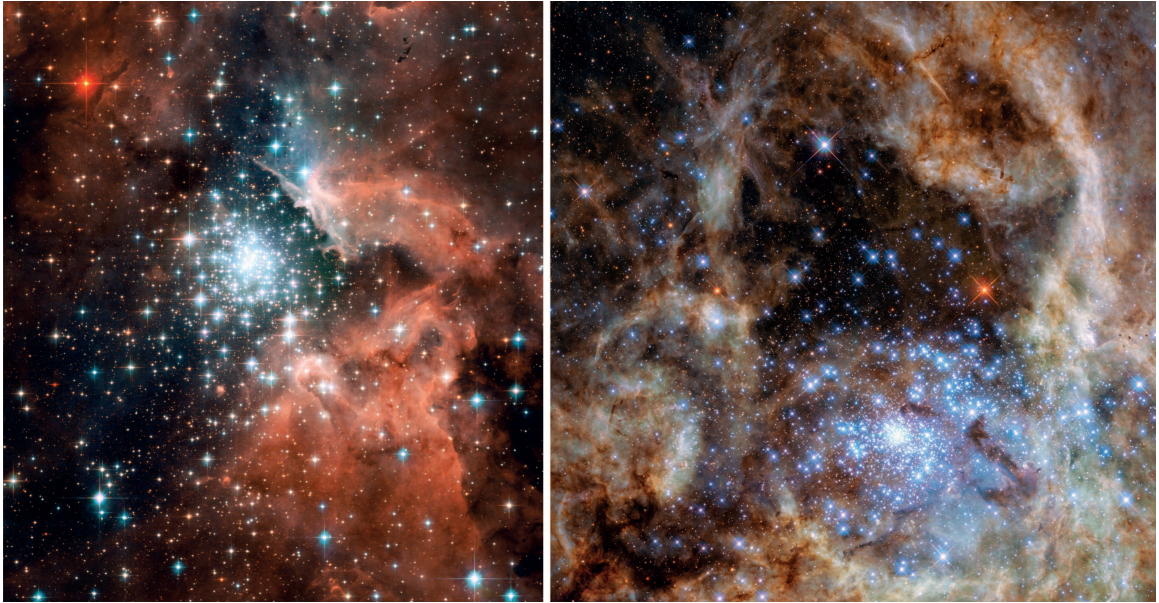


Figure 1.2.1: The YMCs NGC 3603 (left, *Credit: NASA, ESA and the Hubble Heritage (STScI/AURA)-ESA/Hubble Collaboration*) and R136 (right, *Credit: ESA/Hubble & NASA, P. Crowther (University of Sheffield)*) both observed with the *Hubble* Space Telescope.

than 5 Myr. The slope of the present-day mass function (PDMF) varies between different clusters and can be shallower, similar, or steeper than the ordinary [Salpeter \(1955\)](#) or [Kroupa \(2001\)](#) initial mass function (IMF). If known, all clusters show a significant degree of mass segregation.

NGC 346

The YMC NGC 346 is located in the SMC at a distance of $d = 39$ kpc and has an age of ~ 3 Myr ([Bouret et al. 2003](#)) with a total stellar mass of $8 \cdot 10^4 M_{\odot}$ ([Sabbi et al. 2007](#)). It is the central ionizing star cluster of the largest and brightest H II region N66 in the SMC and contains the majority of the known O-stars (33 known in NGC 346) in the SMC of which 11 are of spectral type O6.5V or earlier ([Walborn and Blades 1986](#); [Massey et al. 1989](#)).

Different studies of the region have shown a complex star formation history ([Sabbi et al. 2007](#)). There is evidence for an old episode of star formation assigned to the oldest population (~ 10 Gyr) observed in the SMC. The last moderate enhancement was probably 150 Myr ago. The population of NGC 346 (1–3 Myr) is distributed in at least 15 most likely coeval sub-clusters. [Cignoni et al. \(2011\)](#) showed that the latest star formation episode started 6–8 Myr ago and peaked about 3 Myr ago at $2 \cdot 10^{-5} M_{\odot} \text{ yr}^{-1} \text{ pc}^{-2}$.

[Nota et al. \(2006\)](#) pointed out the existence of an extended low-mass ($0.6\text{--}3 M_{\odot}$) PMS population associated with NGC 346, indicating on-going star formation, which is supported by the discovery of a population of YSOs still embedded in the gas clouds by [Bolatto et al.](#)

Table 1.2.1. Overview over the most prominent young massive star clusters

NAME	R.A.	decl. (J2000)	MASS [$10^4 M_{\odot}$]	AGE [Myr]	DIST. [kpc]	PDMF slope Γ	MASS SEGREGATION
NGC 346	$00^h 59^m 05^s .2$	$-72^{\circ} 10' 28''$	~ 8	~ 3	60.6	-1.43 ± 0.18	yes, likely primordial
ONC	$05^h 35^m 17^s .3$	$-05^{\circ} 23' 28''$	0.46	1–2	0.4	≈ -1.3	yes, likely primordial
R136	$05^h 38^m 52^s .4$	$-69^{\circ} 06' 03''$	2.2–5	~ 1.5	48.5	-1.2 ± 0.2	unknown
Westerlund 2	$10^h 23^m 58^s .1$	$-57^{\circ} 45' 49''$	~ 3.6	1–2	4.16	-1.53 ± 0.05	yes, likely primordial
Trumpler 14	$10^h 43^m 56^s .0$	$-59^{\circ} 00' 33''$	~ 1	≤ 2	~ 2.3	-1.3 ± 0.1	maybe, dynamical
NGC 3603	$11^h 15^m 23^s .0$	$-61^{\circ} 15' 00''$	~ 1	1–2	4.9	-0.88 ± 0.15	yes, dynamical
Westerlund 1	$16^h 47^m 04^s .0$	$-45^{\circ} 51' 04''$	4.9	4 ± 0.5	4.0	$-1.44^{+0.20}_{-0.08}$	yes, dynamical
Arches	$17^h 45^m 50^s .5$	$-28^{\circ} 49' 28''$	~ 1	~ 2	~ 8	-0.8 ± 0.2	yes, unknown
Quintuplet	$17^h 46^m 15^s .0$	$-28^{\circ} 49' 41''$	~ 2	3 ± 0.5	~ 8	$-0.68^{+0.13}_{-0.09}$	unknown

Note. — In this table we present the summary of the basic properties from the most prominent YMC in the MW and Magellanic Clouds. All parameters are described in this Section including their references. The properties for Wd2 are based on this work. Column 1 gives the clusters name, while Column 2 and 3 provides the coordinates of the cluster centers. Column 4 and 5 shows the most recent estimation of the clusters mass and age, respectively. Column 6 shows the heliocentric distance. Column 7 provides information whether the cluster is mass segregated and the its origin.

(2007) using observations from the *Spitzer* Space Telescope. De Marchi et al. (2011a) discovered 680 bona fide PMS candidates between $0.4 M_{\odot}$ and $4 M_{\odot}$ showing active mass accretion via their $H\alpha$ excess emission. The median mass accretion rate was estimated to be $\dot{M}_{\text{acc}} = 3.9 \cdot 10^{-8} M_{\odot} \text{ yr}^{-1}$.

An analysis of the PDMF by Sabbi et al. (2008) down to the Solar mass regime revealed a slope of $\Gamma = -1.43 \pm 0.18$, consistent with a Salpeter (1955) IMF. An analysis of the radial dependence of the PDMF slope in combination with the cluster’s age showed that NGC 346 is (most likely) primordially mass segregated.

Orion Nebula Cluster

Clearly one of the most outstanding and probably the most frequently observed nearby ($d < 1$ kpc) star forming region is the ONC with its four central prominent OB stars, forming the Trapezium cluster (Trumpler 1931). It seems that a convergence for the distance to the ONC has been found around $d = 400$ pc, using different distance measurement techniques, yet most measurements have uncertainties of 15–20% (see extensive discussion in Muench et al. 2008). The age of the ONC is estimated to 1–2 Myr.

Due to its close proximity, the ONC revealed the earliest and one of the most astonishing images of circumstellar disks and envelopes of protoplanetary disks (proplyds, see right, mid panel of Fig. 1.1.2) observed with the *Hubble* Space Telescope (e.g., O’Dell et al. 2008). Hillenbrand and Hartmann (1998) find a total stellar mass for the ONC of $M = 4600 M_{\odot}$.

Different analyses of the proper motions and radial velocities of ONC members showed that the velocity dispersion in the ONC is about $\sigma_v = 2.3 \text{ km s}^{-1}$ (e.g., Jones and Walker 1988; Sicilia-Aguilar et al. 2005; Tobin et al. 2009; Da Rio et al. 2014, and references therein). This velocity dispersion, in combination with the stellar mass of $M = 4.6 \cdot 10^3 M_{\odot}$

places the ONC in a supervirial state (Da Rio et al. 2014), leading to its probable dissolution in the future (infant mortality).

The PDMF is well studied (e.g., Hillenbrand and Carpenter 2000; Slesnick et al. 2004; Da Rio et al. 2010) with general agreement on a Salpeter (1955) like slope of $\Gamma = -1.35$ flattening to a plateau around $0.2\text{--}0.3 M_{\odot}$. Due to its close proximity, the ONC is the perfect testbed to study the PDMF down to the brown dwarf limit (e.g., Da Rio et al. 2012), yet there is no consent on its shape in this low-mass regime. The ONC shows hints of mass segregation (Hillenbrand and Carpenter 2000) for the highest mass stars (in total 20 OB stars have been revealed), which is suggested to be primordial regarding the young age of the cluster. A detailed description of the ONC stellar population can be found in Muench et al. (2008) and O'Dell et al. (2008).

R136

The R136 cluster is a bound super star cluster in the center of the star forming region NGC 2070 in the Taratula Nebula (30 Doradus) at a distance of 48.5 kpc. It contains at least $2.2 \cdot 10^4 M_{\odot}$ within a radius of 4.7 pc (Hunter et al. 1995), while Andersen et al. (2009) estimate its mass to be $5 \cdot 10^4 M_{\odot}$. Cignoni et al. (2015) showed that the mass estimate depends on the degree of contamination from the halo of NGC 2070 for which they estimate a total stellar mass of $9 \cdot 10^4 M_{\odot}$ using data from the Hubble Tarantula Treasury Project (HTTP, Sabbi et al. 2013).

Walborn and Blades (1997) suggest that the R136 cluster population has an age of 2–3 Myr and possibly triggered a ~ 1 Myr population in the immediate surrounding. This result is consistent with the findings of Sabbi et al. (2012), which show that stars in R136 are at most 2 Myr old. Crowther et al. (2016) estimate the cluster age to be $1.5^{+0.3}_{-0.7}$ Myr using UV spectroscopy of the brightest stars, in agreement with the above results.

R136 hosts the most luminous and massive stars known with masses of $100\text{--}150 M_{\odot}$ and spectral types of O2–3V (Crowther et al. 2016). The whole 30 Doradus region shows an extremely high rate of star formation with about 25% of the massive recent (< 10 Myr) star formation in the LMC (Kennicutt 1991). The estimated star formation rate in R136 is $2.8 \cdot 10^{-4} M_{\odot} \text{ yr}^{-1} \text{ pc}^{-2}$, more than a magnitude higher than in NGC 346 in the SMC (Cignoni et al. 2015). Andersen et al. (2009) derived a PDMF with a slope of $\Gamma = -1.2 \pm 0.2$ similar to the Salpeter (1955) slope, but so far it was not investigated whether R136 is mass segregated.

Trumpler 14

The young massive star cluster Trumpler 14 (Tr 14) is about 1–3 Myr old (Hur et al. 2012) and is part of the Carina Nebula (NGC 3372; for an overview we refer to Smith and Brooks 2008). As a member of the Carina Nebula, Tr 14 is located at a distance of about 2.3 pc in the Carina-Sagittarius spiral arm of the MW (Allen and Hillier 1993; Walborn 1995; Smith 2002). Tr 14 has an abnormal extinction law of $R_V = 4.4 \pm 0.2$ (Hur et al. 2012).

Tr 14 hosts at least 15 OB-stars (Smith 2006). The most massive one has a spectral type of O2 IF*. Together with Trumpler 16, of which the star η Car is the most luminous member, and a few other smaller clusters, Tr 14 is part of the central main energy source powering the Carina Nebula.

Using $UBVI_C$ photometry, Hur et al. (2012) derived a mass function down to $1.5 M_{\odot}$ with a slope of $\Gamma = -1.3 \pm 0.1$ similar to the Salpeter (1955) IMF. Adopting a Kroupa (2001) IMF, Ascenso et al. (2007b) estimated a total mass of $0.9\text{--}1.1 \cdot 10^4 M_{\odot}$ for Tr 14 while Sana et al. (2010) obtained an integrated total mass of $\sim 4.3_{-1.5}^{+3.3} \cdot 10^3 M_{\odot}$ also using a Kroupa (2001) IMF but using different observations. Both groups argue that the largest uncertainty originates from the imperfect foreground population subtraction.

Sana et al. (2010) investigated a possible mass segregation scenario for Tr 14. They see hints that the brightest stars seem to be more concentrated toward the cluster center, which they interpret as hint for mass segregation but so far it has not been confirmed by other studies. By comparing the dynamical friction time scale with the cluster's age, they argued that if mass segregation is present it does not need to be primordial and can be explained by dynamical evolution.

Using the same technique as for NGC 346, Beccari et al. (2015) discovered 356 bona fide PMS $H\alpha$ excess emitters in Tr 14. The $H\alpha$ emission originates from active mass accretion from the surrounding proto-stellar disks of the PMS stars.

NGC 3603

The central cluster HD 97950 of the giant H II region NGC 3603 is one of the most massive star clusters in the MW and has been subject to many studies. At a distance of 6.9 kpc (derived via isochrone fitting to CMDs, Sung and Bessell 2004), the cluster contains three Wolf-Rayet and around 50 O-type stars with spectral types up to O3V (Drissen et al. 1995).

The photometric mass is estimated to be $\sim 10^4 M_{\odot}$ (using the AO system NACO at the VLT for the $JHLSL'$ filterset, Harayama et al. 2008), while Pang et al. (2013) determined a dynamical mass of $(1.9 \pm 0.6) \cdot 10^4 M_{\odot}$. This dynamical mass was estimated via the 1D velocity dispersion computed from proper motions of member stars using two epochs of HST/WFPC2 data.

Fitting isochrones to CMDs show an age of 1–2 Myr for HD 97950 with a non-significant age spread (Stolte et al. 2004; Pang et al. 2013).

Over the past decades, the PDMF of HD 97950 has been widely discussed in literature. The slope of the PDMF ranges from $\Gamma = -0.73$ ($1\text{--}30 M_{\odot}$ Eisenhauer et al. 1998), $\Gamma = -0.95 \pm 0.1$ ($2.5\text{--}100 M_{\odot}$ Sung and Bessell 2004), $\Gamma = -0.91 \pm 0.15$ ($0.4\text{--}20 M_{\odot}$ Stolte et al. 2006), $\Gamma = -0.74_{-0.47}^{+0.62}$ ($0.4\text{--}20 M_{\odot}$ Harayama et al. 2008), to $\Gamma = -0.88 \pm 0.15$ ($> 4 M_{\odot}$ Pang et al. 2013). All these studies agree quite well and show a much shallower slope than a Salpeter (1955) IMF. In the latest study of NGC 3603, Pang et al. (2013) demonstrated in detail the high degree of mass segregation in the HD 97950 cluster. Estimating the dynamical

mass segregation timescale, [Pang et al. \(2013\)](#) concluded that HD 97950 is dynamically mass segregated.

Westerlund 1

At a distance of (4.0 ± 0.2) kpc Westerlund 1 (Wd1) is with $4.91_{-0.49}^{+1.79} \cdot 10^4 M_{\odot}$ (using NTT/SofI J and K_S broadband photometry, [Gennaro et al. 2011](#)) the most massive YMC in the MW. Using the radial velocity dispersion of 10 stars (determined via VLT/ISAAC near-infrared spectra) [Mengel and Tacconi-Garman \(2009\)](#) estimated a dynamical mass of $1.5_{-0.7}^{+0.9} \cdot 10^5 M_{\odot}$ and concluded that Westerlund 1 will not dissolve in the future.

Different studies converge at an Wd1 cluster age of about 5 Myr. While [Gennaro et al. \(2011\)](#) estimate an age between 3 Myr and 5 Myr using near IR photometry, [Crowther et al. \(2006\)](#) suggested an age of 4.5–5 Myr by comparing the number of Wolf-Rayet stars to the number of cool hypergiants. [Negueruela et al. \(2010\)](#) favors an age of ≥ 5 Myr studying the massive, spectroscopically classified stars.

Using the FORS2 instrument at the VLT, [Negueruela et al. \(2010\)](#) obtained intermediate-resolution spectroscopy over the range 5800–9000 Å and identified 57 stars as OB cluster members with spectral types of O9–B0. According to an estimate of [Muno et al. \(2006\)](#) Wd1 has already undergone about 65 supernova events. [Crowther et al. \(2006\)](#) showed that Wd1 hosts at least 24 Wolf-Rayet stars.

[Gennaro et al. \(2011\)](#) fitted a typical [Salpeter \(1955\)](#) or [Kroupa \(2001\)](#) shaped high-mass IMF to the PDMF for all stars above $3.5 M_{\odot}$ finding a slightly steeper slope of $\Gamma = -1.44_{-0.08}^{+0.20}$. The spatial variation of the PDMF slope and the density distribution of the massive stars suggest that Wd1 is mass segregated. Comparing the dynamical time scale of Wd1 with its age leads to the conclusion that primordial mass segregation is not necessary to explain the present-day distribution of the massive stars. Its elongated shape suggests that Wd1 is likely the product of subcluster merging.

The Arches cluster

The Arches Cluster is located near (projected distance ~ 25 pc) the Galactic Center about ~ 8 kpc away from the Sun ([McNamara et al. 2000](#)). The Galactic Center counts as one of the most extreme star forming environments in the MW, dominated by the high stellar and gas density, tidal torques, turbulent motion, and a steep gravitational potential. Despite these destructive forces the high gas densities lead to the Galactic center being the most efficient star forming environment in the MW.

With an estimated mass of $10^4 M_{\odot}$ and a central density of $3 \cdot 10^5 M_{\odot} \text{pc}^{-3}$, the Arches Cluster is the densest YMC known in the MW ([Figer et al. 1999b](#); [Stolte et al. 2002](#); [Habibi et al. 2013](#)). [Harfst et al. \(2010\)](#) estimated the dynamical mass to be $4 \cdot 10^4 M_{\odot}$ using N-body simulations. Studying the properties of Wolf-Rayet stars [Blum et al. \(2001\)](#) estimated an age between 2 Myr and 4.5 Myr.

The Arches cluster is believed to host at least 125 O-type stars (Lang et al. 2001). Because of this violent environment it came as a surprise when Stolte et al. (2010) found 21 IR excess emission sources (using deep Keck/NIRC2 $HK'L'$ photometry), of which 3 show the signature of a circumstellar disk.

For the slope of the PDMF of the Arches cluster Figer et al. (1999b) determined a slope of $\Gamma = -0.7$ for stars more massive than $10 M_{\odot}$. Using HST/NICMOS ($F160W$ and $F205W$ filters) and AO Gemini (H and K' filters) data, Stolte et al. (2002) derived slopes of $\Gamma = -0.82 \pm 0.14$ and $\Gamma = -0.7 \pm 0.16$, respectively. Both were derived for a mass range between $10 M_{\odot}$ and $65 M_{\odot}$. All derived PDMFs show slopes less steep than the Salpeter (1955) slope. The radial analysis of the PDMF shows an almost flat slope in the cluster center while a slope of $\Gamma = -1.7 \pm 0.7$ applies for the outer regions, showing that the Arches cluster is heavily mass segregated (Stolte et al. 2002, 2005). Close to the Galactic Center simulations suggest that the initial conditions are canceled out within 1 Myr so dynamical and primordial mass segregation cannot be distinguished at the age of the Arches cluster of ~ 2 Myr.

The Quintuplet cluster

Besides the Arches Cluster, the Quintuplet cluster is the second YMC located in the Galactic center. It is named after five prominent bright stars (Nagata et al. 1990) and is located in a projected distance of 30 pc from Sagittarius A*, the supermassive black hole located at the center of the MW. Based on K -band spectra Liermann et al. (2012) and Liermann et al. (2014) estimated an age of 3.0 ± 0.5 Myr by constructing a Hertzsprung-Russel diagram. The cluster's stellar mass comprises $\sim 2 \cdot 10^4 M_{\odot}$ (Shin and Kim 2016).

So far 21 Wolf-Rayet stars (Liermann et al. 2009, 2010) and 93 OB stars (Figer et al. 1999a) have been identified. After finding disk-bearing objects in the Arches cluster (Stolte et al. 2010) in close proximity to such a large population of massive OB stars, Stolte et al. (2015) used the VLT/NACO ($K_S L'$) and HST/WFC3 ($F125W$ and $F160W$) observations to also find such objects in the Quintuplet cluster. 26 L -band excess objects were found.

Using high-resolution H and K_S -band observations obtained with the ESO/VLT NACO instrument Hußmann et al. (2012) determined a slope of $\Gamma = -0.68^{+0.13}_{-0.09}$ for the PDMF, shallower than the Salpeter (1955) slope. Up to now the question about mass segregation remains unanswered.

2

The young massive star cluster Westerlund 2

Parts of this chapter are included in Sect. 1 of [Zeidler et al. 2015, AJ, 150, 78](#), [Zeidler et al. 2016, AJ, 152, 4](#) and [Zeidler et al. 2016, AJ, submitted](#).

The young massive star cluster Westerlund 2 (hereafter Wd2) was discovered in 1961 ([Westerlund 1961](#)) by, and later named after, Bengt Westerlund a Swedish astronomer. He identified it as a “fairly strong H II region”. It had been already reported by [Hill et al. \(1958\)](#) as being a radio source not connected to any optical source known at that time. [Westerlund \(1961\)](#) concluded that the source he detected is “an H II region excited by an association of young stars with a dense cluster in one part and a WN6¹ star in another”. According to his analysis Wd2 is about 6 kpc away with a varying extinction between $A_V = 1$ and 6 mag.

Since its discovery 55 years ago Wd2 has been discussed in multiple studies, yet many parameters, such as distance, age, and mass remained unclear. With an estimated stellar mass of $M \geq 10^4 M_\odot$ ([Ascenso et al. 2007a](#)) and an estimated molecular cloud mass of $(1.7 \pm 0.8 - 7.5) \cdot 10^5 M_\odot$ ([Furukawa et al. 2009](#); [Dame 2007](#), both based on millimeter CO spectroscopy), the young massive star cluster Wd2 is one of the most massive young star clusters known in the Milky Way (MW). It is embedded in the H II region RCW 49 ([Rodgers et al. 1960](#)) and located in the Carina-Sagittarius spiral arm $(\alpha, \delta) = (10^h 23^m 58^s .1, -57^\circ 45' 49'')$ (J2000), $(l, b) = (284.3^\circ, -0.34^\circ)$. [Moffat et al. \(1991a\)](#) suggest that Wd2 contains more than 80 O-type stars.

¹A WN6 star is a Wolf-Rayet star with an effective temperature of about $T_e = 56000$ K, and the following spectral features: $1.25 < \text{He II}/\text{He I} < 4$ and $0.2 < \text{NV}/\text{N III} < 0.5$ ([Smith et al. 1996](#)).

2.1 The RCW 49 H II region - the birthplace of Wd2

The giant H II region RCW 49 (Rodgers et al. 1960), also referred to as NGC 3247, is shown in Fig. 2.1.1 as a color composite image from observations obtained with the Infrared Array Camera (IRAC, Fazio et al. 2004) on board the *Spitzer* Space Telescope (Werner et al. 2004) for the Galactic Legacy Infrared Mid-Plane Survey Extraordinaire (GLIMPSE). The observations were carried out in the IRAC bands 1 to 4 with central wavelengths of $3.6 \mu\text{m}$, $4.5 \mu\text{m}$, $5.8 \mu\text{m}$, and $8.0 \mu\text{m}$, respectively. Further details on this program are provided in Benjamin et al. (2003). We marked some features such as the two Wolf-Rayet stars WR20a (e.g., Bonanos et al. 2004) and WR20b (e.g. van der Hucht 2001) and bow shocks created by the winds of individual O-stars colliding with large-scale interstellar gas flows (Povich et al. 2008).

RCW 49 and the Wd2 cluster were studied in more detail by Furukawa et al. (2009, 2014) and Ohama et al. (2010) using the NANTEN 2 4 m submillimeter/millimeter telescope (from the NANTEN CO Galactic Plane Survey (Mizuno and Fukui 2004)) in combination with *Spitzer* data (see Fig 2.1.1). They detected three different CO clouds with three different velocities (16 , 4 , and -4 km s^{-1} , relative to the local standard of rest (LSR), see Fig. 1 in Ohama et al. (2010) and Fig. 1 in Furukawa et al. (2009)). Furukawa et al. (2009, 2014) and Ohama et al. (2010) suggested that the creation of the RCW 49 region, with the Wd2 cluster as its central ionizing cluster, was induced by a cloud-cloud collision of two of these observed molecular clouds.

Fujita et al. (2009) observed the RCW 49 region using the Suzaku X-ray satellite. They detected a diffuse X-ray emission extending 8 arcmin from the cluster center. They concluded that this X-ray emission was caused by a star exploded as a hypernova. Since then, no such event was indicated by any other observation or study.

The presence of a faint, uniformly distributed low-mass population ($< 0.15 M_{\odot}$), visible throughout the RCW 49 area, is a hint that the actual star forming region is more extended than the Wd2 cluster. This phenomenon was already observed by Whitney et al. (2004), identifying ~ 300 young stellar object candidates in the giant H II region of RCW 49 using *Spitzer* IRAC MIR data of the GLIMPSE survey (Benjamin et al. 2003). Churchwell et al. (2004) described the RCW 49 gas and dust distribution as “a complex network of thin filaments, pillars, sharp boundaries, and knots”. This irregular distribution and the associated gas, probably created by the feedback of the massive stellar population, is a perfect birthplace for a new population of stars. Whitney et al. (2004) identified five more star-forming sites throughout the RCW 49 cloud. This is also known from other young star clusters e.g., NGC 3603, the ONC (e.g., Hillenbrand 1997), or the 30 Doradus region (e.g., Walborn et al. 1999; Brandner et al. 2001).

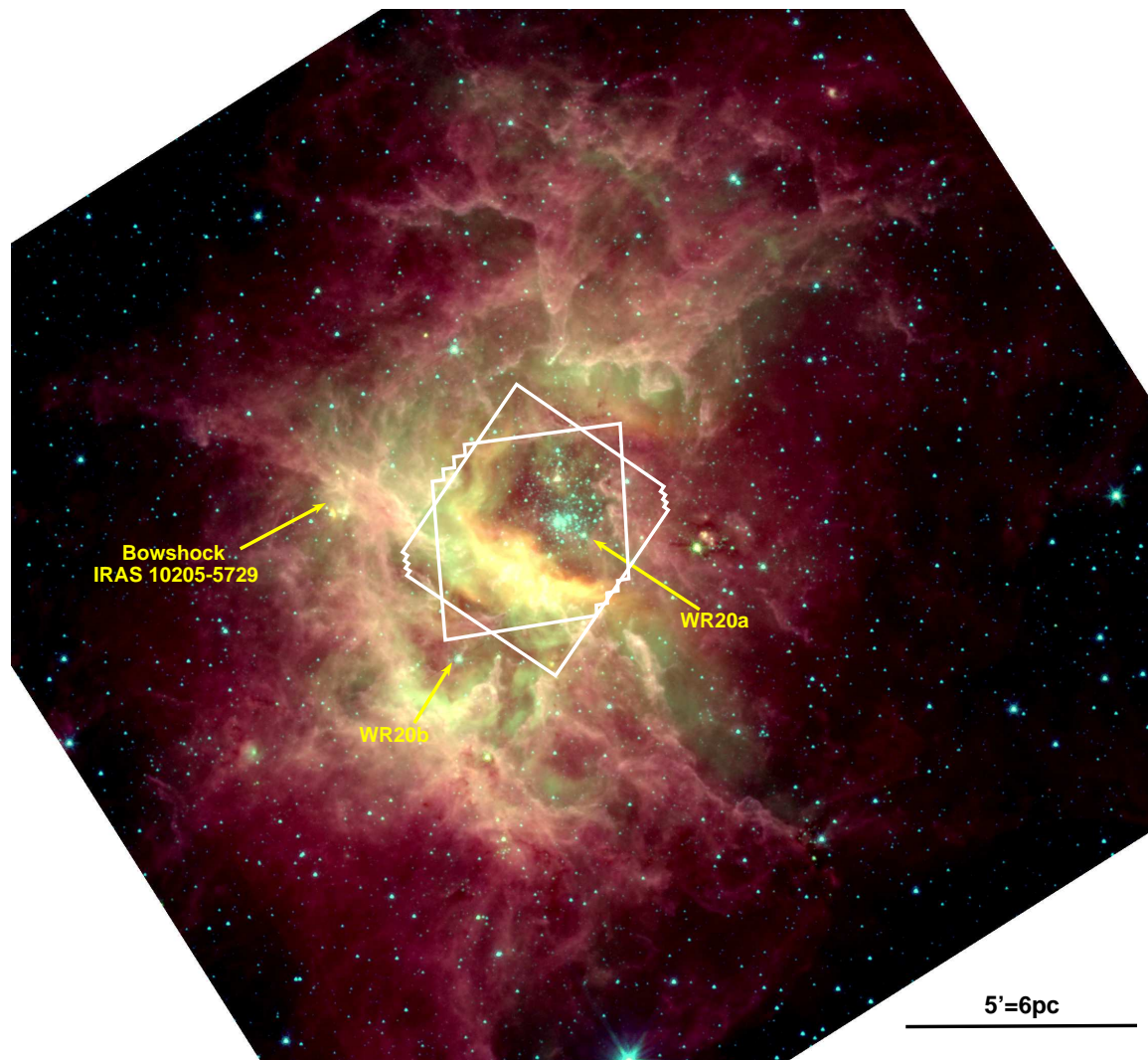


Figure 2.1.1: Color composite image of the *Spitzer* data of RCW 49, including the IRAC 1 ($3.6 \mu\text{m}$), IRAC 2 ($4.5 \mu\text{m}$), and IRAC 4 ($8.0 \mu\text{m}$) bands as red, green, and blue, respectively. North is up, East to the left. We show few features such as the two Wolf-Rayet stars WR20a and WR20b. Additionally, we give the outlines of the survey area of our HST observations (see Fig. 2.2.1)

2.2 Wd2 - A local laboratory for massive cluster evolution

Very few young ($< 5 \text{ Myr}$) and massive ($> 10^4 M_{\odot}$) star clusters are known in the MW, but they are frequently observed in the Magellanic Clouds as well as in the more distant Universe, especially in disk and starburst galaxies (e.g., [Gascoigne and Kron 1952](#); [Hodge 1961](#); [Clark et al. 2005](#)). Therefore, Wd2 is a perfect target to study the star formation process and feedback of the gas in the presence of massive stars as well as the possible triggering of star formation in the surrounding molecular cloud (suggested to occur in RCW 49 by [Whitney](#)

et al. 2004; Churchwell et al. 2004, using *Spitzer* mid-IR images). Additionally, there is no hint for a supernova explosion in Wd2, meaning no such destructive event has altered the cluster environment yet. This makes Wd2 a optimum target to study the PDMF of a young massive cluster very close to its initial conditions. It is possible to study the PDMF of the full upper MS intact, without any massive star already evolved away. However, the only study of the PDMF of Wd2 so far was carried out by Ascenso et al. (2007a) using ground-based JHK_s photometry. Ascenso et al. (2007a) derived a slope of the mass function of $\Gamma = -1.20 \pm 0.16$ assuming a distance of 2.8 kpc.

Due to Wd2's young age it is also perfect to study accretion processes of the PMS stars in the presence of a large number (~ 80 , see Moffat et al. 1991a) of O and B stars. In close proximity to OB stars, the disks may be expected to be destroyed faster by the external UV radiation originating from these massive stars. This would lead to a lower excess of $H\alpha$ emission in the direct neighborhood of the OB stars (Anderson et al. 2013; Clarke 2007). This gradient can be observed, when studying the PMS population of such a cluster.

In Fig. 2.2.1 we present the color-composite image of our optical and near-infrared (NIR) survey of Wd2, executed with the *Hubble* Space Telescope (HST). This image was chosen to be the official Hubble 25th anniversary image².

2.2.1 The distance to Wd2

The Wd2 cluster has been widely discussed in the literature over the last decade, yet its physical properties are poorly known. There is a considerable disagreement about the distance of Wd2: A value of 2.8 kpc was determined by Ascenso et al. (2007a) using isochrone fitting to ground-based JHK_s photometry and ZAMS fitting by Carraro et al. (2013) using UBV photometry. Vargas Álvarez et al. (2013) inferred a distance of 4.16 kpc using ZAMS fitting to 29 O-stars with HST/WFPC2 photometry and comparing the spectral types of these O-stars to models. 5.7 kpc was suggested by Piatti et al. (1998) based on a subset of O stars (Moffat et al. 1991b), while 6.4 kpc was determined by Carraro and Munari (2004) via isochrones fitting to $UBVRI$ photometry. A distance of $7.9^{+1.2}_{-1.0}$ kpc was estimated by (Moffat et al. 1991b) using UBV photometry and low resolution spectroscopy in order to classify six O-stars within Wd2. The largest distance of 8 kpc was suggested by Rauw et al. (2007) and Rauw et al. (2011) by a spectro-photometric fitting of 12 O-stars.

The studies of the CO emission spectrum in combination with the 21 cm absorption spectrum by Dame (2007) suggest that Wd2 must be located in between two molecular clouds, located at 6.5 kpc and 5.2 kpc. One major difficulty of this method is that Wd2 is located close to the tangent point of the Carina Arm as seen from us (i.e. Grabelsky et al. 1987), meaning that for gas clouds with a distance to the Sun smaller and larger than Wd2, the distance determination is degenerate.

²<http://hubblesite.org/newscenter/archive/releases/2015/12/image/a/>



Figure 2.2.1: Color composite image of the HST ACS and WFC3/IR data of Wd2, including the F_{125W} (red), F_{814W} (green), and F_{555W} (blue) filters. North is up, East to the left. The FOV is ~ 4 arcmin \times 4 arcmin. This image was chosen to be the official Hubble 25th anniversary image. Credit: NASA, ESA, the Hubble Heritage Team (STScI/AURA), A. Nota (ESA/STScI), and the Westerlund 2 Science Team.

2.2.2 The reddening toward Wd2

Wd2 is located at a Galactic latitude of $b = 0.34^\circ$ directly inside the Galactic plane, leading to a high extinction caused by the surrounding molecular gas and dust cloud of RCW 49, as well as the interstellar medium of the MW disk. In the past, several groups have tried to estimate the total-to-selective extinction toward Wd2.

Using the $J - K_s$ colors of the observed stars and the theoretical color inferred from fitting isochrones to the observed population, [Ascenso et al. \(2007a\)](#) estimated a total visual extinction of $A_V = 5.8 \pm 0.5$ mag as best fit, which does not exceed 10 mag throughout the cluster.

Using spectroscopic and photometric observations to fit SEDs for each of the stars with known spectral types and the theoretical absolute magnitudes and intrinsic colors known from model isochrones, [Vargas Álvarez et al. \(2013\)](#) estimated an average total-to-selective extinction of $R_V = 3.77 \pm 0.09$ and a visual extinction of $A_V = 6.51 \pm 0.38$ mag.

Carraro et al. (2013) used *UBVRI* photometry to fit O-type stars to the ZAMS, knowing their intrinsic colors. With this analysis they computed $R_V = 3.88 \pm 0.18$, in good agreement with the value found by Vargas Álvarez et al. (2013).

From the fitting of SEDs of O- and B-type stars observed with the VLT Survey Telescope and complemented with 2MASS Skrutskie et al. (2006) NIR photometry Mohr-Smith et al. (2015) derived $R_V = 3.96^{+0.14}_{-0.12}$ and $A_V = 6.34^{+0.44}_{-0.32}$ mag, both in excellent agreement with the above studies by Carraro et al. (2013) and Vargas Álvarez et al. (2013).

All R_V values are substantially larger than the MW average of $R_V = 3.1$ (Mathis and Wallenhorst 1981).

2.2.3 The stellar content of Wd2

The high-mass population

Wd2 contains a large number of massive, O and B-type stars. While the total content of O-type stars in Wd2 was estimated to be ~ 80 (Moffat et al. 1991a), different spectroscopic studies (Vargas Álvarez et al. 2013; Rauw et al. 2007, 2011) tried to reveal the existing massive stellar population. Up to this day the total count is 37, much lower than what (Moffat et al. 1991a) estimated. The spectral types range from B1V to O3V (for comparison see Tab. 2.2.1).

A series of spectra of WR20a were taken and analyzed by Rauw et al. (2004). They found that WR20a is a double-lined binary with a preferred orbital period of 3.675 ± 0.030 days, with component minimum masses of $68.8 \pm 3.8 M_\odot$ and $70.7 \pm 4.0 M_\odot$. They suggest a spectral type of WN6ha for both components. Bonanos et al. (2004) discovered it was also an eclipsing binary and refined those values to even higher masses of $83.0 \pm 5.0 M_\odot$ and $82.0 \pm 5.0 M_\odot$ since they also measured the inclination. Aharonian et al. (2007) suggested WR20a as a source for the observed γ -rays, using the High Energy Stereoscopic System (H.E.S.S) telescope. Rauw et al. (2005) and Carraro et al. (2013) discussed the location of WR20a outside the cluster center (projected distance: $d \approx 30''$). Both groups argue that WR20a is most likely a member of Wd2 but it is odd that the two most massive member stars of Wd2 are located outside the cluster center. One possibility would be that turbulences in the molecular cloud led to multiple sites of star formation and WR20a actually formed at its current location but so far there is no evidence of an overdensity of a low-mass PMS population in this region (see Sect. 8.3). Another possibility would be that WR20a actually formed in the cluster center and got ejected. Rauw et al. (2005) argue that the rather low velocity of $\sim 0.5 \text{ km s}^{-1}$ (for an age of 1.5 Myr) would not make the binary leave the cluster. The initial ejection velocity could have been larger, depending on the cluster's potential.

Table 2.2.1. Comparison to spectroscopic data

ID	RA (J2000)	Dec. (J2000)	SPEC. TYPE	MUTIPL.	identifier	reference	COMMENT
1	10:23:55.176	-57:45:26.89	O4 V	—	MSP 165	VA13	
2	10:23:56.160	-57:45:29.99	O4 V–III((f))	—	MSP 182	R07	
3	10:23:57.715	-57:45:34.27	O-B V	—	MSP 201	VA13	
4	10:23:57.152	-57:45:49.00	WN6ha+WN6ha	b	—	R04	WR20a
5	10:23:59.201	-57:45:40.53	O7.5 V	b	MSP 223	R11	(eclipsing)
6	10:24:01.920	-57:45:32.62	O8.5 V	—	MSP 196a	VA13	
7	10:24:00.353	-57:45:42.71	O8 V	—	MSP 229a	VA13	
8	10:24:00.475	-57:44:37.50	O-B V	—	MSP 28	VA13	
9	10:23:00.480	-57:45:24.01	O4 V	—	MSP 151	VA13	
10	10:24:00.499	-57:44:44.53	B1 V + PMS (K-type)	b	MSP 44	R11	eclipsing
11	10:24:00.528	-57:44:26.59	O-B V	—	VA 556	VA13	
12	10:24:00.713	-57:45:25.42	O8 V	—	MSP 157b	VA13	
13	10:24:00.816	-57:45:25.87	O6.5 V	—	MSP 157a	R07	
14	10:24:00.979	-57:45:05.50	B1 V + B1 V	b	MSP 96	R11	eclipsing
15	10:24:01.070	-57:45:45.73	O9.5 V	—	MSP 233	VA13	
16	10:24:01.200	-57:45:31.07	O3 V	b	MSP 188	VA13	(O4 + O5.5)
17	10:24:01.392	-57:45:29.66	O4 V	(b)	MSP 175	VA13	
18	10:24:01.454	-57:45:31.33	O3 V	(b)	VA 714	VA13	
19	10:24:01.524	-57:45:57.06	O6 V	—	MSP 263	R07	
20	10:24:01.610	-57:45:27.89	O5.5 V	—	MSP 168	VA13	
21	10:24:01.889	-57:45:40.05	O9.5 V	—	MSP 219	VA13	
22	10:24:01.889	-57:45:28.00	O8 V	—	MSP 167b	VA13	
23	10:24:02.064	-57:45:28.01	O6 III	(b)	MSP 167a	R11	
24	10:24:02.186	-57:45:31.32	O9.5 V	—	MSP 183d	R11	
25	10:24:02.256	-57:45:35.12	O4–5 V	—	MSP 203a	R11	
26	10:24:02.304	-57:45:35.53	O4.5 V	—	MSP 444a	VA13	
27	10:24:02.376	-57:45:30.64	O3 V((f))	—	MSP 183a	R11	
28	10:24:02.400	-57:45:38.16	O-B V	—	VA 878	VA13	
29	10:24:02.414	-57:45:47.11	O9.5 V	—	MSP 235	VA13	
30	10:24:02.448	-57:44:36.13	O5 V–III	(b)	MSP 18	R11	
31	10:24:02.518	-57:45:31.47	O8.5 V	—	MSP 183b	VA13	
32	10:24:02.555	-57:45:30.52	O8.5 V	—	MSP 183c	VA13	
33	10:24:02.604	-57:45:32.26	O6–7 V	—	VA 906	R11	
34	10:24:02.664	-57:45:34.38	O3–4 V	—	MSP 199	R11	
35	10:24:02.789	-57:45:30.05	O8 V	—	VA 924	R11	
36	10:24:03.787	-57:44:39.87	O9.5 V	—	MSP 32	VA13	
37	10:24:04.901	-57:45:28.43	O4–5 V	—	MSP 171	R11	

Note. — All stars with a determined spectroscopic type from [Vargas Álvarez et al. \(2013\)](#) and [Rauw et al. \(2007, 2011\)](#). Column 1 shows the stellar ID used to refer to a specific star. Columns 2 and 3 list the J2000 coordinates followed by the spectral type. Column 5 gives information about the binarity of the stars. The brackets indicate a binary candidate, whose binarity has not been confirmed due to insufficient data. Column 6 provides the MSP ([Moffat et al. 1991a](#)) identifier or the VA ([Vargas Álvarez et al. 2013](#)) identifier. Column 7 list the reference for the latest spectral classification: R07 for [Rauw et al. \(2007\)](#), R11 for [Rauw et al. \(2011\)](#), and VA13 for [Vargas Álvarez et al. \(2013\)](#). Column 8 gives additional information.

Three other Wolf-Rayet stars (WR20aa, WR20b, WR20c), located in the surroundings of Wd2, are also believed to be runaway members of Wd2. Due to the similar reddening of WR20b and WR20a and the location close to the cluster (see Fig. 2.1.1), it is very likely that WR20b is a cluster member (Carraro et al. 2013). Roman-Lopes et al. (2011) suggest that also the two Wolf-Rayet stars WR20aa (projected distance: $d \approx 15.7'$) and WR20c (projected distance: $d \approx 25'$) got ejected from the cluster core through interactions with each other, based on the perfect projected alignment between the two stars and the Wd2 cluster core.

Additionally to the WR20a star, two more O-stars are known eclipsing binaries. Rauw et al. (2011) determined orbital solutions using VLT/FLAMES spectra. For the binary system MSP 96 (see Moffat et al. 1991a) they determined an orbital period of 1.0728 ± 0.0006 days. They suggest minimum masses of $M_p \sin^3 i = 11.1 \pm 3.0 M_\odot$ and $M_s \sin^3 i = 13.8 \pm 6.6 M_\odot$ for the primary and secondary component, respectively. Their *BV* photometry supports absolute masses of $M_p = 12.0 \pm 3.3 M_\odot$ and $M_s = 15.0 \pm 7.2 M_\odot$ and a spectral type of B1V is suggested for both components. For the binary system MSP 44 (see Moffat et al. 1991a) Rauw et al. (2011) determined an orbital period of 5.176 ± 0.029 days. From a very low mass ratio, they inferred a B1 primary with a mass of 10–12 M_\odot and a PMS companion with a mass of 1.4–1.6 M_\odot , most likely being an F-type star.

The PMS population

Most of the work that has been done so far on Wd2 was addressing the high-mass stellar population. Due to the high extinction, the observation of the low-mass population is rather challenging. (Whitney et al. 2004) used *Spitzer* space telescope data to identify ~ 300 YSO candidates in the whole RCW 49 region via SED fitting. Due to the limited spatial distribution and the dense stellar population it was impossible to study the PMS population in detail.

Using ground-based *JHK_s* near IR data Ascenso et al. (2007a) extracted PMS stars down to 1 M_\odot . Inferring a distance of 2.8 kpc using isochrone fitting and a Kroupa (2001) like PDMF, they estimated a total mass of $\sim 10^4 M_\odot$ for Wd2. Additionally, they suggest a significant mass segregation of the massive stars. The ground-based data is seeing limited at a spatial resolution of 0.6'', which influences their completeness in the dense cluster center.

2.2.4 The age of Wd2

A consensus has not been reached on the age of Wd2 either, although there seems to be general agreement that the cluster as a whole is younger than 3 Myr and that the core may be even younger than 2 Myr (Ascenso et al. 2007a; Carraro et al. 2013). Both Ascenso et al. (2007a) and Carraro et al. (2013) inferred the age by comparing the locus of the brightest stars with the locus of isochrones. Additionally, Carraro et al. (2013) used *Chandra* X-ray data. An upper age limit of ~ 3 Myr is also in agreement with the typical lifetime of most of the O3–O5 stars of ~ 2 –5 Myr (e.g., Sparke and Gallagher 2007), since until now there is no hint for a supernova explosion in Wd2.

This young age combined with the cluster's half-light radius³ of about 2.4 pc and its total mass make it likely that Wd2 is younger than half of its typical crossing time⁴ (~ 5.5 Myr, [Gieles and Portegies Zwart 2011](#)). Therefore, the physical conditions of Wd2 are very close to its initial conditions.

³The half-light radius defined by the circular area in which half of the total emitted light is emitted.

⁴The crossing time is the time needed, for a typical cluster star, to cross the cluster once ([Binney and Tremaine 1987](#)).

Deine Augen können dich täuschen, traue ihnen nicht.

— Obi-Wan Kenobi

3

HST observations and data reduction

This chapter is included in Sect. 2 of [Zeidler et al. 2015, AJ, 150, 78](#).

3.1 Observations

Our observations of Wd2 were performed with the HST during Cycle 20 using the Advanced Camera for Surveys (ACS, [Ubeda et al. 2012](#)) and the Infrared Channel of the WFC3/IR ([Dressel 2012](#)). Six orbits were granted and the science images were taken on 2013 September 2–8 (ID: 13038, PI: A. Nota).

We acquired data in six different filters: four wide band filters and two narrow band filters. We imaged Wd2 with ACS (resolution $0.049''/\text{px}$) through the $F555W$ and $F814W$ filters, corresponding to the V and I -bands, as well as the $F658N$ filter, centered on the $H\alpha$ line. We also observed the cluster with WFC3/IR (resolution $0.135''/\text{px}$) in the $F125W$ and $F160W$ filters matching the J and H -band, as well as the $F128N$ filter corresponding to the $\text{Pa}\beta$ line. In addition, short exposures were acquired in the $F555W$ and $F814W$ bands (hereafter denoted as $F555W(s)$ and $F814W(s)$) to reduce saturation of the O-type stars in the very bright cluster center and across the field of view (FOV).

In total a FOV of $\sim 200'' \times 200''$ was needed to cover the Wd2 cluster and parts of its surround H II region. Therefore, we used one ACS pointing to cover Wd2 and a dither pattern with four positions for the long-exposures (350 s each) in the broad band filters, subsequently replaced by a two-position dithering for the $F658N$ filter (for a total exposure time of 1400 s). The short exposures were only observed at one position, each with an exposure time of 3 s. The ACS dither pattern was performed with a shift in x and y direction with an offset of $\Delta x = 15''$ and $\Delta y = 15''$ between two exposures, expressed in the internal detector

Table 3.1.1. Overview over the observations

DATASET	FILTER	CAMERA	RA(J2000)	DEC(J2000)	EXP. TIME [s]	# EXP.	DATE
IBYA01010	<i>F555W</i>	ACS	10:24:08.989	-57:46:20.95	1400	4	2013-09-02
IBYA01010	<i>F555W(s)</i>	ACS	10:24:08.989	-57:46:20.95	3	1	2013-09-02
JBYA01020	<i>F658N</i>	ACS	10:24:03.756	-57:45:33.02	1400	2	2013-09-02
JBYA01030	<i>F814W</i>	ACS	10:24:08.989	-57:46:20.95	1400	4	2013-09-02
JBYA01030	<i>F814W(s)</i>	ACS	10:24:08.989	-57:46:20.95	3	4	2013-09-02
IBYA08010	<i>F125W</i>	WFC3/IR	10:24:07.294	-57:44:05.26	947	4	2013-09-02
IBYA09010	<i>F125W</i>	WFC3/IR	10:24:16.116	-57:45:48.56	947	4	2013-09-02
IBYA10010	<i>F125W</i>	WFC3/IR	10:24:55.869	-57:45:07.69	947	4	2013-09-03
IBYA11010	<i>F125W</i>	WFC3/IR	10:24:04.686	-57:46:51.05	947	4	2013-09-08
IBYA08030	<i>F128N</i>	WFC3/IR	10:24:07.294	-57:44:05.26	748	3	2013-09-02
IBYA09030	<i>F128N</i>	WFC3/IR	10:24:16.116	-57:45:48.56	748	3	2013-09-02
IBYA10030	<i>F128N</i>	WFC3/IR	10:24:55.869	-57:45:07.69	748	3	2013-09-03
IBYA11030	<i>F128N</i>	WFC3/IR	10:24:04.686	-57:46:51.05	748	3	2013-09-08
IBYA08020	<i>F160W</i>	WFC3/IR	10:24:07.294	-57:44:05.26	947	4	2013-09-02
IBYA09020	<i>F160W</i>	WFC3/IR	10:24:16.116	-57:45:48.56	947	4	2013-09-02
IBYA10020	<i>F160W</i>	WFC3/IR	10:24:55.869	-57:45:07.69	947	4	2013-09-03
IBYA11020	<i>F160W</i>	WFC3/IR	10:24:04.686	-57:46:51.05	947	4	2013-09-08

Note. — This table summarizes the observations of Wd2 taken with the ACS and WFC3/IR cameras aboard HST. Given are the identifiers of the datasets, the filter, camera, as well as the central coordinates of each dither position. The exposure time is the total exposure time of all dither positions combined. We also give the observation date for each image.

coordinate system, leading to a total shift of $45''$ in both directions between the first and the last exposure ($15''$ for the narrow-band observations). For the WFC3/IR observations mosaics of 2×2 tiles were required since the WFC3/IR has a smaller FOV than the ACS ($\text{FOV}_{\text{ACS}} = 202 \times 202$ arcsec and $\text{FOV}_{\text{WFC3}} = 123 \times 136$ arcsec). Each wide-band tile consists of four dither positions with a total exposure time of 947 s (3×250 s and 1×200 s). The narrow band tiles consist of three dither positions with a total exposure time of 748 s (250 s each). The WFC3/IR dither pattern was a shift in x and y direction with an offset of $\Delta x = 7''$ and $\Delta y = 7''$ between two exposures, expressed in the internal detector coordinate system, leading to a total shift of $21''$ in both directions between the first and the last exposure ($14''$ for the narrow-band observations). The log of the observations is reported in Tab. 3.1.1 together with the filters and exposure times used. An overview of the spatial positions of all images as well as their alignment is given in Fig. 3.1.1.

3.2 Data reduction

The observed data were first processed with the internal pipeline (Ubeda et al. 2012; Dreschel 2012) (from now on referred to as raw data), which delivers pipeline flat-fielded files (`flt.fits` for WFC3) or charge-transfer efficiency (CTE) corrected images (`flc.fits` for ACS).

The reduction of the raw data was performed with AstroDrizzle (Fruchter 2010), the follow-up tool of MultiDrizzle in the HST pipeline. Since the instruments (ACS and WFC3) and the pipeline data products are substantially different we treat the related images sep-

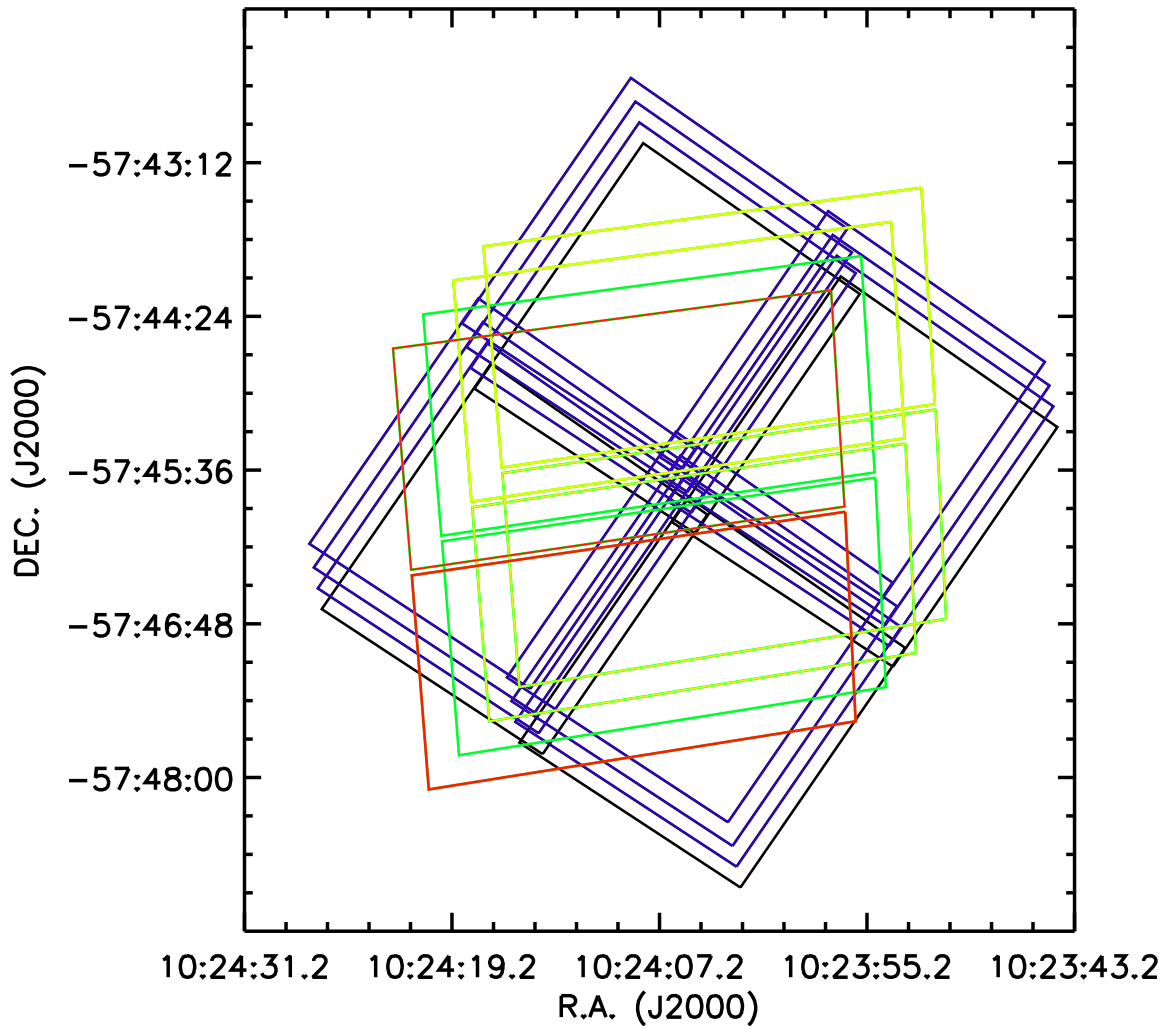


Figure 3.1.1: The field of view for the different exposures taken with the WFC3/IR and ACS filters. The blue and black fields together, represent the F_{125W} and F_{160W} WFC3/IR exposures, while the blue fields alone represent the F_{128N} WFC3/IR dithered images. The yellow, green, and red fields together represent the ACS F_{814W} and F_{555W} long exposures, while the yellow fields represent the F_{658N} dither positions. The red field alone represents the short exposures for ACS F_{814W} and F_{555W} .

arately. First we will give a brief overview over AstroDrizzle and then we discuss the data reduction of the two instruments separately.

3.2.1 The AstroDrizzle package

The reduction of the raw data consists of multiple steps performed by AstroDrizzle, which was mainly developed to improve the handling of astrometric and geometric distortion corrections. The major goal of AstroDrizzle is to reconstruct and recover the spatial information of a set of images while preserving the signal-to-noise ratio (S/N). In AstroDrizzle, this is done

by the method formally known as variable-pixel linear reconstruction (commonly known as Drizzle) developed by Andy Fruchter and Richard Hook (Fruchter and Hook 1997). A detailed description of the package can be found in the manual of DrizzlePac (<http://drizzlepac.stsci.edu>). The DrizzlePac is a package of different software modules, delivered as a bundle that supports the AstroDrizzle routine. The different modules are:

- `tweakreg` and `tweakback` for the alignment of images of different visits to one reference coordinate system,
- `pixtop` to transform the x and y coordinates to the distortion corrected coordinates x' and y' ,
- `skytopy` and `pixtosky` to transform sky coordinates to pixel coordinates and vice versa.

AstroDrizzle performs its tasks on pipeline flat-fielded files (`_flt.fits`) or charge-transfer-efficiency (CTE) corrected images (`_flc.fits`). The general concept of AstroDrizzle is to partly recover the high frequency information smeared out by the detector pixel response function via combining the sub-pixel dithered images. This algorithm gives us the chance of recovering spatial information of the under-sampled¹ WFC3/IR images to reconstruct a final combined image with a higher spatial resolution. In the case of multiple dither-positions the final combined (drizzled) image is free of cosmic rays and detector defects, such as hot and dead pixels. As an example we show a part our $F814W$ observations (see Fig. 3.2.1). We marked examples of cosmic rays, hot and dead pixels, as well as stars where the geometric distortion correction becomes obvious when comparing the two images. At the end all images are aligned to the same reference frame, provided by the world coordinate system (WCS) information in the header of one of the images.

The algorithm maps pixels of the original input images (x_i and y_i , with i being the different dither positions of the same pointing) onto the new, spatially higher resolved, pixel grid x' and y' . It takes into account the shifts and rotations between the images, as well as the optical distortion of the camera, provided by calibration files. The new pixel size is controlled by the `pixfrac` parameter (as percentage of the detector pixel size). This process is visualized in Fig. 3.2.2.

The input pixels x_i and y_i , which are mapped onto the same output pixel x' and y' , are combined in a way that their fluxes are distributed with weights proportional to the area of overlap between the original pixels and the new pixel grid. The `pixfrac` parameter needs to be chosen such that the convolution of the image with a too large input pixel footprint is avoided, and yet sufficiently large so that small enough variations in the input pixels contribute to each output pixel. To quantify the weight of each pixel, so-called weighted maps are created (as example see Fig. 3.2.3 for the $F555W$ filter). The remaining weighted maps are shown in the Appendix A. These maps contain information about bad pixels as well as saturated sources, and assign a lower weight to these pixels so that their contribution to the final drizzled image is less. These weighted maps need by-eye inspection.

¹The WFC3/IR images are under sampled means that the spatial resolution is limited by the pixel size of the camera.

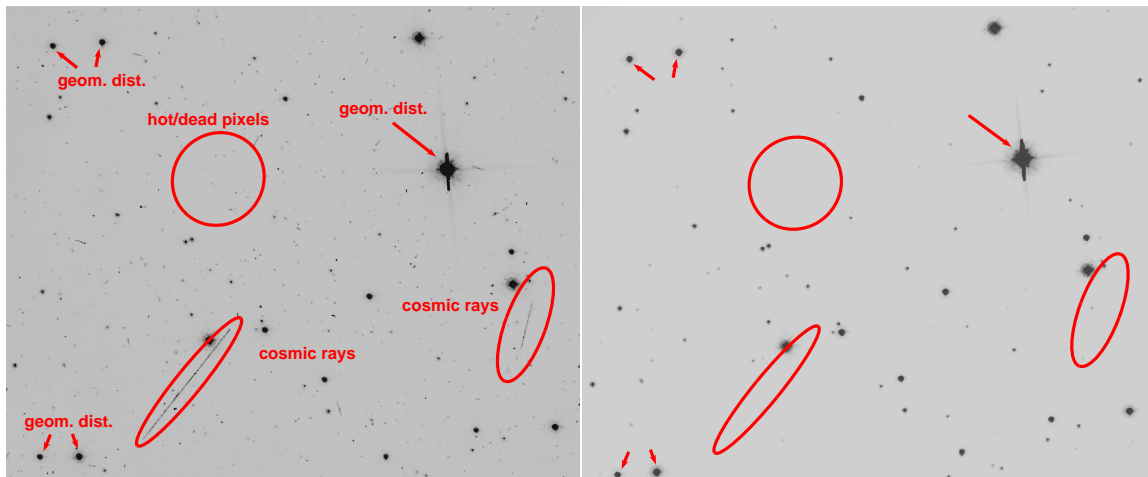


Figure 3.2.1: Part of the $F814W$ image before (left) and after (right) cosmic ray and detector defect cleaning and geometric distortion correction. On the left image we marked examples for cosmic rays and hot and dead pixels. The same regions are marked on the right image. We also marked distinct stars where the geometric distortion correction becomes visible, either by the location of the stars (the same WCS region is shown in both images) or by the angle between the diffraction spikes of a bright star.

3.2.2 The ACS data

During the whole process, the short exposures for the $F555W$ and the $F814W$ filters are treated individually and are labeled as $F555W(s)$ and $F814W(s)$, since AstroDrizzle cannot effectively combine images of very different exposure times.

For all ACS images we used a $\text{pxfrac}=0.9$ for the drizzling process meaning that each pixel is shrunk by 10% in size before being mapped onto the output grid. This value was chosen so that the size of the point-spread-function (PSF) of the drizzled image reaches a minimum while mapping all pixels properly to the output grid (see Sect. 3.3). The output pixel grid has the same pixel size as the original image (0.049 arcsec/pixel). Since there is only one dither position available for the short exposures (see Fig. 3.1.1), the cosmic-ray and detector defect removal could not be accomplished. Nevertheless, we drizzled those images to correct them for geometric distortion and to align them properly to the reference frame. The short exposures are only taken to recover the photometry of sources that are saturated in the long exposures.

3.2.3 The WFC3/IR data

The PSF of the IR data is under-sampled. Therefore, we reduced the pixel size of the output grid to recover as much spatial information as possible for the determination of the optimal pixel size. If the pixel size in combination with the pixel fraction is shrunk too much, there is not enough information left for mapping the pixels properly onto the output grid without generating “holes” of empty pixels. Taking into account the weighted maps (see Fig. A.0.3, Fig. A.0.4, and Fig. A.0.5) representing the contribution of each pixel to the final image

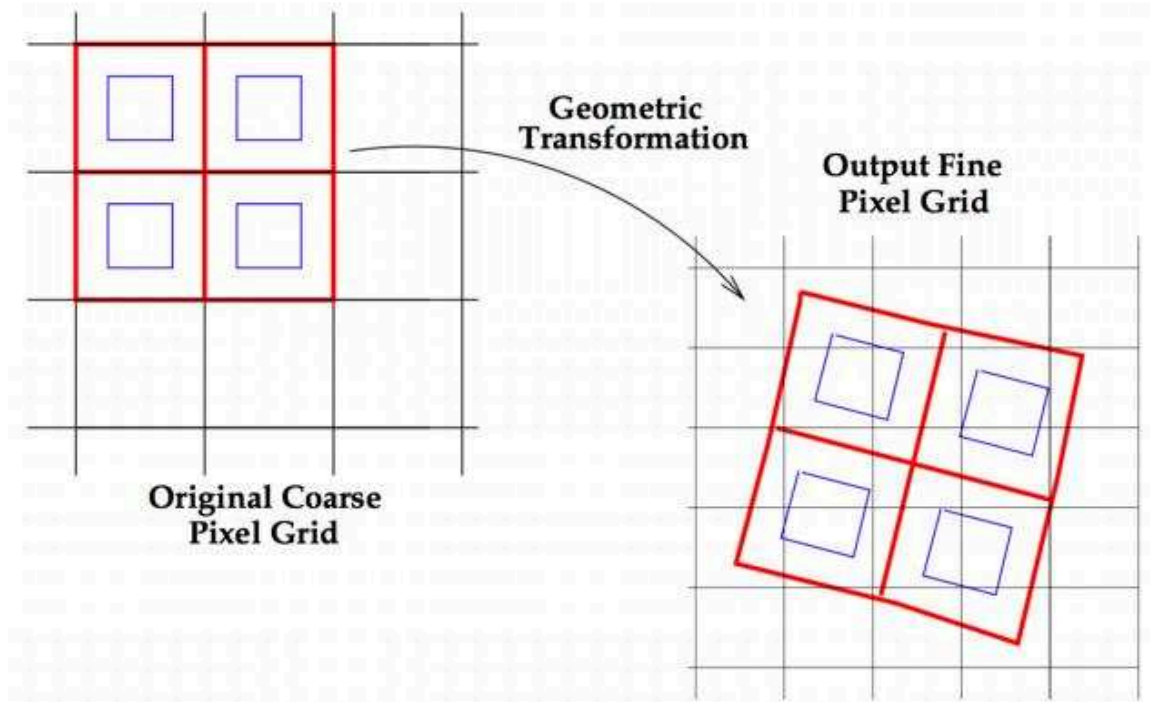


Figure 3.2.2: The schematic illustration of the drizzle process, representing the mapping of the observed pixel values onto a new smaller grid, taking into account rotations, shifts, and distortion corrections. Image credit: <http://drizzlepac.stsci.edu>

and the final FWHM of the PSFs of some representative stars, we chose a final pixel size of 0.098 arcsec/px with a $\text{pxfrac}=0.8$. The data would have allowed us to reduce the pixel size slightly more, but we found it convenient to have a pixel size twice that of the ACS, so each WFC3IR pixel is covered by four ACS pixels. In addition, we mosaicked the four different pointings into a single image.

In the end we had five combined images for the ACS data set, one for the narrow-band and two (short and long exposures) for the wide-band filters. For the WFC3/IR filters we had three mosaics in total, one for each filter. The mosaics of the final ACS (long exposures) and WFC3/IR images are shown in the Appendix B, in Fig. B.0.1, Fig. B.0.2, Fig. B.0.3, Fig. B.0.4, Fig. B.0.5, and Fig. B.0.6.

3.3 Quality check of the final images

In order to check the quality of the drizzled ACS images, we tested the stability of the weighted maps (see Sect. 3.2.1) of the final products. In order to determine the variations in the weighted maps, 28 boxes (20 for the $F658N$ filter) of 100×100 pixels and 16 boxes of 250×250 pixels were selected across the image. In each box the standard deviation of

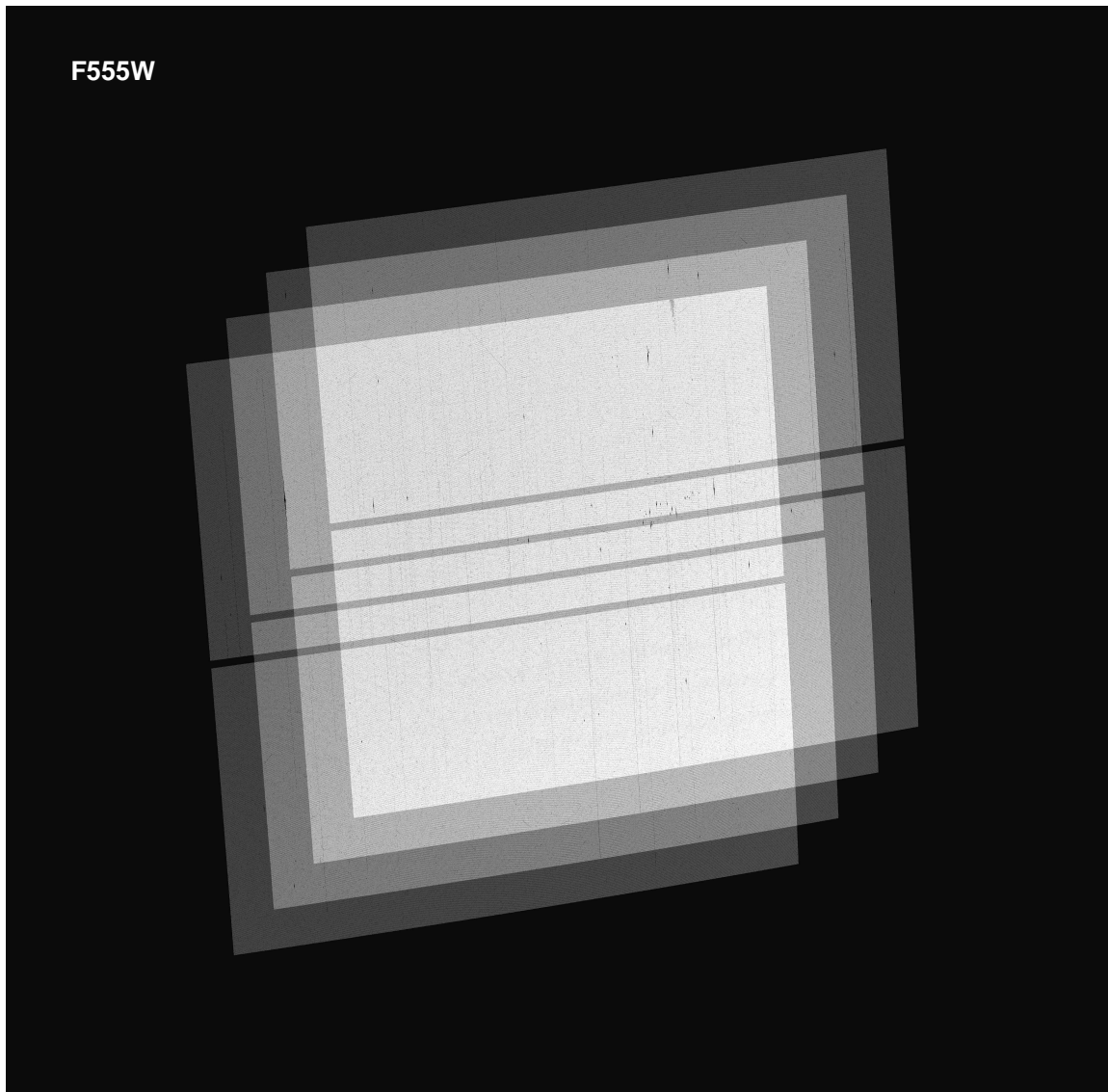


Figure 3.2.3: The *F555W* weighted map for the final drizzled and aligned image.

the median was determined using the IRAF² task IMEXAMINE. This ratio should be below 0.2 following the DrizzlePac manual, meaning that the deviation of the weights of the different pixels should be less than 20%. This test could not be performed for the IR data due to the different readout method. The results of this test show that the deviation is below 20% for both the small and the large boxes, leading to the conclusion that the quality of the final products is fine. The results are shown in Table 3.3.1.

²IRAF is contributed by the National Optical Astronomy Observatory, which is operated by the Association for Research in Astronomy, Inc., under cooperative agreement with the National Science Foundation.

Table 3.3.1. Summary of the weighted maps of the AstroDrizzle pipeline

FILTER	# BOXES	BOXSIZE [px]	median	σ	$\frac{\sigma}{\text{median}}$
<i>F555W</i>	28	100 × 100	1318	147.7	0.1147
<i>F555W</i>	16	250 × 250	1325	142.2	0.1099
<i>F658N</i>	20	100 × 100	1336	208.5	0.1618
<i>F658N</i>	16	250 × 250	1339	206.7	0.1599
<i>F814W</i>	28	100 × 100	1317	147.3	0.1145
<i>F814W</i>	16	250 × 250	1322	147.7	0.1137

Note. — In this table we give a summary of the tests for the weighted maps. The first column shows the corresponding filter. Column 2 gives the number of boxes per image. Column 3 lists the boxsizes for calculating the median and the standard deviation of the pixel values. Column 4 and 5 show the median and the standard deviation of the pixel values, respectively. Column 6 lists the ratio of the standard deviation and the median.

Table 3.3.2. The mean FWHM of the PSFs in the different filters

FILTER	FWHM [px]	σ_{FWHM} [px]	FWHM [arcsec]	σ_{FWHM} [arcsec]
<i>F555W</i>	2.154	0.1044	0.1055	0.0125
<i>F658N</i>	2.034	0.3848	0.0997	0.0187
<i>F814W</i>	2.011	0.2304	0.0986	0.0113
<i>F125W</i>	2.188	0.2145	0.2144	0.0210
<i>F128N</i>	2.410	0.2362	0.2362	0.0231
<i>F160W</i>	2.242	0.2197	0.2197	0.0215

Note. — The mean FWHM of the PSF of 25 selected stars in each filter. The first column shows the corresponding filter. Column 2 and 3 show the FWHM and the standard deviation in pixels and column 4 and 5 show the FWHM and the standard deviation in arcsec.

In addition, we determined the FWHM of a sample of 25 carefully selected stars across each field with the IRAF task IMEXAMINE. We chose medium bright, isolated, non-saturated stars so that the PSFs are not contaminated by close neighbors or remaining detector artifacts. For the PSF determination, all ACS images were divided into four quadrants. The mean FWHM of the 25 selected stars in each filter is listed in Tab. 3.3.2. The FWHM range over the whole chip is given in the ACS manual (Ubeda et al. 2012), with the FWHM of $F555M = 2.12\text{--}2.49$ pixels as reference. The FWHM is quite constant between the different ACS filters and even the WFC3/IR filters. Our determined values are within the PSF range in the $F555M$ filter, meaning that quality and, therefore, the drizzle parameters are fine.

Zwar weiß ich viel, doch möcht ich alles wissen.

— Johann Wolfgang von Goethe: Faust, Vers 317

4

The photometric catalog

This chapter is included in Sect. 3 of [Zeidler et al. 2015, AJ, 150, 78](#).

The source detection and photometry were performed with the DOLPHOT¹ package, including the extensions for ACS and WFC3/IR written by Andrew Dolphin.

4.1 Source detection and photometry

DOLPHOT is a modified version of HSTphot ([Dolphin 2000](#)). It is a stellar photometry package that supports two modes: 1) a generic PSF-fitting package (using analytic PSF models for any camera) and 2) using ACS PSFs and calibrations. Throughout the thesis we use DOLPHOT to refer to the photometric package and `dolphot` to refer to the actual photometry routine. In this chapter we only give a brief overview of the parts of the DOLPHOT package we used for our data reduction. A more detailed description with all possible settings can be found at <http://americano.dolphinsim.com/dolphot/>.

DOLPHOT handles the image preparation, meaning the masking of bad pixels (`acsmask` and `wfc3mask`), such as camera defects, warm and hot pixels, filter defects, and saturated pixels using the weighted maps from AstroDrizzle. It is also capable of performing image cleaning e.g., cosmic ray removal and image combination (dithered observations and mosaics), for which we used AstroDrizzle (see Sect. 3.2.1). The `calcsky` routine is used to create a skymap for all processed images to determine the background. This is the mandatory final step before running the photometric routine `dolphot`. The sky is determined locally as the mean within an annulus around each star. The size of the annulus r_{in} and r_{out} , the rejection

¹<http://americano.dolphinsim.com/dolphot/>

Table 4.1.1. The parameters used to run the photometric routine

PARAMETER	<i>F555W</i>	<i>F555W</i> (s)	<i>F658N</i>	<i>F814W</i>	<i>F814W</i> (s)	<i>F125W</i>	<i>F128N</i>	<i>F160W</i>
shift	0 0	0 0	0 0	0 0	0 0	0 0	0 0	0 0
xform	1 0 0	1 0 0	1 0 0	1 0 0	1 0 0	1 0 0	1 0 0	1 0 0
apsky	15 25	15 25	15 25	15 25	15 25	15 25	15 25	15 25
RAper	4	4	4	4	4	3	3	3
RSky0	15	15	15	15	15	8	8	8
RSky1	35	35	35	35	35	20	20	20
RPSF	10	10	10	10	10	10	10	10
RCentroid	2	2	2	2	2	2	2	2
SigFind	3.0	3.0	3.0	3.0	3.0	3.0	3.0	3.0
SigFindMult	0.85	0.85	0.85	0.85	0.85	0.85	0.85	0.85
SigFinal	3.0	3.0	3.0	3.0	3.0	7.0	7.0	7.0
MaxIT	25	25	25	25	25	25	25	25
PSFPhot	1	1	1	1	1	1	1	1
FitSky	3	3	3	3	3	3	3	3
SkipSky	2	2	2	2	2	1	1	1
SkySig	2.25	2.25	2.25	2.25	2.25	2.25	2.25	2.25
NoiseMult	0.10	0.10	0.10	0.10	0.10	0.10	0.10	0.10
FSat	0.999	0.999	0.999	0.999	0.999	0.999	0.999	0.999
PosStep	0.25	0.25	0.25	0.25	0.25	0.25	0.25	0.25
dPosMax	3.0	3.0	3.0	3.0	3.0	3.0	3.0	3.0
RCombine	1.5	1.5	1.5	1.5	1.5	1.5	1.5	1.5
SigPSF	5.0	5.0	5.0	5.0	5.0	5.0	5.0	5.0
UseWCS	1	1	1	1	1	1	1	1
Align	4	4	4	4	4	3	3	3
AlignIter	4	4	4	4	4	4	4	4
useCTE	0	0	0	0	0	0	0	0
Rotate	1	1	1	1	1	1	1	1
SecondPass	5	5	5	5	5	3	3	3
Force1	0	0	1	0	0	1	1	1
PSFres	1	1	1	1	1	1	1	1
psfoff	0.0	0.0	0.0	0.0	0.0	0.0	0.0	0.0
ApCor	1	1	1	1	1	1	1	1

Note. — In this table we give, for each filter, the different parameters used to run the DOLPHOT photometric routine. We want to note here that due to an update, some of the parameter names have changed between the time we obtained the photometry and the time we ran the artificial star tests (see Sect. 5). We give here the updated names at the time we ran the artificial stars.

threshold of the deviation from the mean σ_{low} and σ_{high} , as well as the number of iterations, are defined by the user. The parameters used for our data are listed in Table 4.1.1.

After preprocessing all images, the `dolphot` photometric routine can be run. Depending on the observations either the ACS module or the WFC3/IR module needs to be applied. The different parameters, with which `dolphot` can be run are listed in the DOLPHOT manual and in the manual of each module (the newest version is available on <http://americano.dolphinsim.com/dolphot/>). For each module, pixel area maps and precomputed PSFs (for each filter) are available and need to be installed. The source detection runs iteratively to find an optimal solution for the detection and the photometry of all stars by removing sources for which the detection has already converged. After a final number of steps (set by the user), or when all detections converged, aperture corrections are applied to the photometry.

For the source detection and photometry we adopted individual parameters for each

filter. We considered the size of the PSFs, the different saturation limits, and the nebulosity conditions (due to the very different level of gas and stellar density). The main effort was to detect all sources and yet to avoid as much contamination by spurious objects as possible in order to make the cleaning procedure later-on easier. Spurious detections may happen in particular in regions with varying background brightness due to the varying gas and dust density in the H II region and stellar crowding.

DOLPHOT uses the drizzled images for the source detection and works on images (flcs and flts) with geometric-distortion-corrected headers (performed by AstroDrizzle) (from now on called processed images). To perform the source detection, several steps have to be applied in a given order: `acsmask` (`wfc3mask`) to mask the processed images for detector artifacts and other defects using the weighted maps, `splitgroups` to create single chip and single layered fits files, and `calcsky` to create a skymap for all the processed images.

After those preparatory steps the actual `dolphot` routine was used to create a point-source catalog using the PSF and pixel area maps from an analytic model of ACS and WFC3/IR, provided on the DOLPHOT webpage. The output of DOLPHOT is one catalog per filter and exposure, containing amongst others, the pixel coordinates of the stars and their magnitudes as well as different kinds of quality flags, which are used later in the catalog cleaning process. So in total 8 catalogs were produced. We list the parameters, which we used to run the photometric routine, in Table 4.1.1.

4.2 Improving the quality of the Photometric Catalogs

Initially, the photometric catalogs contain a number of spurious objects, which must be removed. We cleaned the photometric catalogs by applying appropriately chosen trimming parameters for each of the filters. The trimming values for the WFC3/IR and ACS instruments are given in the DOLPHOT manual. In order to ensure that as many spurious objects as possible were deleted, still preserving all real objects especially in the nebular regions and the dense cluster center, we had to find the optimal parameter set for DOLPHOT. These values were adjusted by visual inspections of the observations of the removed and the kept objects.

4.2.1 Object Type

The objects are classified as different types (OT) by DOLPHOT: good star (1), star too faint for PSF determination (2), elongated object (3), object too sharp (4), extended object (5). We only kept the objects with OT=1, which removed already more than half of the false detections. For the WFC3/IR filters we did not select by object type in order not to lose any objects, since an bye-eye inspection showed that also and OTs different than 1 were assigned to stars. The distribution of the OTs for the ACS filters can be seen in Fig 4.2.1.

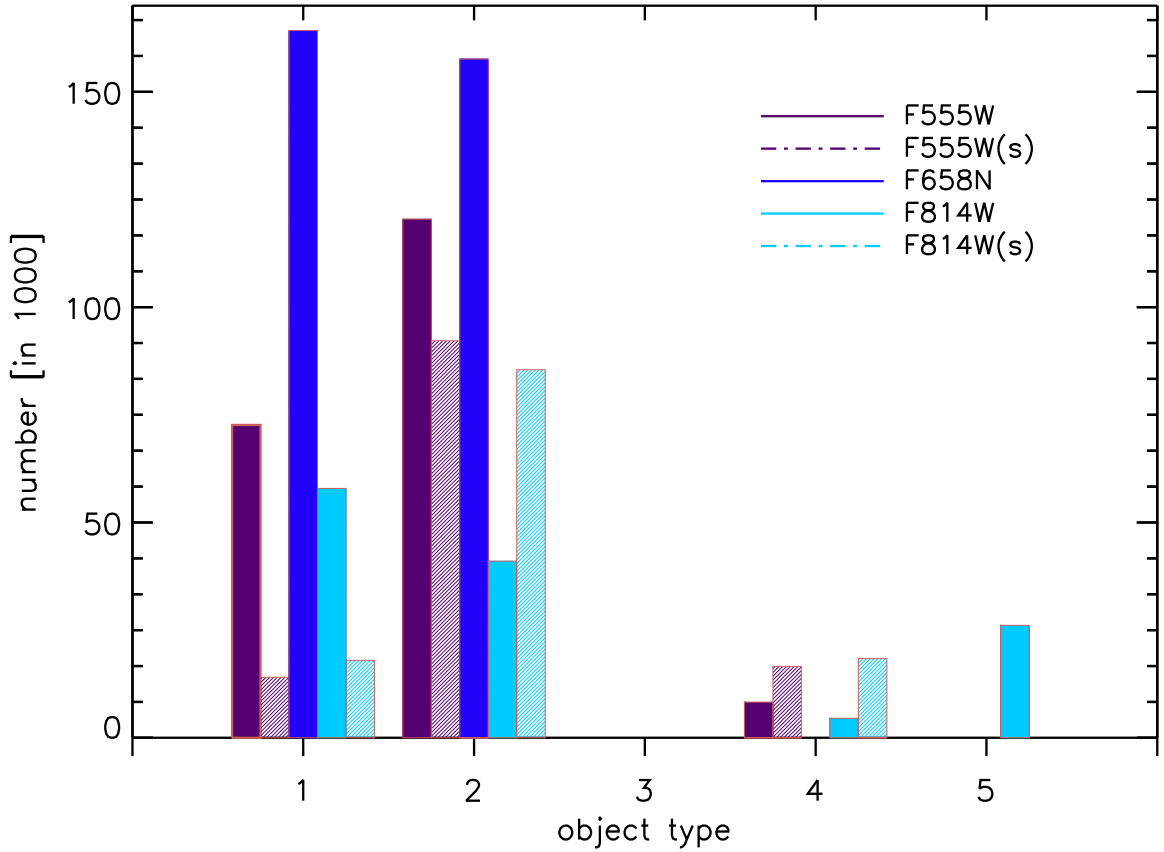


Figure 4.2.1: The total number of stars for different object types per ACS filter in the catalogs created by DOLPHOT. For a better presentations we plotted the different filters per OT next to each other. OTs are always integer values. We decided to keep only those objects with OT=1 to reduce the number of spurious detections.

4.2.2 Magnitude error

We restricted the catalogs to contain only those stars with magnitude errors above a given threshold, which depends on the filter. The cuts for the different filters are listed in column 2 of Tab. 4.2.1.

4.2.3 Sharpness

The “sharpness” parameter allows us to assess how well the PSF of a star is fitted. For a perfectly-fitted star the value is zero, positive for a point-source that is too peaked as compared to a typical stellar PSF such as a cosmic ray, and negative for a point source that is too broad in its light profile and that might be a background galaxy. Typical values range from -0.3 to $+0.3$ for an uncrowded region. The values chosen as our selection criteria are given in column 3 of Tab. 4.2.1. The short exposures and the *F658N* filter contain more cosmic rays than the other observations since only one or two dither positions were obtained,

leading to a reduced cosmic ray removal efficiency. For the $F128N$ filter a cut was impossible without losing real objects. The distribution of the sharpness as a function of magnitude can be seen in Fig. 4.2.2. For selecting these cuts a by-eye inspection of the source detection was performed.

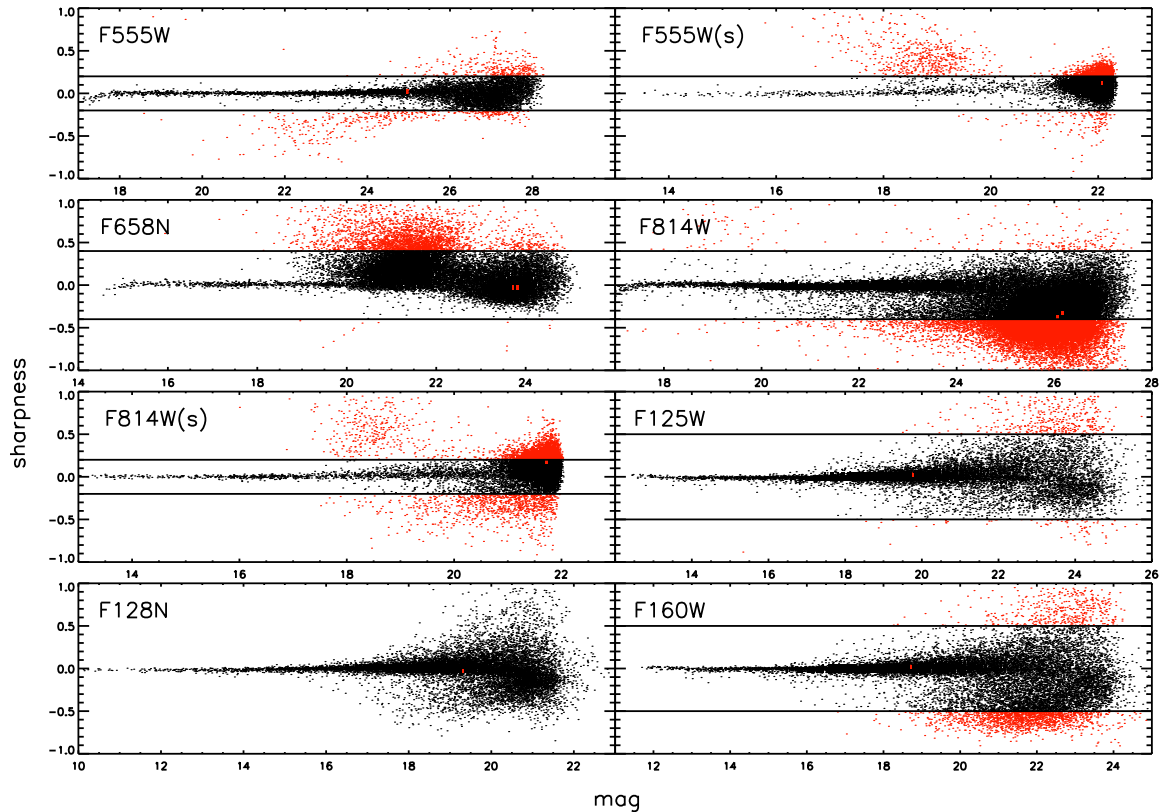


Figure 4.2.2: The distribution of the sharpness, a measure of how peaked the source is compared to a stellar PSF as function of magnitude for each filter. The black dots represent the data retained.

4.2.4 Crowding

The crowding is a measure of the flux contamination by the surrounding objects. For an isolated star the value is zero. Crowding effects become especially important in very densely populated regions or in areas around very bright saturated stars since the crowding parameter gives a value in magnitudes by how much brighter a star would have been measured if nearby stars would not have been fit simultaneously. Our values are chosen to select only those stars with a well-defined PSF and very low contamination can be seen in column 4 of Tab. 4.2.1. This selection is visualized in Fig. 4.2.3.

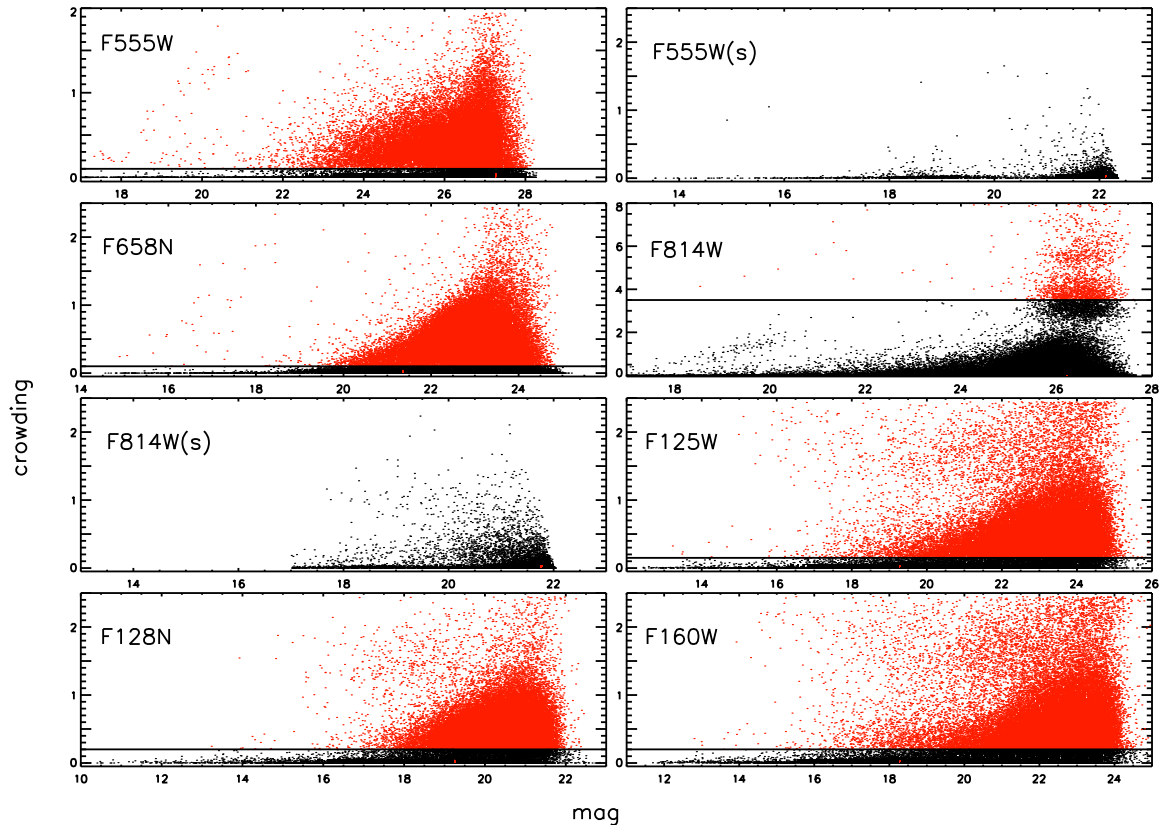


Figure 4.2.3: The crowding as a function of magnitude for each filter. The black dots represent the data retained.

4.3 Merging the different filters

For the creation of the final catalog we merged the different filter catalogs. We used the pixel coordinates of the resampled images and we established a maximum radial distance of 1.5 pixels (0.0735 arcsec) for merging the different filters. This means that the position of an object in two different filters is not allowed to radially deviate by more than 1.5 pixels from each other.

First, we combined the long and the short exposures for the *F555W* and the *F814W* band. Then, we used the *F814W* catalog as the basis, and subsequently added one filter after another. At the end, we adopted the WCS that is provided by the processed long exposures in the *F814W* filter as the common coordinate system for all exposures.

In order to merge the long and short exposure catalogs this procedure was repeated with a maximum radial distance of 1 pixel, between the same object in the short and long exposures. Objects from the short exposures were only taken into account for magnitudes brighter than 20 mag. For fainter objects, the long exposures were not saturated and offered a higher S/N than the short exposures.

Table 4.2.1. The thresholds for cleaning the catalogs

FILTER	σ [mag]	SHARPNESS	CROWDING
<i>F555W</i>	0.5	± 0.2	0.10
<i>F555W(s)</i>	0.5	± 0.2	2.50
<i>F658N</i>	0.5	± 0.4	0.10
<i>F814W</i>	0.5	± 0.4	3.50
<i>F814W(s)</i>	0.5	± 0.2	2.50
<i>F125W</i>	0.2	± 0.5	0.15
<i>F128N</i>	0.2	± 0.5	0.20
<i>F160W</i>	0.1	—	0.20

Note. — In this table we give the different thresholds for cleaning the photometric catalogs from spurious objects. The columns 2–4 refer to the quality parameters for point-source photometry as provided DOLPHOT. Objects with values equal to or smaller than the listed thresholds were retained.

For all objects available in both exposures ($n_{F555W}=246$ and $n_{F814W}=673$, where n is the number of objects) we chose to adopt the point-source photometry with the smaller photometric error which always came, as expected, from the long exposures.

After all filters had been merged into one catalog, all objects that were not detected in at least two filters, were deleted. It is unlikely that a star is only detected in one filter. This is not true for the *F160W* band, however, it can happen that a very young object emits only far to near-infrared radiation (Lada and Wilking 1984) and, therefore, is only detected in the *H*-band. In order not to lose those (potentially interesting) objects we decided not to remove the *F160W*-only detections.

At the end we have a catalog consisting of objects detected at least in two filters (except for the *F160W* filter) with a common coordinate system in pixel coordinates, as well as a WCS based on the *F814W* images.

4.4 Properties of the photometric catalog

The final catalog consists of 17121 objects in total. For an overview of the magnitude range as well as of the depth of each band, we refer to Fig. 4.4.1. The arrows mark the limiting magnitudes up to where 90% of all sources are located. A summary of the number of point-source detections in the combined catalog is given in Tab. 4.4.1. An excerpt of the final catalog is given in Tab. 4.4.2.

The photometric errors are, of course, below the cuts set in the cleaning process. As one can see in Fig. 4.4.2 most sources have much smaller errors than these limits. The limiting errors and resulting magnitudes comprise 90% of all detected point sources in a given filter, when no cuts are imposed, and are given in Tab. 4.4.1.

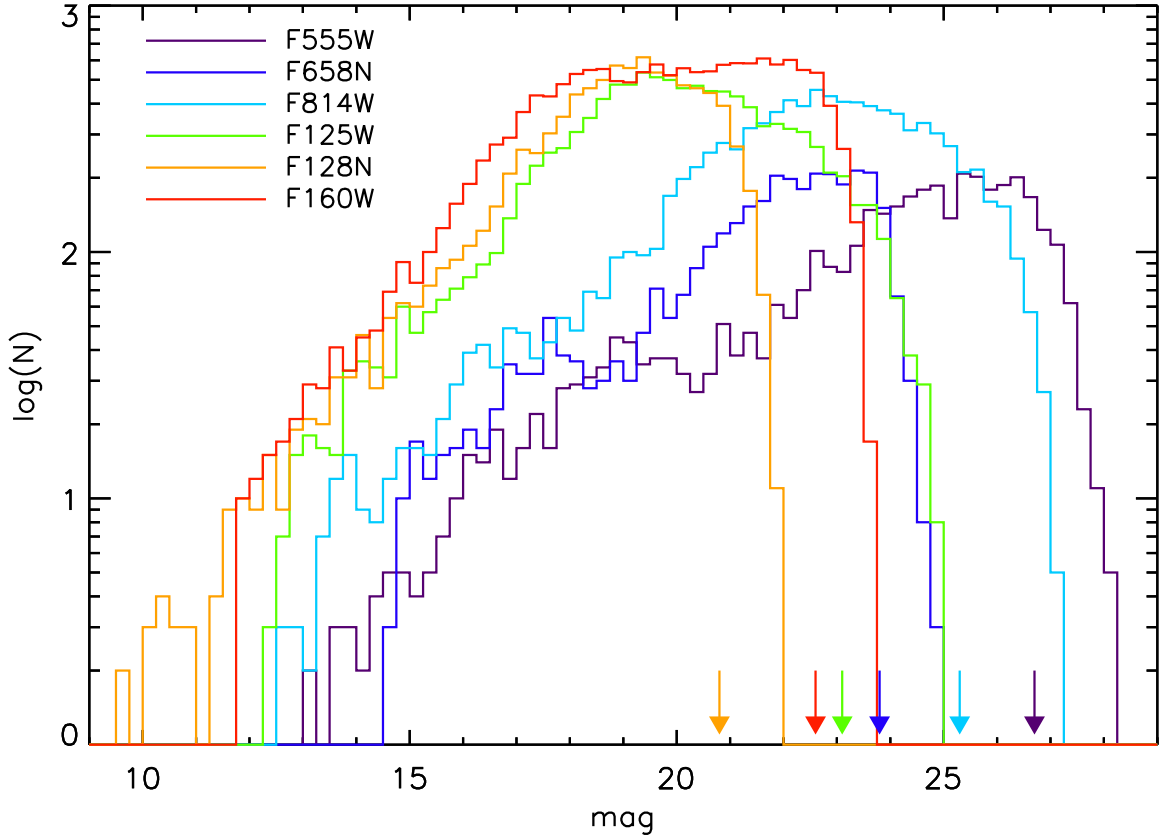


Figure 4.4.1: The magnitude distribution of the detections contained in the final Wd2 catalog. The plateau at the faint-end detections in the $F160W$ filter is due to the inclusion of all single-band detections. The arrows mark the limiting magnitudes up to where 90% of all sources are located (see Tab. 4.4.1).

4.5 The photometric improvement

The photometric data of our survey are the deepest data obtained for Wd2 so far. The Wide-Field Planetary Camera 2 (WFPC2) (Gonzaga and Biretta 2010) HST data of Vargas Álvarez et al. (2013) reach a photometric uncertainty level of 0.2 mag at a depth of ~ 21.5 mag and ~ 21.0 mag in the $F555W$ and $F814W$ filters, respectively. At the same level of photometric uncertainty we go down to ~ 27 mag in the $F555W$ filter and to ~ 26 mag in the $F814W$ filter, implying that our data are > 5 mag deeper in the optical. Comparing the $F555W$ and $F814W$ photometry of Vargas Álvarez et al. (2013) and ours, the median difference is $\Delta m_{F555W} = -0.04$ and $\Delta m_{F814W} = 0.06$. A small difference is expectable since Vargas Álvarez et al. (2013) used the WFPC2 camera instead of ACS, resulting in small differences for the filters. Nevertheless, these two datasets compare very well. The J and H band photometry by Ascenso et al. (2007a) has a limiting magnitude of ~ 20 mag and ~ 18.5 mag at a photometric uncertainty limit of 0.1 mag, respectively. Our HST photometry in the $F125W$ and $F160W$ filter goes down to ~ 23.5 mag and ~ 23 mag at the same uncertainty levels.

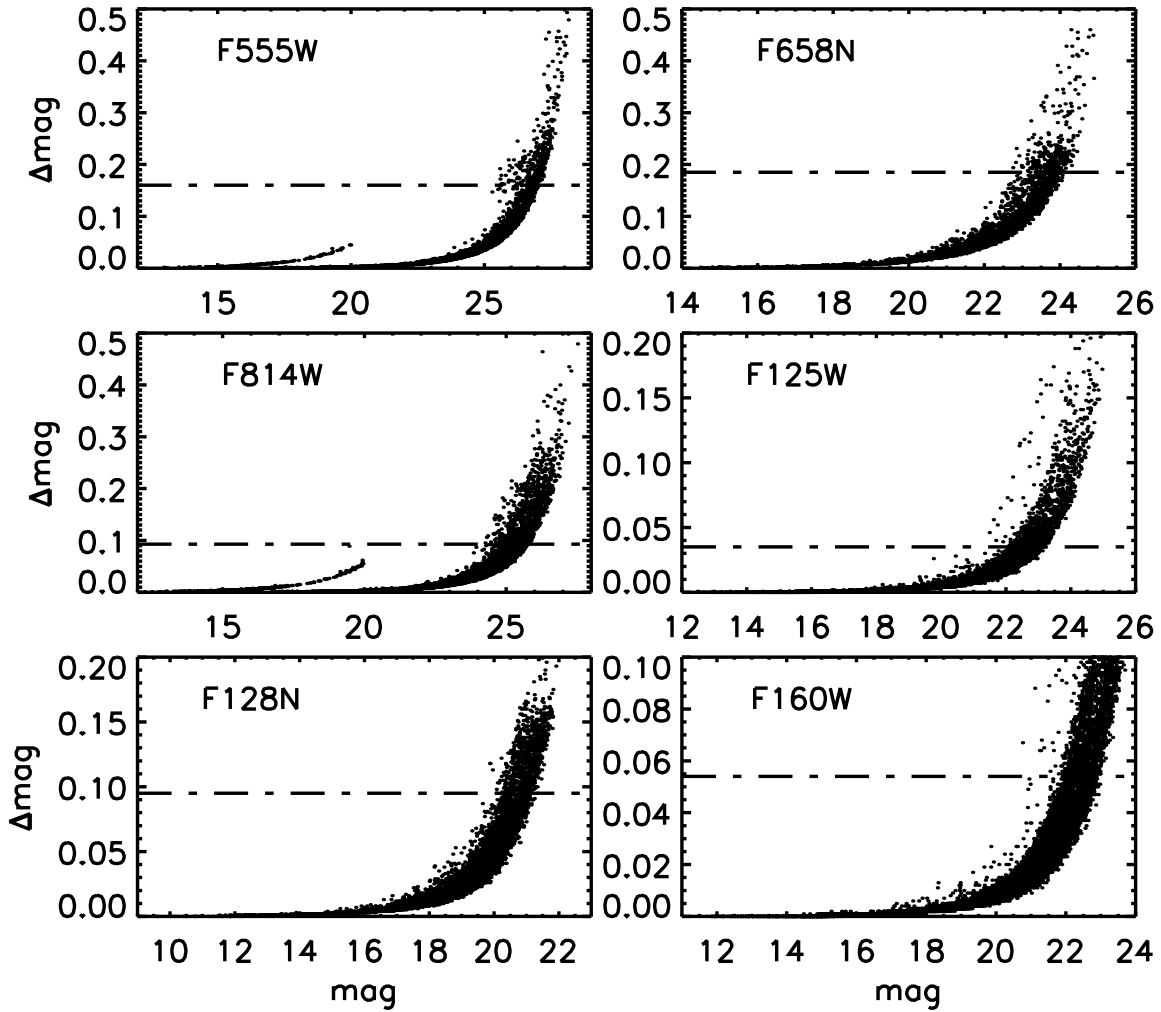


Figure 4.4.2: The photometric errors in each filter produced by the Dolphot pipeline. The horizontal lines show the limits below which 90% of all sources are located in the deep exposures (see Tab. 4.4.1).

Also in the near infrared (NIR) filters our data go $\sim 3\text{--}5$ mag deeper than the photometric catalog of [Vargas Álvarez et al. \(2013\)](#).

The spatial resolution of our dataset is also unprecedented. Especially due to the sub pixel drizzling we are able to reach a resolution of $0.049 \text{ arcsec pixel}^{-1}$ in the optical and $0.098 \text{ arcsec pixel}^{-1}$ in the IR. This is almost 50% higher than the pixel resolution of the data of [Ascenso et al. \(2007a\)](#) ($0.144\text{--}0.288 \text{ arcsec pixel}^{-1}$) and more than eight times higher than the optical resolution of [Carraro et al. \(2013\)](#) ($0.435 \text{ arcsec pixel}^{-1}$), both ground-based observations. If we compare our resolution to their seeing limits, which was $0.6''$ for the observations from [Ascenso et al. \(2007a\)](#) and $0.9\text{--}1.4''$ for the observations of [Carraro et al. \(2013\)](#) $0.9\text{--}1.4''$, we even reach a resolution ~ 12 times higher in the IR and $\sim 10\text{--}14$ times higher in the optical.

Table 4.4.1. Properties of the final catalog

FILTER	TOTAL NUMBER	mag-LIMIT [mag]	σ -limit [mag]
<i>F555W</i>	3922	26.7	0.160
<i>F658N</i>	3556	23.8	0.185
<i>F814W</i>	9281	25.3	0.093
<i>F125W</i>	10981	23.1	0.035
<i>F128N</i>	8955	20.8	0.095
<i>F160W</i>	15355	22.6	0.054

Note. — In this table we give the main properties of the final photometric catalog. In column 2 we show the total number of all objects per filter. Column 3 and 4 give the limits in magnitudes and the photometric error below which 90% of all sources are located. In total, 17121 objects were detected. 2236 point sources had a detection found in all filters.

These deep high resolution data in 6 filters give us the unique opportunity to study the properties of Wd2 at an unprecedented level of accuracy and depth. They reveal the young low-mass population (see Sect. 8.2) and provide us with new information on the spatial distribution of the cluster members (see Sect. 8.3), making it possible to create for the first time a high resolution pixel-to-pixel map of the color excess in order to correct for differential reddening (see Sect. 6) and to improve the cluster age determination. The high photometric accuracy gives us the opportunity to identify mass-accreting PMS stars via their $H\alpha$ excess emission due to mass in-fall (see Sect. 9). Using extensive artificial star tests, we will also determine the mass function of the Wd2 cluster and its sub regions (see Sect.10).

Table 4.4.2. The final catalog

ID	R.A. (J2000)	decl.	$F555W$		$F658N$		$F814W$		$F125W$		$F128N$		$F160W$		$E(B - V)_g$	
			[mag]	σ [mag]	[mag]	σ [mag]										
1	10:23:45.0	-57:45:17	—	—	—	—	—	—	99.999	9.999	—	—	99.999	9.999	—	—
2	10:23:45.0	-57:44:44	—	—	—	—	—	—	99.999	9.999	—	—	99.999	9.999	—	—
...																
4192	10:23:59.2	-57:44:56	27.525	0.269	—	—	25.098	0.070	—	—	—	—	—	—	1.747	0.033
4193	10:23:59.2	-57:46:23	—	—	—	—	25.515	0.078	21.626	0.012	—	—	20.198	0.007	2.248	0.061
4194	10:23:59.2	-57:45:07	—	—	—	—	22.766	0.013	—	—	19.034	0.022	—	—	1.693	0.031
4195	10:23:59.2	-57:44:03	—	—	—	—	25.584	0.094	21.480	0.012	21.320	0.108	19.968	0.007	1.829	0.045
4196	10:23:59.2	-57:45:05	23.968	0.019	21.243	0.030	20.235	0.003	17.522	0.001	17.148	0.008	16.427	0.001	1.703	0.031
4197	10:23:59.2	-57:44:35	25.725	0.061	23.669	0.166	22.088	0.008	20.134	0.004	19.943	0.038	19.558	0.005	1.797	0.033
4198	10:23:59.2	-57:44:31	—	—	—	—	—	—	—	—	—	—	23.332	0.081	1.877	0.036
4199	10:23:59.2	-57:45:25	18.100	0.001	16.503	0.002	15.366	0.005	13.042	0.000	12.841	0.001	12.102	0.000	1.920	0.038
4200	10:23:59.2	-57:46:59	27.314	0.259	—	—	25.886	0.158	—	—	—	—	—	—	2.733	0.034
4201	10:23:59.2	-57:44:22	24.614	0.028	22.538	0.062	21.256	0.005	—	—	—	—	—	—	1.996	0.045
4202	10:23:59.2	-57:45:16	23.774	0.020	21.586	0.048	19.899	0.003	16.988	0.001	16.648	0.005	15.955	0.001	1.775	0.038
4203	10:23:59.2	-57:45:45	—	—	—	—	22.385	0.010	18.986	0.003	18.649	0.022	17.813	0.002	1.911	0.037
4204	10:23:59.2	-57:45:03	26.673	0.145	—	—	22.186	0.009	19.198	0.004	18.887	0.023	18.115	0.003	1.694	0.029
4205	10:23:59.2	-57:44:39	—	—	—	—	25.722	0.110	21.845	0.013	—	—	20.915	0.011	1.782	0.030
4206	10:23:59.2	-57:44:23	—	—	—	—	23.052	0.015	19.500	0.003	19.272	0.019	18.381	0.002	1.953	0.042
4207	10:23:59.2	-57:47:15	—	—	—	—	26.126	0.308	—	—	21.002	0.128	—	—	—	—
4208	10:23:59.2	-57:44:50	—	—	—	—	25.877	0.131	—	—	21.422	0.145	20.121	0.007	1.682	0.032
4209	10:23:59.2	-57:46:17	—	—	—	—	—	—	23.497	0.055	—	—	22.586	0.041	2.249	0.045
4210	10:23:59.2	-57:45:46	24.858	0.034	22.292	0.060	20.682	0.004	17.710	0.001	17.421	0.011	16.601	0.001	1.923	0.038
4211	10:23:59.2	-57:45:39	18.419	0.001	16.983	0.003	15.939	0.006	14.061	0.000	13.948	0.001	13.506	0.000	2.096	0.051
4212	10:23:59.2	-57:44:22	25.877	0.076	23.627	0.142	21.255	0.005	—	—	17.705	0.009	16.845	0.001	1.979	0.045
4213	10:23:59.3	-57:44:38	—	—	23.787	0.192	—	—	—	—	21.309	0.118	—	—	1.783	0.030
4214	10:23:59.3	-57:47:32	—	—	—	—	—	—	19.858	0.006	19.482	0.040	19.365	0.006	—	—
4215	10:23:59.3	-57:44:24	—	—	—	—	23.611	0.020	21.063	0.008	20.989	0.081	20.194	0.007	1.949	0.040
4216	10:23:59.3	-57:46:05	—	—	—	—	23.085	0.015	19.573	0.003	19.257	0.030	18.463	0.003	1.983	0.033
4217	10:23:59.3	-57:45:34	23.638	0.016	21.313	0.029	19.530	0.002	—	—	16.242	0.004	15.465	0.001	2.017	0.040
4218	10:23:59.3	-57:43:47	21.595	0.007	20.347	0.015	19.068	0.002	—	—	17.135	0.007	—	—	2.023	0.055
...																
5577	10:24:00.9	-57:46:52	18.383	0.001	16.622	0.002	15.264	0.004	12.838	0.000	12.688	0.001	12.130	0.000	2.428	0.029
5578	10:24:00.9	-57:45:43	24.979	0.038	22.528	0.073	20.320	0.003	17.061	0.001	16.775	0.006	15.944	0.001	1.881	0.036
5579	10:24:00.9	-57:45:56	25.128	0.041	22.825	0.086	20.775	0.004	—	—	—	—	—	—	2.061	0.042
5580	10:24:00.9	-57:47:26	23.082	0.016	—	—	20.362	0.005	18.756	0.003	18.323	0.019	18.167	0.003	—	—
5581	10:24:00.9	-57:44:29	24.231	0.022	21.751	0.057	20.240	0.003	17.230	0.001	16.914	0.006	16.120	0.001	1.749	0.035
5582	10:24:00.9	-57:45:01	24.576	0.028	22.082	0.055	20.780	0.004	17.967	0.001	17.659	0.009	16.964	0.001	1.670	0.027
...																
17119	10:24:24.6	-57:46:22	—	—	—	—	—	—	22.540	0.033	—	—	21.364	0.022	—	—
17120	10:24:24.8	-57:46:18	—	—	—	—	—	—	19.176	0.003	18.953	0.024	18.312	0.003	—	—

Note. — This table represents an example of our photometric catalog. In total it contains 17121 objects, at least detected in two filters. Column 1 represents the unique identifier. Column 2 and 3 shows the coordinates in R.A. and decl. Column 4–15 gives the magnitudes of the 6 filters including the photometric uncertainties derived from the S/N. Column 16 and 17 shows the values of the gas extinction $E(B - V)_g$ and their uncertainties. The magnitude 99.999 and magnitude uncertainty 9.999 represent sources for which a source was detected but the photometry did not converge (because it was too faint or the detector saturated).

Tu es oder tu es nicht. Es gibt kein Versuchen.

— Yoda

5

The artificial star test and completeness corrections

This chapter is included in Sect. 3 of [Zeidler et al. 2016, AJ, submitted](#).

The high number of luminous OB stars, the high stellar surface density, and the differential reddening across the Wd2 area cause varying position-dependent detection limits for fainter stars. In the cluster center, where crowding is significant, the brightness limit for a certain detection fraction is, as expected, higher than in the less densely populated outer regions. This impacts the estimate of the stellar surface density and density profile, especially since completeness depends on location and filter.

To characterize and compensate for these completeness effects a common and often applied technique is used: artificial star tests. This method uses a dense grid of artificially created stars throughout the FOV. It adds artificial stars to the image, which are then retrieved using the same process applied to the real data. In order to provide a statistically significant correction factor, the artificial star tests were performed $5 \cdot 10^6$ times. Each time, only one artificial star was added in order to minimize an increase of crowding. The input catalog is well controlled in terms of magnitude and position of the input star, so it is possible to determine the exact fraction of artificial stars recovered for a certain brightness and position. The high surface density of the artificial stars ensures that the FOV is well covered and despite a random but uniform grid of the locations of the artificial stars, that all pixels of the observed images are well covered.

Table 5.1.1. Artificial star test results

FILTER	# INPUT STARS	# RECOVERED STARS	Σ [px ⁻¹]	Σ [arcsec ⁻²]
<i>F555W</i>	1 847 822	1 446 659	0.074	30.88
<i>F814W</i>	1 847 822	1 496 963	0.077	31.96
<i>F125W</i>	1 960 996	1 575 256	0.075	31.32
<i>F160W</i>	1 960 996	1 575 289	0.075	32.32

Note. — In this table we present the result of the artificial star tests. The first column shows the filter. Column 2 shows the number of artificial stars inside the FOV of each stacked and mosaicked observation. Column 3 shows the number of recovered artificial stars, applying the same cuts as for the scientific photometric catalog. Column 4 shows the mean stellar surface density per pixel.

5.1 The artificial star test

A grid of $5 \cdot 10^6$ artificial stars was created and used for all filters. The artificial star catalogs are populated down to ~ 30 mag and are at least 2 mag deeper than the observed photometric catalog to ensure a proper coverage of the magnitude and colors of the stars. The color dependence is important because the stars used to determine the MF need to be detected in two filters simultaneously, e.g., a IR-bright star can be too faint in the optical to be detected. Therefore, this star needs to be counted as lost when deriving the surface density profile or the MF. We used the observed color of the stars to retrieve the completeness fraction of each observed star at its spatial position for each filter combination (see eq. 5.2), depending on which filter combination one uses. As a result, we obtained the completeness information at each position of the survey area per magnitude and color bin (dependent on the filter combination), thus we can correct each star individually (depending on its position, magnitude, and color). The size of the artificial star grid was chosen in a way that each bin contains an average number of 500 artificial stars (bin size is: ~ 91 px² or ~ 0.22 arcsec²). The magnitude binsize is 0.1 mag. We now can assign to each star in each of the wide-band filters its individual completeness level.

For the artificial star tests we used the photometry software DOLPHOT¹ (Dolphin 2000), with the same setup as adopted for the original photometry (see Sect. 4.1) now with the parameter “fakeStars=1”. To clean the catalogs from spurious sources we applied the same statistical cuts used for the original photometry (see Sect. 4). Additionally, those artificial stars that coincided with very bright stars and hence had recovered magnitudes 0.75 mag brighter² than their input ones, were treated as lost due to crowding. In Tab. 5.1.1 we present the numbers of the artificial star tests for each filter before and after the cleaning process. In column 2 we provide the input number of artificial stars within the FOV and in column 3 the total number of recovered stars after all statistical cuts were applied.

¹<http://americano.dolphinim.com/dolphot/>

²A recovered magnitude 0.75 mag brighter than the input magnitude means that the majority of the flux is emitted by surrounding stars due to crowding.

Table 5.2.1. The completeness limits for different regions

FILTER	50%	COMPLETE SURVEY AREA		GAS RIDGE ^a		Wd2 ^b		MC		NC		
		M [M_{\odot}]	75%	M [M_{\odot}]	50%	M [M_{\odot}]	50%	M [M_{\odot}]	50%	M [M_{\odot}]	50%	M [M_{\odot}]
<i>F555W</i>	26.7	0.35	23.6	1.15	26.2	0.52	26.6	0.34	25.6	0.52	26.5	0.41
<i>F814W</i>	24.7	0.10	21.8	0.45	24.7	0.12	25.3	0.10	22.8	0.26	24.6	0.12
<i>F125W</i>	22.1	< 0.1	18.5	0.48	21.7	< 0.1	22.0	< 0.1	18.7	0.44	21.2	< 0.1
<i>F160W</i>	21.1	< 0.1	17.8	0.45	20.9	< 0.1	20.9	< 0.1	17.6	0.46	20.2	< 0.1
<i>E(B - V)</i>		1.55 mag			1.60 mag		1.65 mag		1.53 mag		1.49 mag	

Note. — In this table we list the mean magnitudes and the corresponding stellar masses for various region for a completeness limit of 50%. The stellar masses correspond to a stellar age of 1 Myr. The $E(B - V)$ color excess is used to obtain masses from the isochrones and is obtained from our high-resolution, 2D color excess map.

^aAs the gas ridge we refer to the HII region of RCW 49 toward the south east of the cluster.

^bAs the area of Wd2 we refer to the region within the 2σ boundary of the spatial distribution (see Sect. 8.3).

5.2 The global completeness limits of Wd2

The level of completeness is defined by the ratio between the number of recovered stars and the number of input stars for each magnitude bin and position for a binsize of 0.1 mag. The completeness level as a function of magnitude for the four wide-band filters is presented in Fig. 5.2.1. We reach a completeness level of 50% (green dashed lines in Fig. 5.2.1) at the following magnitudes: $F555W = 26.7$ mag, $F814W = 24.7$ mag, $F125W = 22.1$ mag, and $F160W = 21.1$ mag. The 75% limit (blue dashed lines in Fig. 5.2.1) is reached at the following magnitudes: $F555W = 23.6$ mag, $F814W = 21.8$ mag, $F125W = 18.5$ mag, and $F160W = 17.8$ mag. An overview is given in Tab. 5.2.1.

Toward the bright end, the completeness of the ACS filters decreases drastically. This is the point at which the saturation limit of the detector is reached. For the ACS filters we recover the brighter stars using the 3 s short exposures to complete the catalog. Yet, the brightest stars are still saturated.

5.3 The 2D completeness map of Wd2

The spatially variable extinction and position-dependent surface density require position-dependent completeness maps. In this way the stellar numbers can be corrected as a function of spatial position in the image.

The size of the spatial grid to calculate the completeness fraction throughout the FOV is chosen in a way that each bin contains an average number of ~ 500 artificial stars (leading to a bin size of: $\sim 91 \text{ px}^2$ or $\sim 0.22 \text{ arcsec}^2$). The magnitude binsize is 0.1 mag. To reduce statistical fluctuations for each magnitude bin n we applied a running mean to the completeness fraction $f_c(n)$:

$$\overline{f_c(n)} = \frac{f_c(n-1) + f_c(n) + f_c(n+1)}{3}. \quad (5.1)$$

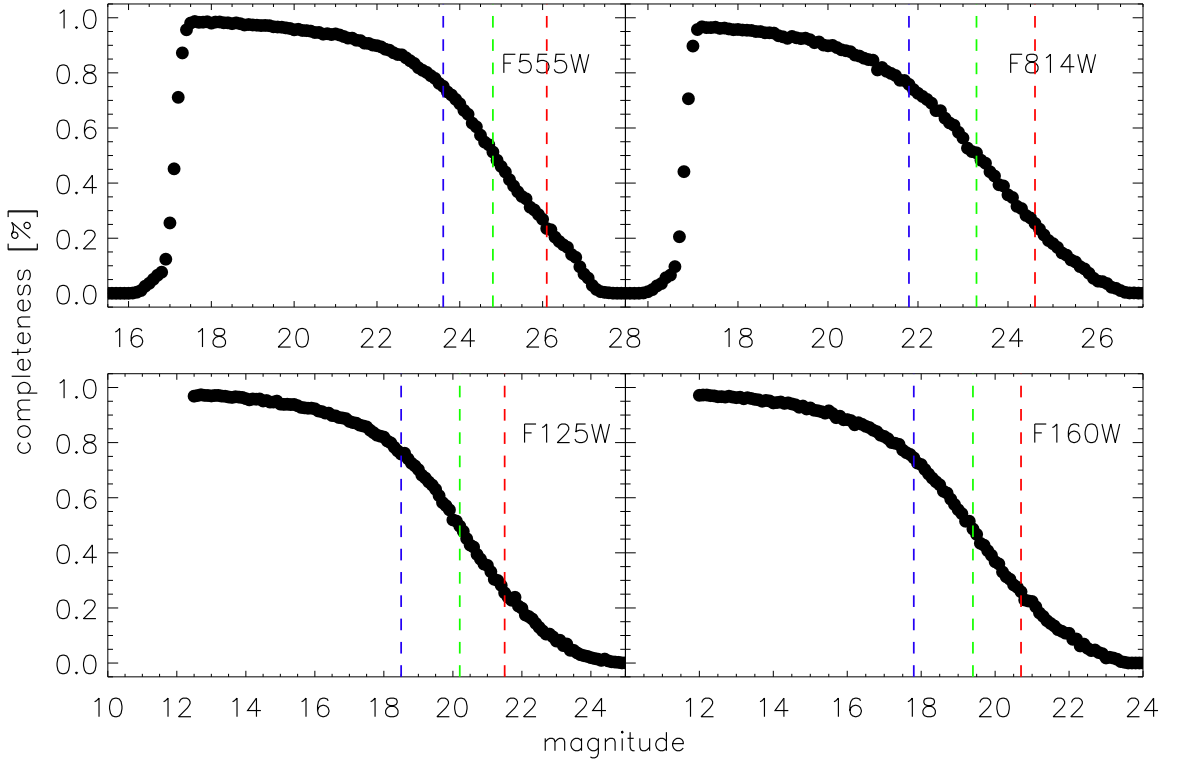


Figure 5.2.1: The mean completeness distribution for the four wide band filters with a binsize of 0.1 mag. The dashed lines represent the 75% (blue), 50% (green), and 25% (red) completeness limits (see Tab. 5.2.1).

The completeness fractions can be defined as the probability of detecting a star of certain magnitude in a specific region of the observation. Therefore, to detect a star in multiple bands, or in other words to take into account the color of the star, the completeness fractions are multiplicative at each individual position in the FOV:

$$N_{\text{corr.}} = \prod_{n=1}^{\#_{\text{filter}}} \frac{1}{f_n} \cdot N_{\text{obs.}}, \quad (5.2)$$

where N is the number of observed and completeness-corrected stars and f_n completeness fraction at each position.

In Fig. 5.3.1 we show the 2D maps for a completeness limit of 50% in the four filters. The 2D maps for the 25% and 75% completeness limit are shown in the Appendix C. In Tab. 5.2.1 we list the mean magnitude for a completeness limit in several regions including the gas and dust ridge. The masses are computed using a 1 Myr isochrone at Solar metallicity of $Z_{\odot} = 0.0152$ taken from the PADOVA AND TRIESTE STELLAR EVOLUTION CODE³ (hereafter: PARSEC 1.2S, Bressan et al. 2012).

³<http://stev.oapd.inaf.it/cmd>

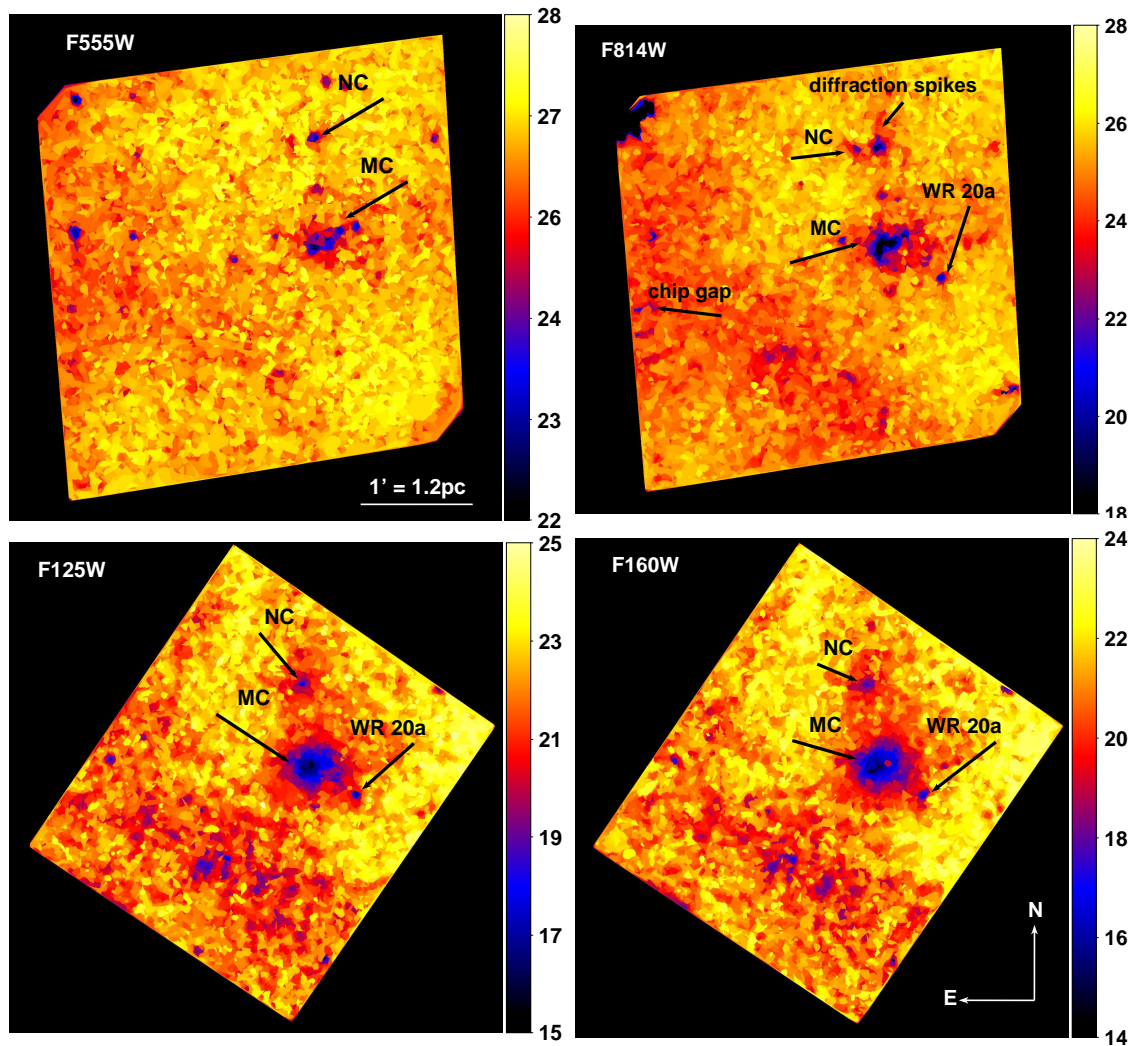


Figure 5.3.1: The 50% completeness map for all four wide-band filters. The color bar indicates the magnitude at which such a completeness value is reached. We marked some features in each of the panels, such as the two clumps (MC, NC), the Wolf-Rayet star WR20a, the imprint of diffraction spikes, and the defect in the image caused the chip gaps for the ACS camera.

Besides the two clumps and several luminous stars, such as foreground stars, the luminous Wolf-Rayet star WR20a (e.g., [Bonanos et al. 2004](#)), and their diffraction spikes, the 50% completeness level is quite uniformly distributed throughout the whole FOV in all filters (see Fig. 5.3.1). While in the *F555W* filter stars of masses of $0.35 M_{\odot}$ can be detected ($0.55\text{--}0.68 M_{\odot}$ in the two clumps, depending on the position), $0.1 M_{\odot}$ stars can only be detected in the *F814W* filter ($0.12\text{--}0.6 M_{\odot}$ in the two clumps, depending on the position). In the IR filters stars with a mass of $0.1 M_{\odot}$ or lower are detected ($0.44\text{--}0.75 M_{\odot}$ in the two clumps, depending on the position). We emphasize that these numbers are mean values across different regions.

5.3.1 The $F555W$ filter

The 50% completeness level is quite uniformly distributed throughout the whole FOV (see top left panel of Fig. 5.3.1). The mean magnitude limit for which a 50% completeness fraction is reached is 26.7 mag, which corresponds to a 1 Myr old, $0.35 M_{\odot}$ star. Although the mean level of completeness in the in the molecular cloud of RCW 49 (south-east of Wd2) is $0.5 M_{\odot}$, this level cannot be reached in the regions of the highest gas and dust density, such as the tips of the nebular pillars ($0.7 M_{\odot}$). The 50% completeness limit in the cluster center is $0.65 M_{\odot}$ and significantly lower than the overall FOV average ($0.35 M_{\odot}$). This is caused by crowding and the presence of the OB stars.

5.3.2 The $F814W$ filter

The extinction caused by the gas and dust in the RCW 49 cloud affects the $F814W$ filter less than the $F555W$ filter. As a result, on average, $0.1 M_{\odot}$ stars can be detected at a 50% completeness level, corresponding to 24.7 mag (see top, right panel of Fig. 5.3.1). In the surroundings of the Wd2 (at a distance of about 2 pc) cluster even stars below $0.1 M_{\odot}$ is observable. The 50% completeness limit in the cluster center is 22.8 mag, corresponding to $0.26 M_{\odot}$. The bright diffraction spikes around bright stars in the observations are a distinct feature in the completeness map. The low-level completeness to the south west of Wd2 is caused by the luminous Wolf-Rayet star WR20a (e.g., [Bonanos et al. 2004](#)).

5.3.3 The $F125W$ and $F160W$ filters

The further we move toward longer wavelengths, the less the molecular clouds hamper the detection of stars. The main cause for a lower level of completeness in the IR filters is crowding caused by the luminous O and B stars in the center of the cluster. Outside Wd2, stars with masses below $0.1 M_{\odot}$ are detectable. In the cluster center stars with masses down to $0.75 M_{\odot}$ and $0.65 M_{\odot}$ can be detected in the $F125W$ and $F160W$ filters, respectively.

5.4 The true photometric uncertainties

The photometric uncertainties provided by DOLPHOT are the uncertainties calculated from the signal-to-noise ratio (S/N) of the measurements. These uncertainties are a lower limit to the real uncertainties, which are also influenced by the local environment of a source, such as crowding and extinction. The artificial star tests give us the opportunity to properly determine the real photometric uncertainties, since we know the input magnitude and the measured output magnitude of the recovered stars. The photometric uncertainty can be estimated by using the scatter of the measured photometry of the artificial stars. In Fig. 5.4.1 we show the difference between the input and measured photometry for each of the wide-band filters. Negative values are due to the measured magnitude being smaller than the input one, implying that the star appears brighter.

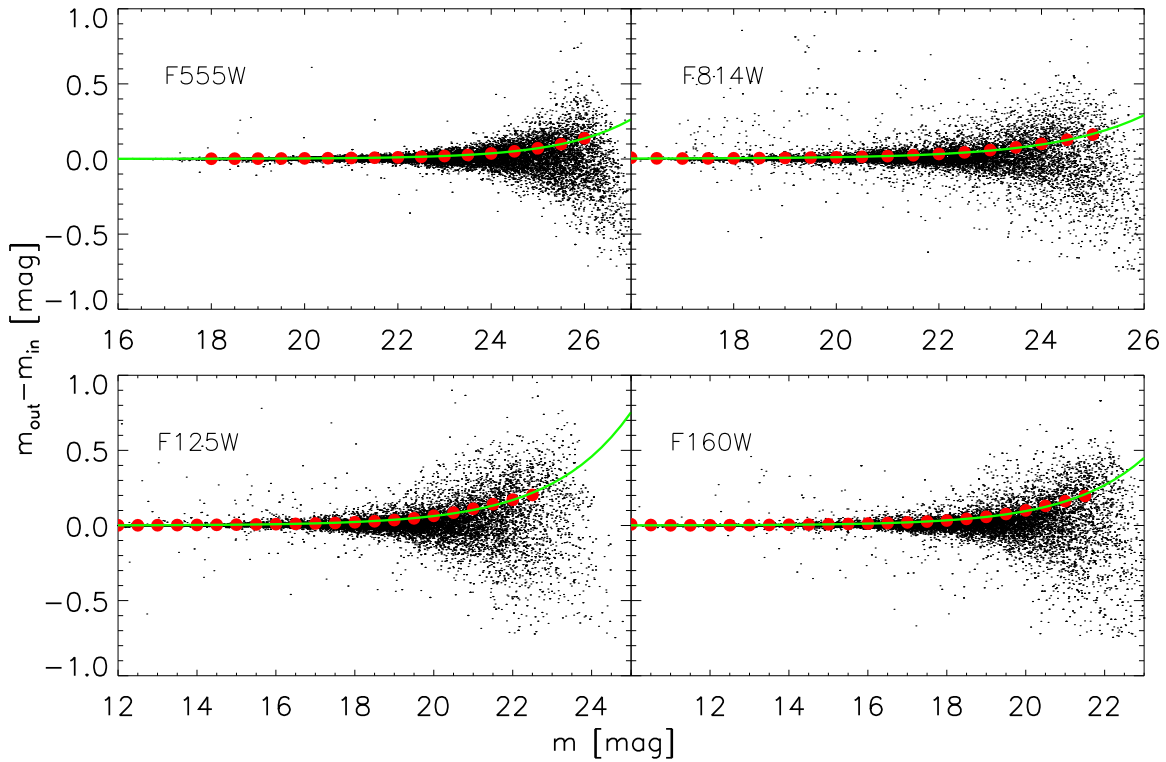


Figure 5.4.1: The difference between the input magnitude and the measured magnitude of the artificial stars as a function of magnitude. The green line is an exponential fit of the absolute mean scatter and defines the true photometric uncertainties. For visualization reasons we only plot 10% of all data points. One can see a clear asymmetry toward fainter magnitudes showing that artificial stars are more often recovered with magnitudes brighter than their input caused by significant blending in our images.

The absolute scatter is calculated as:

$$\Delta m = \|m_{\text{out}} - m_{\text{in}}\|. \quad (5.3)$$

We fitted an exponential to the scatter values as a function of input magnitude of the following form:

$$\Delta m = a \cdot \exp(b \cdot m_{\text{in}}) + c. \quad (5.4)$$

The obtained values for a , b , and c for each filter are listed in Tab. 5.4.1.

After fitting an exponential we can assign the real photometric uncertainty for each star in each of the four wide-band filters and compare it with the uncertainty obtained from the observations with DOLPHOT at the magnitude below which 10%, 50%, and 90% of all sources are found. We list both uncertainties for each filter in Tab. 5.4.2. As one can see, the uncertainties derived from the S/N are consistently smaller, especially for faint magnitudes.

Table 5.4.1. The results of the photometric uncertainty fit

Filter	a	b	c
<i>F555W</i>	$5.13 \cdot 10^{-9}$	0.66	$1.32 \cdot 10^{-3}$
<i>F814W</i>	$1.36 \cdot 10^{-7}$	0.56	$2.23 \cdot 10^{-3}$
<i>F125W</i>	$3.03 \cdot 10^{-6}$	0.50	$8.48 \cdot 10^{-5}$
<i>F160W</i>	$3.07 \cdot 10^{-6}$	0.52	$5.62 \cdot 10^{-4}$

Note. — The resulted values obtained for the photometric uncertainty by fitting an exponential function (eq. 5.4) to the absolute scatter Δm .

Table 5.4.2. The photometric uncertainty

Filter	mag-limit [mag]			σ_m [mag]			Δm [mag]		
	10%	50%	90%	10%	50%	90%	10%	50%	90%
<i>F555W</i>	19.3	24.5	26.7	0.002	0.037	0.160	0.003	0.052	0.216
<i>F814W</i>	19.4	22.7	25.3	0.002	0.011	0.093	0.009	0.048	0.197
<i>F125W</i>	17.2	19.9	22.7	0.001	0.005	0.035	0.016	0.060	0.240
<i>F160W</i>	16.6	19.8	22.6	0.001	0.006	0.054	0.017	0.087	0.330

Note. — The uncertainties for each of the broad-band filters at the magnitude below which 10%, 50%, and 90% of all sources are found. Column 2 gives the magnitude while Column 3–5 and 6–8 list the magnitude uncertainties determined with DOLPHOT and the uncertainties determined via the artificial star test, respectively.

Wenn du eine weise Antwort verlangst,
musst du vernünftig fragen.

— Johann Wolfgang von Goethe

6

A high-resolution 2D map of the color excess

This chapter is included in Sect. 4 of [Zeidler et al. 2015, AJ, 150, 78](#).

Wd2 is located in the Carina-Sagittarius arm of the MW, and thus the local extinction due to interstellar dust is expected to be high. A high resolution, spatially resolved characterization of the extinction in the region is key to a precise determination of age and distance for the Wd2 cluster, and to investigate the existence of an age spread. Following the methodology outlined by [Pang et al. \(2011\)](#) for NGC 3603, we used a combination of $H\alpha$ and $Pa\beta$ images ($F658N$ and $F128N$) to derive a high resolution, pixel-to-pixel map of the color excess of the gas $E(B - V)_g$ of the Wd2 region.

6.1 $H\alpha$ and $Pa\beta$ emission

In order to construct the pixel-to-pixel color excess map, we exploited the fact that radiation emitted at shorter wavelengths is absorbed more easily by dust than radiation emitted at longer wavelengths. Therefore, the interstellar dust attenuates the light from a given source emitted in the $H\alpha$ line (rest-frame wavelength 6563 Å) more than the light emitted in the $Pa\beta$ line (rest-frame wavelength 12802 Å). Consequently, the observed flux ratio of $H\alpha/Pa\beta$ is always smaller than the theoretical (reddening free) ratio computed for the same conditions of electron density and electron temperature.

Calzetti et al. (1996) provide a relation between the color-excess $E(B - V)_g$ of the interstellar gas and the observed (R_{obs}) and theoretical (R_{int}) flux ratio H α /Pa β with an assumed extinction law, represented by the total to selective extinction $\kappa(\lambda) = A(\lambda)/E(B - V)$ for a given wavelength λ :

$$E(B - V) = \frac{-\log(R_{\text{obs}}/R_{\text{int}})}{0.4[\kappa(\text{H}\alpha) - \kappa(\text{Pa}\beta)]}. \quad (6.1)$$

To use Eq. 6.1 we need to get the pixel-to-pixel H α /Pa β flux ratio from our observations. We applied the following steps to properly remove the stellar emission:

- First, we repeated the drizzling process (see Sec. 3) for the ACS images adopting the same pixel size as for the WFC3/IR images (0.098 arcsec pixel⁻¹). A visual inspection ensured that the images were properly aligned.
- Due to the use of different instruments covering the whole wavelength range we needed to correct our images to ensure that they have the same PSFs. Therefore, we used 40 stars that were non-saturated and without a very close neighbor in each of the six filters in order to determine the PSF. The PSF was largest in the $F128N$ image with a FWHM of 2.26 ± 0.312 pixels. Hence we degraded all the other images to the same resolution by convolving them with a Gaussian whose dispersion (σ^2) is the difference between the $F128N$ filter and the one of the filter in question.
- We calibrated all images in flux f by multiplying them by their specific PHOTFLAM¹ value given in the respective header:

$$\begin{aligned} f_{F658N} &= f_{F658N,\text{uncal.}} \cdot \text{PHOTFLAM}_{F658N} \\ f_{F128N} &= f_{F128N,\text{uncal.}} \cdot \text{PHOTFLAM}_{F128N}. \end{aligned} \quad (6.2)$$

- The continuum flux centered at the H α and Pa β wavelength was derived by linear extrapolation of the fluxes in the $F555W$ and $F814W$ ($F125W$ and $F160W$) image pixel-by-pixel at the $F658N$ ($F128N$) wavelength:

$$\begin{aligned} f_{F658N,\text{cont.}} &= a_{\text{H}\alpha} + b_{\text{H}\alpha} \cdot \lambda_{F658N}, \text{ with} \\ a_{\text{H}\alpha} &= f_{F555W} - b_{\text{H}\alpha} \cdot \lambda_{F555W}, \text{ and} \\ b_{\text{H}\alpha} &= \frac{f_{F814W} - f_{F555W}}{\lambda_{F814W} - \lambda_{F555W}}, \end{aligned} \quad (6.3)$$

$$\begin{aligned} f_{F128N,\text{cont.}} &= a_{\text{Pa}\beta} + b_{\text{Pa}\beta} \cdot \lambda_{F128N}, \text{ with} \\ a_{\text{Pa}\beta} &= f_{F125W} - b_{\text{Pa}\beta} \cdot \lambda_{F125W}, \text{ and} \\ b_{\text{Pa}\beta} &= \frac{f_{F160W} - f_{F125W}}{\lambda_{F160W} - \lambda_{F125W}}. \end{aligned} \quad (6.4)$$

¹The PHOTFLAM value provides the inverse sensitivity of the pixel values in ergs s⁻¹ Å⁻¹ electron⁻¹

With such an extrapolation we take into account the slope of the continuum emission of the stars in order to better remove them from the final, pure line-emission images.

- The interpolated continuum image was then subtracted for properly removing the stars from the F_{658N} (F_{128N}) image:

$$\begin{aligned} f_{F_{658N},\text{em.}} &= f_{F_{658N}} - f_{F_{658N},\text{cont.}} \\ f_{F_{128N},\text{em.}} &= f_{F_{128N}} - f_{F_{128N},\text{cont.}} \end{aligned} \quad (6.5)$$

- Afterwards each pixel value was multiplied by the respective bandwidth $\Delta\lambda$ resulting in the pure line emission image as well as the R_{obs} flux ratio:

$$\begin{aligned} F_{F_{658N},\text{em.}} &= f_{F_{658N},\text{em.}} \cdot \Delta\lambda_{F_{658N}} \\ F_{F_{128N},\text{em.}} &= f_{F_{128N},\text{em.}} \cdot \Delta\lambda_{F_{128N}} \end{aligned} \quad (6.6)$$

- For the theoretical flux ratio of $\text{H}\alpha/\text{Pa}\beta$, R_{int} , we derived a value of 17.546 with an assumed electron temperature of 10000 K and an electron density of 100 cm^{-3} (Osterbrock and Bochkarev 1989). Both values have been found in typical HII regions outside highly ionized regions such as pillars (e.g., McLeod et al. 2015). Additionally, as it is shown later (Sect. 6.3), the $E(B - V)_g$ map is not sensitive to these values. We adopted a normal total-to-selective extinction of $R_V = 3.1$. From the extinction law of Cardelli et al. (1989) we derived $\kappa(\text{H}\alpha) = 2.437$ and $\kappa(\text{Pa}\beta) = 0.8035$. With Fitzpatrick (1999) we derived $\kappa(\text{H}\alpha) = 2.346$ and $\kappa(\text{Pa}\beta) = 0.7621$.
- Finally we were able to apply Eq. 6.1 to construct the pixel-to-pixel map of $E(B - V)_g$ shown in Fig. 6.1.1.

6.2 The features of the color excess map

The two-dimensional color-excess map (see Fig. 6.1.1) was created with a spatial resolution ($0.098 \text{ arcsec pixel}^{-1}$) that had never been reached before for this region. The very inhomogeneous distribution of the dust extinction shows that differential reddening must be taken into account before any conclusion can be reached on the physical parameters of Wd2. We will use this map to get a dereddened cluster population, where for each of the stars the individual reddening is estimated locally (see Sect. 8.2).

In Fig. 6.2.1, the reddening map is shown on the left in black and white over-plotted with the selected cluster members (see Sect. 8.2) in green, and contours representing $E(B - V)_g$. On the right we show the RGB image of the same spatial extent over-plotted with the same $E(B - V)_g$ contours. This image emphasizes the location of the stellar population of Wd2 with respect to the highly variable color excess on small scales. Here it becomes clear that this map will improve the correction for differential reddening of each star individually.

The color excess map is morphologically very inhomogeneous. In the center where the cluster is located (marked by a cross in Fig. 6.1.1), $E(B - V)_g$ has a value of $\sim 1.8 \text{ mag}$. Here

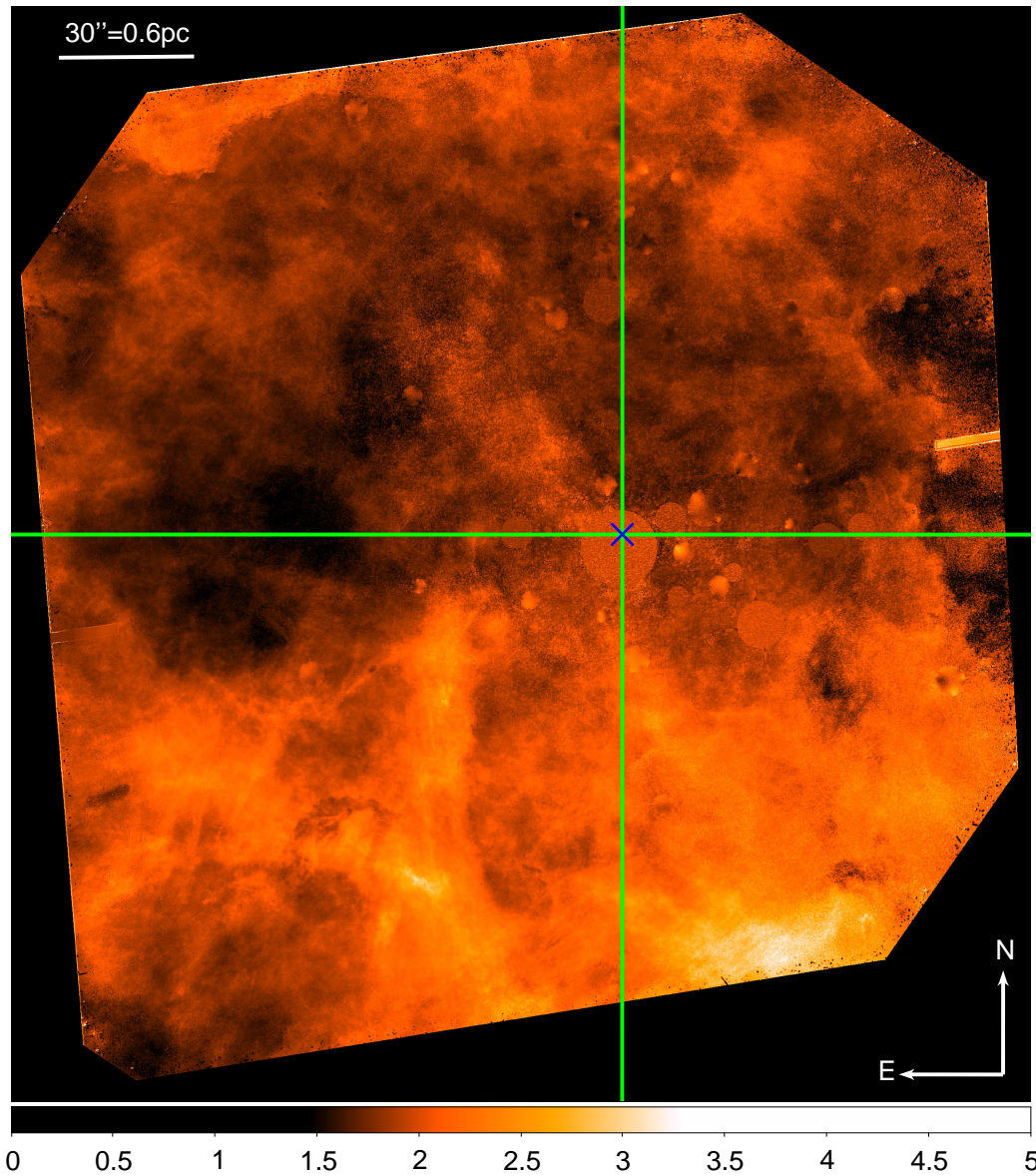


Figure 6.1.1: The pixel-to-pixel map of the color excess of the gas $E(B - V)_g$, covering the area where all six filters are available (see Fig. 3.1.1). The cross marks the center of Wd2, as given in Simbad. The green lines indicate the separation in four quadrants (see Sect. 6.2). $E(B - V)_{g,\min} = 0.002 \text{ mag}$ and $E(B - V)_{g,\max} = 11.7 \text{ mag}$. The colorbar shows the color excess in magnitudes. All pixels with $E(B - V)_g > 5 \text{ mag}$ are shown in white. The circular areas near and in the cluster center are caused by the substitution of the saturated pixels by the median of the surrounding area. The two slightly inclined short stripes (one on the left, one on the right side) are caused by the gap between the two ACS chips (see Fig. 3.1.1). They remain at locations in the combined image where only one dither position is available.

we also see most of the very bright stars in the color composite image (see Fig. 6.2.1). Also in the very central region around the cluster there still seems to be a concentration of gas and

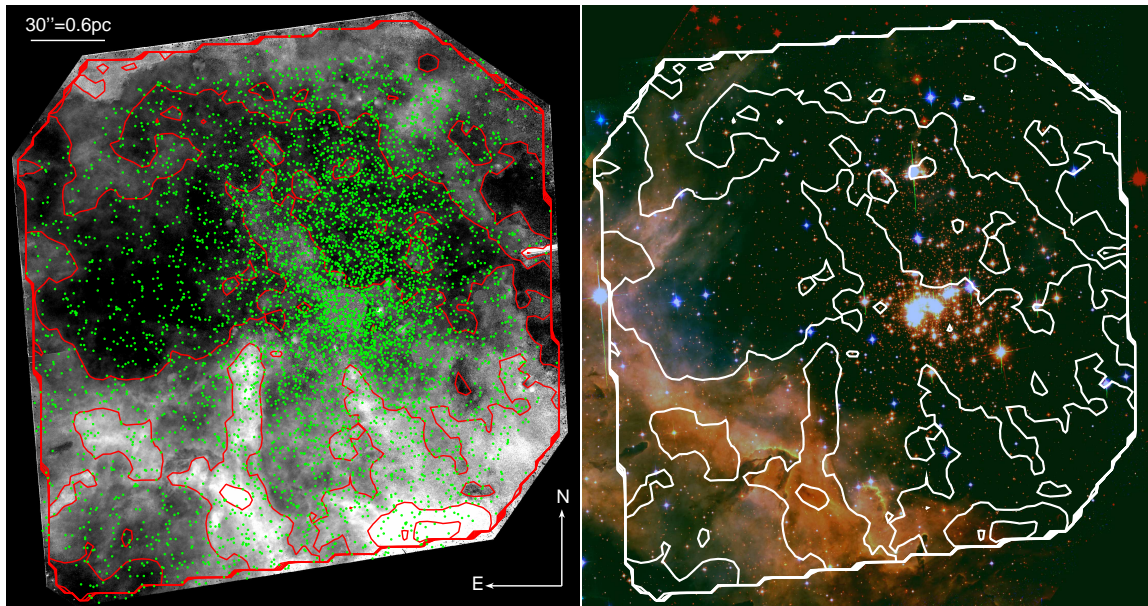


Figure 6.2.1: **Left:** The pixel-to-pixel map of the color excess $E(B - V)_g$ covering the area where all six filters are available (see Fig. 3.1.1). The green points are the stars in RCW 49 (see Sect. 8.2), and the contours represent $E(B - V)_g$ in the range of 0 to 2.86 in 9 linear steps. **Right:** RGB composite image of the $F125W$ (red), $F814W$ (green), and $F555W$ (blue) filter.

dust, although we cannot say whether these components are mainly located in front of the cluster as seen along our line of sight, or in the cluster. A “bridge” with a slightly increased $E(B - V)_g \approx 1.9$ mag extends from the cluster center to the North-East. In Fig. 6.2.1 one can see that there are no massive luminous stars visible within this “bridge”. This “bridge” is not visible in the RGB image. Towards the South and the East where a higher concentration of dust and gas is observed, the color excess increases to values larger than 2.0 mag. In very dense regions it even can exceed 2.5 mag. The color excess map follows very well the morphology of the gas clouds showing a direct connection between the color excess $E(B - V)_g$ and the cloud structure. As expected the color excess is higher where the clouds are denser.

The median reddening of the pixels across the reddening map is $E(B - V)_g = 1.87$ mag. The vast majority of all pixels have $E(B - V)_g$ between 1–3 mag. Only 10742 pixels (0.23%) have $E(B - V)_g > 3.0$ mag and only 1018 pixels (0.02%) exceed 5.0 mag. The distribution of the nebular color excess values can be seen in Fig. 6.2.2.

As shown in Fig. 6.1.1 the range of $E(B - V)_g$ values are quite large. We carried out an analysis of the radial distribution of the color excess. We divided the color excess map into four quadrants (NW, NE, SW, SE) (see Fig. 6.1.1), with the origin at the center of the cluster (cross in Fig. 6.1.1). In Fig. 6.2.3 one can see the azimuthal dependence of the color excess. The dashed-dotted line shows the average of all quadrants. To the South the color excess increases almost constantly from ~ 1.86 mag to 2.15 mag in the South-West and ~ 2.0 mag in the South-East. To the North, $E(B - V)_g$ decreases to ~ 1.7 mag.

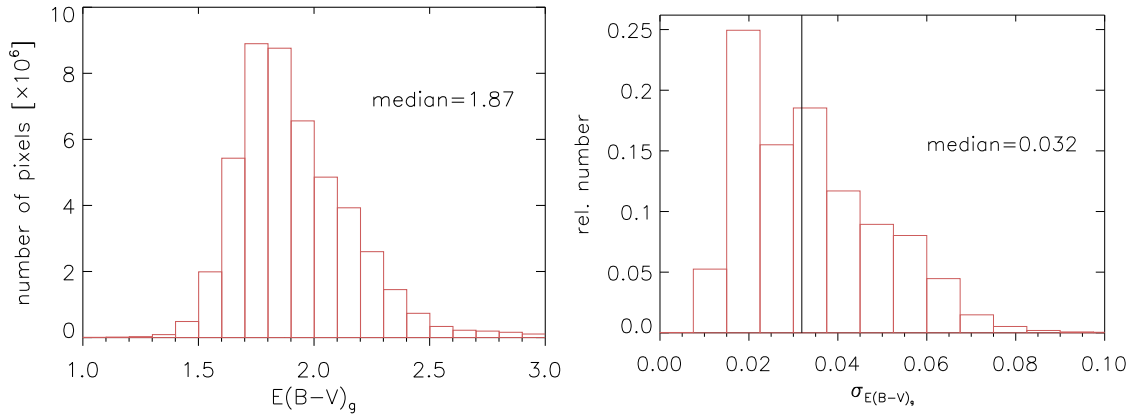


Figure 6.2.2: **Left:** The distribution of the color excess $E(B-V)_g$ with a median of 1.87 mag. Only 10742 pixels (0.23%) have a value of $E(B-V)_g > 3.0$ mag and only 1018 pixels (0.02%) exceed 5.0 mag. **Right:** The distribution of $\sigma_{E(B-V)_g}$ with a binsize of 0.0075 mag. The median value is 0.032 mag. The number is normalized to the total number of pixels.

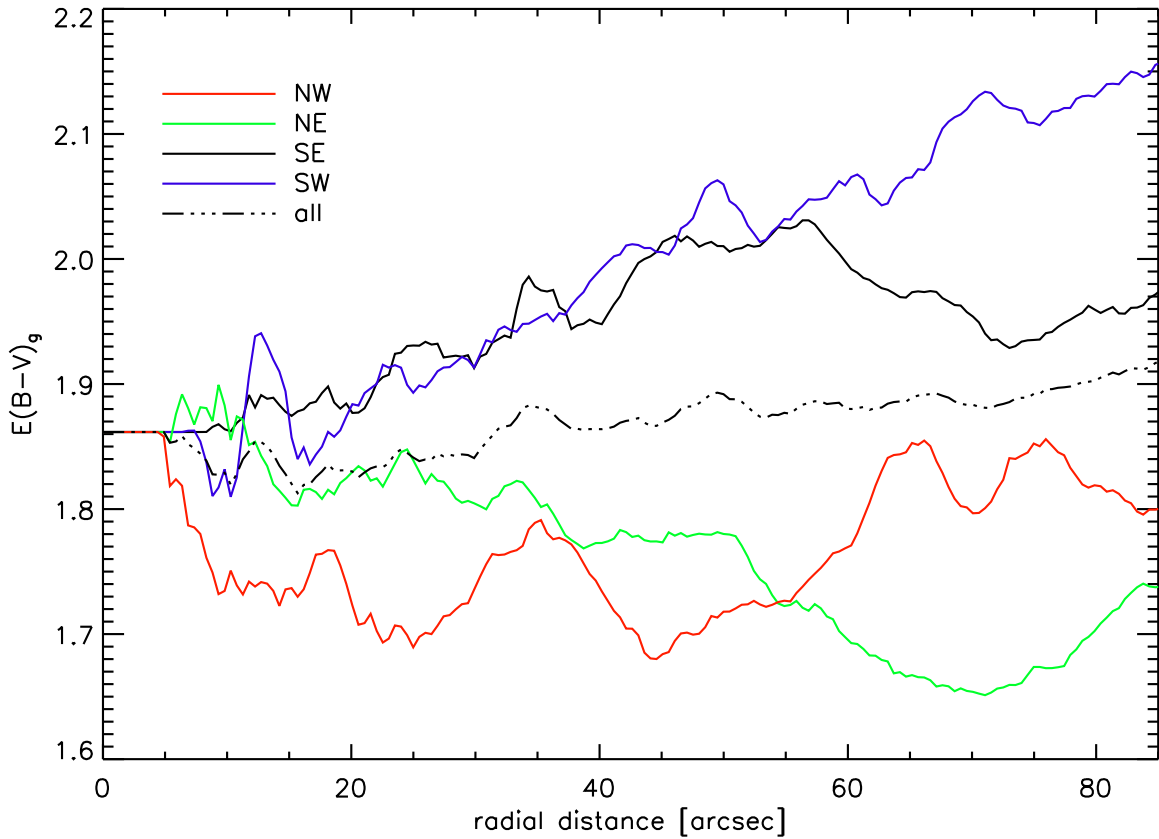


Figure 6.2.3: The averaged radial distribution of the color excess $E(B-V)_g$ in the four quadrants around the cluster center (cross in Fig. 6.1.1) including the average over all directions (dashed-dotted line).

6.3 Uncertainties of the color excess map

6.3.1 Uncertainties due to the electron counts

Before applying the reddening map to our photometric measurements, we needed to assess the accuracy of the map itself. We did that by assuming that the electron counts on the detector follow a Poisson distribution. We started with a Poisson error of the counts per pixel and performed a proper error propagation throughout our whole computation, beginning with the continuum interpolation up to the final $E(B - V)_g$ from Eq. 6.1:

$$\sigma E(B - V) = \left| \frac{1}{0.4 (\kappa(\text{H}\alpha) - \kappa(\text{Pa}\beta)) \ln(10) R_{\text{obs}}} \right| \cdot \sigma(R_{\text{obs}}), \quad (6.7)$$

$\sigma(R_{\text{obs}})$ is derived the following:

$$\sigma(R_{\text{obs}}) = \sqrt{\frac{1}{f_{F658N,\text{em.}}^2} \sigma f_{F658N,\text{em.}}^2 + \frac{f_{F658N,\text{em.}}^2}{f_{F128N,\text{em.}}^4} \sigma f_{F128N,\text{em.}}^2}. \quad (6.8)$$

The uncertainty in the uncalibrated flux is the Poisson error \sqrt{N} of the electron count $N = f_{F658N,\text{uncal.}}/\text{EXP}_{F658N}$ and $N = f_{F128N,\text{uncal.}}/\text{EXP}_{F128N}$, where EXP is the exposure time in each filter:

$$\begin{aligned} \sigma f_{F658N} &= \sqrt{\frac{f_{F658N,\text{uncal.}}}{\text{EXP}_{F658N}}} \\ \sigma f_{F128N} &= \sqrt{\frac{f_{F128N,\text{uncal.}}}{\text{EXP}_{F128N}}}. \end{aligned} \quad (6.9)$$

Combining eq. 6.7–eq. 6.9 we obtain for the total pixel-to-pixel uncertainty for the color excess map:

$$\begin{aligned}
\sigma E(B - V) = & \left| \frac{1}{0.4 (\kappa(\text{H}\alpha) - \kappa(\text{Pa}\beta)) \ln(10) R_{\text{obs}}} \right| \cdot \\
& \cdot \left[\frac{1}{F_{F128N,\text{em.}}^2} \Delta \lambda_{F658N}^2 \left[\frac{f_{F658N,\text{uncal.}} \cdot \text{PHOTFLAM}_{F658N}}{\text{EXP}_{F658N}} + \right. \right. \\
& + \left(\frac{\lambda_{F658N} - \lambda_{F555W}}{\lambda_{F814W} - \lambda_{F555W}} \right)^2 \frac{f_{F814W,\text{uncal.}} \cdot \text{PHOTFLAM}_{F814W}}{\text{EXP}_{F814W}} + \\
& + \left. \left(1 - \frac{\lambda_{F658N} - \lambda_{F555W}}{\lambda_{F814W} - \lambda_{F555W}} \right)^2 \frac{f_{F555W,\text{uncal.}} \cdot \text{PHOTFLAM}_{F555W}}{\text{EXP}_{F555W}} \right] + \\
& + \frac{F_{F658N,\text{em.}}^2}{F_{F128N,\text{em.}}^4} \Delta \lambda_{F128N}^2 \left[\frac{f_{F128N,\text{uncal.}} \cdot \text{PHOTFLAM}_{F128N}}{\text{EXP}_{F128N}} + \right. \\
& + \left(\frac{\lambda_{F128N} - \lambda_{F125W}}{\lambda_{F160W} - \lambda_{F125W}} \right)^2 \frac{f_{F160W,\text{uncal.}} \cdot \text{PHOTFLAM}_{F160W}}{\text{EXP}_{F160W}} + \\
& + \left. \left(1 - \frac{\lambda_{F128N} - \lambda_{F125W}}{\lambda_{F160W} - \lambda_{F125W}} \right)^2 \frac{f_{F125W,\text{uncal.}} \cdot \text{PHOTFLAM}_{F125W}}{\text{EXP}_{F125W}} \right] \Bigg]^{1/2} \quad (6.10)
\end{aligned}$$

In Fig. 6.2.2 we show the distribution of $\sigma E(B - V)_g$ (derived in Eq. 6.10) with a median of 0.032 mag. 90% of all pixels have an error smaller than 0.057 mag in the inferred nebular color excess.

6.3.2 Variations in the extinction law

As mentioned before, the reddening map depends on the adopted extinction law. For all further analyses we used the extinction law of [Cardelli et al. \(1989\)](#), hereafter denoted with the subscript C). For the sake of comparison, we also created the color excess map with the extinction law of [Fitzpatrick \(1999\)](#), hereafter denoted with the subscript FP). Both extinction laws are almost identical in the optical regime and so are the results. The median of the difference between $E(B - V)_{FP}$ and $E(B - V)_C$ is 0.05 ± 0.018 mag.

6.3.3 Line emission contamination

A non-negligible effect is the contamination of the wide-band filters with emission lines (e.g.: O III, S III, H β). Due to a lack of spectra of the gas and the large differences in published line emissions between different H II regions, we are unable to estimate the amount of contamination due to those lines. Compared to the Pa β line emission we expect this contamination in the wide-band filters to be small.

In order to visualize the possible contamination of the color excess map by nebular line emission we show in Fig. 6.3.1 the throughputs (top panel) of our filters together with the

simulated spectral lines (bottom panel) of a typical H II region using the H II Regions Library² based on the code CLOUDY (Panuzzo et al. 2003). For the model parameters we adopted the values ($n_{\text{H}} \sim 100 \text{ cm}^{-3}$, $Q_0 = 4.2 \cdot 10^{51} \text{ s}^{-1}$) of Pellegrini et al. (2011, and references therein) for the massive star cluster R136. Since we are only qualitatively interested in the possible gas emission lines the adopted values fulfill our needs.

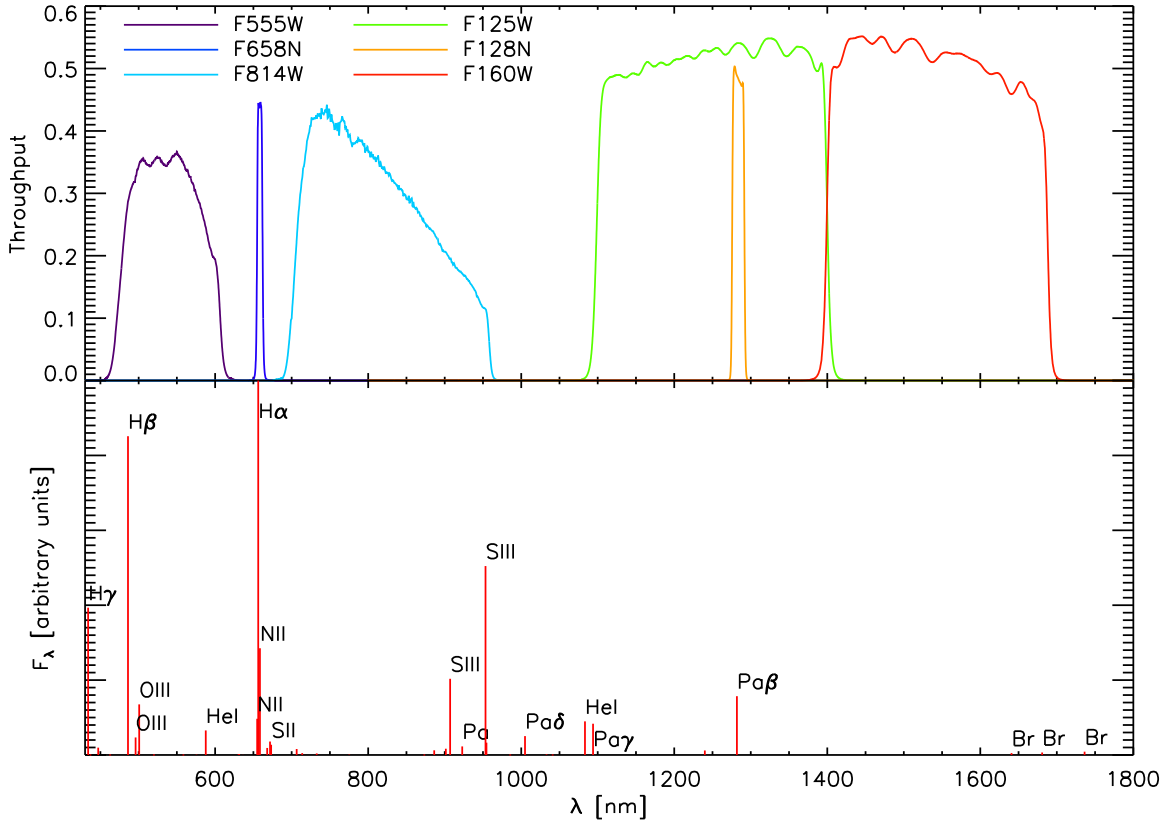


Figure 6.3.1: **Top:** Shown are the throughputs of the six used filters, derived with Synphot. The $F128N$ passband is located within the wavelength range covered by the $F125W$ filter. Therefore, the $\text{Pa}\beta$ emission line contributes to the $F125W$ continuum. **Bottom:** Synthetic spectral lines from the H II Regions Library (Panuzzo et al. 2003) show the emission features contaminating the continuum filters. The $\text{H}\alpha$ line is truncated for plotting reasons.

The $\text{Pa}\beta$ line is the only line for which we have information in our survey. $\text{H}\alpha$ is located outside the broadband filters and, therefore, not contaminating the continuum. Assuming the flux density to be the same in $F125W$ and $F128N$, we can derive the contribution of $\text{Pa}\beta$ via the flux ratio $F125W/F128N$. Both filters were multiplied by their respective bandwidth and PHOTFLAM value. We estimate the contamination of the continuum by the $\text{Pa}\beta$ line to be $\sim 22\%$.

²<http://pasquale.panuzzo.free.fr/hii/>

Taking into account results from Pang et al. (2011) we estimate the contamination of the other possible emission lines in the other filters to be about 10-15% which could increase the overall color excess by ~ 0.1 - 0.15 mag.

Finally, the $E(B - V)_g$ excess is also affected by the electron density and temperature used to calculate the R_{int} ratio. We calculated $E(B - V)_g$ for different electron densities and temperatures. For an increase of the electron density by a factor of two, $E(B - V)_g$ decreases by 0.00124 mag. For the extreme cases of $N_e = 10000(100) \text{ cm}^{-3}$ and $T_e = 5000(20000) \text{ K}$, $E(B - V)_g$ changes by $+0.028(-0.034)$ mag.

In summary, we can say that the uncertainties in electron density and temperature are introducing a small spread, which is below the 90% limit of the photometric uncertainty of the different filters (see Fig. 4.4.2). The unknown line contamination, on the other hand, introduces a possible increase of the color excess of the gas $E(B - V)_g$ of ~ 0.1 - 0.15 mag. This shift can be calibrated out when transforming $E(B - V)_g$ to the stellar color excess $E(B - V)_\star$ (see eq. 7.4).

6.4 Limitations of the color excess map

The removal of the stellar contamination by interpolating and subtracting the continuum emission worked well for all objects up to a certain brightness limit. Problems occurred for saturated objects and their spikes as well as for those objects with diffraction rings. At the positions of these sources, the pixel values are not reliable anymore. Therefore, the interpolation and thus the subtraction might partly or totally fail for these objects.

For small areas with just a few unreliable pixel values we were able to clean the final reddening map by performing a spline interpolation. This problem appears for objects close to the saturation limit meaning that only a few pixels are saturated or the object is saturated just in one filter.

For cosmic rays, dead and hot pixels, being these cases where just a single pixel is defective, we were able to clean the final map by replacing the affected pixels by the median value of their surrounding.

For the very bright objects as well as for the whole cluster center, the area of saturated pixels was too large for a meaningful interpolation. Here we replaced the entire affected area by the median reddening calculated over an annulus around that area. Those values should thus be handled with caution. To create a smoother looking map for presentations (see Fig. 6.1.1) we additionally introduced a random Poisson noise to the interpolated pixel values (see Fig. 4.4.2). For any scientific use of the map the values without Poisson noise are used.

Wo viel Licht ist, ist auch viel Schatten.

— Johann Wolfgang von Goethe: Götz von
Berlichingen

7

The stellar reddening toward the direction of Wd2

This chapter is included as Sect. 5 of [Zeidler et al. 2015, AJ, 150, 78](#) and as Appendix B of [Zeidler et al. 2016, AJ, 152, 4](#).

After creating the pixel-to-pixel gas excess map $E(B-V)_g$ there was the need to translate this color excess into a stellar color excess $E(B-V)_*$ in order to properly deredden the stellar photometry. [Calzetti \(1997\)](#) and [Calzetti et al. \(2000\)](#) found a linear empirical relation between the stellar and the gas reddening ($E(B-V)_* \sim f \cdot E(B-V)_g$). In star forming regions, the dust in front of the stars is removed or destroyed by stellar feedback. Therefore, the stellar reddening is smaller than the reddening of the gas. The interstellar medium (ISM) consists of a different composition (grain size, density, etc.) throughout the Galaxy. Therefore, this linear, empirical relation is only valid for a small range in color excess $E(B-V)$ and needs to be determined for each cluster independently.

7.1 Transformation of the color excess between filter systems

We used the results of the ground-based optical spectral types of massive stars in Wd2 from [Vargas Álvarez et al. \(2013\)](#) and [Rauw et al. \(2007, 2011\)](#) to obtain the bolometric magnitude of each of those stars using Tab 1.4 of [Sparke and Gallagher \(2007\)](#) combined with the zero-age-main-sequence (ZAMS)¹. We used this information to determine the color excess of

¹The ZAMS was derived combining isochrones from the PADOVA AND TRIESTE STELLAR EVOLUTION CODE (<http://stev.oapd.inaf.it/cmd>) (hereafter: PARSEC, [Bressan et al. 2012](#)), at which age a star for a certain mass interval reaches the main sequence.

Table 7.1.1. The transformation parameters

FILTER	FILTER SYSTEM	λ_P [nm]	a	b
<i>F336W</i>	WFPC2	334.44	0.87338	2.37152
<i>F439W</i>	WFPC2	431.13	0.99552	1.12082
<i>B</i>	—	445 ²	1.00213	0.94137
<i>V</i>	—	551 ¹	1	0
<i>F555W</i>	ACS	536.10	1.00699	0.06883
<i>F555W</i>	WFPC2	543.90	1.00311	0.02704
<i>F814W</i>	WFPC2	801.22	0.78049	-0.57273
<i>F814W</i>	ACS	805.70	0.77652	-0.58020
<i>F125W</i>	WFC3IR	1248.6	0.40149	-0.36821
<i>F160W</i>	WFC3IR	1536.9	0.28735	-0.26382

Note. — The parameters a and b for transforming the color excess of the stars $E(\lambda_1 - \lambda_2)$ to an excess $E(B - V)$. The parameters a and b are calculated with Eq. 3a and 3b from [Cardelli et al. \(1989\)](#).

the star combining the intrinsic color and the color derived with the photometric catalog of [Vargas Álvarez et al. \(2013\)](#) ($E(B - V)_* = (B - V)_* - (B - V)_{th}$) since our photometric catalog does not cover the B -band. We then used the proper transformation of the photometry from the WFPC2 photometric system to the Johnson-Cousins system:

$$\frac{E(\lambda_1 - \lambda_2)_g}{E(B - V)_g} = \frac{a_{\lambda_1} + \frac{b_{\lambda_1}}{R_V} - a_{\lambda_2} - \frac{b_{\lambda_2}}{R_V}}{a_B + \frac{b_B}{R_V} - a_V - \frac{b_V}{R_V}}. \quad (7.1)$$

The parameters a and b are calculated with Eq. 3a and 3b from [Cardelli et al. \(1989\)](#) and given in Tab. 7.1.1. λ_1 and λ_2 are the pivot wavelengths λ_P of the *F439W* and *F555W* filters, respectively. For the total-to-selective extinction, we used the same value as in the color excess map ($R_V = 3.1$). We should note that even though we inferred an R_V here in order to determine $E(B - V)_*$, we analyze R_V in Sect. 8.2.1. The inferred range of values of R_V between 3.1 and 4.0 leads to a change in $E(B - V)_*$ of $\sim 0.6\%$.

The HST filters are just a rough representation of the Johnson-Cousins photometric system ([Johnson and Morgan 1953](#)) and constitute their own photometric system (see throughput curves of Fig. 13 of [Sirianni et al. 2005](#)). A detailed description and calibration cookbook for the HST/ACS filters are provided in [Sirianni et al. \(2005\)](#). So far we always used the internal HST filter sets apart from the reddening correction via the color excess map $E(B - V)$. The [Cardelli et al. \(1989\)](#) extinction law depends on the total-to-selective extinction parameter R_V and assumes a different analytical form depending on the wavelength, divided into three wavelength regimes: infrared, optical/near-infrared, and ultraviolet. In the optical/near-infrared it is described as a seventh degree polynomial (see Eq. 1, 3a, b of

Cardelli et al. 1989) that fits their five passbands (*UBVRI*).

We detected a discrepancy in the colors when we used the *F555W* filter between the reddening-corrected photometric catalog and the theoretical PARSEC 1.2S isochrones (Bresnan et al. 2012). We translated the color excess $E(B - V)$ to a total extinction $A(\lambda)$ at the pivot wavelength λ_P for each of the used HST filters using the definition of the total-to-selective extinction $R_V = A_V/E(B - V)$ and Eq. (1) of Cardelli et al. (1989):

$$A(\lambda) = [a(x) \cdot R_V + b(x)] \cdot E(B - V). \quad (7.2)$$

Here, $x = 1/\lambda$ [μm^{-1}] while $a(x)$ and $b(x)$ are the inverse wavelength-dependent coefficients of Cardelli's extinction law (Cardelli et al. 1989) at the pivot wavelength λ_P of the HST filters (see Tab. 7.1.1). The *F555W* filter is the only filter in our observations whose pivot wavelength of $\lambda_P = 536.1$ nm is bluer than Johnsons-Cousin's *V*-band, while the width is larger than the *V*-band width (see Fig. 1, Maíz Apellániz 2013). The pivot wavelength is a weighted mean taking into account the filter's throughput curve. The extinction law is just evaluated at one point. This fact is also mentioned by Maíz Apellániz (2013) and Sirianni et al. (2005). At the location of the *V*-band the inverse wavelength-dependent coefficient $b(x)$ of Cardelli's extinction law (Cardelli et al. 1989) changes its sign and so the evaluation of the $A(F555W)/A(V)$ at just $\lambda_P = 536.1$ nm can cause errors. In our case this leads to an under-correction of the reddening for the *F555W* filter. In the left panel of Fig. 7.1.1 we give the example of the reddening-corrected ($F555W - F814W$) vs. ($F814W - F160W$) two-color diagram (TCD).

To correct $A(F555W)/A(V)$ we used four TCDs based on the *F814W*, *F658N*, *F125W*, and *F160W* filters. We selected the MS stars and fitted them simultaneously to the ZAMS by adjusting $A(F555W)/A(V)$ taking into account the photometric errors. It is possible to reduce this problem to a linear fit of the following form:

$$(F555W - X_0) - (F555W - X)_{ZAMS} = \frac{A(F555W)}{A(V)} \cdot E(B - V). \quad (7.3)$$

X represents the different filters. In Fig. 7.3 the relations for four different filters are plotted including the overall best fit, which results in $A(F555W)/A(V) = 1.038$. This implies an increase of 1.4% for the ratio $A(F555W)/A(V)$ with a total-to-selective extinction of $R_V = 3.95$ (see Sect. 8.2.1). As an example and comparison, we give in the right panel of Fig. 7.1.1 the reddening-corrected ($F555W - F814W$) vs. ($F814W - F160W$) TCD for the adjusted $A(F555W)/A(V)$ value.

This analysis leads to an adjustment of $a(x) \cdot R_V + b(x)$ to 4.10158 for the *F555W* filter.

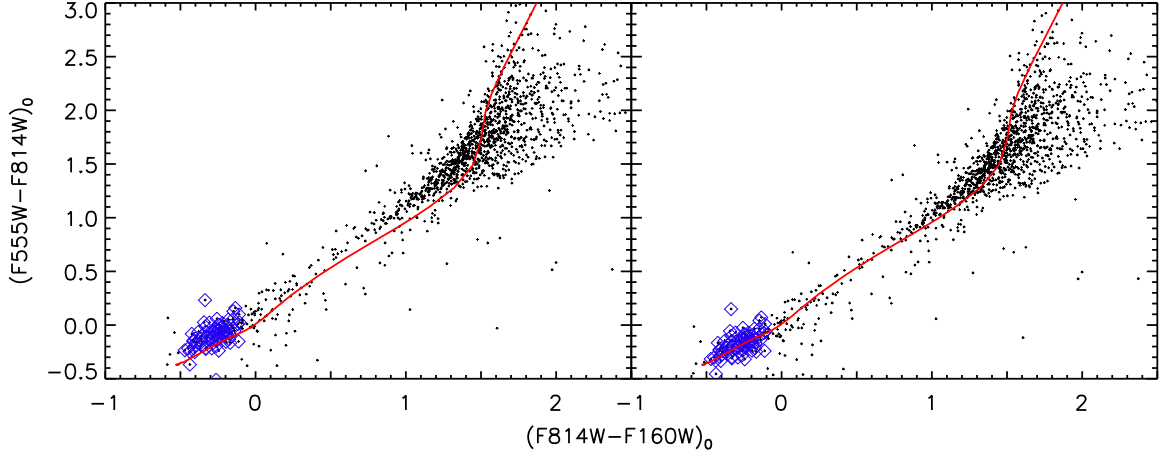


Figure 7.1.1: The reddening-corrected $(F555W - F814W)$ vs. $(F814W - F160W)$ TCD of the selected stars in RCW 49. **Left:** The dereddening was performed with a color-excess transformation $A(F555W)/A(V) = 1.024$ using the pivot wavelength of the $F555W$ filter. **Right:** We used a color-excess transformation $A(F555W)/A(V) = 1.038$ for the dereddening to fit the MS to the ZAMS in the TCDs. The blue diamonds are the selected MS stars used for the fit. The red line represents the ZAMS from the PARSEC 2.1S models.

7.2 Transformation of the gas excess map to the stellar excess map

In order to get the transformation between the stellar excess and the gas excess we used all stars with spectroscopy that have individual reddening values (e.g.: are not located in the center) and are main-sequence stars (class V without special line features). A linear, error weighted regression revealed the following relation between the gas and the stellar extinction:

$$E(B - V)_* = 0.4314 \cdot E(B - V)_g + 0.7400. \quad (7.4)$$

It is satisfactory to use a total-to-selective extinction of $R_V = 3.1$ for creating the color-excess map of the gas (see Sect. 6) since a different R_V will be compensated by different regression parameters in Eq. 7.4 and, therefore, leaves the overall outcome for $E(B - V)_*$ unaffected. This results in an intercept greater than zero. Eq. 7.4 now allows us to translate the $E(B - V)_g$ gas extinction map into a map of the stellar extinction $E(B - V)_*$. The overall median of $E(B - V)_g = 1.87$ mag transforms to $E(B - V)_* = 1.55$ mag. In Fig. 7.2.1 one can see the stars used to calculate the transformation.

In Fig. 7.2.1 the histogram of the distribution of the color excess $E(B - V)$ is plotted for each of the 14199 objects in the catalog spatially covered by the color excess map. The gas excess distribution is shown in red while the stellar excess distribution is shown in blue. The asterisks mark the color excesses of the thirteen stars with spectral types, which we used to obtain the linear regression for transforming the gas excess into a stellar excess.

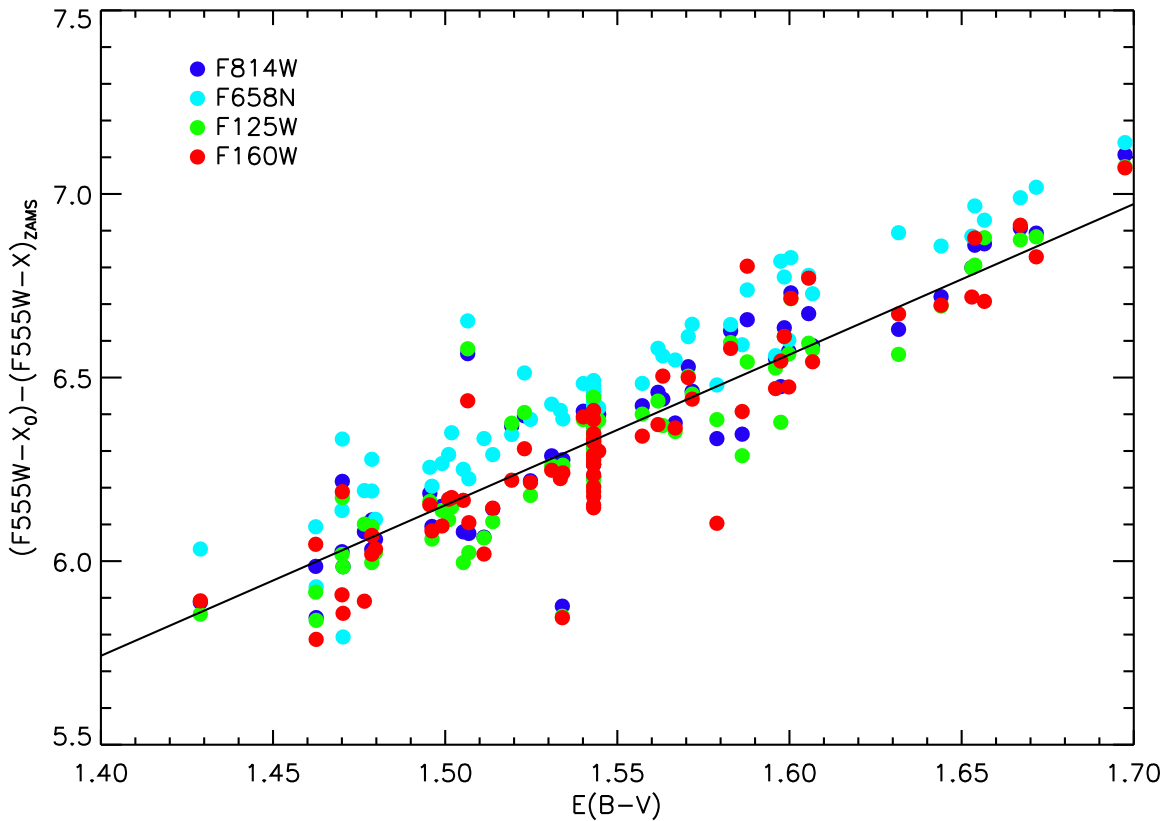


Figure 7.1.2: The linear fit for the reddening correction using all main-sequence stars for the four TCDs involving the $F555W$ band. The straight line represents the best fit taking into account photometric errors.

It can be seen that the color excess of the 13 stars is equally distributed over the whole range in color excess of all objects in the catalog. Therefore, the linear approach is valid for the complete catalog. However, we caution that this transformation cannot be used to extrapolate to $E(B - V)_g = 0$ mag or to very high $E(B - V)_g$ values.

7.3 The stellar color excess derived with UBV photometry

An independent way of deriving the stellar reddening towards Wd2 is to use UBV TCD. Since our own photometric catalog lacks the U -band photometry, we used the photometric catalog of Vargas Álvarez et al. (2013), including the spectroscopy derived by Rauw et al. (2007, 2011), and Vargas Álvarez et al. (2013). We used all stars with a spectral classification of luminosity class V, meaning that they are located on the main-sequence, and have no abnormal line features (see Tab. 7.3.1) and a determined photometry in the $F439W$ and $F555W$ WFPC2 filters.

Using the PARSEC ZAMS with the same procedure as described in Sect. 7.1, we were able to obtain the locus of the spectroscopically determined stars on the main-sequence in

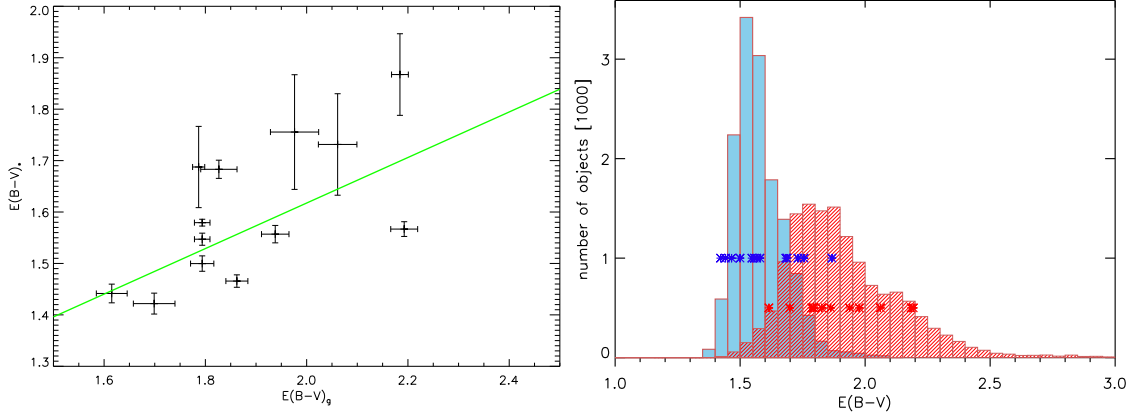


Figure 7.2.1: **Left:** The 13 stars with spectroscopic data used to calculate the transformation between the pixel-to-pixel gas excess map $E(B - V)_g$ to the stellar excess $E(B - V)_*$ are shown here. The green line is the best fit linear regression including error weighting. **Right:** The distribution of the color excess $E(B - V)$ for each of the 14199 objects in the catalog, covered by the color excess map. The gas excess distribution is shown in red while the stellar excess distribution is shown in blue. The asterisks mark the color excesses of the thirteen stars with spectral types used to obtain the linear regression for transforming the gas excess into a stellar excess.

the *UBV* TCD. By shifting the individual stars in the TCD to their theoretical loci on the main sequence we could derive the stellar color excess $E(F439W - F555W)_*$ and $E(F336W - F439W)_*$. Column 7 of Tab. 7.3.1 lists the derived values transformed to the Johnson-Cousins photometric system with the extinction law of Cardelli et al. (1989) (see Eq. 7.1).

The slope of the two-color excess in the TCD gives a ratio of $E(U - B)/E(B - V) = 0.85 \pm 0.033$. Therefore, it is larger than the mean throughout the MW, which amounts to $E(U - B)/E(B - V) = 0.72$ (Fitzgerald 1970). This is consistent with the higher total-to-selective extinction derived in Sect. 8.2.1. The mean of the color excess of the stars derived via the TCD is $E(B - V)_* = 1.62 \pm 0.113$. The median of the color excess of the stars derived with the color excess map was $E(B - V)_* = 1.55$. Comparing the individual values of $E(B - V)_*$ derived with the TCD with those of the color excess map reveals a mean difference of $\Delta E(B - V)_* = 0.087 \pm 0.129$. We can say, within the errors, that our method of deriving the pixel-to-pixel gas excess map and transferring it to an excess map of the stars was successful and we can confidently use this map to deredden our photometry of the cluster members.

Table 7.3.1. Comparison to spectroscopic data

ID	RA J2000	DEC J2000	SPEC. TYPE	$F555W$	$(F439W - F555W)$		TCD	$E(B - V)_*$		$E(B - V)_g$		An.
					int,th	V.-A.		map	σ_{map}	map	σ_{map}	
1	10:23:55.176	-57:45:26.89	O4 V	15.610	-0.281	1.776	1.841	1.526	0.013	1.822	0.024	b
2	10:23:56.160	-57:45:29.99	O4 V-III((f))	14.514	-0.281	1.451	—	1.488	0.006	1.734	0.020	b
5	10:23:59.201	-57:45:40.53	O7.5 V	16.015	-0.270	1.666	1.734	1.629	0.099	2.061	0.038	b
6	10:24:01.920	-57:45:32.62	O8.5 V	16.100	-0.263	1.489	1.574	1.686	0.014	2.193	0.027	a,b
7	10:24:00.353	-57:45:42.71	O8 V	15.863	-0.267	1.615	1.687	1.528	0.018	1.827	0.036	b
9	10:23:00.480	-57:45:24.01	O4 V	14.546	-0.281	1.485	1.581	1.514	0.007	1.794	0.015	b
10	10:24:00.499	-57:44:44.53	B1 V	15.587	-0.254	1.358	1.441	1.437	0.018	1.615	0.030	b
12	10:24:00.713	-57:45:25.42	O8 V	15.466	-0.267	1.410	1.503	1.514	0.015	1.794	0.023	b
13	10:24:00.816	-57:45:25.87	O6.5 V	14.866	-0.276	1.454	1.549	1.514	0.012	1.794	0.015	b
14	10:24:00.979	-57:45:05.50	B1 V	16.111	-0.254	1.336	1.421	1.473	0.020	1.699	0.041	a,b
15	10:24:01.070	-57:45:45.73	O9.5 V	16.239	-0.259	1.482	1.561	1.576	0.017	1.938	0.027	b
16	10:24:01.200	-57:45:31.07	O3 V	13.487	-0.283	1.513	1.608	1.543	0.017	1.862	0.006	
17	10:24:01.392	-57:45:29.66	O4 V	14.084	-0.281	1.411	1.515	1.543	0.006	1.862	0.007	
18	10:24:01.454	-57:45:31.33	O3 V	15.042	-0.283	1.403	1.510	1.543	0.007	1.862	0.017	
19	10:24:01.524	-57:45:57.06	O6 V	15.053	-0.278	1.810	1.868	1.682	0.079	2.184	0.017	b
20	10:24:01.610	-57:45:27.89	O5.5 V	14.921	-0.278	1.378	1.482	1.543	0.008	1.862	0.027	
21	10:24:01.889	-57:45:40.05	O9.5 V	16.574	-0.259	1.656	1.717	1.543	0.023	1.862	0.042	a
22	10:24:01.889	-57:45:28.00	O8 V	15.524	-0.267	1.510	1.593	1.543	0.015	1.862	0.022	
23	10:24:02.064	-57:45:28.01	O6 III	14.453	-0.278	1.664	—	1.543	0.010	1.862	0.009	
24	10:24:02.186	-57:45:31.32	O9.5 V	16.609	-0.259	1.601	1.668	1.543	0.020	1.862	0.040	a
25	10:24:02.256	-57:45:35.12	O4-5 V	14.736	-0.281	1.498	1.592	1.543	0.007	1.862	0.018	
26	10:24:02.304	-57:45:35.53	O4.5 V	13.893	-0.281	1.475	1.571	1.543	0.006	1.862	0.008	
27	10:24:02.376	-57:45:30.64	O3 V((f))	13.878	-0.283	1.618	—	1.543	0.018	1.862	0.004	
29	10:24:02.414	-57:45:47.11	O9.5 V	16.637	-0.259	1.704	1.760	1.592	0.112	1.976	0.048	a,b
30	10:24:02.448	-57:44:36.13	O5 V-III	13.155	-0.280	1.359	—	1.479	0.052	1.712	0.003	b
31	10:24:02.518	-57:45:31.47	O8.5 V	15.790	-0.263	1.598	1.671	1.543	0.014	1.862	0.033	
32	10:24:02.555	-57:45:30.52	O8.5 V	16.243	-0.263	1.649	1.717	1.543	0.017	1.862	0.030	
33	10:24:02.604	-57:45:32.26	O6-7 V	16.118	-0.276	1.579	1.661	1.543	0.016	1.862	0.039	
34	10:24:02.664	-57:45:34.38	O3-4 V	14.554	-0.282	1.528	1.620	1.543	0.005	1.862	0.016	
35	10:24:02.789	-57:45:30.05	O8 V	15.963	-0.267	1.593	1.667	1.543	0.017	1.862	0.035	
36	10:24:03.787	-57:44:39.87	O9.5 V	15.349	-0.259	1.380	1.470	1.543	0.012	1.862	0.022	b
37	10:24:04.901	-57:45:28.43	O4-5 V	14.528	-0.281	1.606	1.688	1.511	0.079	1.787	0.012	b

Note. — All stars with a determined spectroscopic type and existing photometry in the two filters $F439W$ and $F555W$ from Vargas Álvarez et al. (2013) and Rauw et al. (2007, 2011). All WFPC2 photometry was adopted from Vargas Álvarez et al. (2013). Column 1 shows the identical stellar ID as in Tab. 2.2.1. Columns 2–3 list the J2000 coordinates followed by the spectral type. Column 5 gives the WFPC2 $F555W$ magnitude. Columns 6 gives the WFPC2 $F439W - F555W$ theoretical intrinsic colors, derived from (p.23, Tab.1.4, Sparke and Gallagher 2007) in combination with the PARSEC ZAMS. Column 7 lists the stellar WFPC2 $F439W - F555W$ colors. Column 8 gives the stellar excess derived from the UBV TCD. Columns 9–12 list the stellar and gas excess $E(B - V)$ and their respective uncertainties derived from our color excess map. Column 13 gives additional information: (a) stars have a proper $F160W$ and $F814W$ photometry in our data and are shown in our CMD (Fig. 8.2.3), (b) individual reddening from the gas extinction map is available.

Das also war des Pudels Kern!

— Johann Wolfgang von Goethe: Faust, Vers 1323

8

The stellar population of the RCW 49 region

This chapter is included as Sect. 6 and Sect. 7 of [Zeidler et al. 2015, AJ, 150, 78](#) and as Sect. 3 of [Zeidler et al. 2016, AJ, 152, 4](#).

In this chapter, we present the analysis of the global stellar population of the RCW 49 region and the Wd2 cluster.

8.1 The separation of the cluster population from the field stars

In order to understand the stellar populations in our dataset we plotted the $F814W - F160W$ vs. $F814W$ CMD of our catalog (see Fig. 8.1.1). This CMD contains 7697 objects in total. Looking at the CMD it immediately becomes clear that we observe a composite population. There are two parallel sequences: a blue one at $F814W - F160W \sim 2-4$ mag, and a redder one, at $F814W - F160W \sim 4-8$ mag (with approximate boundaries represented by the green lines in Fig. 8.1.1). The bluer population seems to consist of two branches, probably due to stars at different distances along the line of sight through the Galactic disk. The brightest objects can be seen at $F814W \approx 14$ mag.

The bluer sequence of the two clearly separated populations can be explained with the foreground population of the Galactic disk toward Wd2 (see Sect. 8.2). This population is located closer to us and hence less reddened. This makes those stars appear bluer in the CMD. The red sequence of the CMD is most likely the cluster population of Wd2 (see Sect. 8.1).

Our data suffer from saturation of the very bright objects (see Sect. 4), and for this reason we do lose stars in the CMD at the bright end. Due to the detection method in the

WFC3/IR filters (see Sect. 3) saturation occurs only in the optical filters but on the other hand the WFC3/IR filters suffer from severe crowding in the cluster center. Comparing our objects with detections in at least two filters with more shallow photometric studies from the literature (Vargas Álvarez et al. 2013) and the spectroscopically classified stars we conclude that we miss a minimum of 49 luminous stars, at the bright end of our photometry. For a detailed discussion see Sect. 10.1.

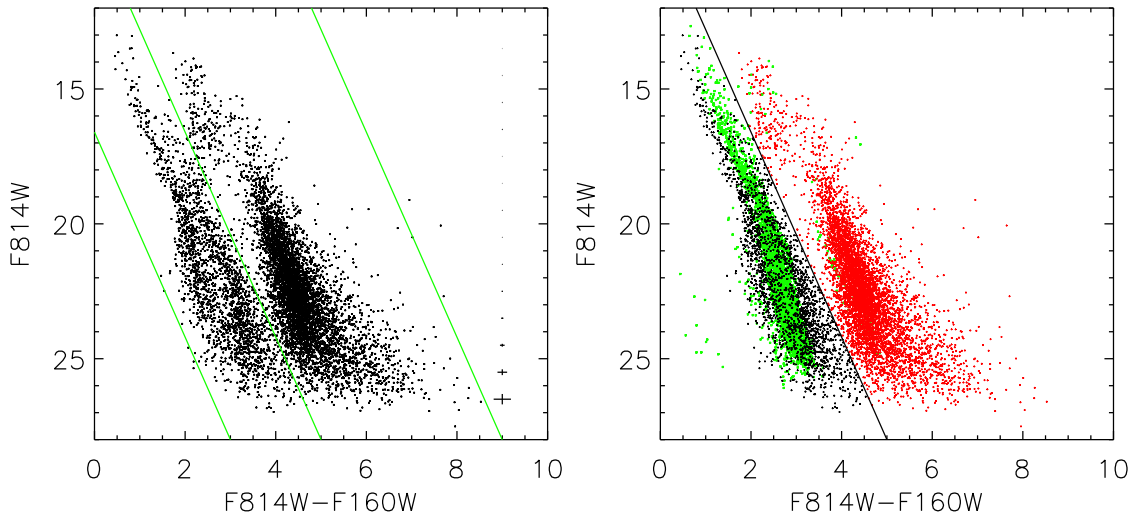


Figure 8.1.1: The $F814W$ vs. $(F814W - F160W)$ CMD of the Wd2 region. The plot contains 7697 objects. On the right representative photometric error bars are shown in bins of 1 mag. **Left:** The green lines represent the separation between the two parallel sequences of likely foreground stars (blue sequence) and point sources likely associated with Wd2. **Right:** The red points represent likely members of the RCW 49 region (including cluster members). The black sources are probable foreground stars. The green points indicate the location of the synthetic objects from the Besançon model in the direction of Wd2 up to the cluster distance of 4.16 kpc falling within a FOV corresponding in size to our survey area (~ 21 arcmin²). Their superposition with the black points suggests that the latter are less reddened foreground stars. The black solid line marks our arbitrary separation between cluster and field stars.

In order to study the properties of Wd2 and the spatial morphology of the stellar content we need to extract a sample of probable RCW 49 member stars. Therefore, we need to clean the catalog from foreground objects (see Sect. 8.1).

The RCW 49 member selection was performed using the $F814W - F160W$ vs. $F814W$ CMD of our catalog. As a first step, we divided the data in likely foreground population stars (2093) (marked by black points) and the likely RCW 49 member stars (5604), indicated by red points (see Fig. 8.1.1). Distinguishing these two populations by defining a diagonal line was possible due to the clear separation of the two sequences and even at the faint end of the CMD the photometric uncertainties are still small enough to clearly separate the sequence formed by unrelated foreground Galactic disk objects and by the RCW 49 members.

To test whether the black objects are indeed contaminant stars of the Galactic plane, we simulated the MW disk in the direction of Wd2 with the Model of stellar population synthesis of the Galaxy, the Besançon model (Robin et al. 2003). This model adopts the

extinction law of [Mathis \(1990\)](#). It lacks the spiral arm structure ([Robin et al. 2003](#)), but since we are just sampling one line of sight, this should not be a problem. We simulated the color-magnitude locus of the expected stars in the Galactic plane up to the cluster distance of 4.16 kpc across a FOV corresponding in size to our survey area (~ 21 arcmin²). The simulated stellar distribution is visualized by the green points in Fig. 8.1.1. We transformed the model colors and bands, which are by default in the Johnson-Cousins photometric system ([Johnson and Morgan 1953](#)), into the HST photometric system with the SYNPHOT/CALCPHOT routine¹ ([Laidler et al. 2005](#)) for consistency with the data. It looks like the green points are centered between the two slightly separated populations of the foreground, most likely originating from a non-uniformly distributed ISM in the line of sight towards Wd2. The green points do indeed nicely overlap with the blue diagonal sequence of suspected foreground stars, supporting our assumption. Since we do not know the distribution of the foreground reddening we cannot reproduce the exactly observed distribution of the foreground populations.

8.2 The global, physical parameters of Wd2

Using our high resolution dataset in combination with the 2D color excess map we are able to determine the physical properties of Wd2.

8.2.1 The total-to-selective extinction toward the direction of Wd2

In order to correct for the high differential reddening, visible in the map of the color excess $E(B-V)_g$ (see Fig. 6.1.1.), we need to get a better insight in the total-to-selective extinction ratio R_V :

$$R_V = \frac{A_V}{E(B-V)}, \quad (8.1)$$

where A_V represents the total extinction in the visible.

Since the distance modulus for Wd2 is not yet fixed, we used the TCD to derive a value for R_V , since TCDs have the advantage of being distance independent. To derive R_V , we had to find the best fit of the ZAMS to the likely main-sequence stars of our photometric catalog. Therefore, we used all stars brighter than $F814W > 18$ mag of the RCW 49 members (red points in Fig. 8.2.1 and Fig. 8.2.1 selected through the CMD of Fig. 8.1.1). We used three different TCDs: $F555W - F814W$ vs. $F814W - F125W$, $F555W - F814W$ vs. $F125W - F160W$, and $(F439W - F555W)_{\text{WFPC2}}$ vs. $(F555W - F814W)_{\text{WFPC2}}$. Here again, we also used the WFPC2 data from the photometric catalog of [Vargas Álvarez et al. \(2013\)](#). The PARSEC ZAMS was used for Solar metallicity $Z = 0.0152$ ([Caffau et al. 2011](#)).

¹Synphot is a product of the Space Telescope Science Institute, which is operated by AURA for NASA.

In order to deredden the stars onto the locus of the ZAMS in the TCDs we used the extinction law of [Cardelli et al. \(1989\)](#) (see Eq. 7.1) to calculate the absolute extinction A_λ in dependence of R_V . In order to get the best fit for the three TCDs we needed to apply values of $R_V = 3.81$ for $F555W - F814W$ vs. $F814W - F125W$ (see Fig. 8.2.1), $R_V = 3.96$ for $F555W - F814W$ vs. $F125W - F160W$ (see Fig. 8.2.1), and $R_V = 4.08$ for $(F439W - F555W)_{\text{WFPC2}}$ vs. $(F555W - F814W)_{\text{WFPC2}}$ (see Fig. 8.2.1). In the corresponding Fig. 8.2.1, Fig. 8.2.1, and Fig. 8.2.1 we show the stellar population including the ZAMS and the reddening vector. The red points represent the likely MS stars, the blue diamonds represent the objects for which spectroscopy is available. The discrepancies at the red end of the IR filters in the TCD with respect to the remaining objects (black points) originate from the very numerous PMS population appearing redder due to their circumstellar dusty envelopes. Because of the high number of spectroscopically observed stars in Fig. 8.2.1, we only used those objects for fitting. The ZAMS fitting gives us a mean value of $R_V = 3.95 \pm 0.135$. Spectroscopic observations of the most massive stars ([Vargas Álvarez et al. 2013](#); [Rauw et al. 2007, 2011](#)) and a photometric study of [Hur et al. \(2015\)](#) show that Wd2 has a total to selective extinction in the visual ($R_V = A_V/E(B - V)$) of about 3.64–3.85, which agrees with our value within the uncertainties. From the spectral-energy distribution (SED) fitting of O and B-type stars observed with the VLT Survey Telescope (VST) [Mohr-Smith et al. \(2015\)](#) recently derived $R_V = 3.96^{+0.12}_{-0.14}$, also in excellent agreement with our finding.

8.2.2 The extinction correction of our cluster CMD

The high resolution color excess map of the gas $E(B - V)_g$, was transformed to the stellar color excess $E(B - V)_*$ (see Sect. 7.2) and used to correct the CMD for differential reddening. In other words, we used the resulting stellar color excess estimate at the position of the stars to subtract the foreground reddening. For the color excess $E(B - V)_*$ at each stellar position, the median $E(B - V)_*$ within three sigma of the mean PSF was calculated and then translated into the total extinction A_λ at the pivot wavelength λ of the HST filters, using again the extinction law of [Cardelli et al. \(1989\)](#) (see Eq. 7.2).

In Fig. 8.2.2 we show the CMD of the Wd2 members as observed (left) as well as the individually dereddened CMD (right). The red arrow shows the overall median reddening of $E(B - V)_* = 1.55$ with $R_V = 3.95$ (see Sect. 8.2.1 for determining R_V). We should note here that for objects lying in regions where the color excess map needed to be interpolated or substituted by the median (see Sect. 6.4), the uncertainty of the dereddening is bound to the uncertainty of the estimation of the values of the saturated pixels. Consequently, individual dereddening means using the individual stellar excess for each star and the extrapolated/substituted value for the stars where the color-excess map has corrupt pixels. As one can see from the color representation of the density in the plot, a tightening of the CMD was achieved. Nevertheless, the spread cannot be reduced to less than the intrinsic age spread of ~ 2 Myr. Also effects like rotation and binarity play a role. PMS stars have their own circumstellar effects, in addition to the general differential reddening, causing broadening of the CMD.

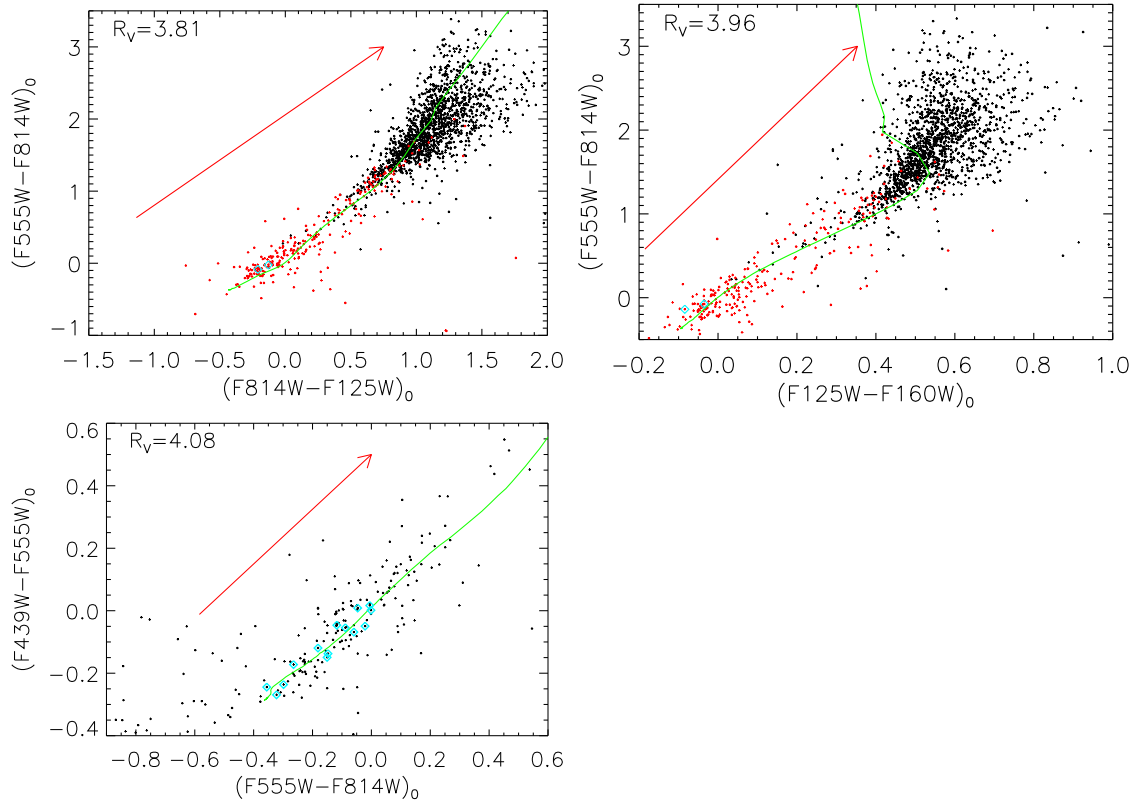


Figure 8.2.1: The $F555W - F814W$ vs. $F814W - F125W$ TCD (top, left), the $F555W - F814W$ vs. $F125W - F160W$ TCD (top, right), and the $(F439W - F555W)_{\text{WFPC2}}$ vs. $(F555W - F814W)_{\text{WFPC2}}$ TCD (bottom, left) of the Wd2 photometric catalog (the WFPC2 photometry is from Vargas Álvarez et al. (2013)). The green line represents the PARSEC ZAMS. We show in red the reddening vector for $E(B - V)_* = 1.55$ mag and $R_V = 3.81$, $R_V = 3.96$, and $R_V = 4.08$, respectively. The red points represent the likely MS stars (all RCW 49 members brighter than $F814W < 18$ mag). The discrepancies at the red end originate from the rich PMS population appearing redder due to the persisting dusty envelopes around the stars. The blue diamonds mark the stars with spectral types from Vargas Álvarez et al. (2013).

8.2.3 The distance and age

The distance to Wd2 is still subject of debate in the literature. Published values range from 2.8 kpc (Rauw et al. 2007; Ascenso et al. 2007a; Carraro et al. 2013), to 4.16 kpc (Vargas Álvarez et al. 2013), 5.7 kpc (Piatti et al. 1998), 6.4 kpc (Carraro and Munari 2004) to 8 kpc (Rauw et al. 2007, 2011). Discrepancies also exist in the published ages: an upper age limit of 3 Myr was inferred for the whole cluster and 2 Myr for the core by Ascenso et al. (2007a) and Carraro et al. (2013).

To determine the distance and age of Wd2 we used the method of over-plotting isochrones to our $F814W_0$ vs. $(F814W - F160W)_0$ CMD. We especially focused on the turn-on (TO), since here the isochrones are not degenerate in age and most distinguishable from each other. We used PARSEC isochrones for 0.5–2.0 Myr and Solar metallicity of $Z_{\odot} = 0.0152$.

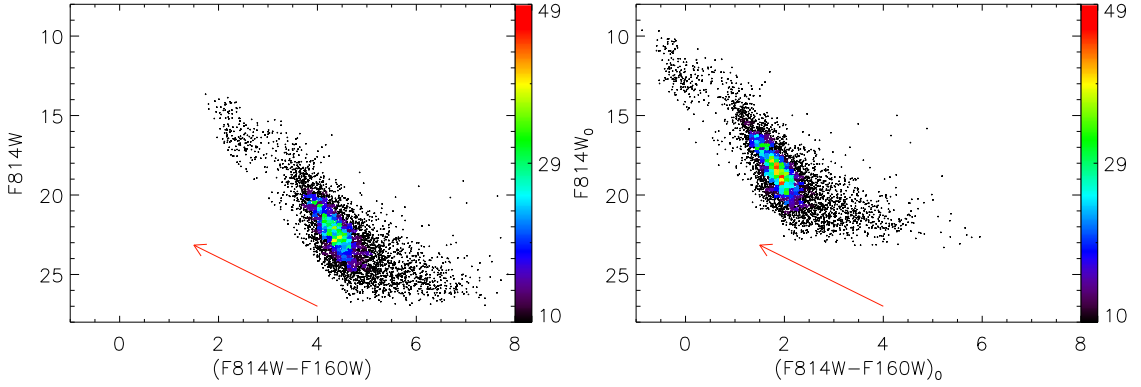


Figure 8.2.2: **Left:** The observed $F814W$ vs. $(F814W - F160W)$ CMD of the likely cluster members. **Right:** The $F814W_0$ vs. $(F814W - F160W)_0$ CMD of the of the individually dereddened cluster stars. The red arrow marks the reddening vector corresponding to the median $E(B - V)_* = 1.55$ mag with $R_V = 3.95$. The colorbar represents the number of objects per bin (binsize: 0.1×0.2 mag). The range in color is the same in both plots.

To determine the best distance, we used the already dereddened CMD (see Fig. 8.2.3, right panel). We corrected the chosen PARSEC isochrones (Bressan et al. 2012) for the distance modulus. We applied different values for the distance and assessed the best fit to both the locus of the TO region and the PMS population. This corresponded to a distance of $d = 4$ kpc and is in good agreement with the distance inferred from the spectroscopic observations of Vargas Álvarez et al. (2013). Their distance is based on the physical constraints derived from the spectral types of the most massive stars in Wd2. The method they adopted is more accurate than our empirical fit, and, therefore, we will assume for all the subsequent calculations their value of $d = 4.16$ kpc.

Taking into account the magnitude range of the TO we can conclude that the age for the whole cluster is in the range of 0.5–2.0 Myr. The uncertainty in the total-to-selective extinction, $\Delta R_V \pm 0.135$, results in an age uncertainty of ~ 0.5 Myr assuming that the luminosity of the stars is constant. The impact on the distance is ± 0.01 kpc and, therefore, negligible.

8.3 The spatial distribution of the stellar population

Vargas Álvarez et al. (2013) and Hur et al. (2015) pointed out that Wd2 shows a smaller density clump northwards of the MC. Hur et al. (2015) named this concentration of stars “northern clump”, while Vargas Álvarez et al. (2013) also noticed a “a secondary concentration of stars $45''$ to the North”. To further determine the spatial distribution of the stars we analyze the surface density variations of the stellar population.

In order to determine the surface density distribution of the stellar population of Wd2, we corrected our photometric catalog for completeness as described in Sect. 5. Although the level of completeness is very high across the cluster area (see Sect. 5.3), in the cluster center, very close to the O and B stars, the detection rate drops rapidly in all filters. In order to correct properly for incompleteness, brightness cuts are needed in the two filters used for

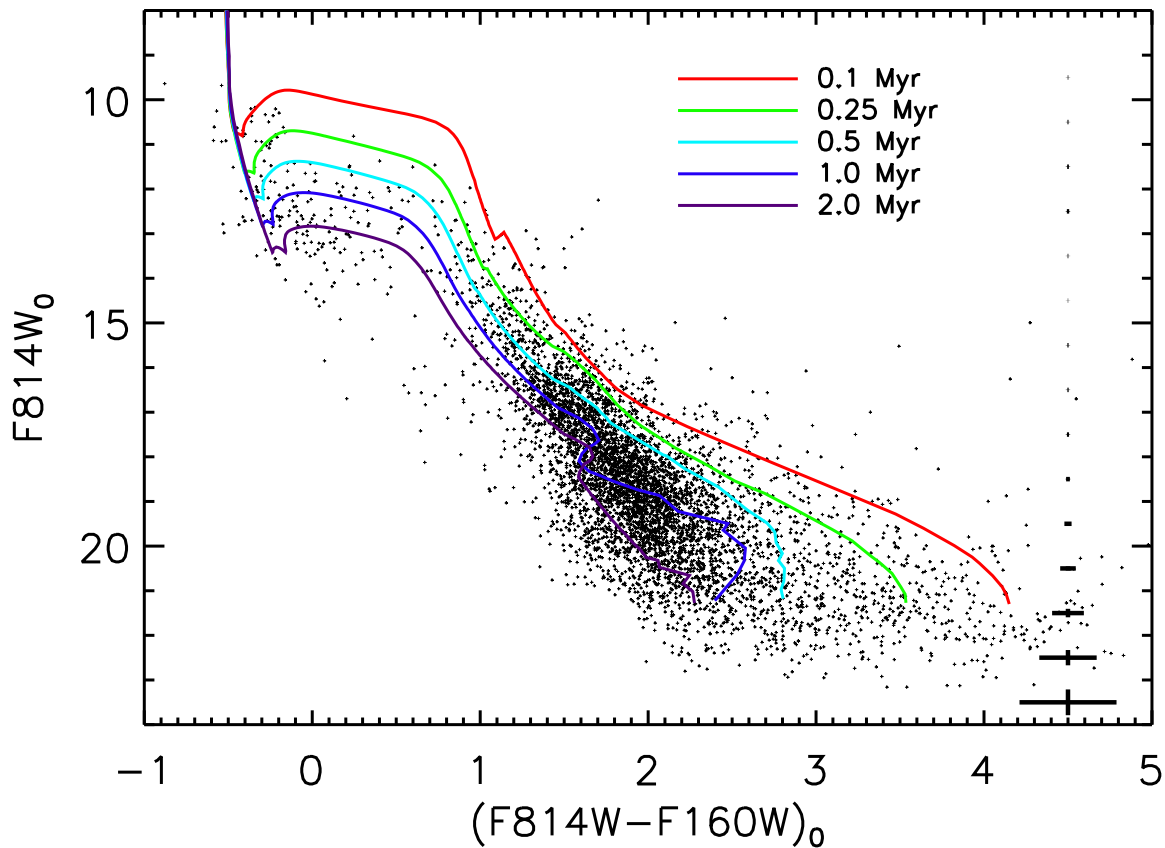


Figure 8.2.3: The extinction corrected $F814W_0$ vs. $(F814W - F160W)_0$ CMD of the 5418 point sources left after the Wd2 member selection. The colored lines represent the PARSEC PMS isochrones for 0.5–2.0 Myrs best fitting the TO of the main sequence. The error bars represent the typical photometric uncertainties in different magnitude bins. We applied an $R_V = 3.95$ with a distance of 4.16 kpc. The red diamonds mark the stars for which spectroscopic data are available (see Tab. 7.3.1). The dashed-dotted lines represent the maximum possible shifts of the isochrones for $\Delta R_V \pm 0.135$ assuming a constant luminosity of the stars.

the selection of cluster members. These are $F814W = 21.8$ mag and $F160W = 17.8$ mag and correspond to a 75% completeness level in each filter ($M \sim 0.5 M_\odot$). These limits have been chosen, so that in the center of the clumps a completeness level of 50% is reached.

We then calculated the surface density of the remaining cluster members, obtaining the local, completeness-corrected surface density around each star (within a radius of 10.8 arcsec) brighter than $F814W = 21.8$ mag and $F160W = 17.8$ mag. This rather irregular grid was then triangulated to a regular grid of 392×403 bins (binsize: 1.08 arcsec), using the `Triangulate` and `TriGrid` routines of IDL². The resulting surface density map is shown in Fig. 8.3.1.

²Additional data analyses were done using IDL version 8.5 (Exelis Visual Information Solutions, Boulder, Colorado).

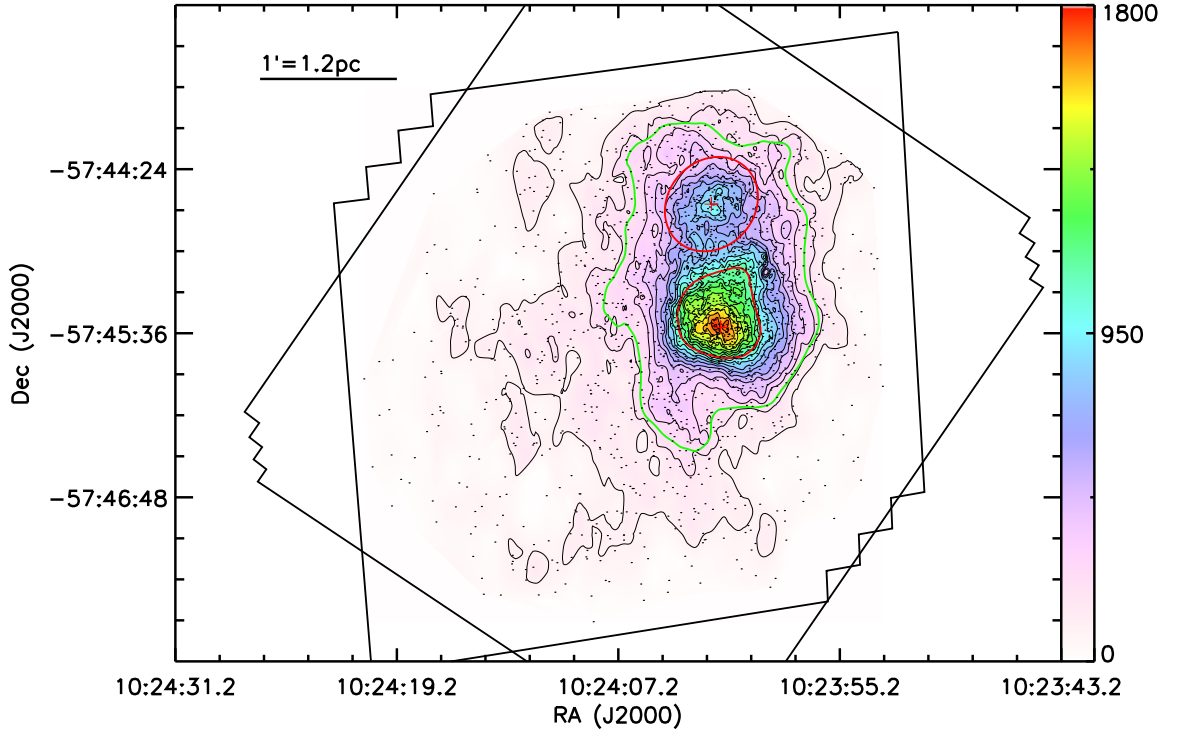


Figure 8.3.1: The surface density map of the likely RCW 49 members. The colorbar represents the stellar surface density in number arcmin^{-2} . The contours show the density in 15 linear steps from 0–1800 arcmin^{-2} . The black dots represent the stars used to produce the density map. The survey areas of the two instruments are shown as the black outlines. The red lines represent the determined boundaries of the MC and NC, the crosses mark their respective center. The green line is the 2σ outline of the 2D-Gaussian fit, marking the boundary within which stars are considered as cluster members of Wd2.

To determine the surface density profile of Wd2, as well as the shapes and spatial extents of the two clumps, we fitted a combination of two 2D-Gaussians, including rotation of the axes, and a common offset. We first smoothed the density distribution with a binsize of four, in order to flatten the small scale fluctuations produced by local inhomogeneities. We used this smoothed density distribution to determine the peak positions and their maximum densities. The peak coordinates (J2000) for the MC are $\text{R.A.} = 10^{\text{h}}24^{\text{m}}01^{\text{s}}.65$ and $\text{decl.} = -57^{\circ}45'33.4''$ with a peak density of 1863 stars arcmin^{-2} . For the NC we obtained $\text{R.A.} = 10^{\text{h}}24^{\text{m}}02^{\text{s}}.16$ and $\text{decl.} = -57^{\circ}44'39.3''$ with a peak density of 937 stars arcmin^{-2} . This leads to a projected central distance between the peaks of the two clumps of $d = 54.25$ arcsec (1.09 pc) at the distance of 4.16 kpc (Vargas Álvarez et al. 2013; Zeidler et al. 2015). In Fig. 8.3.2 one can see the 3D plot of the smoothed density map. The xy-plane represents the coordinates in R.A. and decl. and the z-axis represents the surface density in arcmin^{-2} , which is identical to Fig. 8.3.1 For orientation purposes, the same contours as in Fig. 8.3.1 are shown in the xy-plane

To analyze and compare the properties of the two clumps, we defined the 1σ width of the fitted Gaussian distributions as the size of the two clumps. An elliptical shape distribution

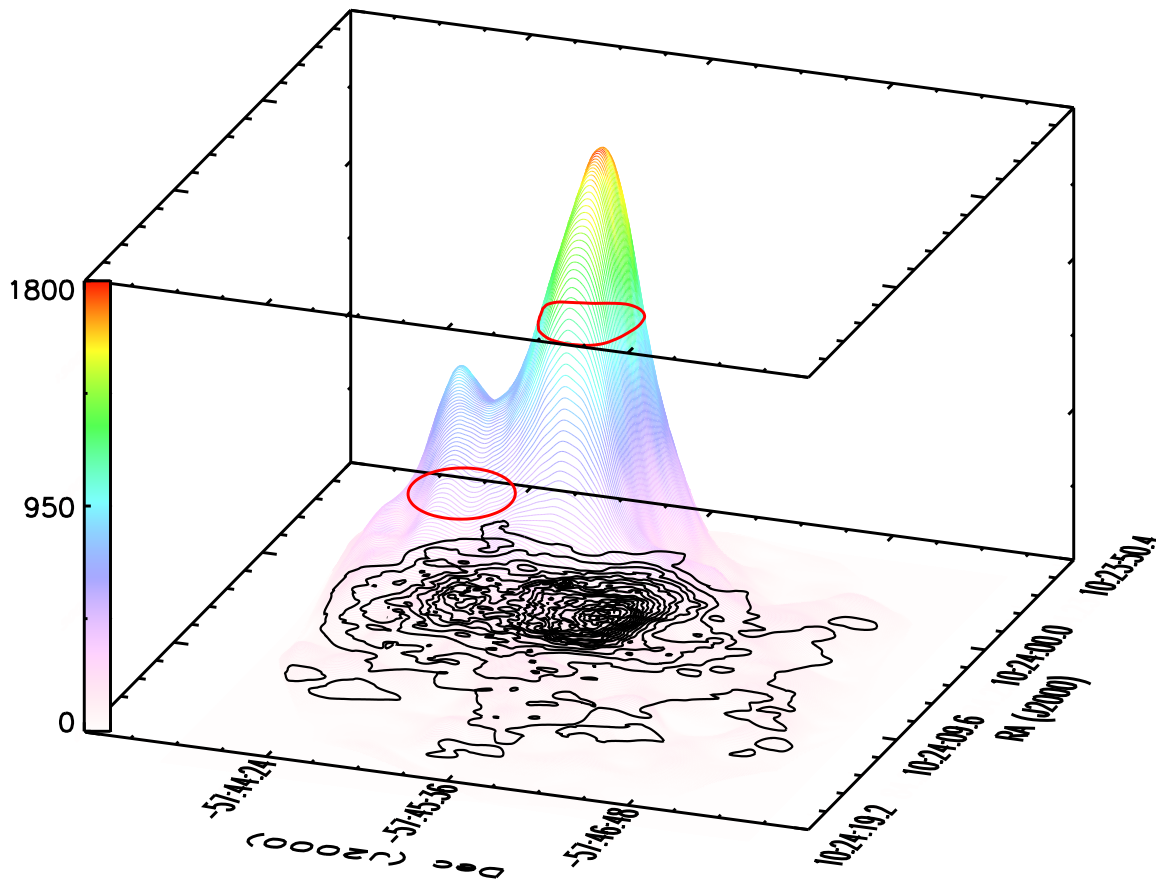


Figure 8.3.2: The three dimensional plot of the smoothed surface density map of the likely RCW 49 members. The xy-plane represents the coordinates in R.A. and decl. and the z-axis represents the surface density including the colorbar in number arcmin^{-2} . It is identical to the colorbar of Fig. 8.3.1. In the xy-plane the same contours as in Fig. 8.3.1 are shown. The contours traces the density in 15 linear steps. The red contour lines represent the determined 1σ boundaries of the MC and NC.

for the MC is not a very accurate representation and for this reason we used the contour line at the 1σ width of the Gaussian fit. The NC is partly embedded in the wings of the MC distribution so we could not use a closed contour line for the 1σ density. Instead we approximated it with an ellipse, which is the result of the 2D Gaussian fit. The major and minor axes represent the 1σ width of the Gaussian distribution. Within these boundaries, the MC and NC cover an area of 0.31 arcmin^2 (0.44 pc^2) and 0.27 arcmin^2 (0.38 pc^2), respectively.

To separate the cluster of Wd2 from the periphery of RCW 49, we defined its 2σ density contour as the cluster boundary. Its projected area is 2.57 arcmin^2 (3.74 pc^2). The sizes of our clumps are comparable with the core radii that [Kuhn et al. \(2014\)](#) derived in their analysis of the sub-clustering of 17 regions in the Massive Young Star-Forming Complex Study in Infrared and X-ray (MYSTiX, see [Feigelson et al. 2013](#)) project. The sizes of the cores in their study range from 0.01 pc to > 2 pc, where 68% of their core radii are between 0.06 and 0.45 pc.

The MC includes 378 observed PMS members (490 after completeness correction) leading to a completeness-corrected surface density of $\Sigma_{\text{MC}} = 1114 \text{ stars pc}^{-2}$, while the NC comprises 157 observed PMS members (211 after completeness correction) resulting in a completeness-corrected surface density of $\Sigma_{\text{NC}} = 555 \text{ stars pc}^{-2}$. The surface density of the Wd2 cluster as a whole, including MC and NC, is $\Sigma_{\text{Wd2}} = 264 \text{ stars pc}^{-2}$. We note here again that all surface densities are based on a lower mass cutoff at $0.5 M_{\odot}$.

8.3.1 The uniformly distributed low-mass stellar population

We analyzed the observed and completeness-corrected spatial distributions of the stellar population in RCW 49 in different brightness bins. Outside the two clumps we can analyze stars with masses lower than $0.5 M_{\odot}$. The spatial distribution of the lowest-mass stars ($< 0.15 M_{\odot}$ down to the detection limit of $\sim 0.09 M_{\odot}$) outside the two clumps appears uniform throughout the RCW 49 region. In total, 1293 low-mass cluster members ($< 0.15 M_{\odot}$) are detected. This gives a total, completeness-corrected number of 1494 low-mass stars, down to the detection limit $\sim 0.08 M_{\odot}$, defining a stellar surface density of $\Sigma = 105 \text{ stars pc}^{-2}$, not including the regions of the NC and the MC (see Sect. 5.2.1).

This uniformly distributed low-mass stellar population extends to the ridges of the surrounding gas and dust cloud. Additionally, we found a small age gradient of $\sim 0.15 \text{ Myr}$ decreasing from the Wd2 center toward the gaseous ridge, which suggests that the OB star population of Wd2 might be triggering star formation in the surrounding gas cloud.

This phenomenon was already observed by [Whitney et al. \(2004\)](#) who identified ~ 300 candidate young stellar objects (cYSOs) in the giant H II region of RCW 49 using data obtained with the Infrared Array Camera (IRAC, [Fazio et al. 2004](#)) on board the *Spitzer* Space Telescope ([Werner et al. 2004](#)) for the Galactic Legacy Infrared Mid-Plane Survey Extraordinaire (GLIMPSE). The observations were carried out in the IRAC bands 1 to 4 with central wavelengths of $3.6 \mu\text{m}$, $4.5 \mu\text{m}$, $5.8 \mu\text{m}$, and $8.0 \mu\text{m}$, respectively. Further details on this program are provided in [Benjamin et al. \(2003\)](#). [Whitney et al. \(2004\)](#) concluded that the central cluster had induced a second generation of star formation through feedback, similar to what was observed in NGC 602 in the Small Magellanic Cloud by [Carlson et al. \(2007\)](#). However, because of the limited spatial resolution of the *Spitzer* Space Telescope, the lower mass limit of the observations of [Whitney et al. \(2004\)](#) is $2.5 M_{\odot}$. We calculated that, using our data in the central area, this limit translates into missing the vast majority ($\sim 95\%$) of PMS stars.

8.3.2 The red tail of the PMS population

The dereddened $F814W_0$ vs. $(F814W - F160W)_0$ CMD shows 304 faint, very red objects with $F814W_0 > 18.0 \text{ mag}$ and $(F814W - F160W)_0 > 3.2 \text{ mag}$. In Fig. 8.3.3, we overplotted these selected objects as magenta dots on the $F814W$ image of our observations and our 2D high-resolution reddening map. These red stars are concentrated in the south-west corner of the FOV. Since all these objects were individually dereddened using the gas extinction map,

the distribution should be uniform throughout the field (assuming that the gas extinction map provides a fair representation of also the stellar extinction). The right panel of Fig. 8.3.3 shows the reddening map including nine contour levels with linear steps between $0 \leq E(B - V)_g \leq 2.89$ mag. No obvious spatial correlation between the red objects (marked in both frames within the green ellipse) and the distribution of the gas and dust is visible. On the other hand, the gas excess map only represents the nebular extinction (through the $H\alpha$ and $Pa\beta$ line emission). Within the ellipse, the median $E(B - V)_g$ is with 2.1 mag, 0.23 mag higher than the global median of the gas extinction map.

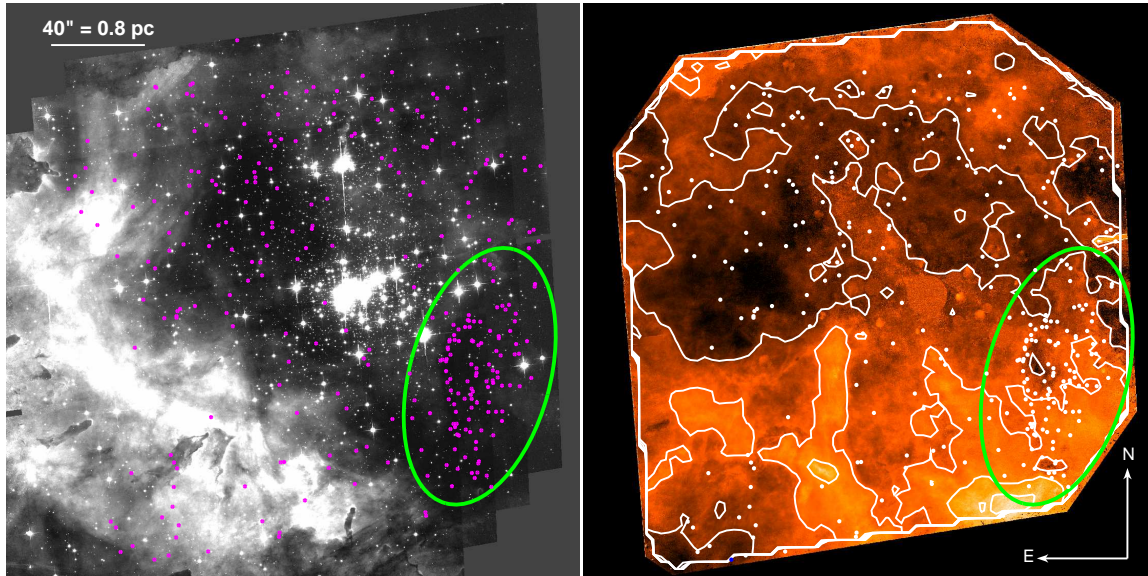


Figure 8.3.3: The left panel show the $F814W$ image (corresponding to the I -band) of the Wd2 region. The right panel shows the $E(B - V)_g$ color-excess map created in Sect. 6. Over-plotted are (in magenta (left) or white(right)) the objects of the red tail. The green ellipse marks the region of over density.

Moving toward the mid-infrared

The filter with the longest wavelength available in our HST survey is the $F160W$ filter, corresponding to the H -band in the NIR. To detect molecular gas and dust clouds the use of filters with wavelengths in the mid-infrared (MIR) and sub-millimeter becomes necessary. In Fig. 8.3.4 we show the zoomed-in region in which the red tail stars (over-plotted as red points) are located. The left panel shows the inverted $F658N$ image, sampling the $H\alpha$ emission. In the right panel we show a three-color composite image using the IRAC 2 ($4.5 \mu\text{m}$), 3 ($5.8 \mu\text{m}$), and 4 ($8.0 \mu\text{m}$) *Spitzer* observations for blue, green, and red, respectively, based on data from the GLIMPSE survey (Benjamin et al. 2003). The ellipse marks the region of the overdensity and is identical to the one in Fig. 8.3.3.

From the examination of the *Spitzer* color-composite image, we see a molecular cloud at the same location. The [3.6], [5.8], and [8.0] IRAC bands show different emission features of polycyclic aromatic hydrocarbons (PAHs). The [3.6], [5.8], and [8.0] bands contain the $3.3\ \mu\text{m}$, $6.2\ \mu\text{m}$, and $7.7\ \mu\text{m}$ C–H stretching modes, respectively. The [8.0] band additionally contains the $8.6\ \mu\text{m}$ C–H in-plane bending mode (Draine 2003), while the IRAC [4.5] band contains the bright $\text{Br}\alpha$ hydrogen line (centered at $4.05\ \mu\text{m}$). Churchwell et al. (2004) predicted that the $\text{Br}\alpha$ emission contains $\sim 20\%$ of the non-stellar flux observed in RCW 49. Looking at the colors of the right panel in Fig. 8.3.4, the clouds containing the overdensity of the red tail objects appear to be dominated in the [5.8] IRAC-3 band by PAH emission produced by molecules with C and O atoms in their structure. In areas where we can see the $\text{Br}\alpha$ emission (blue), we also can see a higher flux in the $\text{H}\alpha$ image (left frame).

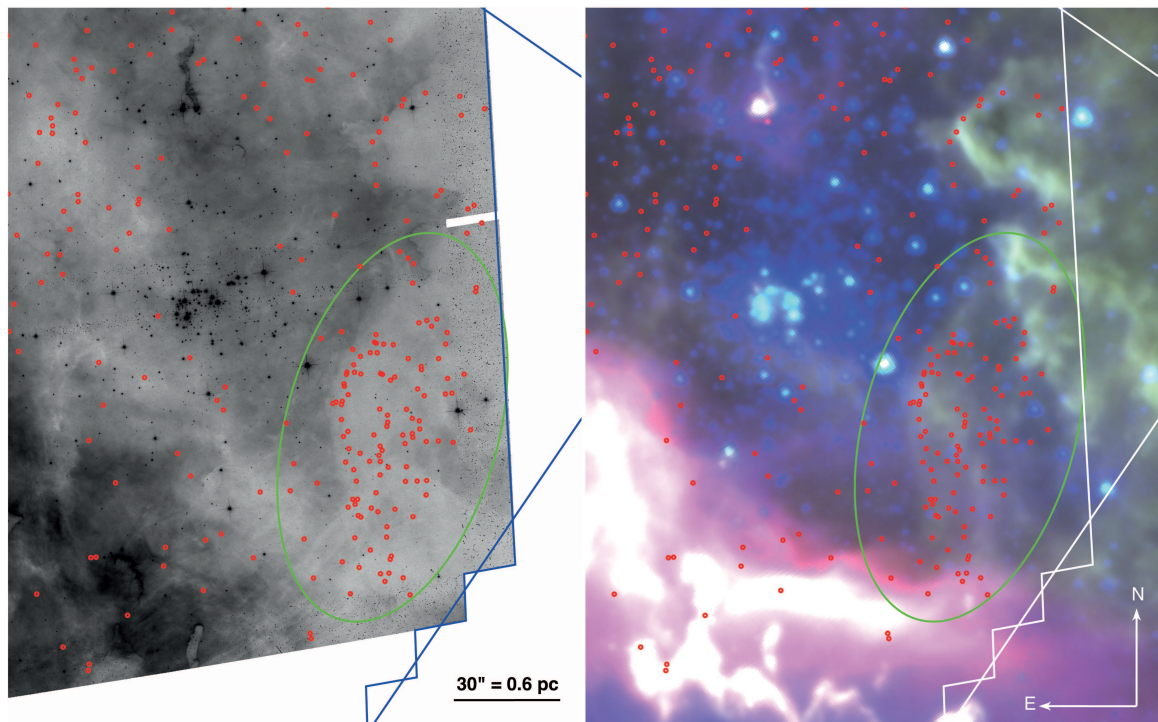


Figure 8.3.4: In the left panel we show the inverted $F658N$ image from our observations, mapping the $\text{H}\alpha$ emission. Dark regions are bright in $\text{H}\alpha$. The right panel shows the three color-composite image from the *Spitzer* GLIMPSE survey (Benjamin et al. 2003). The [8.0], [5.8], and [4.5]-band are shown in red, green, and blue, respectively. The blue (left) and white (right) line trace the FOV of our HST observations. The objects in the red tail are over plotted in red. The green ellipse marks the region of the red tail overdensity (same as in Fig. 8.3.3). The objects in the red tail overdensity are located in a region of negligible $\text{H}\alpha$ emission, while there is PAH emission visible in green in the *Spitzer* image.

The ^{12}CO and ^{13}CO transition lines

The properties of the molecular gas associated with Wd2 have been analyzed in several studies. The major difficulty is that Wd2 is located close to the tangent point of the Carina

Arm as seen from us (i.e., [Grabelsky et al. 1987](#)), meaning that for gas clouds with a distance to the Sun smaller and larger than Wd2 the distance determination is degenerate. The studies of the CO emission spectrum in combination with the 21 cm absorption spectrum by [Dame \(2007\)](#) suggest that Wd2 must be located in between two molecular clouds. Wd2 was studied in more detail by [Furukawa et al. \(2009, 2014\)](#) and [Ohama et al. \(2010\)](#) using the NANTEN 2 4 m submillimeter/millimeter telescope (from the NANTEN CO Galactic Plane Survey, [Mizuno and Fukui 2004](#)) in combination with *Spitzer* data. They detected three different CO clouds with 3 different velocities (16, 4, and -4 km s^{-1} , relative to the local standard of rest (LSR), see Fig. 1 in [Ohama et al. \(2010\)](#) and Fig. 1 in [Furukawa et al. \(2009\)](#)). The cloud with a peak velocity of -4 km s^{-1} spatially coincides very well with the location of the molecular cloud where the red tail overdensity is located (see bottom right of Fig. 1 in [Furukawa et al. \(2009\)](#) and bottom panels in Fig. 1 of [Ohama et al. \(2010\)](#)). Using the rotation curve of [Brand and Blitz \(1993\)](#), [Furukawa et al. \(2009\)](#) obtained kinematic distances of 6.5, 5.2, and 4.0 kpc for the 16, 4, and -4 km s^{-1} clouds, respectively. [Furukawa et al. \(2009, 2014\)](#) and [Ohama et al. \(2010\)](#) also suggested that the creation of the RCW 49 region, with the Wd2 cluster as its central ionizing cluster, was induced by a cloud-cloud collision of two of these observed molecular clouds. This collision may have caused the formation of the spatially uniformly distributed low-mass PMS stars that we see in our HST data. Such a mechanism can induce star formation throughout the molecular cloud.

As we can only see an additional reddening in the region where the -4 km s^{-1} molecular cloud is located, we conclude that this cloud lies in front of Wd2. This indicates that the other clouds are located in the background of Wd2, which would confirm our determined distance of 4.16 kpc. Thus any extinction caused by these clouds would only affect objects located behind the cluster as seen from us and hence be undetectable in our data. The cloud kinematics of [Dame \(2007\)](#) and [Furukawa et al. \(2009\)](#) suggest that Wd2 is located behind the 4, and -4 km s^{-1} clouds, which is in contradiction to our distance estimate. On the other hand, if we underestimated the extinction toward Wd2, our distance modulus is then overestimated leading to an even closer distance. We suggest that Wd2 is located between the 4 and -4 km s^{-1} clouds confirming our distance of 4.16 kpc.

The stars of the red tail are probably RCW 49 PMS stars that are still not corrected completely for extinction and, therefore, appear too red. Because the molecular gas is not located directly along the line of sight to Wd2, we can also conclude that for the remaining part of RCW 49 in our observed FOV, our method for the correction for extinction is not significantly contaminated by molecular extinction.

8.4 A more detailed look at the stellar population

To investigate the PMS population in more detail, we defined all objects brighter than $F_{814W_0} = 15.0 \text{ mag}$ and bluer than $(F_{814W} - F_{160W})_0 = 0.7 \text{ mag}$ as a member of the MS or TO region (see Fig. 8.2.3). This selection leaves us with 5404 PMS and 200 MS and TO objects. In Sect. 9 we will select 240 stars with $H\alpha$ excess emission and discuss them in detail. To get an overview over the complete stellar population of Wd2, we already discuss

in the following section some their properties, such as fractions and numbers, in relation to all stellar members.

For a proper comparison, we use different selection criteria for different samples of PMS stars:

- For the 5404 PMS star candidates selected in Sect. 8.1 (using their loci in the CMD), we require detection in both the $F814W$ and $F160W$ filters (from now on denoted as full-sample PMS stars).
- $H\alpha$ excess emission sources need to be detected in the $F555W$, $F814W$, $F160W$, and $F658N$ filters and have an $H\alpha$ excess (see green dots in Fig. 8.4.1 and also see Sect. 9.2 and Fig. 9.3.1).
- Because the $F555W$ and $F658N$ images are less deep than $F814W$ and $F160W$ we selected 1690 PMS stars from the full sample with the same detection criteria as our $H\alpha$ excess emission stars (see Sect. 9.2). This means they have to be probable cluster members and need to be detected in the $F555W$, $F814W$, $F160W$, and $F658N$ filters. From now on they are denoted as our reduced-sample PMS stars. These stars do not have necessarily $H\alpha$ excess emission.

The full-sample PMS stars are used for the properties of the Wd2 cluster and the RCW 49 region, while the reduced sample is always used to compare the $H\alpha$ excess emitting stars with the non-emitting stars. The limiting magnitude is $F814W_0 \approx 19$ mag which corresponds to a $\sim 0.3 M_{\odot}$ star at an age of 1 Myr. We selected 240 $H\alpha$ excess sources (green dots in Fig. 9.3.1). The detailed determination, as well as the mass accretion rates are demonstrated in Sect. 9.2.

In Fig. 8.4.2 we plotted the cumulative distributions of the radial distance of the full-sample PMS, the reduced-sample PMS, and the $H\alpha$ excess emission sources. The coordinates of the central density peak of the MC, $(\alpha, \delta) = (10^h 24^m 02^s .4, -57^{\circ} 45' 33.44'')$ (J2000), (Sect. 8.3) were used as origin. A Kolmogorov-Smirnov (K-S) test yields a probability of only $\sim 11\%$ that the $H\alpha$ excess sources and the full-sample PMS share the same radial distribution, while it yields a $\sim 74\%$ probability that the $H\alpha$ excess sources and the reduced-sample PMS have the same radial distribution. This test and the distribution itself (see Fig. 8.4.2) confirm that for comparing the stars with $H\alpha$ excess emission to the cluster members, the reduced sample of PMS stars needs to be used.

8.4.1 A closer look at the PMS ages

In this section we compare the age distribution of the reduced sample of PMS stars in Wd2. In Tab. 8.4.1 we list all 240 $H\alpha$ excess objects and the 1690 reduced-sample PMS stars for different ages. For comparison we also list the 5404 full-sample PMS stars.

The age distribution of what we call the reduced-sample PMS stars shows a mean age of 0.84 ± 0.64 Myr, while the mean age of the stars with $H\alpha$ excess is 0.62 ± 0.57 Myr. In comparison the full-sample PMS stars have a mean age of 1.04 ± 0.71 Myr. The difference in age between the full sample and the reduced sample most likely originates from the

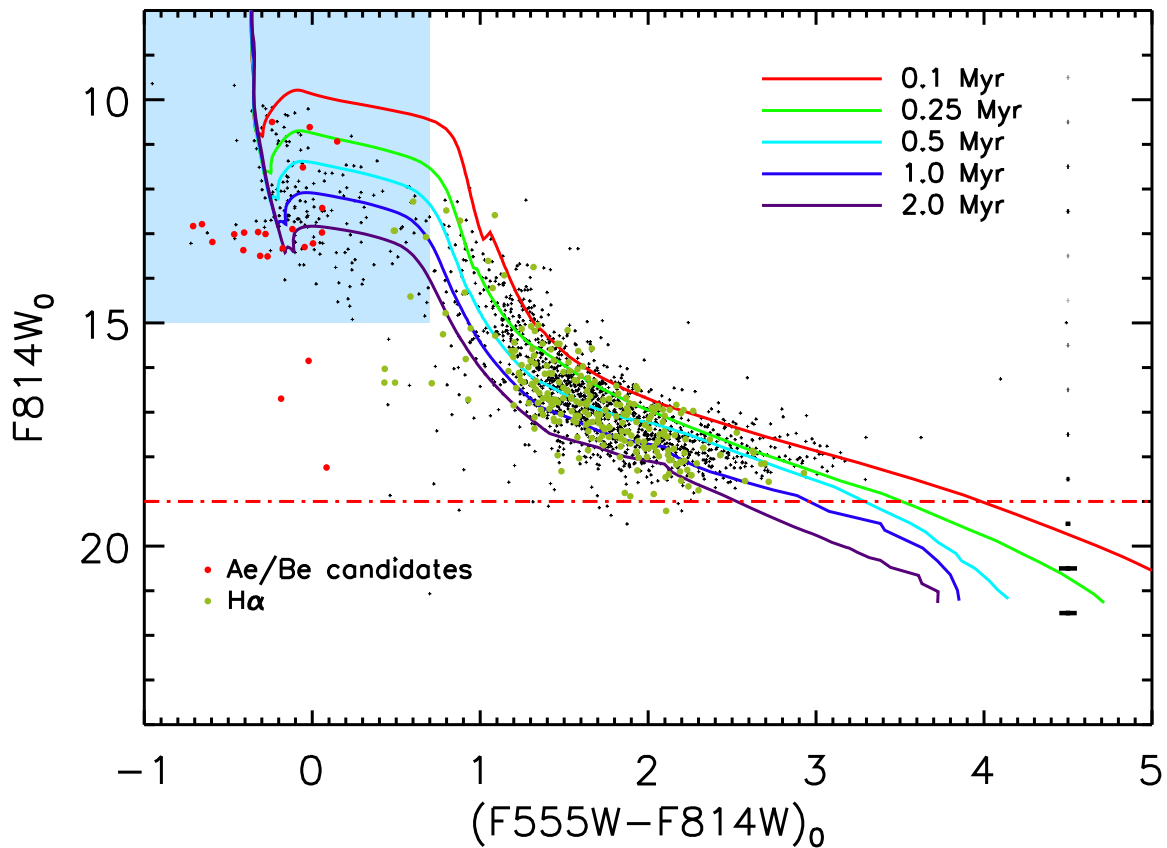


Figure 8.4.1: The $F814W_0$ vs. $(F555W - F814W)_0$ CMD of the RCW 49 members (black dots). We defined all objects brighter than $F814W_0 = 15.0$ mag and bluer than $(F814W - F160W)_0 = 0.7$ mag as MS and TO members (light blue area). The red dots mark the 24 Ae/Be candidates, namely all stars showing $H\alpha$ excess and having an $EW > 10 \text{ \AA}$ but being bluer than $F555W - F814W = 0.2$ mag (see Sect. 9). The green dots show all $H\alpha$ excess PMS objects. Overplotted are the PARSEC 1.2S isochrones (Bressan et al. 2012) between 0.1 and 2.0 Myr for a Solar metallicity $Z = 0.0152$ and a distance $d = 4.16$ kpc. The red dashed-dotted line marks the detection limit set by the $F555W$ and $F658N$ filters ($\sim 0.3 M_\odot$ at an age of 1 Myr), both needed to determine the $H\alpha$ excess stars. On the right side typical photometric uncertainties are shown as a function of magnitude.

requirement that the latter additionally needs to be detected in the $F555W$ filter, which is less deep than the other filters (see Sect. 3). This argument is supported by the $F814W_0$ vs. $(F555W - F814W)_0$ CMD (see Fig. 8.4.1). The slope of the locus of PMS stars in the CMD becomes shallower for lower masses, indicating that the effect on the mean age is an effect due to the detection limit of the $F555W$ filter. We conclude that the age estimate from the full sample (1.04 ± 0.71 Myr) better represents the age of the Wd2 region. It is in good agreement with the age determined by Ascenso et al. (2007a) of 1.5–2 Myr and is in agreement with the MS lifetime of O3–O5 stars of $\sim 2 - 5$ Myr (see Tab 1.1, Sparke and Gallagher 2007). Wd2 appears to be of the same age or even younger than the massive star cluster HD97950 in the giant HII region NGC 3603 (Pang et al. 2013), which has an age of about 1 Myr, Trumpler 14 (≤ 2 Myr, Carraro et al. 2004) in the Carina Nebula (Smith and

Table 8.4.1. The age distribution of the PMS and H α excess sources

Source	Panel	0.1 Myr		0.25 Myr		0.5 Myr		1.0 Myr		2.0 Myr		Total
Full-sample PMS stars		547	(10.1%)	550	(10.2%)	1081	(20.0%)	1552	(28.7%)	1674	(31.0%)	5404
Main cluster	a	18	(3.6%)	44	(10.7%)	107	(21.5%)	144	(28.9%)	185	(35.3%)	498
Northern clump	b	9	(2.9%)	22	(7.1%)	70	(22.6%)	101	(32.6%)	108	(34.8%)	310
Westerlund 2	c	99	(5.4%)	155	(7.3%)	366	(19.8%)	635	(34.4%)	589	(33.1%)	1844
Periphery	d	421	(15.4%)	329	(12.0%)	538	(19.6%)	672	(24.5%)	792	(28.5%)	2752
Reduced-sample PMS stars		192	(11.0%)	242	(16.8%)	485	(30.5%)	440	(25.5%)	331	(16.2%)	1690
Main cluster	a	15	(5.7%)	35	(13.3%)	80	(30.4%)	79	(30.0%)	54	(20.6%)	263
Northern clump	b	5	(3.5%)	14	(9.9%)	53	(37.3%)	37	(26.1%)	33	(23.2%)	142
Westerlund 2	c	60	(8.9%)	108	(16.0%)	203	(30.2%)	190	(28.2%)	112	(16.7%)	673
Periphery	d	112	(19.9%)	85	(13.9%)	149	(24.3%)	134	(21.9%)	132	(20.0%)	612
H α -excess		54	(22.5%)	49	(20.4%)	66	(27.5%)	45	(18.8%)	26	(10.8%)	240

Note. — For each age bin we give the number of sources and in brackets the fraction of sources compared to the total number of objects. For each sample we also list the distribution within the sub-region described in (Sect. 8.3). Column 2 (panel) gives the letter denoting the panel of the region in Fig. 8.4.3.

Brooks 2008), Arches (~ 2 Myr, Figer et al. 2002; Figer 2005), R136 in the LMC (1–4 Myr, Hunter et al. 1995; Walborn and Blades 1997; Sabbi et al. 2012, 2016), and younger than Westerlund 1 (5.0 ± 1.0 Myr, Clark et al. 2005; Gennaro et al. 2011; Lim et al. 2013).

8.4.2 The individual regions in RCW 49

The stellar surface density map (see Sect. 8.3) of the RCW 49 region shows that this region can be divided in four parts: the MC, the NC, the remaining parts of the Wd2 cluster (1σ contour of the density profile excluding the MC and NC), and the Wd2 periphery. These regions are defined by a fit of two 2D Gaussian distributions to the completeness-corrected stellar surface-density map of the RCW 49 member stars. We show a detailed analysis in Sect. 8.3. In Fig. 8.4.3 we show the $F814W_0$ vs. $(F814W - F160W)_0$ CMDs for each subregion. In the following Section we will analyze the distribution and properties of the different areas.

While we focus in Tab. 8.4.1 on the number of PMS stars per sample for each age bin, in Tab. 8.4.2 we focus on the mean properties of the four different regions.

The MC hosts a well-populated MS, TO, and PMS. We selected 498 full-sample PMS members. The full-sample PMS stars define an age of 1.04 ± 0.71 Myr. The uncertainties are represented by the standard deviation of the ages. The 263 PMS stars of the reduced sample show a younger estimated age of 0.84 ± 0.64 Myr, while the 36 H α stars located in the area of the MC have an estimated age of 0.69 ± 0.57 Myr (see Tab. 8.4.2). The lack of very faint objects (compared to the other three regions) is caused by crowding and completeness effects (see Sect. 5).

The NC hosts 310 full-sample PMS members. The full-sample PMS members lead to an age estimate of 1.16 ± 0.67 Myr and thus are coeval with the MC. Also their age distribution is similar to that in the MC (see Tab. 8.4.1). The NC hosts in total 26 H α excess stars with a mean age of 0.76 ± 0.60 Myr.

The Wd2 cluster shows an extended halo (2σ boundary, Sect. 8.3) around the MC and NC. At least 1814 objects in this region are defined PMS with the same mean age as the MC

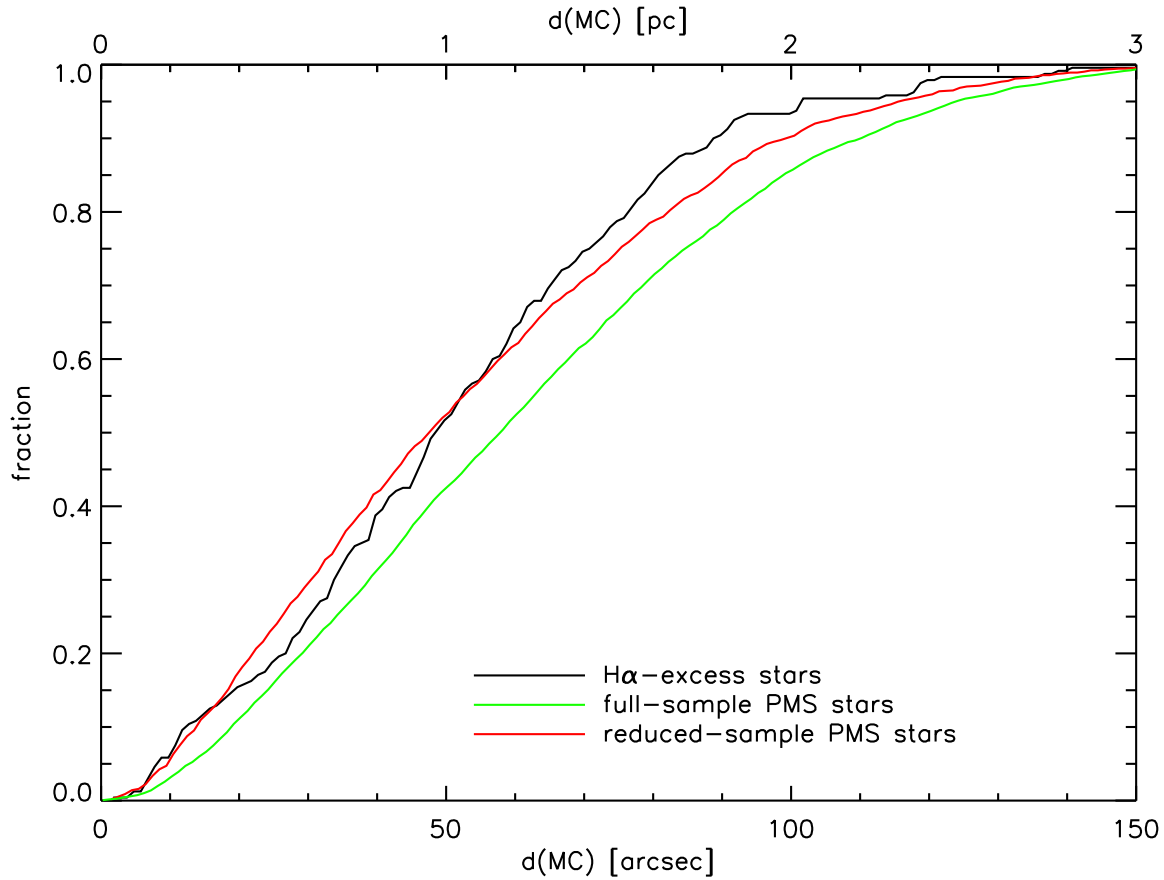


Figure 8.4.2: The cumulative radial distribution in distance of the objects from the peak coordinates of the MC (α, δ) = ($10^h 24^m 02^s .4, -57^\circ 45' 33.44''$; J2000), determined with a 2D Gaussian fit (see Sect. 8.3). At a distance of 4.16 kpc from the Sun 50'' correspond to 1 pc.

and NC. The MC and NC are excluded from this region. The 106 H α excess stars have an age of 0.60 ± 0.56 Myr.

2752 full-sample PMS members are found in the periphery of RCW 49. Most of the objects in this region are fairly faint and red (compared to the distribution in the other three areas). With a mean age of 0.96 ± 0.73 Myr the periphery is indistinguishable in age from the Wd2 cluster, implying that star formation in the surrounding cloud set in at roughly the same time. It hosts at least 72 H α excess stars.

8.5 Summary and conclusions

In this Chapter we analyzed the stellar population of RCW 49 and its distribution.

We used a combination of two 2D-Gaussians to fit the stellar spatial distribution of the completeness-corrected cluster members. For the peak coordinates of the MC we got

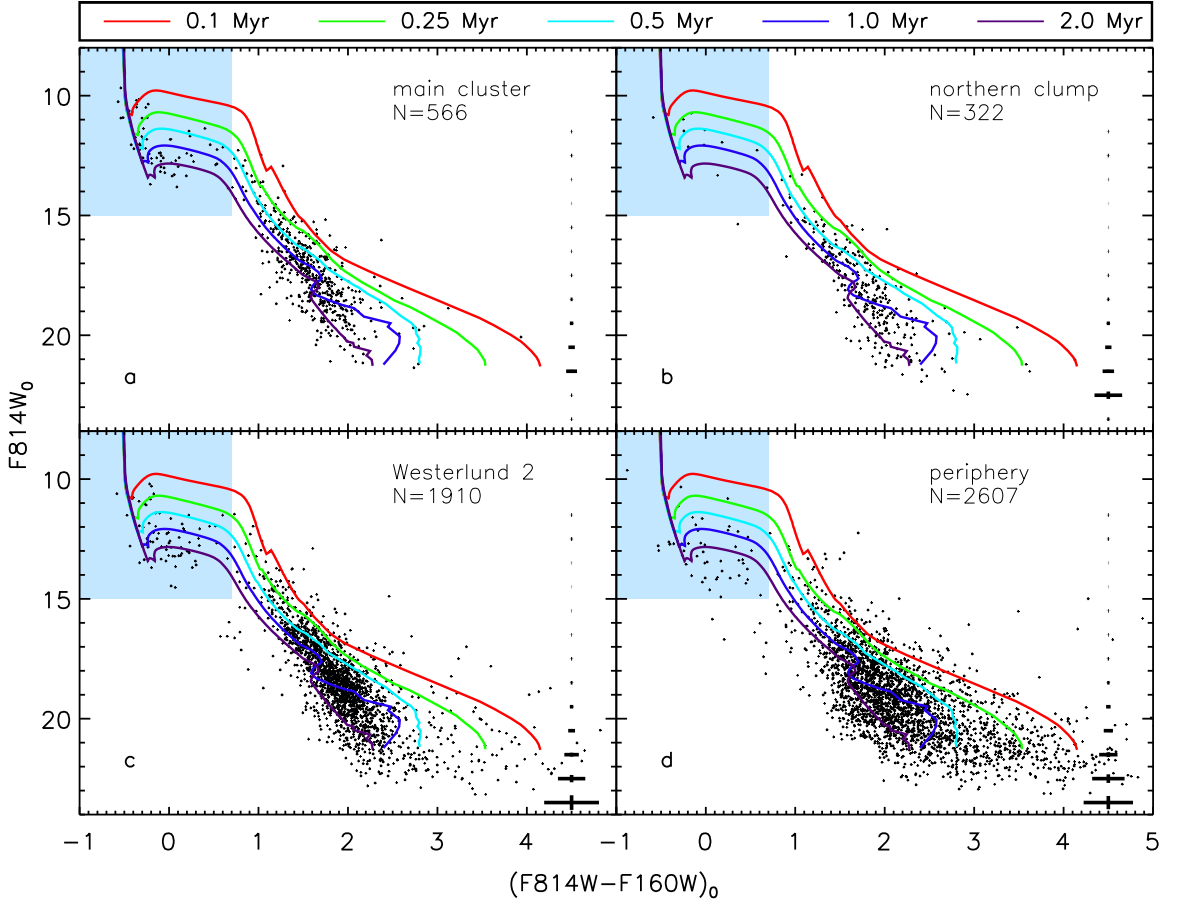


Figure 8.4.3: The $F814W_0$ vs. $(F814W - F160W)_0$ CMDs of the four different regions of RCW 49. All objects brighter than $F814W_0 = 15.0$ mag and bluer than $(F814W - F160W)_0 = 0.7$ mag are defined as MS or TO members (light blue area). Overplotted are the PARSEC 1.2S isochrones (Bressan et al. 2012) between 0.1 and 2.0 Myr for a Solar metallicity of $Z = 0.0152$ and a distance of $d = 4.16$ kpc. On the right side typical photometric uncertainties are shown.

R.A. = $10^{\text{h}}24^{\text{m}}01^{\text{s}}.65$ and decl. = $-57^{\circ}45'33.4''$ with a peak density of $\Sigma = 1863$ stars pc^{-2} . For the NC we got R.A. = $10^{\text{h}}24^{\text{m}}02^{\text{s}}.16$ and decl. = $-57^{\circ}44'39.3''$ with a peak density of $\Sigma = 937$ stars pc^{-2} . We defined the sizes of the two clumps as the 1σ width of the Gaussian density distributions and the area of the Wd2 cluster as the 2σ width. This led to sizes of 0.31 arcmin 2 (0.44 pc 2) for the MC and 0.27 arcmin 2 (0.38 pc 2) for the NC.

The full sample of 5404 PMS stars (cluster members detected in $F814W$ and $F160W$) has a mean age of 1.04 ± 0.71 Myr with $\sim 60\%$ of all stars being between 1.0–2.0 Myr old. The full sample age is representative for the Wd2 cluster age (see Sect. 8.4.1). The cluster age is also in good agreement with the age estimated by Ascenso et al. (2007a, 1.5–2 Myr) and the theoretical MS lifetime of massive O stars of 2–5 Myr (see Tab 1.1 in Sparke and Gallagher 2007). Therefore, Wd2 has the same age or is even younger than other very young star clusters like NGC 3603 (1 Myr, Pang et al. 2013), Trumpler 14 (≤ 2 Myr, Carraro et al. 2004)

Table 8.4.2. The different areas of RCW 49

	MC (A)		NC (b)		Wd 2 (c)		Periphery (d)		Total
Full-sample PMS stars	498	(9.2%)	310	(5.7%)	1844	(34.2%)	2752	(50.9%)	5404
Mean age [Myr]	1.17 ± 0.69		1.16 ± 0.67		1.11 ± 0.67		0.96 ± 0.73		
Reduced-sample PMS stars	263	(15.6%)	142	(8.4%)	673	(39.8%)	612	(36.2%)	1690
Mean age [Myr]	0.90 ± 0.63		0.94 ± 0.64		0.82 ± 0.61		0.83 ± 0.69		
H α -excess stars	36	(15.0%)	26	(10.8%)	106	(44.2%)	72	(30.0%)	240
Mean age [Myr]	0.64 ± 0.59		0.77 ± 0.61		0.63 ± 0.55		0.54 ± 0.58		
Mean \dot{M} [$10^{-8} M_{\odot} \text{yr}^{-1}$]	3.32		3.12		4.84		5.70		4.43

Note. — In this table we present a summary of the different properties of the stellar population in the different regions of RCW 49. The letters in brackets are the panel numbers in Fig. 8.4.3.

in the Carina Nebula (Smith and Brooks 2008), R136 in the Large Magellanic Cloud (1–4 Myr, Hunter et al. 1995; Walborn and Blades 1997; Sabbi et al. 2012), NGC 602 (Cignoni et al. 2009) and NGC 346 (Cignoni et al. 2010) both in the SMC, or the Arches cluster (Figer et al. 2002; Figer 2005). It is also younger than Westerlund 1 (5.0 ± 1.0 Myr), the most massive young star cluster known in the MW (Clark et al. 2005; Gennaro et al. 2011; Lim et al. 2013). Comparing the four different regions MC, NC, the Wd2 cluster outskirts, and the periphery of RCW 49, we do not find any significant age difference between the regions (see Tab. 8.4.2). It appears that the MC and the NC are coeval.

The comparison of the sub-cluster surface densities calculated in our study ($\Sigma_{NC} = 555 \text{ stars pc}^{-2}$ and $\Sigma_{MC} = 1114 \text{ stars pc}^{-2}$) with the results of Kuhn et al. (2015) places the sub-clusters of Wd2 at the lower end of the stellar surface densities range of ~ 1 to $\sim 30,000 \text{ stars pc}^{-2}$ (Kuhn et al. 2015). Therefore, this result is comparable with the surface density of, e.g., M 17. We have to note here that we made the lower mass cut $0.65 M_{\odot}$, to properly correct for completeness effects. Therefore, our values should be more considered as lower limits. In addition, Kuhn et al. (2015) found that there is no special value for the surface density of sub-clusters.

Banerjee and Kroupa (2015) explore various scenarios of sub-clustering for massive ($> 10^4 M_{\odot}$) star clusters to study the possible scenarios of the formation of the young massive cluster NGC 3603 (e.g., Stolte et al. 2004; Pang et al. 2011). The proposed scenarios are either in-situ monolithic cluster formation, meaning the cluster forms in a single, massive star-formation event, or via merging of less massive sub-clusters, which then move toward each other and merge to the final massive cluster. Banerjee and Kroupa (2015) argue that the monolithic cluster formation with an in-situ scenario fits best the observations of NGC 3603 (Banerjee and Kroupa 2014), but also the scenario of the cluster assembly from sub-clusters within 1 Myr is not ruled out. In one simulation they used as initial conditions a number of 10 sub-clusters, each following a Plummer sphere (Plummer 1911) distribution of gas. The sub-clusters were equally distributed over a sphere with radius $R = 2.5 \text{ pc}$. This simulation gives after 1 Myr a system with two sub-clusters, separated by $\sim 1 \text{ pc}$ (cf. their Panel 5 in Fig. 5 and Panel 3 in Fig. 6). Their simulated system is still in the process of merging at $t \approx 1 \text{ Myr}$ and far from virialization and from a final spherical shape. The distance between the two clumps in Wd2 is 54.2 arcsec or 1.08 pc and therefore well comparable with the

results of these simulations, while the cavity in RCW 49 cleared by the cluster has a radius of ~ 2 pc. Due to the similar age of Wd2 and NGC 3603 and the existence of two coeval sub-clusters that fit well the properties of the simulations in [Banerjee and Kroupa \(2015\)](#) a monolithic formation from sub-clusters is a likely scenario for the formation of Wd2.

The presence of a faint, uniformly distributed low-mass population ($< 0.15M_{\odot}$), visible throughout the RCW 49 area, implies that the actual star forming region is more extended than the Wd2 cluster. This phenomenon was already observed by [Whitney et al. \(2004\)](#) identifying ~ 300 cYSOs in the giant H II region of RCW 49 using *Spitzer* IRAC MIR data of the GLIMPSE survey ([Benjamin et al. 2003](#)). [Churchwell et al. \(2004\)](#) described the RCW 49 gas and dust distribution as “a complex network of thin filaments, pillars, sharp boundaries, and knots”. This irregular distribution and the associated gas, probably created by the feedback of the massive stellar population, is a perfect birthplace for a new population of stars. [Whitney et al. \(2004\)](#) identified 5 more star-forming sites throughout the RCW 49 cloud. This is also known from other young star clusters e.g., NGC 3603, the Orion Nebular Cluster (e.g., [Hillenbrand 1997](#)), or the 30 Doradus region (e.g., [Walborn et al. 1999](#); [Brandner et al. 2001](#)).

A possible scenario for the formation of a massive star cluster is the cloud-cloud collision of giant molecular clouds. This can lead to a long lasting, extended formation of a low-mass stellar population, similar what we see in our data. Cloud-cloud collision is considered as one of the modes for high-mass star formation. Theoretical studies and hydrodynamical simulations for the scenario of cloud-cloud collision were made by [Habe and Ohta \(1992\)](#); [Anathpindika \(2010\)](#) and [Takahira et al. \(2014\)](#). This scenario has been suggested by [Nigra et al. \(2008\)](#) and [Cignoni et al. \(2009\)](#) for the star cluster NGC 602 in the SMC and is also debated for other star clusters such as NGC 3603 ([Fukui et al. 2014](#)) and RCW 38 ([Fukui et al. 2016](#)) in the MW. For the RCW 49 region this scenario is supported by CO observations by [Furukawa et al. \(2009, 2014\)](#) and [Ohama et al. \(2010\)](#) using data of the NANTEN survey ([Mizuno and Fukui 2004](#)) as well as a large population of young PMS stars detected in the RCW 49 gas cloud ([Whitney et al. 2004](#)), far away from the influence of the luminous OB star population. [Ohama et al. \(2010\)](#); [Furukawa et al. \(2009\)](#) and [Furukawa et al. \(2014\)](#) showed that the CO distribution throughout RCW 49 splits up into three different clouds with a LSR velocity of 16, 4, and -4 km s^{-1} , respectively. [Furukawa et al. \(2009\)](#) calculated the respective kinematic distances to be 6.5, 5.2, and 4.0 kpc using the rotation curve of [Brand and Blitz \(1993\)](#).

In the dereddened $F814W_0$ vs. $(F814W - F160W)_0$ CMD we see a red, low-mass population of stars which we refer to as the red tail. We ruled out that photometric uncertainties are responsible for such a feature. Analyzing the location of these red stars on the sky, an over-density to the south-west becomes visible (see Fig. 8.3.3). This over density coincides with an area with low $F814W$ and $H\alpha$ fluxes (left panels of Fig. 8.3.3 and Fig. 8.3.4) and is not correlated with the structure seen in the gas extinction map (right panel of Fig. 8.3.3). Comparing this area to *Spitzer* IRAC observations (see right panel of Fig. 8.3.4) of the GLIMPSE survey ([Benjamin et al. 2003](#)) a molecular cloud becomes visible. This cloud structure is very well visible in the IRAC-3 [5.8] band containing the PAH $6.2\mu\text{m}$ C–C stretching mode ([Draine](#)

2003). This leads to the conclusion that this molecular cloud is located in front of the Wd2 cluster. This conclusion is emphasized by the fact that we cannot see the cloud in our $H\alpha$ and $Pa\beta$ line emissions and therefore we are underestimating the gas extinction $E(B - V)_g$. This is the reason we can see those objects as the red tail. The CO cloud located at a distance of 4.0 kpc (Furukawa et al. 2009, 2014; Ohama et al. 2010) coincides with the location of the molecular cloud seen in the *Spitzer* data and the location of the red-tail members. The cloud kinematics of Dame (2007) and Furukawa et al. (2009) suggest that Wd2 is located behind the 4, and -4 km s^{-1} clouds which is in contradiction to our distance estimate. On the other hand, if we underestimated the extinction toward Wd2 our distance modulus is than overestimated leading to even closer distance. We suggest that Wd2 is located between the 4, and -4 km s^{-1} clouds confirming our distance of 4.16 kpc determined in Sect. 8.2.3 and by Vargas Álvarez et al. (2013).

Willst du dich am Ganzen erquicken, so musst du das Ganze im Kleinsten erblicken.

— Johann Wolfgang von Goethe: Gott, Gemüt und Welt

9

The mass-accreting PMS stars

This chapter is included in Sect. 1, Sect. 4, and Appendix A of [Zeidler et al. 2016, AJ, 152, 4](#).

Over the past decades studies showed that during the PMS phase, low-mass stars grow in mass through accretion of matter from their circumstellar disk (e.g., [Lynden-Bell and Pringle 1974](#); [Calvet et al. 2000](#), and references therein). These disks form due to the conservation of angular momentum following infall of mass onto the star, tracing magnetic field lines connecting the stars and their disks. It is believed that this infall leads to the strong excess emission observed for many PMS stars, originating through gravitational energy being radiated away and exciting the surrounding gas. As a result, this excess can be used to measure accretion rates for these classical T-Tauri stars (especially via $H\alpha$ and $Pa\beta$ emission lines, e.g., [Muzerolle et al. 1998a,b](#)). The accretion luminosity (L_{acc}) can then be used to calculate the mass accretion rate (\dot{M}). Studies of different star formation regions (e.g., Taurus, Ophiuchus, [Sicilia-Aguilar et al. 2006](#)) showed that these accretion rates decrease steadily from $\sim 10^{-8} M_{\odot} \text{yr}^{-1}$ to less than $10^{-9} M_{\odot} \text{yr}^{-1}$ within the first 10 Myr of the PMS star lifetime (e.g., [Muzerolle et al. 2000](#); [Sicilia-Aguilar et al. 2006](#)). This is in good agreement with the expected evolution of viscous disks as described by [Hartmann et al. \(1998\)](#). These studies all agree that the mass accretion rate decreases with the stellar mass.

Understanding these accretion processes plays an important role in understanding disk evolution as well as the PMS cluster population as a whole ([Calvet et al. 2000](#)). Mass accretion onto PMS stars produces distinctive photometric and spectroscopic features. The “standard” way to quantify the mass accretion is through spectroscopy. Usually, one studies the intensity and profile of emission lines such as $H\alpha$, $Pa\beta$, or $Br\gamma$, which requires medium to high resolution spectra. This approach has the disadvantage of long integration times and, therefore, only a small number of stars can usually be observed. In the past, PMS stars were

also photometrically identified using their locus at redder colors than the MS in CMDs (e.g., [Hunter et al. 1995](#); [Brandner et al. 2001](#); [Nota et al. 2006](#); [Zeidler et al. 2016c](#)). A possible disadvantage of this method is the difficulty to distinguish between bona-fide PMS stars and objects that occupy the same region in the CMD (such as reddened background giants).

$H\alpha$ filters have long been used to identify $H\alpha$ emission-line objects in combination with additional broadband and intermediate-band colors (e.g., [Underhill et al. 1982](#)). More recent, [De Marchi et al. \(2010\)](#) presented a method that uses two broadband filters (*V* and *I* in their study) to determine the continuum emission in combination with the narrow-band $H\alpha$ filter to identify PMS stars with disk accretion. For panoramic CCD detectors, the technique was first applied by [Grebel et al. \(1992\)](#) and then developed further for different filter combinations and to quantify the $H\alpha$ emission (e.g., [Grebel et al. 1993](#); [Grebel 1997](#)) and has since been widely used in multiple studies of different regions within the MW and the Magellanic Clouds ([De Marchi et al. 2010, 2011a,b, 2013](#); [Beccari et al. 2010, 2015](#); [Spezzi et al. 2012](#)). [De Marchi et al. \(2010\)](#) used this photometric method to estimate the accretion luminosity of PMS stars. Normally the *R*-band is used as the continuum for the $H\alpha$ filter. [De Marchi et al. \(2010\)](#) showed for the field around SN 1987A ([Romaniello et al. 1998](#); [Panagia et al. 2000](#); [Romaniello et al. 2002](#)), that the ACS filters *F555W* and *F814W* can be similarly used to obtain the continuum for the $H\alpha$ filter. Up to now, this method ([De Marchi and Panagia 2015](#)) has been proven to be successful in studies for different clusters, such as NGC 346 in the Small Magellanic Cloud (SMC, [De Marchi et al. 2011a](#)) and NGC 3603 in the MW ([Beccari et al. 2010](#)).

Due to its young age, Wd2 is a perfect target to study accretion processes of the PMS stars in the presence of a large number of O and B stars. In close proximity to OB stars, the disks may be expected to be destroyed faster by the external UV radiation originating from these massive stars. This would lead to a lower excess of $H\alpha$ emission in the direct neighborhood of the OB stars ([Anderson et al. 2013](#); [Clarke 2007](#)).

9.1 The *R*-band interpolation

The *F658N* filter is located between and does not overlap with the *F555W* and *F814W* filters. To get a better characterization of the continuum contribution at the $H\alpha$ line, we thus combined the *F555W* and *F814W* filters to construct an interpolated *R* filter. In order to study the relation of the Johnson's *R*-band ([Johnson and Morgan 1953](#)) and the ACS/WFC *F555W* and *F814W* filters ([Ubeda et al. 2012](#)) we used the SYNPHOT/CALCPHOT routine¹ ([Laidler et al. 2005](#)) in combination with the ATLAS9 model atmospheres ([Castelli and Kurucz 2003](#)) and the Stellar Spectral Flux Library by [Pickles \(1998\)](#). We determined the artificial stellar magnitudes by folding the respective filter curves with the stellar spectra for main sequence stars (ATLAS9: K7V–A0V and [Pickles \(1998\)](#): M6V–O5V). In Fig. 9.1.1 we show the *F555W* – *R* vs. *F555W* – *F814W* TCD diagram. The red points are the photometry determined using the ATLAS9 models and the green data points are determined using the

¹Synphot is a product of the Space Telescope Science Institute, which is operated by AURA for NASA.

Pickles (1998) library. The black data points, representing the spectral types of A2V–O5V and K7V–K5V, are excluded from the fit because the relation becomes non-linear.

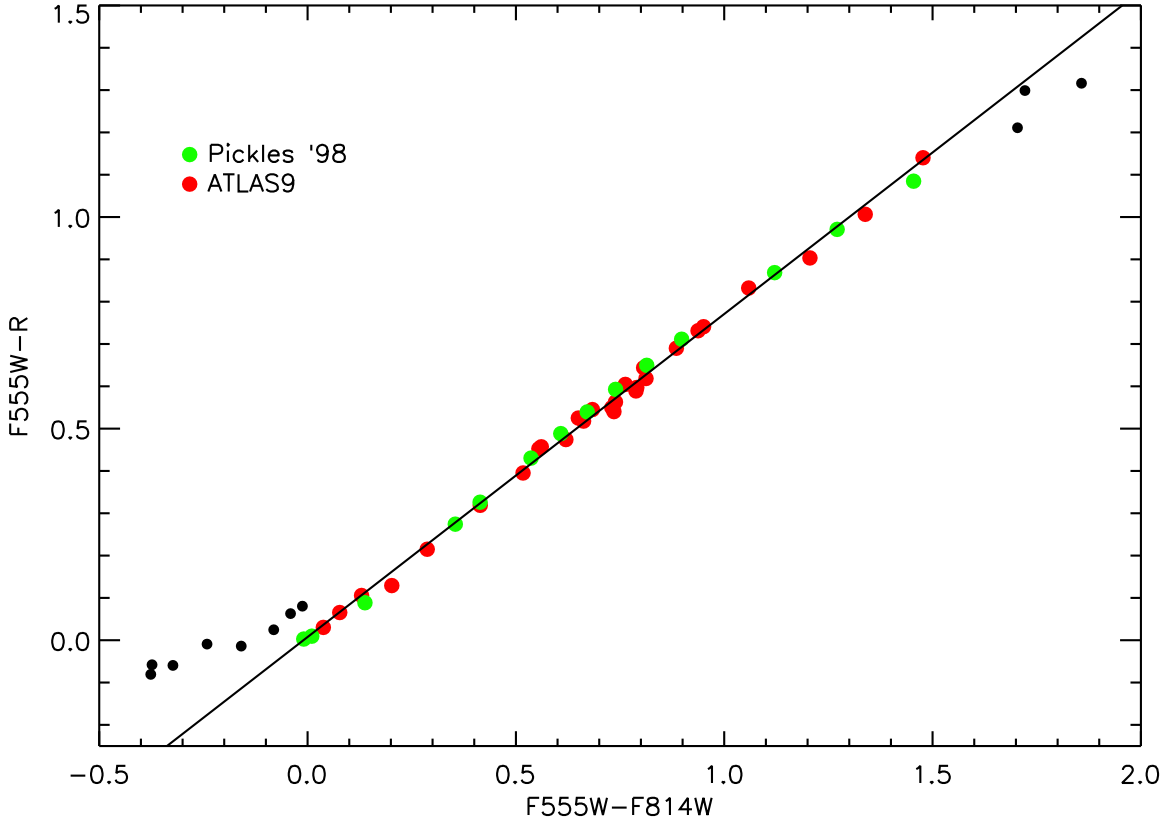


Figure 9.1.1: The $F555W - R$ vs. $F555W - F814W$ TCD for the photometry derived from the ATLAS9 model atmospheres (red points, [Castelli and Kurucz 2003](#)) and the Stellar Spectral Flux Library by [Pickles \(1998\)](#), green points) for spectral types between A0V ($T = 9500$ K) and K5V ($T = 4250$ K). All spectral types between A2V–O5V and K7V–K5V are excluded because of their locations outside the linear regime of the detector response (black dots). The black line marks the least-square linear fit.

For spectral types between A0V ($T = 9500$ K) and K5V ($T = 4250$ K) the photometric relation is remarkably linear. In this range we performed a least-square linear fit. As a result we got

$$R = 0.237 \cdot F555W + 0.763 \cdot F814W - 0.008. \quad (9.1)$$

This relation was then used to calculate the interpolated R -band photometry from the ACS $F555W_0$ and $F814W_0$ photometry.

9.2 The H α excess emission

The method for identifying stars with a strong H α emission line relies on the assumption that the majority of stars in a cluster will not have H α emission. We use the $(F555W - F814W)_0$ vs. $(R - F658N)_0$ TCD (see Fig. 9.2.1) to identify all stars with an excess emission in H α being 5 times their photometric uncertainty above the reference line of the continuum. To do so we defined a reference template of the continuum of all stars in the given $(F555W - F814W)_0$ color range by using an average value of $(R - F658N)_0$ computed as a running mean with bin size of a 100 stars. The result is represented by the green dashed-dotted line in Fig. 9.2.1. The red dashed-dotted line represents the PARSEC 1.2S ZAMS. This method provides us with a reliable baseline because PMS stars show large variations in their H α excess caused by periodic mass accretion (e.g., Smith et al. 1999) on an hourly or daily basis. Therefore, only a fraction of all PMS stars show H α excess above the continuum level at any given time.

The H α excess emission is defined as:

$$\Delta H\alpha = (R - F658N)_{\text{obs}} - (R - F658N)_{\text{ref}}. \quad (9.2)$$

The subscript “obs” indicates the observed color and the subscript “ref” the reference template color at each $(F555W - F814W)_0$.

The combined $\Delta H\alpha$ error is calculated as follows:

$$\sigma_{H\alpha} = \sqrt{(\sigma_{F814W}^2 + \sigma_{F555W}^2 + \sigma_{F658N}^2 + \sigma_{\text{red}}^2) / 4}, \quad (9.3)$$

where σ_{F555W} , σ_{F814W} , and σ_{F658N} represent the photometric uncertainties of the corresponding filters and σ_{red} is the uncertainty from the reddening map (see Sect. 6).

After the determination of $\Delta H\alpha$ it is straightforward to calculate the H α luminosity $L(H\alpha)$:

$$L(H\alpha) = 10^{\frac{\Delta H\alpha}{-2.5}} \cdot \text{PHOTFLAM}_{F658N} \cdot \lambda_{\text{P}}^{F658N} \cdot 4\pi d^2. \quad (9.4)$$

PHOTFLAM is the inverse sensitivity of the instrument with a value of $\text{PHOTFLAM}_{F658N} = 1.98 \cdot 10^{-18} \text{ ergs cm}^{-2} \text{ s}^{-1} \text{ \AA}^{-1}$. $\lambda_{\text{P}}^{F658N}$ is the pivot wavelength of the $F658N$ filter with a value of 6583.9 \AA . $d = 4.16 \text{ kpc}$ is the distance of Wd2.

In Fig. 9.2.2 we show the distribution of the H α luminosity. The median H α luminosity is $L(H\alpha) = 1.67 \cdot 10^{31} \text{ ergs s}^{-1} = (4 \pm 0.36) \cdot 10^{-3} L_{\odot}$ with a total number of 240 H α excess emitting stars. Additionally, we excluded all objects with $(F555W - F814W)_0 < 0.2 \text{ mag}$ for being possible Ae/Be stars (e.g., Scholz et al. 2007). Compared to the 240 H α excess emitting PMS stars Ae/Be stars are MS stars that can show IR emission caused by gaseous circumstellar disks (e.g., Hillenbrand et al. 1993).

At this point we should note that the ACS $F658N$ filter is broader than a typical H α filter so a small portion of the NII doublet at 6549 \AA and 6585 \AA falls into the H α filter (see

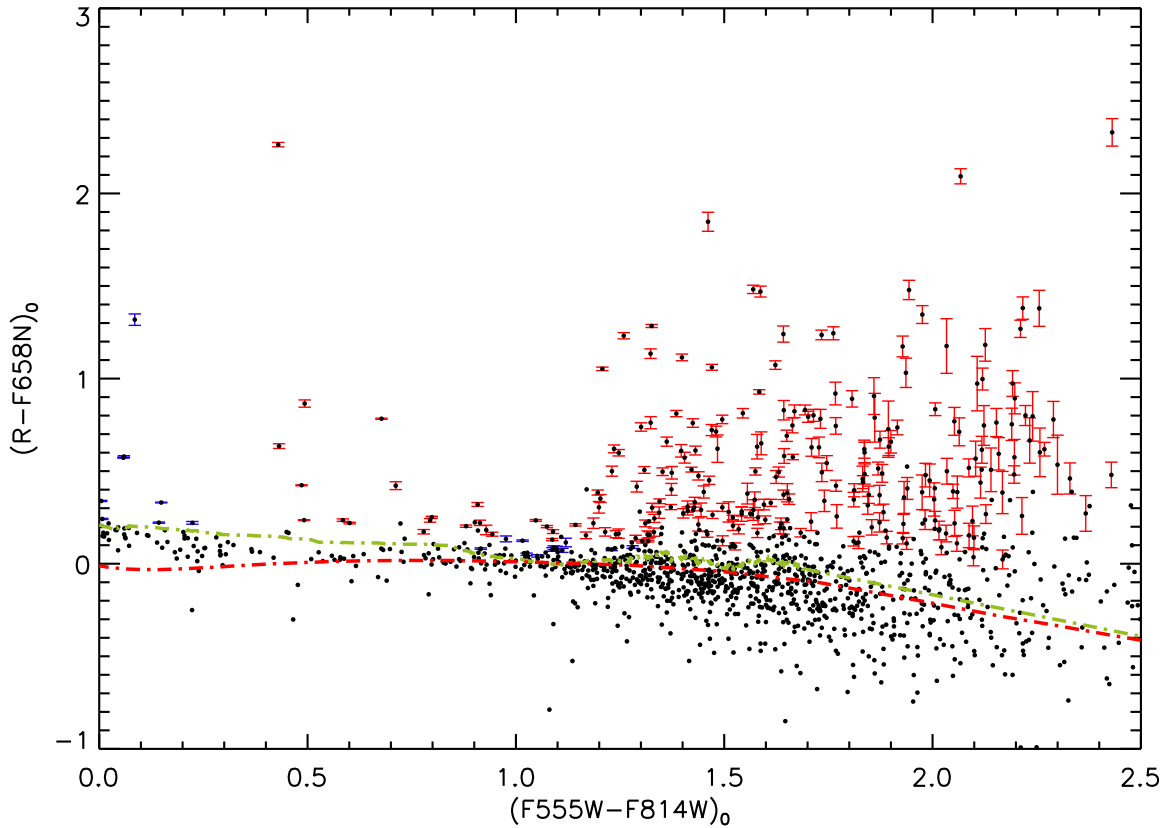


Figure 9.2.1: The $(F555W - F814W)_0$ vs. $(R - F658N)_0$ TCD of all cluster members. All stars in red fulfill the criteria of being 5 times their photometric uncertainty above the reference line of the continuum, having an $EW(H\alpha) > 10$, and having a $(F555W - F814W)_0 > 0.2$ mag. The objects marked with blue symbols have an $EW(H\alpha) < 10$. The red dashed-dotted line represents the PARSEC 1.2S ZAMS, while the green dashed-dotted line represents the photospheric continuum.

Fig. 6.3.1). Using synthetic spectral lines from the HII Regions Library (Panuzzo et al. 2003) and convolving their strength with the throughput curve of the $F658N$ filter, calculated with the bandpar module of Synphot² (Laidler et al. 2005), we get a contribution of 0.59% and 3.1% to the flux of the $H\alpha$ line. This contamination is a systematic effect and affects all stars in the same way. The combined photometric uncertainty, including the one of the color excess map used to deredden our photometry, adds up to 8.2% for $L(H\alpha)$ and dominates the uncertainty. The uncertainty of 0.33 kpc in the distance of Wd2 (Vargas Álvarez et al. 2013; Zeidler et al. 2015) leads to an overall uncertainty of $L(H\alpha)$ of $\sim 15\%$.

²Synphot is a product of the Space Telescope Science Institute, which is operated by AURA for NASA.

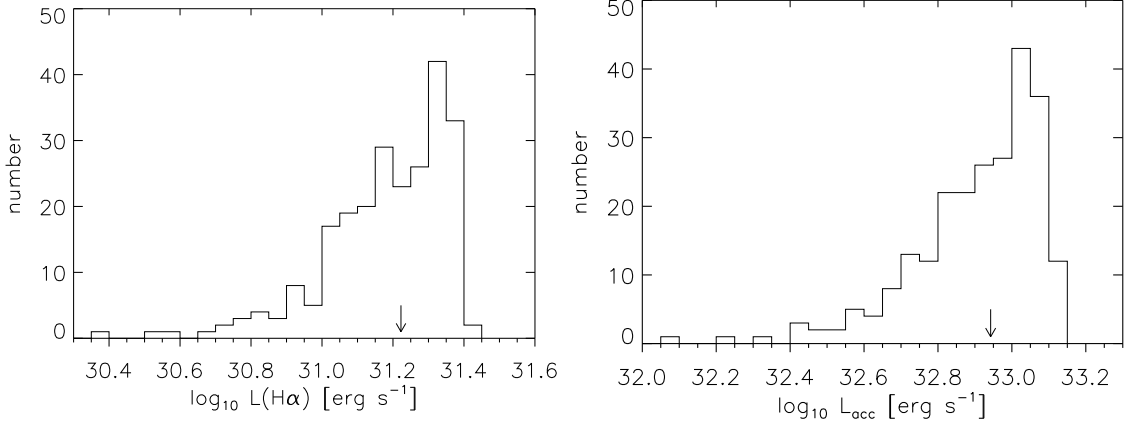


Figure 9.2.2: **Left:** The histogram of the H α emission flux distribution of our 240 bona-fide PMS stars 5σ above the continuum and $(F555W - F814W)_0 > 0.2$ mag. The arrow marks the median value of $(4 \pm 0.36) \cdot 10^{-3} L_{\odot}$. **Right:** The accretion luminosity distribution of our 240 bona-fide PMS stars. The arrow marks the median value of $8.76 \cdot 10^{32} \text{ erg s}^{-1}$. The bin size is 0.05 dex.

9.3 The equivalent width

We use the equivalent width (EW) of the H α line to separate PMS stars from those whose H α excess is due to chromospheric activity ($EW \approx 3 \text{ \AA}$; Panagia et al. 2000, and references therein). Because of the small photometric errors for bright stars, the 5σ threshold is not sufficient to obtain a PMS sample that lies well above the continuum emission. Panagia et al. (2000, and references therein) showed that using an $EW > 10 \text{ \AA}$ is sufficient as an additional selection criterion to select stars well above the continuum.

The EW gives a well-defined, comparable measurement of the strength of a line above the continuum. It is defined as:

$$W_{\text{eq}} = \int (1 - P_{\lambda}) d\lambda, \quad (9.5)$$

with P_{λ} being the line profile. In the following we always consider the absolute value in comparison of W_{eq} ³. In the case of H α falling completely inside the filter width, eq. 9.5 can be calculated with the following relation:

$$W_{\text{eq}}(\text{H}\alpha) = \text{RW} \cdot \left(1 - 10^{-0.4(\text{H}\alpha - \text{H}\alpha^{\text{cont}})}\right), \quad (9.6)$$

where $\text{RW} = 74.96 \text{ \AA}$ represents the rectangular width of the filter. H α is the observed H α magnitude while H α^{cont} is the pure H α continuum. This was determined using the $F555W_0$ and $F814W_0$ magnitudes of the same objects with $m_{\text{H}\alpha^{\text{cont}}} = 0.381m_{F555W} + 0.0619m_{F814W} - 0.156$ (determined with Synphot, see Appendix of De Marchi et al. 2010). De Marchi et al. (2010) showed that this transformation does not significantly change with metallicity.

³One should keep in mind that while looking at emission lines their EW is by definition negative.

We find that 74.6% of all $H\alpha$ excess sources have an $EW > 10 \text{ \AA}$. Additionally removing the 24 Ae/Be candidates (red dots in Fig. 9.3.1) leaves us with 240 objects (67.7%). In Fig. 9.3.2 we show the EW distribution, including the 240 stars considered to be $H\alpha$ -emitting PMS stars (red dots) and the 24 Ae/Be candidates (green dots). The locus of the $H\alpha$ excess stars in the $F814W_0$ vs. $(F814W - F160W)_0$ CMD is shown in Fig. 9.3.1. The majority of the Ae/Be candidates lie, as expected, in the MS and TO regime (blue shaded area in Fig. 9.3.1).

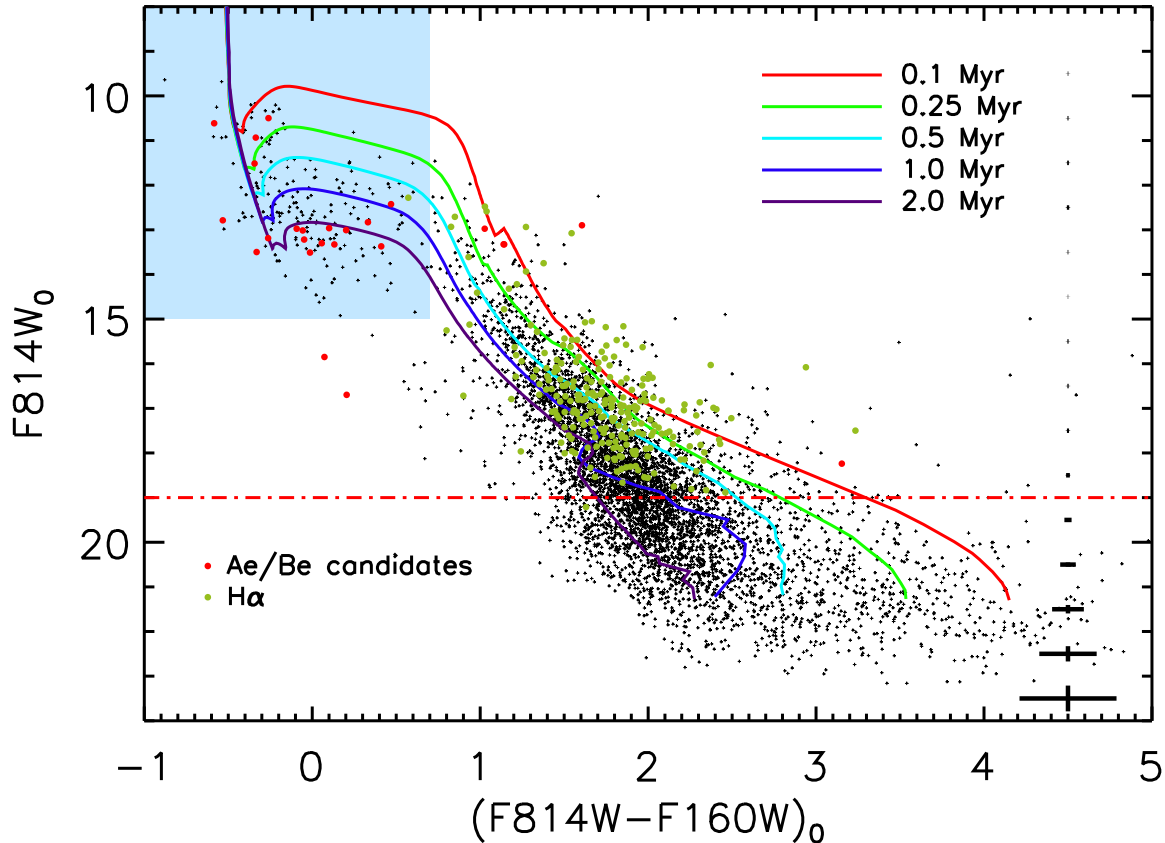


Figure 9.3.1: The $F814W_0$ vs. $(F814W - F160W)_0$ CMD of the RCW 49 members (black dots). We defined all objects brighter than $F814W_0 = 15.0$ mag and bluer than $(F814W - F160W)_0 = 0.7$ mag as MS and TO members (light blue area). The red dots mark the 24 Ae/Be candidates, namely all stars showing $H\alpha$ excess and having an $EW > 10$ but being bluer than $F555W - F814W = 0.2$ mag. The green dots show all $H\alpha$ excess PMS objects. Overplotted are the PARSEC 1.2S isochrones (Bressan et al. 2012) between 0.1 and 2.0 Myr for a Solar metallicity $Z = 0.0152$ and a distance $d = 4.16$ kpc. The red dashed-dotted line marks the detection limit set by the $F555W$ and $F658N$ filters ($\sim 0.3 M_\odot$ at an age of 1 Myr), both needed to identify the $H\alpha$ excess stars. On the right side typical photometric uncertainties are shown as a function of magnitude.

9.4 The Ae/Be star candidates

In the previous section, we classified all stars showing an $H\alpha$ excess 5σ above the continuum with $(F555W - F814W)_0 < 0.2$ mag as possible Ae/Be stars (e.g., Scholz et al. 2007). This

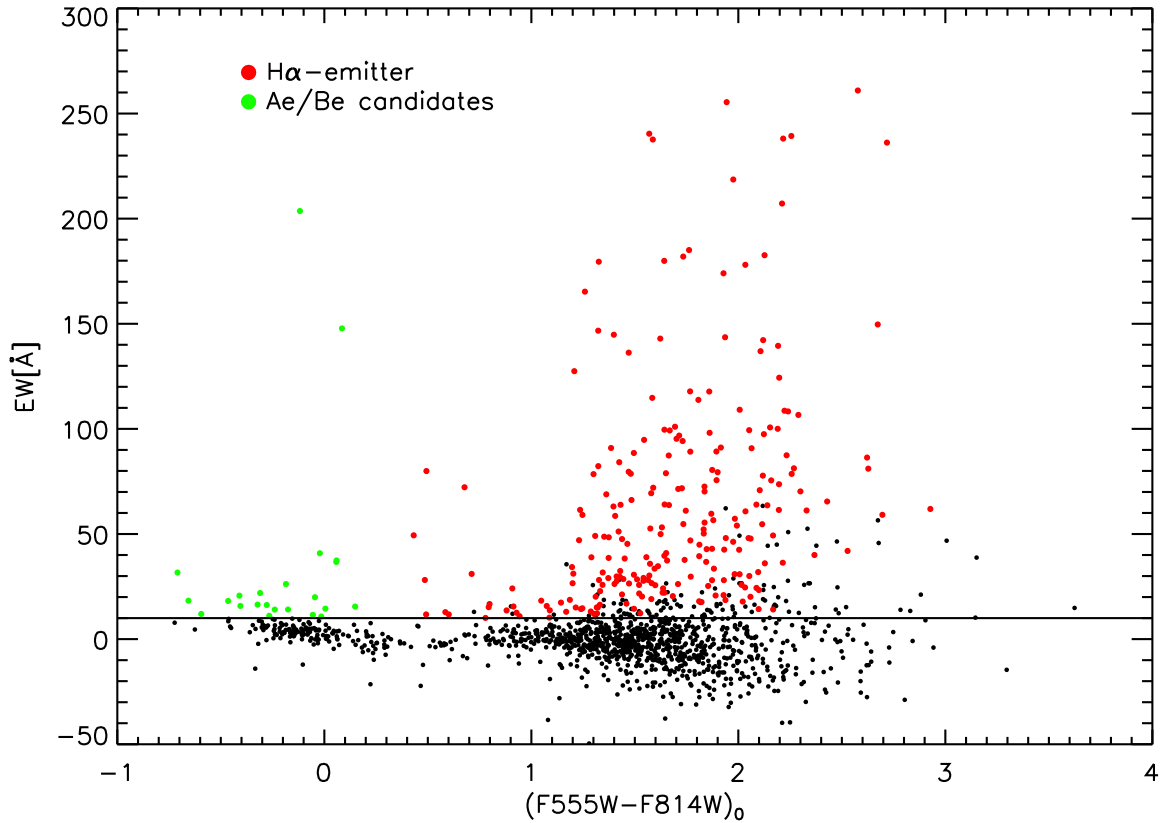


Figure 9.3.2: The distribution of the EWs for the 240 bona fide $H\alpha$ emission PMS stars. On the x-axis the $(F555W - F814W)_0$ color is plotted and on the y-axis the EW in Ångstrom. Objects in red fulfill the selection criteria for PMS stars with $H\alpha$ excess emission. The Ae/Be candidates are represented as green dots.

led to a number of 24 Ae/Be candidates. Some of these stars are located in the same area of the $F814W_0$ vs. $(F814W - F160W)_0$ CMD as the PMS (see Fig. 9.3.1). Classical Ae/Be stars are MS stars that can show IR emission caused by gaseous circumstellar disks (e.g., Hillenbrand et al. 1993) which can lead to a higher $(F814W - F160W)$ color. To check whether they are classical Ae/Be stars or Herbig Ae/Be stars we also analyzed their locus in the $F814W_0$ vs. $(F555W - F814W)_0$ CMD. As can be seen all 24 stars are located well outside the area covered by the PMS. Subramaniam et al. (2006) compared the spectra of classical Ae/Be stars and Herbig Ae/Be stars and showed that the slope of the continuum flux widely differs leading to blue $(F555W - F814W)$ colors for classical Ae/Be stars and red $(F555W - F814W)$ colors for Herbig Ae/Be stars. Since, by selection criterion, all of our candidates have colors bluer than $(F555W - F814W)_0 < 0.2$ mag we can state that these stars are all Ae/Be candidates.

9.5 The accretion luminosity and mass accretion rate

The source of the bolometric accretion luminosity (L_{acc}) is radiation emitted by the accretion process of the disk onto its central star (Hartmann et al. 1998). This leads to a connection between the H α -excess luminosity $L(\text{H}\alpha)$, produced by the same process, and the accretion luminosity. For the logarithmic values of $L(\text{H}\alpha)$ and L_{acc} , theoretical models of Muzerolle et al. (1998b) predict a slope of unity for low accretion rates and shallower slopes for higher accretion rates. The empirical fit of $\log_{10} L_{\text{acc}}$ vs. $\log_{10} L(\text{H}\alpha)$ of 14 members of IC 348 in the Taurus-Auriga association by Dahm (2008) is characterized by a slope of 1.18 ± 0.26 . Taking into account the larger uncertainty associated with our data and the fact that we most likely have a sample with a variety of accretion rates, we will use eq. 5 of De Marchi et al. (2010) obtained from the data presented in Dahm (2008). On this basis L_{acc} is connected with $L(\text{H}\alpha)$ the following way:

$$\log_{10}(L_{\text{acc}}) = (1.72 \pm 0.47) + \log_{10} L(\text{H}\alpha). \quad (9.7)$$

The uncertainty of ± 0.47 shows how difficult it is to find a relation between the two observables, yet it is the best relation that we can use to relate $L(\text{H}\alpha)$ to L_{acc} . Applying the transformation to the accretion luminosity for our objects gives us a median value $L_{\text{acc}} = 0.23 \pm 0.029 L_{\odot}$. The errors represent only the photometric uncertainties. The accretion luminosity distribution is shown in Fig. 9.2.2.

We can now use the free-fall equation to link the accretion luminosity to the accretion mass rate \dot{M}_{acc} in the following manner:

$$L_{\text{acc}} = \frac{GM_{\star}\dot{M}_{\text{acc}}}{R_{\star}} \left(1 - \frac{R_{\star}}{R_{\text{in}}}\right). \quad (9.8)$$

G is the gravitational constant, M_{\star} and R_{\star} are the stellar mass and radius, respectively, while R_{in} is the inner radius of the accretion disk. Following Gullbring et al. (1998), we assume $R_{\text{in}} \approx 5R_{\star}$ for all objects. Combining now eq. 9.7 and eq. 9.8, we get the accretion mass rate as a function of $L(\text{H}\alpha)$:

$$\begin{aligned} \log_{10} \frac{\dot{M}_{\text{acc}}}{M_{\odot}\text{yr}^{-1}} &= -7.39 + \log_{10} \frac{L_{\text{acc}}}{L_{\odot}} + \log_{10} \frac{R_{\star}}{R_{\odot}} - \log_{10} \frac{M_{\star}}{M_{\odot}} \\ &= (-5.67 \pm 0.47) + \log_{10} \frac{L(\text{H}\alpha)}{L_{\odot}} + \log_{10} \frac{R_{\star}}{R_{\odot}} - \log_{10} \frac{M_{\star}}{M_{\odot}}. \end{aligned} \quad (9.9)$$

Calculating the accretion mass rates for our 240 H α excess sources gives a median mass accretion rate $\dot{M} = 4.43 \cdot 10^{-8} M_{\odot}\text{yr}^{-1}$.

The error on the mass accretion rate associated with the uncertainties on the photometry is $0.363 \cdot 10^{-8} M_{\odot} \text{yr}^{-1}$. Another error source is the determination of the stellar parameters L_{\star} , M_{\star} , and T_{\star} . To examine these errors we varied each of the stellar parameters by $\pm 1\%$, $\pm 5\%$, and $\pm 10\%$. This results in an uncertainty on the accretion mass rate of $\pm 2.7\%$, $\pm 10.9\%$, and $\pm 18.7\%$, respectively.

9.5.1 Mass accretion rate as a function of stellar age

We calculated the median mass accretion rate for each age bin (0.1 Myr, 0.25 Myr, 0.5 Myr, 1.0 Myr, and 2.0 Myr; red dots in Fig. 9.5.1 and Fig. 9.5.2) and found that the mass accretion rate decreases with the stellar age ($\dot{M} \propto t^{-\eta}$, with $\eta = 0.48 \pm 0.04$ indicated by red line in Fig. 9.5.1). Hartmann et al. (1998) determined a slope of $\eta \approx 1.5 - 2.7$ with large uncertainties up to $\Delta\eta = 0.7$ for the viscous disk evolution, and stated that “this slope is poorly constrained” (dashed-dotted line in Fig. 9.5.1). We also plotted the age-mass accretion relation derived by De Marchi et al. (2013) for the two cluster NGC 602 and NGC 346 represented by the long-dashed and short-dashed line, respectively. The slopes and mass accretion rates are similar to the ones of Wd2. Comparing the mass accretion rates estimated in this paper with the data collected by Calvet et al. (2000) from multiple sources (Fig. 4, Calvet et al. 2000, and references therein), we can conclude that our mass accretion rates are comparable to these data.

In Fig. 9.5.2 we show the decrease of the mass accretion rates with time for different mass bins ($0.4-0.5 M_{\odot}$, $0.5-0.7 M_{\odot}$, $0.7-0.9 M_{\odot}$, and $0.9-1.5 M_{\odot}$). The error-weighted fit shows an overall decrease of the slope of the relation and is consistent with what De Marchi et al. (2013) found.

9.5.2 The spatial distribution of mass accreting PMS stars

We showed that the mass accretion rate in Wd2 decreases with stellar age as was predicted by e.g., Hartmann et al. (1998) and Sicilia-Aguilar et al. (2006). Another point to take into account is the high number of luminous OB stars especially in the cluster center (MC and NC). These massive, luminous stars emit a large amount of far ultra-violet (FUV) flux that can erode nearby circumstellar disks (e.g., Clarke 2007). Anderson et al. (2013) studied the effects of photoevaporation of disks due to their close proximity to massive OB stars. They found that, depending on the viscosity of the disk, most disks are completely dispersed within 0.5–3.0 Myr. This timescale is so short that, if this effect was present in the center of Wd2, we should already detect this decrease. In addition to the timescale, also the distance to the FUV source plays an important role. The results of Anderson et al. (2013) for the Orion Nebula Cluster indicate that the influence of OB stars only plays a role up to a distance of 0.1–0.5 pc.

In Wd2 we only see a 2D projection of the 3D distribution of the stars. Assuming that the MC and the NC are approximately spherical, their distribution in the z-direction does not differ from that in x and y. In Fig. 9.5.3 the spatial locations of all 240 H α excess stars are

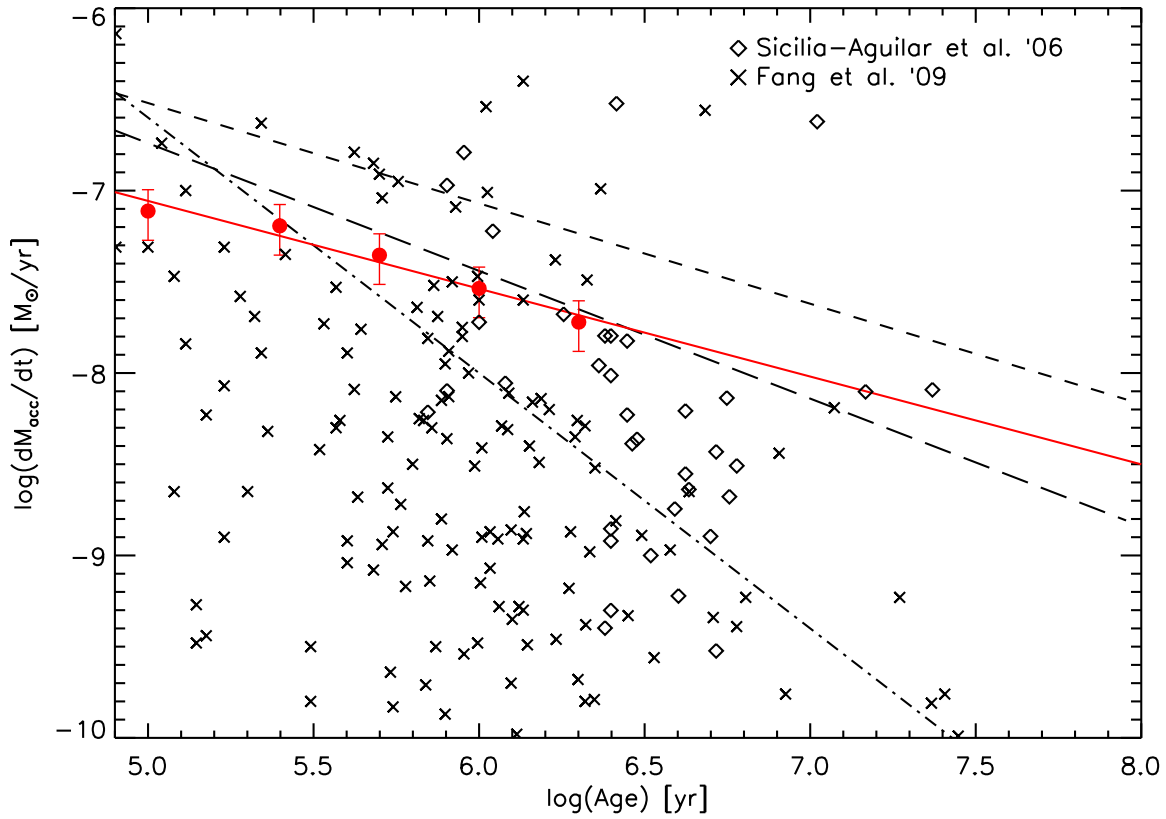


Figure 9.5.1: The median values of the mass accretion rate \dot{M} vs. the stellar age (red solid line). The error bars represent the uncertainty. The mass accretion decreases with age with a slope of $\eta = 0.48 \pm 0.04$. The long-dashed and short-dashed lines represent the age-mass accretion rate relation derived by De Marchi et al. (2013) for the two clusters NGC 602 and NGC 346, respectively. The crosses and diamonds show the mass-accreting stars in Tr 37 (Sicilia-Aguilar et al. 2006) and Orion (Fang et al. 2009). The dashed-dotted line is the relation derived by Hartmann et al. (1998) for the viscous disk evolution.

plotted, color-coded with the amount of the $H\alpha$ excess luminosity. The green asterisks mark all known OB stars in RCW 49. As reference, the FOV of the survey area and the contours of the MC the NC (solid contours), and the Wd2 cluster (dashed dotted contour) are overplotted. The gray, dashed circles indicate the radial distance of the center of the MC in steps of $15''$ or 0.3 pc. The MC is located entirely within a radius of 0.5 pc.

The mass accretion rate is linked to the $H\alpha$ excess luminosity (including the dependence on the mass and age of the star, see eq. 9.9). The median mass accretion rate in the Wd2 cluster outskirts is $4.84 \cdot 10^{-8} M_{\odot} \text{yr}^{-1}$. In comparison, the median mass accretion rate in the MC and NC is $3.32 \cdot 10^{-8} M_{\odot} \text{yr}^{-1}$ and $3.12 \cdot 10^{-8} M_{\odot} \text{yr}^{-1}$, respectively. The lower mass accretion rate in the MC and NC is caused by the presence of a high number of OB stars in their centers. To further analyze this we calculated the projected geometric centers of all OB stars within 0.5 pc of each of the peak positions of the MC and NC. These peak positions are represented with red crosses in Fig. 9.5.3. The geometric center of the OB stars in the

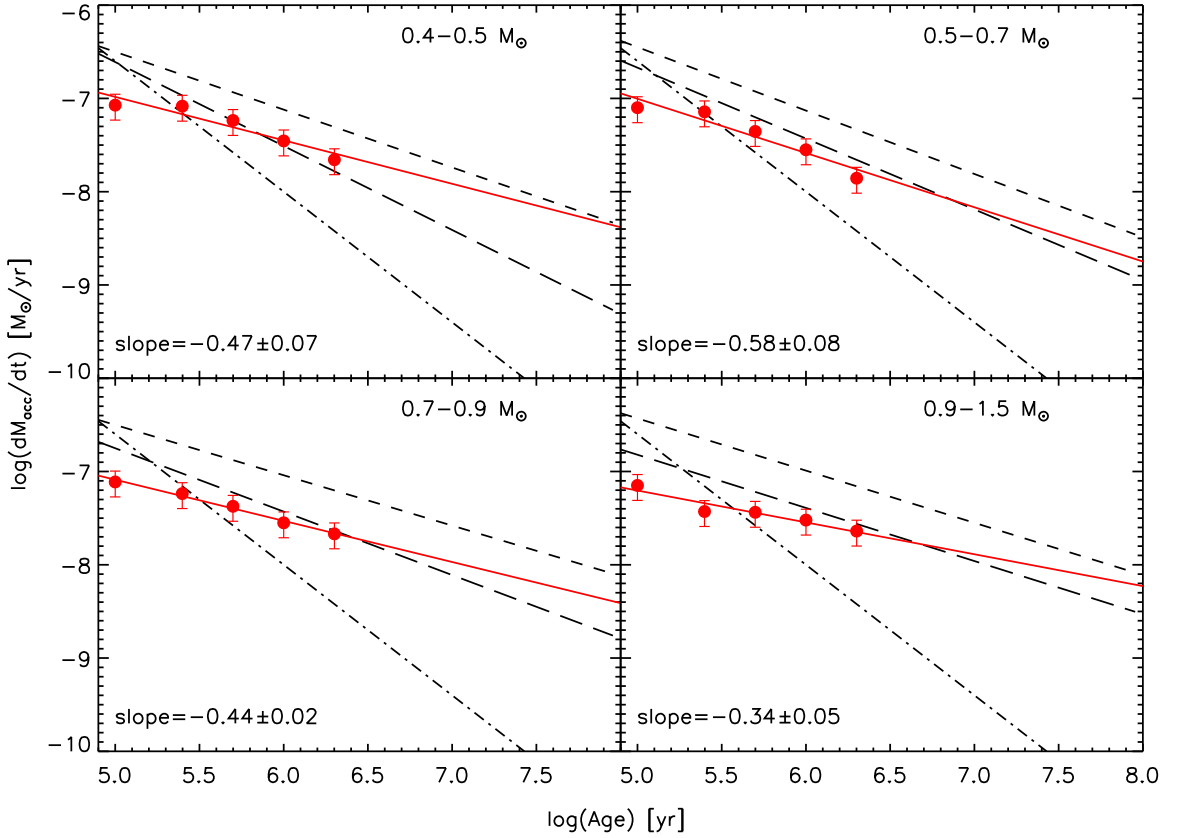


Figure 9.5.2: The median values of the mass accretion rate \dot{M} per age bin vs. the stellar age (red solid line) for different mass bins ($0.4\text{--}0.5 M_{\odot}$, $0.5\text{--}0.7 M_{\odot}$, $0.7\text{--}0.9 M_{\odot}$, $0.9\text{--}1.5 M_{\odot}$). The error bars represent the uncertainty. The long-dashed and short-dashed lines represent the age-mass accretion rate relation derived by [De Marchi et al. \(2013\)](#) for these mass bins for the two clusters NGC 602 and NGC 346, respectively. The dashed-dotted line is the relation derived by [Hartmann et al. \(1998\)](#) for viscous disk evolution.

MC almost coincides with the MC peak position ($d = 0.98''$). For the NC the distance of the geometric center of all OB stars within 0.5 pc from the NC peak position is $5.73''$. We used these centers to calculate the mean mass accretion rate per annulus going outwards in steps of $15''$ or 0.3 pc. The results for both the MC and the NC are represented in Fig. 9.5.4. Each annulus was given a number for an easier reference in the text, starting with 1 in the center (see Fig. 9.5.3 and 9.5.4).

With $3.71 \cdot 10^{-8} M_{\odot}\text{yr}^{-1}$ for the MC and $3.51 \cdot 10^{-8} M_{\odot}\text{yr}^{-1}$ for the NC the mass accretion rate for both clumps is the lowest in their respective OB-star-defined center.

Using the MC center as origin for the radial analysis shows an increase of \dot{M} by $\sim 60\%$ to $5.11 \cdot 10^{-8} M_{\odot}\text{yr}^{-1}$ within the inner $30''$ (0.6 pc), going from the first to the second annulus. The first annulus (innermost $15''$ or 0.3 pc) includes 23 of the OB stars, while the second annulus ($15''\text{--}30''$ or 0.3–0.6 pc) includes only 4 OB stars. The larger distance to the OB stars of the second annulus explains the steep increase of the mass accretion rate. Going

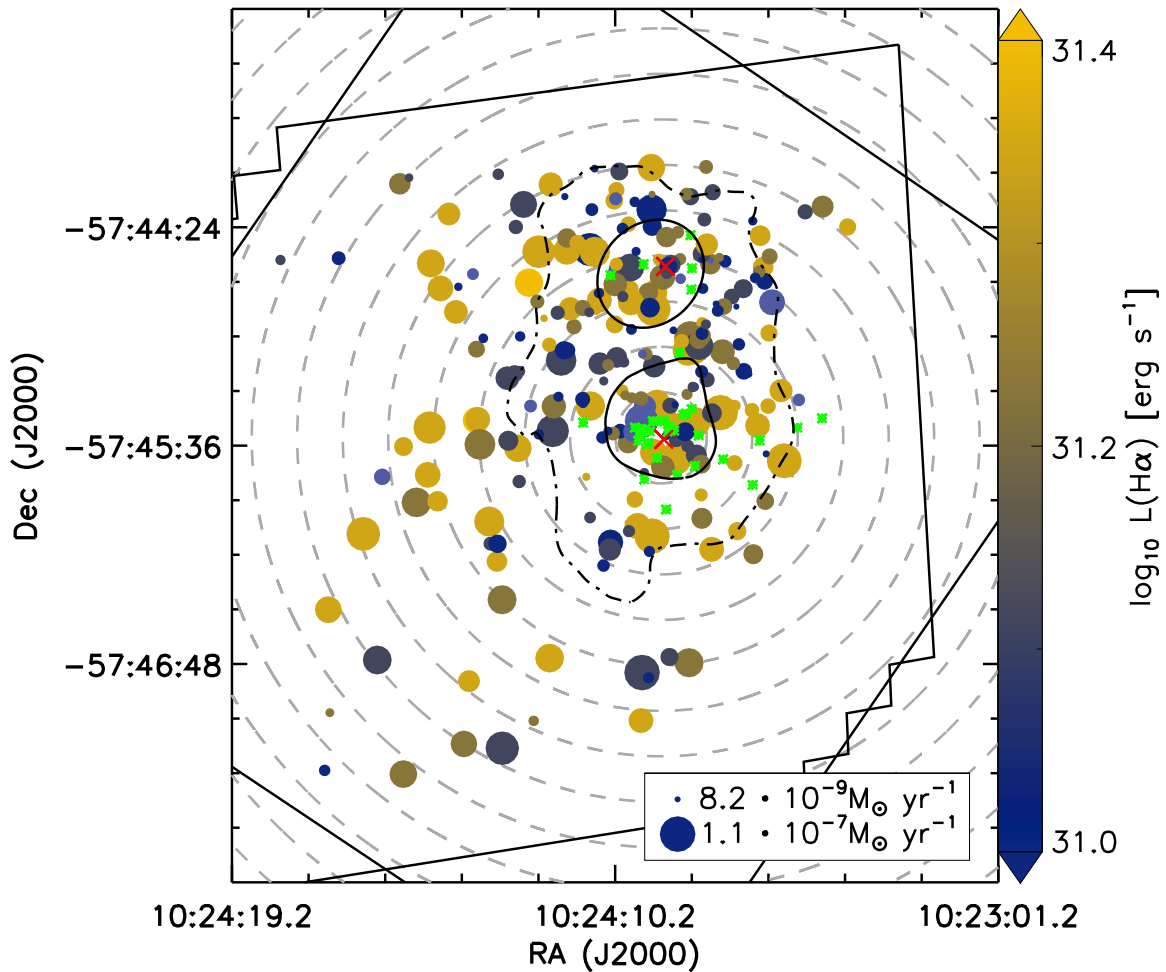


Figure 9.5.3: The 240 $H\alpha$ excess stars are here shown color-coded with their respective $H\alpha$ excess luminosity indicated on the color bar. The sizes of the dots indicate the mass-accretion rate (the larger the dot, the higher the mass-accretion rate). The two solid oval contours mark the MC and the NC while the dash dotted contour marks the overall Wd2 cluster. The gray dashed circles indicate the distance from the MC center in steps of $15''$ or 0.3 pc. The green asterisks mark all known O and B stars while the red crosses mark the geometric center for all known O and B stars within 0.5 pc of the MC and NC, respectively. For orientation purposes, the thick black straight lines mark the outline of the FOV of the survey area.

further outwards to the annuli 3 and 4 ($30''$ – $60''$ or 0.6–1.2 pc), \dot{M} decreases by $\sim 9\%$ to $4.72 \cdot 10^{-8} M_{\odot} \text{yr}^{-1}$. These two annuli contain 9 OB stars, while 4 OB stars are in the NC. These stars probably cause the decrease of the mass accretion rate. In annulus 5 ($60''$ – $75''$ or 1.2–1.5 pc) the mass accretion rate rises to $5.90 \cdot 10^{-8} M_{\odot} \text{yr}^{-1}$. From this point outwards, the OB stars do not affect the mass accretion rate anymore and the fluctuations in \dot{M} are caused by small-number statistics of the $H\alpha$ excess stars (≤ 10). Overall we can see a trend of an increase of the mass accretion rate with increasing distance from the OB stars, indicating that the PMS accretion disks are being rapidly destroyed by the FUV radiation emitted by the OB population.

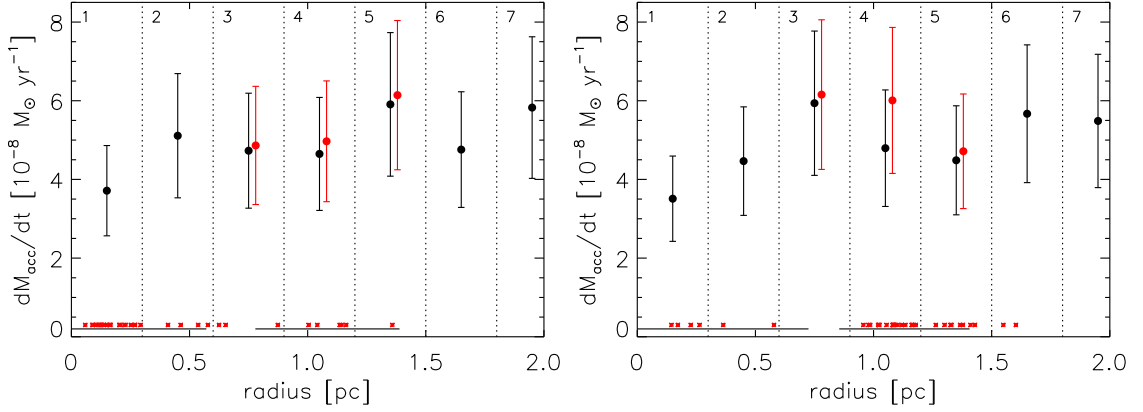


Figure 9.5.4: The mean mass accretion rate as a function of distance from the projected geometric center of the OB stars in the MC and NC going outwards in annuli of $15''$ (0.3 pc). **Left:** The mean mass accretion rate for the MC. **Right:** The mean mass accretion rate for the NC. The two bars at the bottom mark the spatial extent of the MC and NC while all OB stars are represented as red asterisks. The vertical dotted lines indicate the annuli of $15''$, numbered from the center outwards starting with 1. The red points indicate the mass accretion rates in the respective annuli when excluding the MC and NC.

Using the NC center as origin for the radial analysis gives a similar result as for the MC. Going outwards from the center the mass accretion rate increases to $4.47 \cdot 10^{-8} M_{\odot} \text{yr}^{-1}$ in the second annulus and to $5.94 \cdot 10^{-8} M_{\odot} \text{yr}^{-1}$ in the third annulus. This corresponds to an increase of $\sim 68\%$ within the inner $45''$ (0.9 pc). While we have 6 OB stars in the innermost annuli, the number drops to 0 in the third. PMS stars in the third annulus are located in between the two clumps, $\gtrsim 0.5$ pc away from the OB stars, and therefore out of their sphere of influence of 0.1 – 0.5 pc (Clarke 2007). The annuli 4 and 5 ($45''$ – $75''$ or 0.9 – 1.5 pc) cover the area of the MC with a total number of 28 known OB stars. Their FUV radiation makes the mass accretion rate drop by $\sim 20\%$ to $4.79 \cdot 10^{-8} M_{\odot} \text{yr}^{-1}$. From the next annulus outwards ($d \geq 75''$, ≥ 1.5 pc) the mass accretion rate increases to $5.67 \cdot 10^{-8} M_{\odot} \text{yr}^{-1}$. We can thus see the same trend as when are using the MC as center of origin.

With increasing distance from the OB star population, the mass accretion rate increases. This effect is even more pronounced if we exclude the sources with mass accretion of the MC and NC while going outwards from the NC and MC as origin, respectively (see red points in Fig. 9.5.4). For a better overview, we summarized in Tab. 9.5.1 the values for the mass accretion rates for each of the annuli for the respective center of origin (MC and NC).

Despite a few objects in Fig. 9.5.3 showing high $H\alpha$ excess luminosity, which may appear to lie close to OB stars due to the projection of a 3D stellar distribution onto a 2D map, the evolution of the mass accretion rate with distance to the population of luminous OB stars is consistent with theoretical studies (e.g., Clarke 2007) and with the observations made by Anderson et al. (2013) for the Orion Nebula Cluster and De Marchi et al. (2010) in the field around the SN 1987A. With $4.43 \cdot 10^{-8} M_{\odot} \text{yr}^{-1}$ the median mass accretion rate of the PMS stars of Wd2 is 1.5 times higher than in the region surrounding SN 1987A (De Marchi et al. 2010). Taking into account the uncertainties and the younger age of Wd2 the mass accretion

Table 9.5.1. The mean mass-accretion rates

# of annulus	distance to annuli center		\dot{M} [$10^{-8} M_{\odot}\text{yr}^{-1}$]			
	[arcsec]	[pc]	MC	NC	MC	NC
1	0–15	0.0–0.3	3.71	—	3.51	—
2	15–30	0.3–0.6	5.11	—	4.47	—
3	30–45	0.6–0.9	4.72	4.86	5.94	6.16
4	45–60	0.9–1.2	4.64	4.97	4.79	6.01
5	60–75	1.2–1.5	5.90	6.14	4.49	4.72
6	75–90	1.5–1.8	4.76	—	5.67	—
7	90–105	1.8–2.1	5.83	—	5.49	—

Note. — The mean mass accretion rates as a function of distance from the projected geometric center of the OB stars in the MC and NC going outwards in annuli of $15''$ (0.3 pc). Column 1 gives the number for each annulus as used in Fig. 9.5.4. Column 2 and 3 lists the distance of each annulus from the respective centers. Columns 4 and 6 give the mean mass accretion rates in each annulus for the MC and NC, respectively, while Columns 5 and 7 show the mass accretion rate when excluding the MC and NC.

rates are in good agreement with these results. A detailed discussion of the different sources of uncertainties is presented in Sect. 9.7.

9.6 Uncertainties in the $H\alpha$ luminosity and mass accretion rate

To derive and quantify the mass accretion rate and the $H\alpha$ luminosity we compared the observations of our multi-band survey with theoretical models of mass accretion onto T-Tauri stars in combination with empirically derived relations. The resulting mass accretion rates are affected by different kinds of uncertainties:

- The photometric uncertainties (see Sect. 4)
- The uncertainties of the extinction map, used to deredden the photometry (see Sect. 6)
- Uncertainties in the stellar evolution models
- Uncertainty in the adopted stellar abundance
- Uncertainties occurring while fitting the models to the data

Some of these error sources were already briefly discussed in the previous sections. In the following we want to summarize and give an overview of all sources of uncertainties.

9.6.1 Observational uncertainties

To obtain the $H\alpha$ excess emission and the mass accretion rate we used the individually dereddened photometry in the three filters $F555W$, $F814W$, and $F658N$ (see eq. 9.2). This was

achieved using the $E(B - V)$ gas extinction map (see Sect. 6). The observational uncertainties include the combined photometric uncertainties plus the uncertainty originating from the gas extinction map (see eq. 9.2). This gives a total uncertainty of 8.2% for $L(H\alpha)$ or $0.140 \cdot 10^{-8} M_{\odot} \text{yr}^{-1}$ for the mass accretion rate.

Additionally, the N II doublet partially falls into the $F658N$ filter width causing a possible overestimation of the $H\alpha$ flux by 0.59% and 3.1% (see Sect. 9.2).

9.6.2 The locus of the isochrones

The loci of the stars relative to the PARSEC 1.2S isochrones (Bressan et al. 2012) in the $F814W_0$ vs. $(F814W - F160W)_0$ CMD play an important role in defining the stellar and cluster properties.

- 1) The heliocentric distance was determined using the TO region in combination with the results of the spectroscopic analysis of Vargas Álvarez et al. (2013). The uncertainty in the distance $d = 4.16$ kpc between Wd2 and the Sun is $\Delta d = 0.33$ kpc (see Sect. 8.2). This gives a $L(H\alpha)$ uncertainty of 15% (see eq. 9.4).
- 2) The loci of the stars in the CMD define the stellar properties, such as masses, temperatures, bolometric luminosities, and stellar radii. To estimate the possible uncertainties we varied each of the stellar parameters by $\pm 1\%$, $\pm 5\%$, and $\pm 10\%$. This gives overall uncertainties in the mass accretion rate of $\pm 2.7\%$, $\pm 10.9\%$, and $\pm 18.7\%$, respectively.

9.6.3 The stellar metallicity

Based on the hypothesis that Wd2 is a member of the thin disk, we assumed Solar metallicity ($Z = 0.0152$, Caffau et al. 2011). Nevertheless, since we cannot determine the true metallicity of the cluster, we estimate the effects on the mass accretion rate by modifying the metallicity of the stellar evolution models. We varied the assumed metallicity of $Z = 0.0152$ by $\pm 10\%$ (to $Z = 0.0137$ and $Z = 0.0162$) and $\pm 25\%$ (to $Z = 0.0114$ and $Z = 0.019$). Increasing the metallicity by 10% and 25% decreases the mass accretion rate by 4% and 7%, while the decrease of the metallicity by 10% and 25% leads to an increase of the mass accretion rate by 2% and 7%, respectively. Considering the small dependence of the mass accretion rate on metallicity and the fact that the distribution of stars in Wd2 in our CMDs (see Fig. 9.3.1 and Fig. 8.4.1) is best represented by isochrone models of Solar metallicity, supports our assumption of Solar metallicity.

9.6.4 Geometrical alignment

The geometrical orientation of the disks plays an important role for the emitted light that we can detect. Here, we are referring especially to the inclination of a disk relative to the sky plane. Two major cases need to be distinguished:

- 1) A large enough inclination, meaning the orientation is almost edge-on, leads to an obscuration of the star by its surrounding disk. The flux at short (UV, optical, and NIR) wavelengths is blocked by the disk material. Therefore, these objects are not detected in our optical/NIR catalog. Assuming a flared-disk model and comparing with the spectral-energy distribution (SED) modeling of [Chiang and Goldreich \(1999\)](#) this happens at inclination angles $i \gtrsim 55^\circ$. We can conclude that we miss $\sim 40\%$ of the $H\alpha$ excess stars due to this geometrical effect.
- 2) A moderately small inclination ($i \lesssim 55^\circ$, face-on), so the disk does not block the light emitted by the host star. The inclination should play a major role for the shape of the emission lines (e.g., [Muzerolle et al. 2001](#); [Kurosawa et al. 2006](#); [Kurosawa and Romanova 2012](#)) since stellar rotation broadens the emission lines. Comparing this effect with observations ([Appenzeller and Bertout 2013](#)) no significant result has been found yet. Most likely this is because of the the small sample of stars studied so far. [Appenzeller et al. \(2005, observations\)](#) and [Kurosawa et al. \(2006, theory\)](#) found a dependence of the EW on the inclination angle. Using a larger sample of stars, [Appenzeller and Bertout \(2013\)](#) could not find this specific correlation. This leads to the conclusion that, even if there is an effect due to the rotation of the disk of the PMS stars, at the moment there is no way of further quantifying it. The effect on line broadening due to stellar rotation does not play a role for our photometric observations because the broadening is less than the filter width and so the original flux is fully detected.

Because we can only detect disk-accreting PMS stars via the $H\alpha$ excess if the disk is not blocking the light of its central star ([Chiang and Goldreich 1999](#)), the effects on the colors and luminosities of the PMS stars caused by disk obscuration, and a resulting uncertainty in age, are minor.

We should note that some of the ionizing energy may possibly escape without having an effect on the local surrounding gas. This causes an underestimation of the mass accretion rate. This is also the case for all other studies based on hydrogen emission.

Altogether, the different sources of uncertainties are presented in Tab. 9.6.1. They add up to a total uncertainty in the $H\alpha$ luminosity $L(H\alpha) = (1.67 \pm 0.449) \cdot 10^{-31} \text{ erg s}^{-1}$ (26.9%). The total uncertainty on the mass accretion rate (assuming that the stellar parameters are known to a precision of $< 5\%$) amounts to $\Delta \dot{M}_{\text{acc}} = 1.768 \cdot 10^{-8} \text{ M}_\odot \text{ yr}^{-1}$ (39.9%).

9.7 Summary and conclusions

In this Chapter we examined the sources with $H\alpha$ excess emission.

To analyze the PMS population of Wd2 we determined the stellar parameters (T_{eff} , L_{bol} , and M_*) using the PARSEC 1.2S ([Bressan et al. 2012](#)) stellar evolution models. We estimated the ages of the PMS stars using the $F814W_0$ vs. $(F814W - F160W)_0$ CMD in combination with the PARSEC 1.2S isochrones.

Following the method applied in [De Marchi et al. \(2010\)](#) we used the individually extinction-corrected $F555W$, $F814W$, and $F658N$ photometry to select 240 $H\alpha$ excess emission

Table 9.6.1. The sources of uncertainties

Source	Uncert. [%]	$\sigma(\dot{M}_{acc})$ [$10^{-8} M_{\odot} \text{ yr}^{-1}$]	$\sigma(L(\text{H}\alpha))$ [$10^{-31} \text{ erg s}^{-1}$]
Photometry	8.2	0.363	0.136
NII-doublet	3.7	0.164	0.062
Dist. modulus	15	0.665	0.251
Stellar models	11	0.487	—
Metallicity	2	0.089	—
Total	39.9/26.9	1.768	0.449

Note. — The summary of the different sources of uncertainty. The two values of the total uncertainty percentage correspond to the mass accretion rate and to the H α luminosity, respectively.

stars in the RCW 49 region. We used the ATLAS9 model atmospheres (Castelli and Kurucz 2003) and the Stellar Spectral Flux Library by Pickles (1998) to obtain interpolated R -band photometry from the $F555W_0$ and $F814W_0$ filters to get a reference template. Using TCDs we selected all stars as H α excess emission stars that are located at least 5σ above the continuum emission. Additionally, all stars must have an H α emission line $\text{EW} > 10 \text{ \AA}$. A $(F555W - F814W)_0 > 0.2 \text{ mag}$ criterion is used to exclude possible Ae/Be candidates (see Sect. 9.2). This yields 24 Ae/Be candidates (see Sect. 9.4), mainly located in the TO and MS region of the $F814W_0$ vs. $(F814W - F160W)_0$ CMD (see Fig. 8.2.3) and 240 H α excess emission stars with a mean H α luminosity $L(\text{H}\alpha) = (1.67 \pm 0.45) \cdot 10^{-31} \text{ erg s}^{-1}$ and a mass accretion rate of $\dot{M}_{acc} = (4.43 \pm 1.68) \cdot 10^{-8} M_{\odot} \text{ yr}^{-1}$. The mean age is $0.62 \pm 0.57 \text{ Myr}$. The MC and NC host at least 36 and 26 H α excess emission stars, respectively, while the remaining part of Wd2 cluster contains at least 106. The remaining 72 are located in the periphery (see Tab. 8.4.2). The mean mass accretion rate in Wd2 is $\sim 70\%$ higher than in the SN 1987 A field ($\dot{M}_{acc} = 2.6 \cdot 10^{-8} M_{\odot} \text{ yr}^{-1}$, De Marchi et al. 2010), $\sim 77\%$ higher than in NGC 602 ($\sim 2.5 \cdot 10^{-8} M_{\odot} \text{ yr}^{-1}$, De Marchi et al. 2013), and $\sim 14\%$ higher than in NGC 346 ($3.9 \cdot 10^{-8} M_{\odot} \text{ yr}^{-1}$, De Marchi et al. 2011a). With a mean age of $\sim 1 \text{ Myr}$ Wd2 is younger than the PMS populations investigated by the other studies, which explains the higher mass accretion rate. Taking the younger age and the uncertainty range into account, the mass accretion rates determined in this chapter are consistent with the theoretical studies of Hartmann et al. (1998) and the collected data of Calvet et al. (2000) for a number of star-forming regions. Hartmann et al. (1998) showed in their theoretical study of the evolution of viscous disks that the mass accretion rate decreases with increasing age ($\dot{M} \propto t^{-\eta}$). This was confirmed in many observational studies for different regions inside the MW and in nearby galaxies (e.g., Calvet et al. 2000; Sicilia-Aguilar et al. 2006; Fang et al. 2009; De Marchi et al. 2013), yet the slope is poorly constrained. We analyzed our bona-fide sample of 240 mass-accreting stars and determined a decreasing slope of $\eta = 0.44 \pm 0.04$, which is in agreement with other studies, taking into account the large uncertainty.

The FUV flux emitted by the luminous OB stars can lead to a shorter disk lifetime due to erosion (e.g., [Clarke 2007](#)). [Anderson et al. \(2013\)](#) studied the effects of photoevaporation in the close vicinity (0.1–0.5 pc) of OB stars. Most of their disks were completely dispersed within 0.5–3.0 Myr. In our study of Wd2 we used the centers of the MC and NC and calculated the projected geometric center of all known OB stars within 0.5 pc (red crosses in [Fig. 9.5.3](#)). We then calculated the mean mass accretion rate in annuli of 15'' or 0.3 pc going outwards from the respective centers (see [Fig. 9.5.4](#)). The median mass accretion rate in the Wd2 cluster is $4.43 \cdot 10^{-8} M_{\odot} \text{yr}^{-1}$ and thus $\sim 25\text{--}30\%$ higher than in the MC ($3.32 \cdot 10^{-8} M_{\odot} \text{yr}^{-1}$) and NC ($3.12 \cdot 10^{-8} M_{\odot} \text{yr}^{-1}$). With increasing distance from the respective centers of the two density concentrations the mass accretion rate steeply increases by 60% in the MC and 68% in the NC within the innermost 30'' (0.6 pc) and 45'' (0.9 pc), respectively. With an increasing number of OB stars the mass accretion rate drops by 5–22% (see [Fig. 9.5.4](#)). Far away ($\gtrsim 0.5$ pc) from the OB stars the mass accretion rate rises to a peak value of $5.9 \cdot 10^{-8} M_{\odot} \text{yr}^{-1}$. Despite the large uncertainty in the mass accretion rate, the effect of the increased rate of disk destruction is visible. This effect was also seen in other massive star-forming regions, e.g., by [De Marchi et al. \(2010\)](#) for the region around SN 1987 A and by [Stolte et al. \(2004\)](#) for NGC 3603 and supports the theoretical scenario of [Clarke \(2007\)](#) and [Anderson et al. \(2013\)](#).

*Es ist nicht genug, zu wissen, man muss auch anwenden;
es ist nicht genug, zu wollen, man muss auch tun.*

— Johann Wolfgang von Goethe: Wilhelm Meisters
Wanderjahre

10

The present-day stellar mass function of Wd2

This chapter is included in Sect. 5 and Sect. 6 of [Zeidler et al. 2016, AJ, submitted](#).

The only published PDMF of Wd2 was determined by [Ascenso et al. \(2007a\)](#) with ground-based photometry in the NIR (J , H , K_s), who derived a slope of $\Gamma = -1.20 \pm 0.16$. The slope is based on the mass range between 0.8 – $25 M_{\odot}$, representing their completeness limits, for an assumed distance of 2.8 kpc. Using our data we are able to refine the PDMF of Wd2 with a much higher accuracy.

10.1 The stellar masses

To determine the PDMF of Wd2 we need to carefully estimate the masses from the stellar luminosities. For MS stars belonging to single stellar populations this can be done via their locus relative to an isochrone since for MS stars their luminosity is closely correlated with stellar mass. Uncertainties are added by (unknown) stellar rotation and possible binarity and multiplicity. So far we showed that the RCW 49 region mainly consists of PMS stars with an age distribution between 0.1 – 2.0 Myr. However, the locus of the PMS stars in a CMD is not only a function of age, but is also affected by ongoing accretion, presence and viewing angle of protostellar disks, emission lines, etc. To remove the age-dependence of the PMS stars we use evolutionary tracks instead of isochrones. PMS evolutionary tracks have the advantage that they provide us with all the information about the stellar masses relative to their locus in the CMD but are independent of an age-binning, since they follow the evolution of a star with a specific mass on the Hayashi track ([Hayashi 1961](#)).

In order to estimate the stellar masses we determined the locus of each star relative to the evolutionary tracks of [Bressan et al. \(2012\)](#) and [Bressan et al. \(2013\)](#) in combination

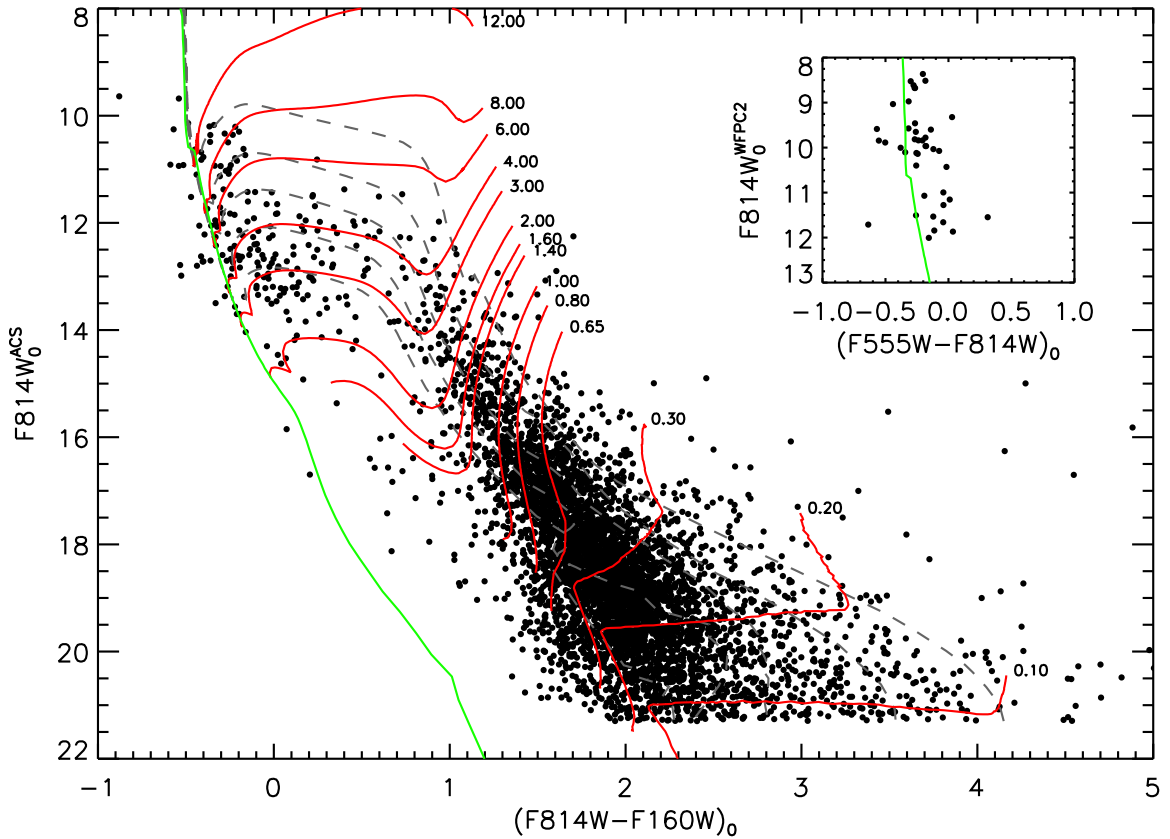


Figure 10.1.1: The $F814W_0$ vs. $(F814W - F160W)_0$ CMD. The evolutionary tracks of [Bressan et al. \(2012\)](#) and [Bressan et al. \(2013\)](#) are traced in red and are labeled with their corresponding masses. The green line represents the ZAMS, inferred from the same models, while the gray dashed lines are the PMS isochrones for 0.1, 0.25, 0.5, 1.0, and 2.0 Myr. Additionally we show in the right top corner the $F814W_0$ vs. $(F555W - F814W)_0$ CMD of the 44 stars added using the WFPC2 photometry from [Vargas Álvarez et al. \(2013\)](#), which includes stars that are saturated in our data.

with the PARSEC 1.2S isochrones. We used mass bins that have a similar distance in $\log(m)$ (see Fig. 10.1.1). We added 44 MS stars from the photometric catalog of [Vargas Álvarez et al. \(2013\)](#) obtained with WFPC2. These are bright MS stars saturated in our observations. Typical uncertainties for stars < 15 mag are < 0.01 mag ([Vargas Álvarez et al. 2013](#)), comparable to the uncertainties of our photometric catalog and so the combination of the two photometric catalogs does not introduce additional uncertainties. A by-eye inspection confirmed that all in our data saturated sources are spatial covered by the ([Vargas Álvarez et al. 2013](#)) photometric catalog. All stellar masses for stars bluer than MS and redder by at most ≤ 0.1 mag than the MS, as well as brighter than $F814W_0 = 14$ mag were determined via their locus relative to the zero-age main sequence (ZAMS) instead of evolutionary tracks, because close to the ZAMS the mass determination via evolutionary tracks is degenerate. In Fig. 10.1.1 we show the cluster members overplotted on the evolutionary tracks (in red) and the ZAMS (in green). In the top right corner we show the CMD for the 44 MS stars added

from the WFPC2 photometry of [Vargas Álvarez et al. \(2013\)](#) as an inset. To determine the masses for the stars with WFPC2 photometry, we used the ZAMS in the WFPC2 photometric system to avoid introducing uncertainties due to different photometric systems.

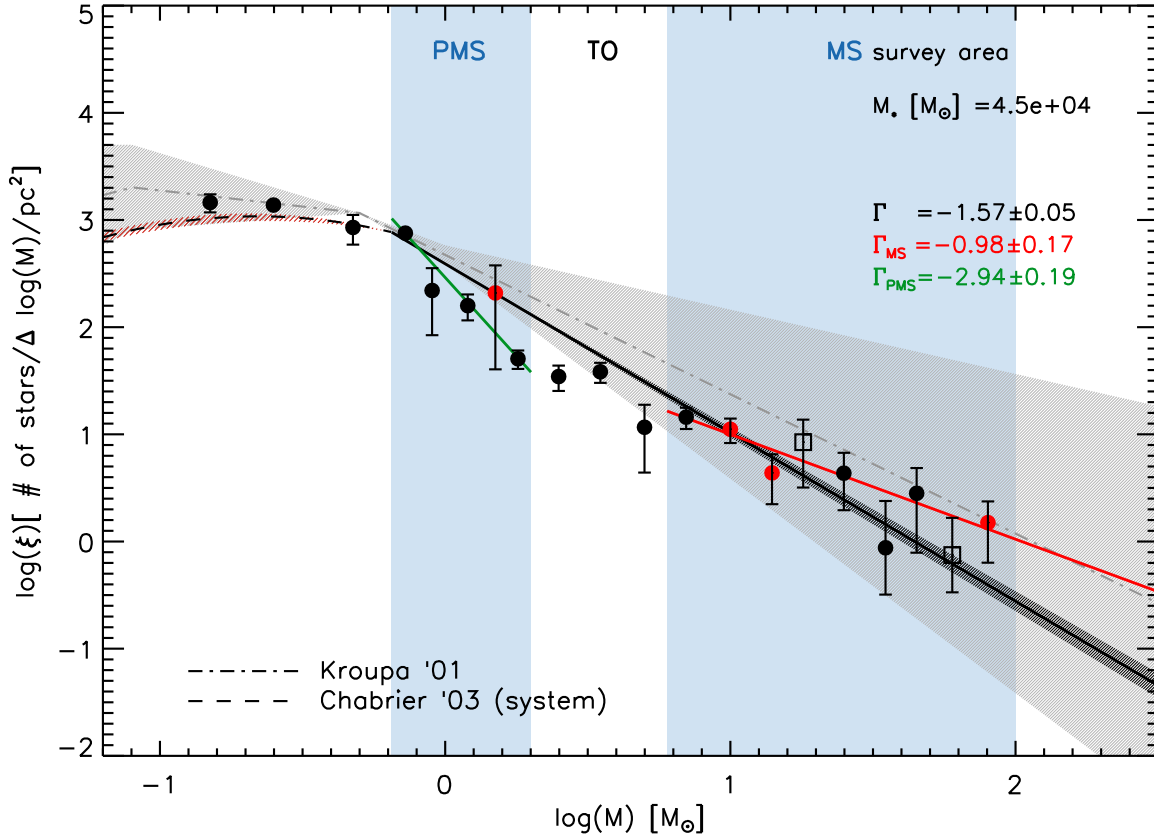


Figure 10.1.2: The PDMF of the full survey area of our HST data. The black filled circles represent the completeness-corrected, normalized number of stars per logarithmic mass bin. The red filled circles stand for those bins for which at least one star’s mass is estimated via orbits of the spectroscopic binary components from the literature. The open squares show the bins where only one filter was not saturated ($F555W$) and the stellar mass is inferred from this magnitude, knowing that it is an MS star. The two blue areas are the regions where the PDMF fit is performed. The black solid line represents the error-weighted fit of the overall PDMF with the uncertainty marked as shaded area. The dash-dotted line is the [Kroupa \(2001\)](#) IMF with the associated uncertainty as gray area. The dashed line is the [Chabrier \(2003b\)](#) IMF with the corresponding uncertainty as reddish area ([Chabrier 2003a](#)) for the low-mass stars. The green and red solid lines indicate the PMS and MS PDMF, respectively.

In order to compute the PDMF of Wd2 we follow the technique presented by [Tarrab \(1982\)](#) and [Massey et al. \(1995\)](#), also adopted by [Sabbi et al. \(2008\)](#) and [Cignoni et al. \(2009\)](#), where stars lying between two evolutionary tracks of different initial mass are assigned to a mass bin. We used the mass bins described above, which were chosen to establish a regular grid in $\log(m)$. The number of stars per mass bin was also corrected for completeness (see Sect. 5). We emphasize here that we corrected each star individually with its specific completeness fraction, depending on its magnitude, color, and position. Some stars

(three for the survey area) are saturated in all but one filter ($F555W$), in both our images and the WFPC2 photometry of Vargas Álvarez et al. (2013). Their spectral types (determined in Rauw et al. 2005, 2007, 2011; Vargas Álvarez et al. 2013) confirm their MS membership and as a result we were able to determine their masses by comparing only the $F555W$ photometry to the ZAMS. For three binary systems, including WR20a (e.g., Bonanos et al. 2004), the orbits of the stellar components are known and the mass determination for the members of these binaries is accurate, so we used these masses (see Tab. 2.2.1).

10.2 The slope of the present-day mass function

The MF is defined as the fractional number of stars per mass interval per unit area. A common parametrization is the one used by Scalo (1986), in the form of $\Gamma = d \log \xi(\log(m)) / d \log(m)$, where m is the stellar mass and $\xi(\log(m))$ the number of stars per logarithmic mass interval. For the Solar neighborhood the slope of the MF is $\Gamma = -1.35$, as derived by Salpeter (1955). In Fig. 10.1.2 we present the MF for the survey area (thick black dots). Mass bins that contain at least one star whose mass is inferred by orbital parameters from spectroscopy are indicated by red filled circles. Mass bins containing stars whose masses are estimated via one filter only are indicated by open squares. There are six objects that were identified spectroscopically as binary candidates but the individual components are unresolved and their masses unknown (see Tab. 2.2.1). To not bias the PDMF with an overestimated mass we decided to exclude these objects. If we treat the photometry of the unresolved binaries in the same way as the remaining single stars, the slope of the mass function changes by 3.1% ($\Delta\Gamma = 0.049$). This shows that excluding these binaries does not significantly affect the PDMF.

To determine the present-day MF (PDMF) we used two regions to fit the slope: the PMS above $0.65 M_{\odot}$ and below $2.0 M_{\odot}$, where the completeness is at least 50% everywhere, and the MS for all stars between $6.0 M_{\odot}$ and $90 M_{\odot}$. Between $2.0 M_{\odot}$ and $6.0 M_{\odot}$ most stars are in the turn-on (TO) region¹ (see Fig. 10.1.1), for which the uncertainties of the stellar evolution models are high, and therefore we excluded this region from the fit. Additionally, all bins containing at least one star for which the mass is estimated via using one filter only are excluded. We used an error-weighted linear fit. For the complete survey area we obtain a PDMF slope of $\Gamma = -1.57 \pm 0.05$. The slope of the MS is $\Gamma_{\text{MS}} = -0.98 \pm 0.17$. The slope based on the PMS is $\Gamma_{\text{PMS}} = -2.94 \pm 0.19$, thus much steeper (see Fig. 10.1.2). The much shallower slope of the PDMF in the MS mass regime as compared to the PDMF computed for the PMS and all stars suggests the existence of mass segregation. We will discuss this in more detail in Sect. 10.5. For the Wd2 cluster (2σ boundary, see Sect. 8.3) we obtain a PDMF slope of $\Gamma = -1.53 \pm 0.05$, which is steeper than the MS slope of $\Gamma_{\text{MS}} = -0.93 \pm 0.17$. The slope based on the PMS is $\Gamma_{\text{PMS}} = -2.89 \pm 0.24$.

¹The turn-on region is transitional region in the CMD, where stars evolve from the PMS onto the ZAMS.

10.3 Uncertainties of the PDMF

To estimate the uncertainties influencing the determination of the PDMF we list the individual sources of uncertainties:

- The photometric errors in each filter, determined via the artificial star tests as described in Sect. 5.4. They affect the luminosity as well as the color of each star and so the stellar mass.
- The uncertainty on the stellar color-excess used to deredden the photometry.
- The uncertainty on the distance to Wd2 of $\delta d = 0.33$ kpc (Vargas Álvarez et al. 2013; Zeidler et al. 2015) resulting in a distance modulus uncertainty of 0.175 mag.
- The statistical uncertainty on the number of stars per mass bin estimated with the Poisson statistics.
- Stellar rotation (although this effect is less severe for low-mass stars, Bastian and de Mink (2009))
- Unresolved binary systems
- High uncertainties of the PMS star masses due to the models

To estimate the uncertainties per mass bin we varied the stellar luminosities according to the uncertainties and estimated the change in the number of stars per mass bin. The photometric uncertainties are more dominant in the low-mass regime, while the statistical sampling (Poisson error) dominates the uncertainties at the high-mass end, where only a few stars are left. For the added binary system components with spectroscopically inferred masses, we used the published mass uncertainties (Vargas Álvarez et al. 2013, and references therein). The total uncertainties are shown by the black error bars in Fig. 10.1.2. The uncertainties propagated to the slope of the PDMF are represented by the gray-shaded area around the PDMF (black solid line).

PMS stellar evolutionary models carry large uncertainties originating from the inaccuracies of the model atmospheres due to necessary simplifications of the physical processes (e.g., Preibisch 2012). Thus mass and age determinations, especially in the low-mass regime for young ages, can come with large uncertainties. Throughout this paper we used the PARSEC 1.2S isochrones and evolutionary tracks (Bressan et al. 2012). This code has the advantage of computing isochrones through the different filter sets of all of the major telescopes, including HST. The MESA Isochrones and Stellar Tracks (MIST, Dotter 2016; Choi et al. 2016) provide similar information. Down to masses of $0.65 M_{\odot}$ the MIST isochrones and evolutionary tracks agree very well with the PARSEC 1.2S ones (see Fig. 10.3.1). Our lower mass limit to determine the PDMF and total masses is $0.65 M_{\odot}$, caused by completeness effects, so these deviations at the low-mass end are minor for our purpose. As one can see in Fig. 10.3.1, the PARSEC 1.2S isochrones follow better our observed low-mass data points, which prompted us to adopt them. Nevertheless, we used the MIST evolutionary track to estimate the model uncertainties. We computed the slope of the mass function and the total mass of the survey area (see next Sect. 10.4) using the MIST model. The slope of the PDMF deviates by $\sim 7\%$, while the total mass deviates by $\sim 17\%$. We introduce these as the model uncertainties.

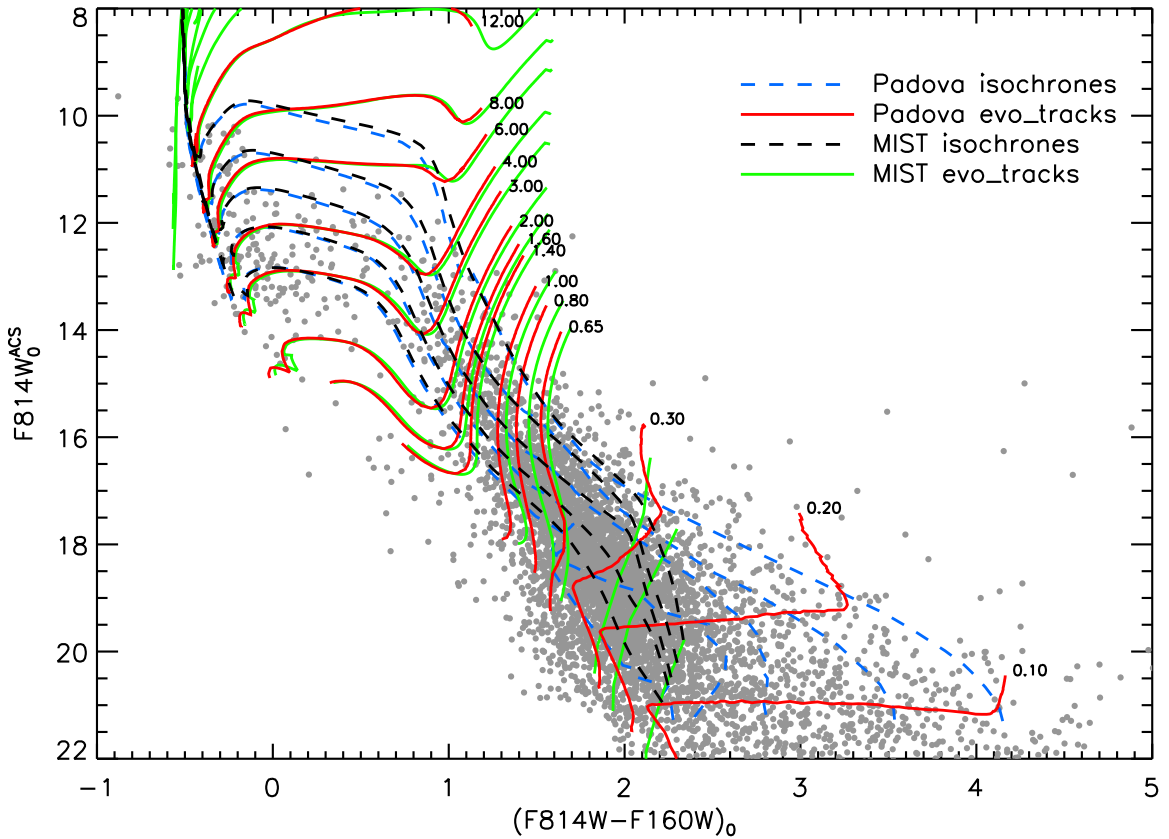


Figure 10.3.1: The $F814W_0$ vs. $(F814W - F160W)_0$ CMD. The Padova PARSEC 1.2S evolutionary tracks are traced in red and are labeled with their corresponding masses, while in green are shown the corresponding MIST evolutionary tracks. The black and blue dashed lines are showing the PMS isochrones for 0.1, 0.25, 0.5, 1.0, and 2.0 Myr.

10.4 The total stellar mass of Wd2

To determine the stellar mass of Wd2 and of the RCW 49 region we separated the stellar distribution into two mass regimes ($M \geq m_{50} = 0.65 M_{\odot}$ and $M < m_{50} = 0.65 M_{\odot}$), where m_{50} is the stellar mass at the 50% completeness limit for a 1 Myr old star. For the mass range above the 50% completeness limit the total mass is calculated by simply summing up the completeness-corrected numbers multiplied by the masses $m_{\text{tot}} = \sum m_i \cdot n_i$. To estimate the integrated stellar mass below the 50% completeness limit we used the [Chabrier \(2003b\)](#) IMF (for unresolved binaries, see Fig. 10.1.2) in the following form:

Table 10.4.1. The integrated stellar masses

Region	$m > m_{50}$ [$10^4 M_{\odot}$]	$m < m_{50}$ [$10^4 M_{\odot}$]	m_{tot} [$10^4 M_{\odot}$]
Survey area	0.5 ± 0.2	3.9 ± 0.1	4.5 ± 0.3
MC	0.3 ± 0.2	2.0 ± 0.1	2.3 ± 0.2
NC	0.03 ± 0.02	0.2 ± 0.01	0.3 ± 0.02
Wd2	0.4 ± 0.2	3.1 ± 0.1	3.6 ± 0.3
Periphery	0.1 ± 0.04	0.4 ± 0.01	0.4 ± 0.04

Note. — The integrated stellar masses of the different regions of Wd2. Wd2 is the region within the 2σ boundary of the surface density fit (see Sect. 8.3) and periphery is the area outside the same boundary. Column 1 shows the different regions as dedicated in Fig. 10.5.1. Column 2 gives the total mass for $m > m_{50}$ determined from the observations. Column 3 gives the total mass for $m < m_{50}$ estimated via the integrated Chabrier (2003b) MF (eq. 10.1). Column 4 lists the inferred total stellar mass of the system.

$$\xi(\log m) = 0.086 \cdot \exp\left(-\frac{(\log m - \log 0.22)^2}{2 \cdot 0.57^2}\right), \quad (10.1)$$

for $m < 0.65 M_{\odot}$,

$$\xi(m) = c \cdot m^{\alpha}, \quad (10.2)$$

for $0.65 M_{\odot} < m$.

The breaking point (where $\xi(m)$ does not follow a power law anymore, Chabrier 2003a,b) is defined at $m = 1 M_{\odot}$ based on empirical fits to observation. To better fit our data, we use as breaking point $m_{50} = 0.65 M_{\odot}$. The normalization is done at the breaking point. The normalization was calculated to fit the slope of the high-mass PDMF determined in the previous section (see Sect. 10.2 and black solid line in Fig. 10.1.2).

To determine the total stellar mass below $M = m_{50}$, we integrated eq. 10.1. For the survey area we determine a total stellar mass of $M_{tot} = (4.5 \pm 0.3) \cdot 10^4 M_{\odot}$, while the Wd2 cluster mass is estimated to be $M_{Wd2} = (3.6 \pm 0.3) \cdot 10^4 M_{\odot}$. In Tab. 10.4.1 we list all masses of the different subregions (as described in Sect. 8.3). Neglecting the unresolved massive binaries causes an additional total mass uncertainty of $\Delta M_{tot} = 199 M_{\odot}$.

Our inferred total stellar mass of $M_{Wd2} = (3.6 \pm 0.3) \cdot 10^4 M_{\odot}$ is in good agreement with the only mass estimate done so far by Ascenso et al. (2007a) who derived a lower limit of $m \geq 10^4 M_{\odot}$. Our estimate shows that Wd2 is $\sim 75\%$ as massive as the most massive young star cluster in the MW, Wd1 ($M_{Wd1} = 4.91_{-0.49}^{+1.79} \cdot 10^4 M_{\odot}$, Gennaro et al. 2011).

10.5 Mass segregation in Wd2

To investigate whether mass segregation has already taken place in the Wd2 cluster we analyze the slope of the PDMF in relation to the distance from the cluster center. As described in Sect. 8.3 Wd2 is characterized by a double-peaked, elliptical stellar distribution, thus the usual approach of determining the slope of the PDMF in annuli around the cluster center (e.g., Sagar et al. 1988; Sabbi et al. 2008; Parker and Goodwin 2015) is not applicable. Instead we chose to use elliptically shaped areas. We defined the midpoint (R.A. = $10^{\text{h}}24^{\text{m}}01^{\text{s}}.94$ and decl. = $-57^{\circ}45'06.7''$) between the centers of the two clumps as the center of the ellipses. To avoid confusion we will call this center “midpoint”. As the innermost region we used the MC with its peak coordinates as origin (red contour in Fig. 10.5.1). We also tried to use the NC but the lower number of stars, especially the low number of high-mass MS stars made it impossible to determine a slope for the MF defined by PMS and MS stars. The next further outwards region is called “annulus 1” (green contour in Fig. 10.5.1) encircling both clumps (MC and NC), but we need to note here that this area excludes the MC and NC stars. The next two annuli (“annulus 2” and “annulus 3”) are shown in yellow and purple contours, while the remaining region around the second annulus we call “outskirts”. So in total we divided the survey area in 5 regions from the midpoint outwards.

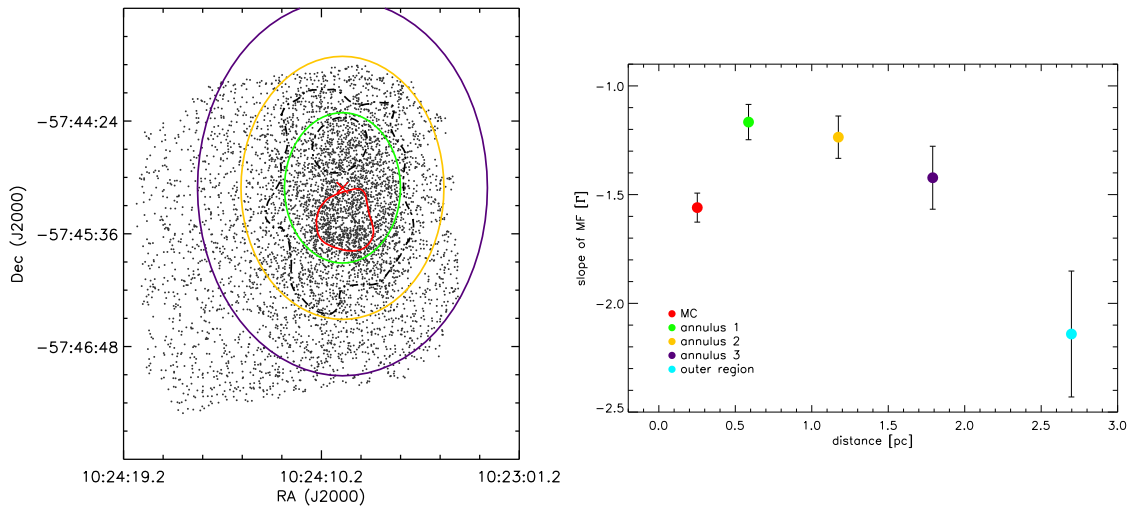


Figure 10.5.1: **Left:** The different areas used to analyze the mass segregation of Wd2. The midpoint is indicated by the red cross. The different areas are named (from the center outwards) : Wd2, annulus 1, annulus 2, annulus 3, outskirts. The NC and the 2σ contours are plotted as reference (dashed contours). **Right:** The slope of the MF for the different regions, plotted against the distance from the center (see Tab. 10.5.1).

We determined the PDMF for each of the different areas. In Tab. 10.5.1 we list the mean stellar distance for each of the individual regions to the midpoint and the PDMF slope. In Fig. 10.5.1 we show the change of the PDMF slope with increasing radial distance from the midpoint. A steeper slope implies many more low-mass stars than high-mass stars. In Fig. 10.5.2 we show the PDMF of each of the individual annuli including the survey area PDMF as a direct comparison.

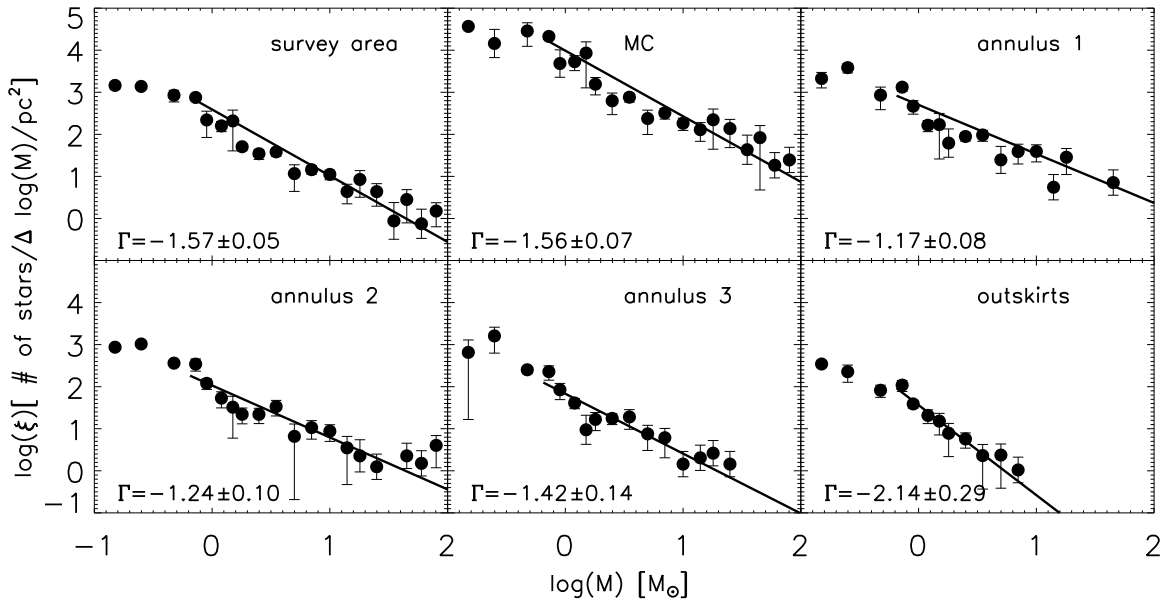


Figure 10.5.2: The PDMFs for the different annuli used to analyze the mass segregation. As comparison we also show the PDMF of the survey area. Each panel shows the completeness-corrected, normalized number of stars per logarithmic mass bin. The two blue areas are the regions where the PDMF fit is performed. The black solid line represents the error-weighted fit of the overall PDMF. In each panel the slope including its uncertainty is printed.

As one can see in Fig. 10.5.1 and Tab. 10.5.1, the slope of the MF gets gradually steeper while moving outwards, away from the cluster center. This means that in the cluster center, there are more massive stars in relation to the lower-mass stars. This implies mass segregation in the cluster center, as is seen in many young massive star clusters like NGC 3603 (Pang et al. 2013) or NGC 346 (Sabbi et al. 2008).

It is still a matter of debate whether mass segregation in such young clusters is primordial, meaning that the more massive stars formed originally in the central regions of the cluster, or whether it is dynamical, implying that they formed equally throughout the region and moved inwards due to interactions with the numerous low-mass stars. To evaluate which of the two scenarios is more probable, we will compare the mass segregation time scale with the mean age of the cluster of ~ 1 Myr.

The mass segregation time scale, t_{msg} , is defined by:

$$t_{\text{msg}} = 2 \cdot t_{\text{relax}} \cdot \frac{m_{\text{av}}}{m_{\text{max}}}, \quad (10.3)$$

where t_{relax} is the relaxation time of the cluster (Spitzer 1969), m_{av} the average stellar mass and m_{max} the mass of the most massive star in the cluster (Kroupa 2004).

Table 10.5.1. The slope of the MF relative to the cluster center

region	mean dist. [pc]	Γ
MC	0.25 ^a	-1.56 ± 0.07
annulus 1	0.59	-1.17 ± 0.08
annulus 2	1.17	-1.24 ± 0.10
annulus 3	1.79	-1.42 ± 0.14
ouskirts	2.70	-2.14 ± 0.29

Note. — The slopes of the MF for the different regions with increasing distance to the midpoint. In column 2 we give the mean distance from the midpoint. Column 3 shows the slope of the MF including the combined observational uncertainties.

^aThe mean distance to the MC peak position

The relaxation time t_{relax} depends on the crossing time:

$$t_{\text{relax}} = \frac{N}{8 \ln N} \cdot t_{\text{cross}}, \quad (10.4)$$

where t_{cross} is the crossing time and N the number of stars in the cluster (e.g., [Binney and Tremaine 1987](#)) with $t_{\text{cross}} = 2 \cdot r^{3/2} \cdot (GM)^{-1/2}$. Here, G is the gravitational constant and r and M are the total radius and mass of the cluster, respectively.

To estimate the mass-segregation time scale we used all stars enclosed by the annulus 2 (enclosing the Wd2 cluster; see Fig. 10.5.1). We calculated an approximate crossing time of $t_{\text{cross}} \approx 1$ Myr using a radius of ~ 2 pc. Combining eq. 10.3 and eq. 10.4 and setting $m_{\text{max}} = 80 M_{\odot}$ based on the most massive star known in Wd2, we find a mass segregation time scale of $t_{\text{msg}} \geq 3$ Myr, which is at least three times the mean age of the cluster. This time-scale estimate is a lower limit to the true time scale for mass segregation, since we have not corrected for unresolved binaries, which would increase the number of stars and, as a result, the relaxation time (compare with eq. 10.4). We can therefore conclude that the mass segregation is, most likely, primordial. We will discuss this in detail in the next Section.

10.6 Discussion and Conclusions

In this chapter we derived and analyzed the PDMF throughout the cluster area. Combining the determined PDMF with a [Chabrier \(2003b\)](#) IMF to fit the low-mass and brown-dwarf regime, we were able to estimate the integrated stellar mass of the Wd2 cluster.

Based on the artificial star tests we carried out a detailed analysis of the PDMF of the Wd2 cluster region. Only one PDMF has been published for Wd2 before by [Ascenso et al. \(2007a\)](#), using ground-based photometry in the NIR (J , H , K_s). The [Ascenso et al. \(2007a\)](#) PDMF is

based on a mass range of $0.8\text{--}25 M_{\odot}$, representing their completeness limits (detection and saturation limits). They used a distance of 2.8 kpc for Wd2 leading to an underestimation of the stellar masses as compared to our study. Because of the larger wavelength coverage of our data we can better separate the foreground population from the cluster population and due to the higher depth we cover a larger mass range, leading to a better determined PDMF.

We used the photometric catalog of [Vargas Álvarez et al. \(2013\)](#), obtained with WFPC2, and spectroscopic data of [Rauw et al. \(2005, 2007, 2011\)](#) and [Vargas Álvarez et al. \(2013\)](#) to complement our photometric catalog (Paper I) at the high-mass end with the most luminous stars that are saturated in our data. Using the PARSEC 1.2S isochrones and evolutionary tracks of [Bressan et al. \(2012\)](#) and [Bressan et al. \(2013\)](#) we estimated masses for all of our cluster members. Binning these stellar masses and correcting the number of stars in each mass bin by the corresponding completeness, we were able to estimate a slope of $\Gamma = -1.57 \pm 0.05$ for the PDMF of the survey area (see Fig. 10.1.2). For the Wd2 cluster we estimated a slope of $\Gamma = -1.53 \pm 0.05$. This slope is slightly steeper than the canonical [Salpeter \(1955\)](#) slope of $\Gamma = -1.35$ or [Kroupa \(2001\)](#) slope of $\Gamma = -1.3 \pm 0.3$ but agrees well within the uncertainties. The slope is also steeper than the slope derived by [Ascenso et al. \(2007a\)](#) of $\Gamma = -1.2 \pm 0.16$, based on NIR photometry. Within the uncertainties, the MS slope of $\Gamma_{\text{MS}} = -0.93 \pm 0.17$ agrees well with the slope derived by [Ascenso et al. \(2007a\)](#).

The PDMF of Wd2 also agree very well with other young massive clusters, such as Westerlund 1, the most massive young Galactic star cluster ($m > 4.91^{+1.79}_{-0.49} \cdot 10^4 M_{\odot}$) with an age of ~ 4 Myr. [Gennaro et al. \(2011\)](#), and references therein) determined a slope of $\Gamma = -1.44^{+0.56}_{-0.08}$ (for stars with $m > 3.5 M_{\odot}$). [Cignoni et al. \(2009\)](#) estimated a slope of $\Gamma = -1.25 \pm 0.22$ for NGC 602 (mass range: $0.7\text{--}30 M_{\odot}$, age: ~ 5 Myr) and [Sabbi et al. \(2008\)](#) a slope of $\Gamma = -1.87 \pm 0.41$ for NGC 346 ($8\text{--}60 M_{\odot}$, age: ~ 3 Myr), both located in the SMC.

[Weisz et al. \(2015\)](#) studied the MFs of 85 resolved, young ($4 \text{ Myr} < t < 25 \text{ Myr}$) star clusters ($10^3\text{--}10^4 M_{\odot}$) in M31 as part of the Panchromatic Hubble Andromeda Treasury program (PHAT, [Dalcanton et al. 2012](#)) and found a quite universal slope of $\Gamma = -1.45^{+0.03}_{-0.06}$ with little variance for stellar masses $> 1 M_{\odot}$. [Weisz et al. \(2015\)](#) reanalyzed also data collected by [Massey \(2003\)](#) for MW and LMC clusters finding slopes of $\Gamma_{\text{MW}} = -1.16$ and $\Gamma_{\text{LMC}} = -1.29$ both with a scatter of $\sigma \sim 0.3\text{--}0.4$, in agreement with other MW studies and our result for Wd2. Although most of these studies are in mass ranges excluding the PMS stars our results are still comparable because the slopes of the PDMFs of the Wd2 cluster derived in this study for the MS and the MS+PMS ($\Gamma_{\text{MS}} = -0.93 \pm 0.17$ and $\Gamma = -1.53 \pm 0.05$, respectively) are, within the uncertainties, in good agreement.

The most massive star WR20a is located outside the cluster center (see Sect. 2.2.3) yet if we look at the mass function of the survey area (see Fig. 10.1.2, the two components of WR20a are located in the last mass bin) it fits the PDMF slope, supporting the membership of WR20a to the Wd2 cluster.

When we subdivide the survey area into elliptical annuli, outwards from the midpoint, defined as the mean distance between the MC and NC and determine the MF for each of the rings, a steepening of the MF slope with increasing distance from the midpoint can be observed (see Fig. 10.5.1 and Tab. 10.5.1). This is a clear indication of a mass-segregated clus-

ter population, which is similarly observed in other young massive clusters such as NGC 3603 (Pang et al. 2013) and the Arches cluster (Stolte et al. 2002) in the MW or NGC 346 (Sabbi et al. 2008) in the SMC.

To answer the question whether the mass segregation is, due to the young age of Wd2, primordial or whether it is caused by two-body relaxation we compared the mean cluster age of 1 Myr with an estimate of the mass segregation time scale (t_{msg}). The mass segregation timescale t_{msg} was estimated using eq. 10.3 with the size of the cluster, its mean stellar mass estimated using the PDMF, and the most massive star detected in Wd2. The estimated lower limit of the mass segregation time scale of 3 Myr indicates that the mass segregation is largely primordial (e.g., Bonnell and Bate 2006) and not caused by an inward migration of massive stars due to interactions with the large low-mass star population.

Primordial mass segregation is also supported by the work of Haghi et al. (2015) on N-body simulations of star clusters. They argue that primordial mass segregation and mass segregation due to dynamical evolution influence the shape of the PDMF slope in the low-mass regime ($m \leq 0.5 M_{\odot}$) differently. In their simulations Haghi et al. (2015) see a significant flattening of the mass function in the low-mass regime similar to what we detect (see Fig. 10.1.2), yet the very low completeness of our data in the center of the two clumps (MC and NC) due to crowding (see Sect. 5) makes it hard to obtain reliable results.

On the other hand e.g., McMillan et al. (2007) and Moeckel and Bonnell (2009) argue that the process of merging subclusters keeps the mass segregation imprint of these individual subclusters. We tried to determine the degree of mass segregation by using elliptical annuli around the center of each of the clumps. Due to the low number of stars we could not determine a statistically significant result. Because of the smaller size and lower mass of the subclusters it is difficult to determine whether the mass segregation in each individual clump is primordial or caused by relaxation. The mass segregation time scale of subclusters is much shorter than the one for Wd2 ($t_{\text{msg}}^{\text{MC}} \approx 0.1 \text{ Myr}$ and $t_{\text{msg}}^{\text{NC}} \approx 0.1 \text{ Myr}$). The results of McMillan et al. (2007) and Moeckel and Bonnell (2009) led to the conclusion that due to the clumpiness of the stellar distribution in Wd2 it is difficult to determine if the mass segregation is primordial or caused by interactions.

To complicate things even further, Allison et al. (2010) argued that mass segregation can be introduced dynamically through violent relaxation much more rapidly than through two-body relaxation. Taking into account all these different scenarios, the origin of mass segregation in Wd2 is most likely a combination of different mechanisms (see also Moeckel and Bonnell (2009)). Nevertheless, due to the cluster's very young age and high degree of mass segregation, we favor the scenario of primordial mass segregation to be the main cause of the observed mass segregation in Wd2.

Adopting the Chabrier (2003b) IMF (see eq. 10.1) for the low-mass regime, where the completeness limits drop below 50%, we estimate a total stellar mass for the Wd2 cluster of $(3.6 \pm 0.3) \cdot 10^4 M_{\odot}$, which is in good agreement with the first estimate of Ascenso et al. (2007a) of $M \geq 10^4 M_{\odot}$. With this mass Wd2 has about 75% of the stellar mass of Wd1 (Gennaro et al. 2011), the most massive star cluster in the MW. This would make Wd2 the second most massive YMC in the MW.

11

Summary and future plans

11.1 Summary and Conclusions

In my thesis, I have presented a multi-band survey with the HST of the young massive star cluster Westerlund 2. In this Chapter, I briefly summarize the most important results of this project. Much more detailed discussions of the results are presented at the end of each Chapter (see Sect. 6.2, 8.5, 9.7, and 10.6). Most of the analysis and results are included in [Zeidler et al. \(2015, 2016a\)](#), and [Zeidler et al. \(2016b\)](#).

Wd2 is one of the most massive YMCs known in the MW, embedded in the giant HII region RCW 49 and located in the Carina-Sagittarius spiral arm at a distance of ~ 4.16 kpc with an age of 0.5–2 Myr (see Sect. 8.2.3). The estimated stellar mass amounts to $3.6 \pm 0.3 \cdot 10^4 M_{\odot}$ (see Sect. 10) with an associated HII region gas mass estimated to be $\sim 10^5 M_{\odot}$ ([Dame 2007](#); [Furukawa et al. 2009](#)). [Moffat et al. \(1991a\)](#) suggested a minimum of 80 O-type stars of which 37 have been spectroscopically confirmed (spectral types up to O3V, [Rauw et al. 2007, 2011](#); [Vargas Álvarez et al. 2013](#)). Due its close proximity, high mass, and its young age, Wd2 is a perfect target to study YMCs and their emergence from their native molecular cloud.

For the last three years I have been studying the young massive star cluster Wd2 ([West-erlund 1961](#)) using a multi-band survey (ID: 13038, PI.: A. Nota) with the *Hubble* Space Telescope. The Wd2 cluster and its surrounding gas cloud RCW 49 ([Rodgers et al. 1960](#)) were observed in six filters: the $F555W$, $F658N$, and $F814W$ in the optical, obtained with the Advanced Camera for Surveys ([Ubeda et al. 2012](#)), and $F125W$, $F128N$, and $F160W$ in the near-infrared with the Wide Field Camera 3 in the IR channel ([Dressel 2012](#)). The two narrow-band filters $F658N$ and $F128N$ are centered on the $H\alpha$ and $Pa\beta$ line emission,

respectively. A total area of $\sim 5' \times 5'$ was mapped. A catalog containing 17121 point sources was created, using the photometric routine Dolphot (Dolphin 2000), with a detection limit of $0.1 M_{\odot}$. 2236 of these point sources were detected in all six filters while 3038 were detected in all four wide-band filters. The color composite image of the Wd2 cluster and its immediate surroundings was chosen to be the 25th anniversary image of the HST (see Fig. 2.2.1).

Giving the dominating presence of the gas and dust, it is absolutely essential to deredden the stellar photometry, dependent on the individual location in the cluster region. We derived a high-resolution pixel-to-pixel $E(B - V)$ extinction map of the gas using the $F658N$ and $F128N$ narrow-band filters. In combination with the spectroscopic information of various OB stars in the cluster we were able to translate the gas extinction to a stellar extinction (median: $E(B - V)_{\star} = 1.56$ mag). In combination with various color-magnitude diagrams, we determined a total-to-selective extinction of $R_V = 3.95$.

We identified and studied 240 bona-fide PMS $H\alpha$ emitters using stellar $H\alpha$ excess emission, which is a very distinct emission feature of PMS stars. We adopted the method, proposed by De Marchi et al. (2010) to combine the $F555W$ and $F814W$ broad-band filters to determine the continuum emission (R -band) in combination with the $H\alpha$ filter, to identify PMS stars with disk accretion. Additionally, 24 Ae/Be candidates were identified. The mean $H\alpha$ luminosity of these 240 PMS $H\alpha$ emitters is $L(H\alpha) = 1.67 \cdot 10^{-31} \text{ erg s}^{-1}$. We estimated the stellar parameters of these 240 PMS $H\alpha$ emitters, using the PARSEC 1.2S isochrones (Bressan et al. 2012) to translate the $H\alpha$ luminosity to a mass accretion rate (Dahm 2008). The mean mass accretion rate is $\dot{M} = 4.43 \cdot 10^{-8} M_{\odot} \text{ yr}^{-1}$. We showed that the mass accretion rate is decreasing with increasing stellar age as predicted by the viscous disk evolution model by Hartmann et al. (1998). Despite large uncertainties originating in the accretion models, we furthermore demonstrated that the mass accretion rate is lowest in the cluster center in close proximity to the numerous O and B stars. These luminous stars are the origin of far-ultraviolet radiation that leads to an accelerated disk dispersal within the inner ~ 0.5 pc (Clarke 2007) around these stars. Within the inner 1.5 pc from the cluster center, the mass accretion rate increases by $\sim 60\%$. The same trend was also observed in other regions, such as the Orion Nebula Cluster (Anderson et al. 2013) or in the region surrounding SN 1987A (De Marchi et al. 2010).

Due to the dense stellar population and the crowding it is necessary to correct for completeness effects to properly analyze the stellar population properties and spatial distribution. Therefore, we performed artificial star tests for all four broad-band filters. A grid of $5 \cdot 10^6$ stars was used per filter to properly cover the complete survey area, as well as the possible magnitude and color space of all cluster stars. The artificial star tests were carried out with Dolphot, in the same setup as adopted for the original photometry. Throughout the survey area, the catalog is 50% complete down to $0.65 M_{\odot}$. We created 2D completeness maps to correct each star individually for its completeness fraction, depending on the spatial position, the magnitude, and the color (for the selected filter combination.)

Fitting a combination of two 2D Gaussians to the stellar distribution (down to $0.65 M_{\odot}$) revealed that Wd2 is composed of two sub-clusters as was already suggested by Hur et al. (2015). The two concentrations are named the “main cluster of Wd2” (MC) and the “north-

ern clump” (NC). We defined the sizes of the two clumps as the 1σ contour of the Gaussian density distributions and the area of the Wd2 cluster as the 2σ contour. This led to sizes of 0.31 arcmin^2 (0.44 pc^2) for the MC and 0.27 arcmin^2 (0.38 pc^2) for the NC. Due to the similar age of Wd2 and NGC 3603 and the existence of two coeval sub-clusters that fit well the properties of the simulations in [Banerjee and Kroupa \(2015\)](#) a monolithic formation from sub-clusters is a likely scenario for the formation of Wd2.

The position-dependent completeness corrections allowed us to study the PDMF in great detail down to a lower mass limit of $0.65 M_{\odot}$. For the Wd2 cluster we determined a steeper slope ($\Gamma = -1.53 \pm 0.05$) than the ordinary [Salpeter \(1955\)](#) slope ($\Gamma = -1.35$), which is also observed in other YMCs such as Westerlund 1 ($\Gamma = -1.44^{+0.56}_{-0.08}$, for stars with $m > 3.5 M_{\odot}$, [Gennaro et al. 2011](#)) or NGC 346 ($\Gamma = -1.87 \pm 0.41$, mass range: 8–60 M_{\odot} , age: $\sim 3 \text{ Myr}$, [Sabbi et al. 2008](#)). Adopting a [Chabrier \(2003b\)](#) initial mass function to estimate the total mass in the low-mass ($< 0.65 M_{\odot}$) stellar and brown dwarf regime, we determined a total stellar mass of $(3.6 \pm 0.3) \cdot 10^4 M_{\odot}$ for the Wd2 cluster.

Studying the PDMF in increasing elliptical annuli around the cluster center revealed a steepening of the PDMF’s slope, leading to the conclusion that mass segregation is present. Comparing the mass segregation time scale with the cluster age indicates that the mass segregation is most likely primordial and could not have formed via inward migration of the massive stars due to interactions with the large number of low-mass stars. Due to its young age Wd2 is very close to its initial conditions so its PDMF well approximates the cluster initial mass function.

The presence of a faint, uniformly distributed low-mass population ($< 0.15 M_{\odot}$), visible throughout the RCW 49 area, implies that the actual star-forming region is more extended than the Wd2 cluster. This phenomenon was already observed by [Whitney et al. \(2004\)](#), who identified ~ 300 cYSOs in the giant H II region of RCW 49 using *Spitzer* IRAC MIR data of the GLIMPSE survey ([Benjamin et al. 2003](#)). [Whitney et al. \(2004\)](#) identified 5 more star-forming sites throughout the RCW 49 cloud. Similar findings exist also in other giant H II regions e.g., NGC 3603, the Orion Nebular Cloud (e.g., [Hillenbrand 1997](#)), or the 30 Doradus region (e.g., [Walborn et al. 1999](#); [Brandner et al. 2001](#)).

The properties determined in this work place Wd2 in the short list of YMCs in the MW. The determined mass makes Wd2 the second most massive YMC in the MW and an interesting and important target to study the early phases of star cluster evolutions. The fact that there has not been found any hint for a supernova explosion makes Wd2 the perfect target to study such a massive cluster in a state, where it has not yet been altered by any such destructive event. Therefore, it is possible to study the PDMF very close to the IMF only influenced by the feedback originated from the large population of massive OB stars.

11.2 Future Work

The extensive work on Wd2 using the multi-band survey observed with the HST has revealed many new insights and interesting results on the population and history of the YMC Wd2.

First, little is still known about the 3D structure and dynamics of Wd2. We only see Wd2 in projection. Therefore, information such as the relative location of the gas and the stars, radial velocities and proper motions are unknown.

Recent observations with the Very Large Telescope's (VLT's) integrated field unit (IFU) MUSE (Multi Unit Spectroscopy Explorer, [Bacon et al. 2010](#)) of the gas component in the vicinity of YMCs have proven very successful in characterizing the physical properties and kinematics of the neutral and ionized gas ([McLeod et al. 2015, 2016](#)). With such observations, it is possible to probe the feedback of massive cluster members on the surrounding gas by measuring the photo-evaporation rate of the molecular cloud structures and pillars, detecting the expanding wind bubbles, and analyzing outflows from a new generation of stars currently forming in the vicinity of the ionizing stars. In addition to the studies of the gas, [Kamann et al. \(2013\)](#) showed in their study of simulated MUSE data, that ~ 5000 useful stellar spectra per arcmin² can be obtained. The expected limit will be ~ 9000 stars arcmin² or ~ 2.5 stars arcsec² with a seeing of $0.8''$. In a recent study of the ultra-faint stellar system Crater, [Voggel et al. \(2016\)](#) showed that this approach is indeed achievable. They reached a radial velocity precision of 2.27 km s^{-1} per object, fitting multiple spectral lines using HST astrometry for the source detection. [Kamann et al. \(2016\)](#) extracted spectra for more than 12000 stars for the Globular Cluster NGC 6397, and despite the limited spectral resolution ($R \approx 1800$ (480 nm)– $R \approx 3500$ (930 nm)) of MUSE, they reached an overall accuracy of 1 km s^{-1} .

I am currently leading a successful VLT/MUSE proposal (ESO ID: 097.C-0044, PI: P. Zeidler) to map the complete Wd2 cluster and parts of the surrounding gas and dust cloud. We are mapping the Wd2 cluster with two different exposure times to cover the gas and the bright OB stars, as well as the low-mass PMS stellar population in the vicinity of the central cluster. Parts of these data have already been observed. In Fig. 11.2.1 we show a color-composite image of the observed (2×3 tiles) mosaic. The colors represent S II (6717\AA) (red), H α (green), and blue: O III (5007\AA) (blue).

Additionally to the MUSE data, we have also obtained a 2nd epoch of HST observations of Wd2. These data, together with another 3 years of approved HST observations, to measure the internal motions with a 1 km s^{-1} accuracy, will allow us to determine proper motions, radial velocities, and a clean membership catalog, in other words to reconstruct the 3D dynamics of the stars and possibly the gas. For the most luminous stars this information can then be compared to the latest Gaia data release. We will study, for the first time, the 3D kinematics and evolution (past and future) of a YMC and hope to determine whether Wd2 is gravitationally bound or will dissolve in the future, which will provide us with a better understanding of the long-term cluster evolution.

The MUSE data provide the possibility to obtain a nearly complete spectral classification of a YMC down to $0.8 M_{\odot}$ and extract low-resolution SEDs of most of the PMS stars ($I \geq 21.5$ mag). This is shown in Fig. 11.2.2 as part of a preliminary analysis of a few stars. We were able to confirm the spectral type of a O8.5V star by comparing it to the [Walborn and Fitzpatrick \(1990\)](#) spectral library (see top, left panel of Fig. 11.2.2). Using the Medium-resolution Isaac Newton Telescope Library of Empirical Spectra (MILES, [Sánchez-Blázquez](#)

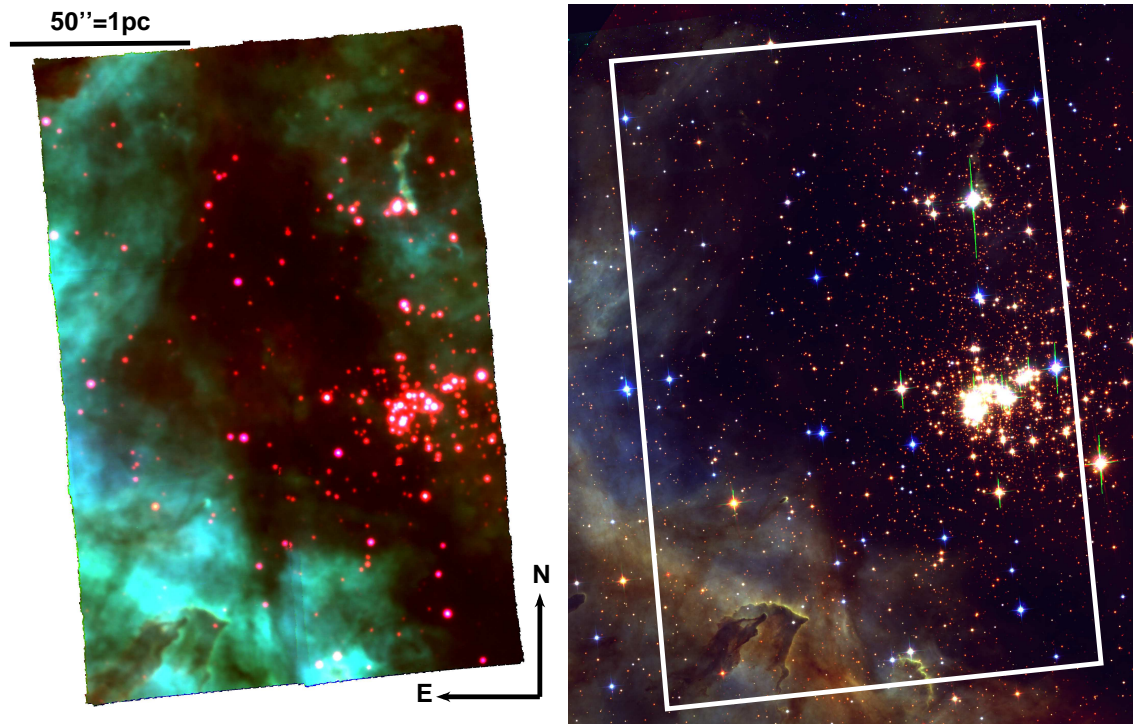


Figure 11.2.1: **Left:** The color-composite image of the MUSE mosaic (2×3 tiles) presented in red: S II (6717\AA), green: $H\alpha$, and blue: O III (5007\AA). **Right:** Color composite image of the HST ACS and WFC3/IR data of Wd2, including the $F125W$ (red), $F814W$ (green), and $F555W$ (blue) filters (this image is similar to Fig. 2.2.1). The white box represents the region already observed with MUSE.

et al. 2006; Falc3n-Barroso et al. 2011) we also were able to estimate a spectral type of A5 for a PMS star (see top, right panel of Fig. 11.2.2).

This kind of information will provide us with a unique insight into the feedback processes occurring within RCW 49 and on the PMS population, in particular, the disk fraction under the violent influence of the surrounding OB-stars. This will be compared to the results from the photometric study presented in this work.

Adding up all the spectra obtained from the spaxels covering the cluster and removing the contamination of the MS and foreground objects, we will produce a template SED of a fully characterized YMC to constrain the stellar populations of unresolved, extragalactic YMCs.

We plan to add more datasets to include other clusters in the MW and in the Magellanic Clouds, like NGC 346, NGC 3603, or NGC 602, to generalize the results. Additionally, this study will help us to determine a proper target selection within Wd2 for the upcoming science with JWST (launch date: October 2018). Compared to the optical wavelength regime of the ground-based data, the science instrument on board the JWST will cover the near- and mid infrared regime ($0.6\text{--}28\ \mu\text{m}$). This will allow us to study protostars emerging from the gas cloud and protostellar disks around PMS stars. The sensitivity and wavelength coverage

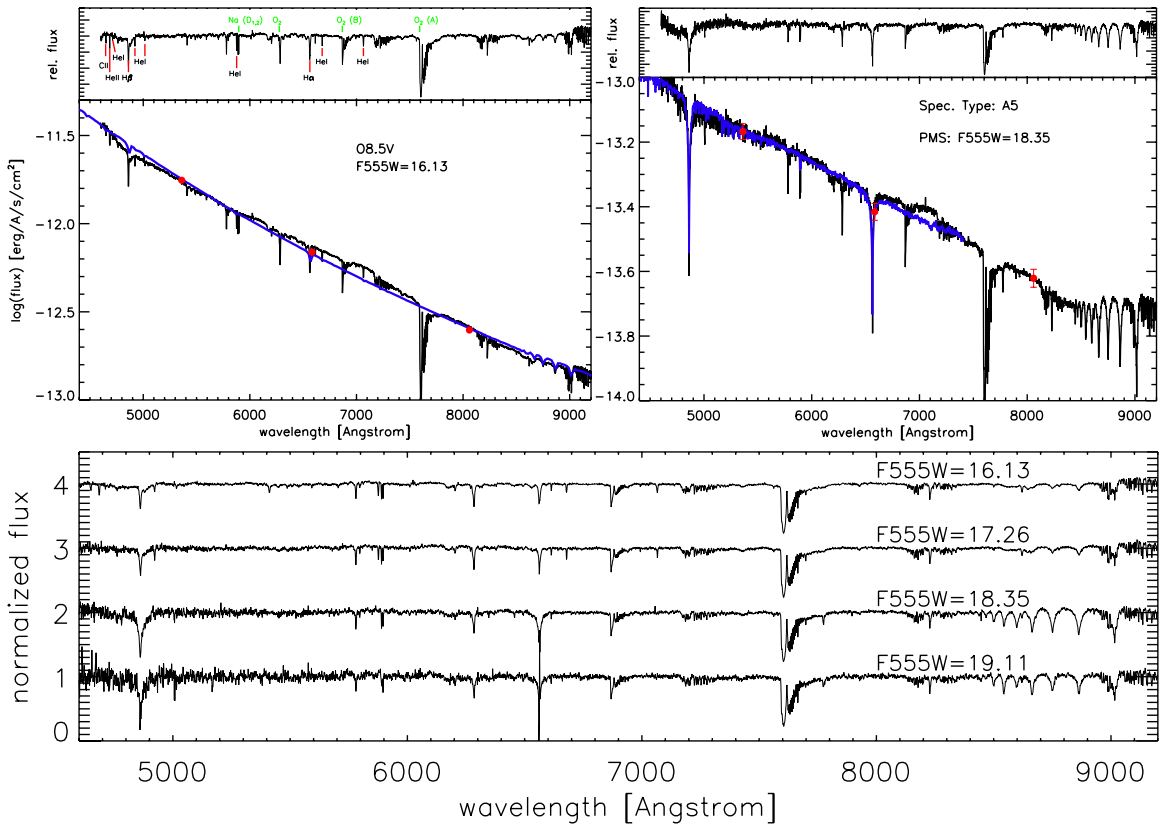


Figure 11.2.2: **Top, left:** The SED of an O8.5V star, with $F555W = 16.13$ mag. The blue, solid line represents the [Castelli and Kurucz \(2003\)](#) model spectrum, while the red points represent the flux, extracted from our HST photometric catalog. The top panel shows the normalized spectrum with the stellar absorption lines marked in red and telluric absorption lines in green. **Top, right:** The SED of an A5 PMS star, with $F555W = 18.35$ mag. The blue solid line represents the MILES model spectrum, while the red points represent the flux extracted from our HST photometric catalog. The top panel shows the normalized spectrum. **Bottom:** Four normalized spectra for an $F555W = 16.13$ mag, $F555W = 17.26$ mag, $F555W = 18.35$ mag, and $F555W = 19.11$ mag star.

of the JWST instruments will also allow us to study the PDMF down to lower masses ($< 0.65 M_{\odot}$) in the case of Wd2) at a statistically significant completeness level to compare them with the [Kroupa \(2001\)](#) IMF or the [Chabrier \(2003b\)](#) IMF.

These new powerful telescopes and instruments will push the frontier of understanding the formation (and evolution) of the stellar populations in galaxies, to add another piece to the puzzle of understanding the Universe as we observe it.



The weighted maps

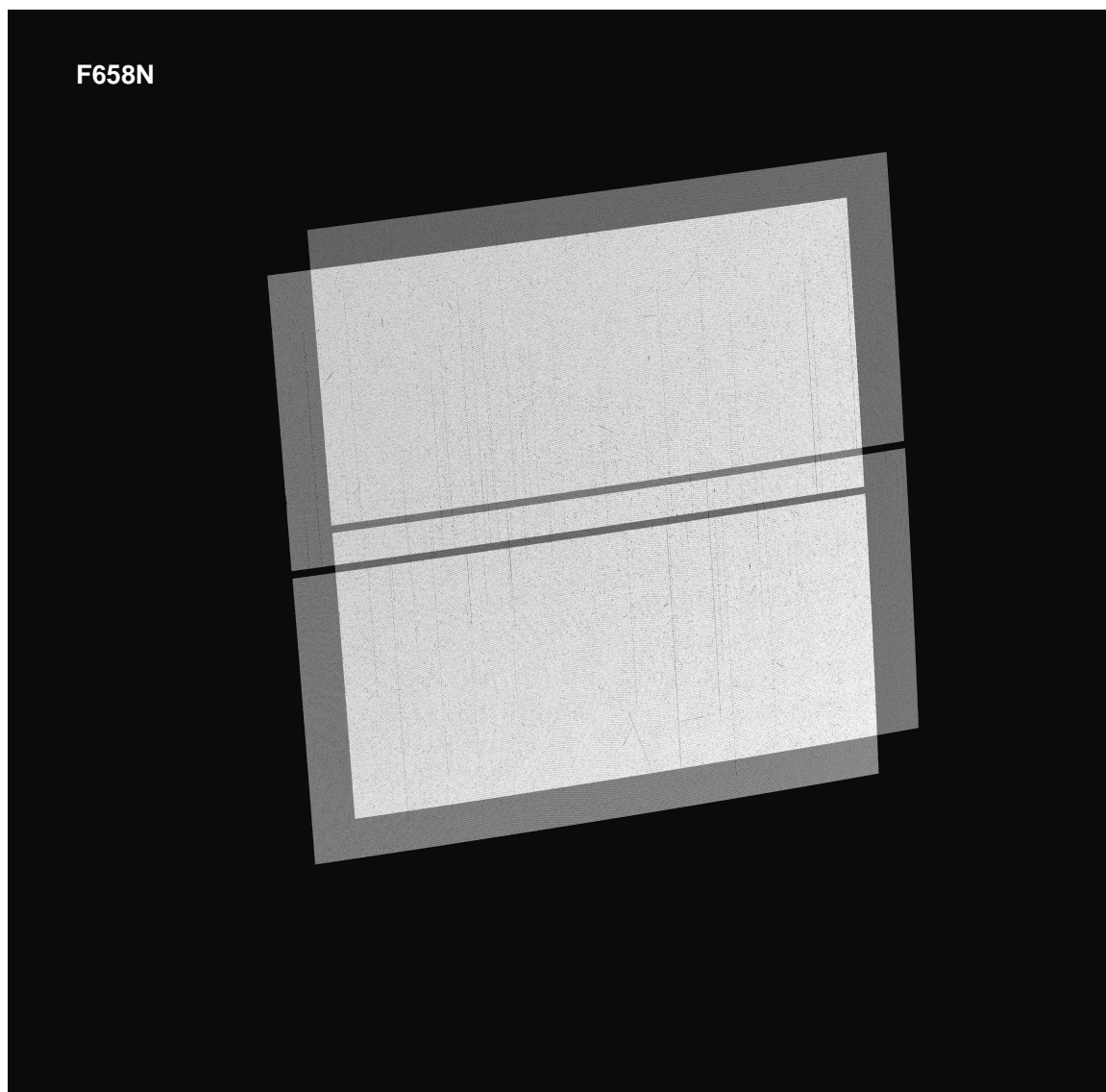


Figure A.0.1: The *F658N* weighted map for the final drizzled and aligned image.

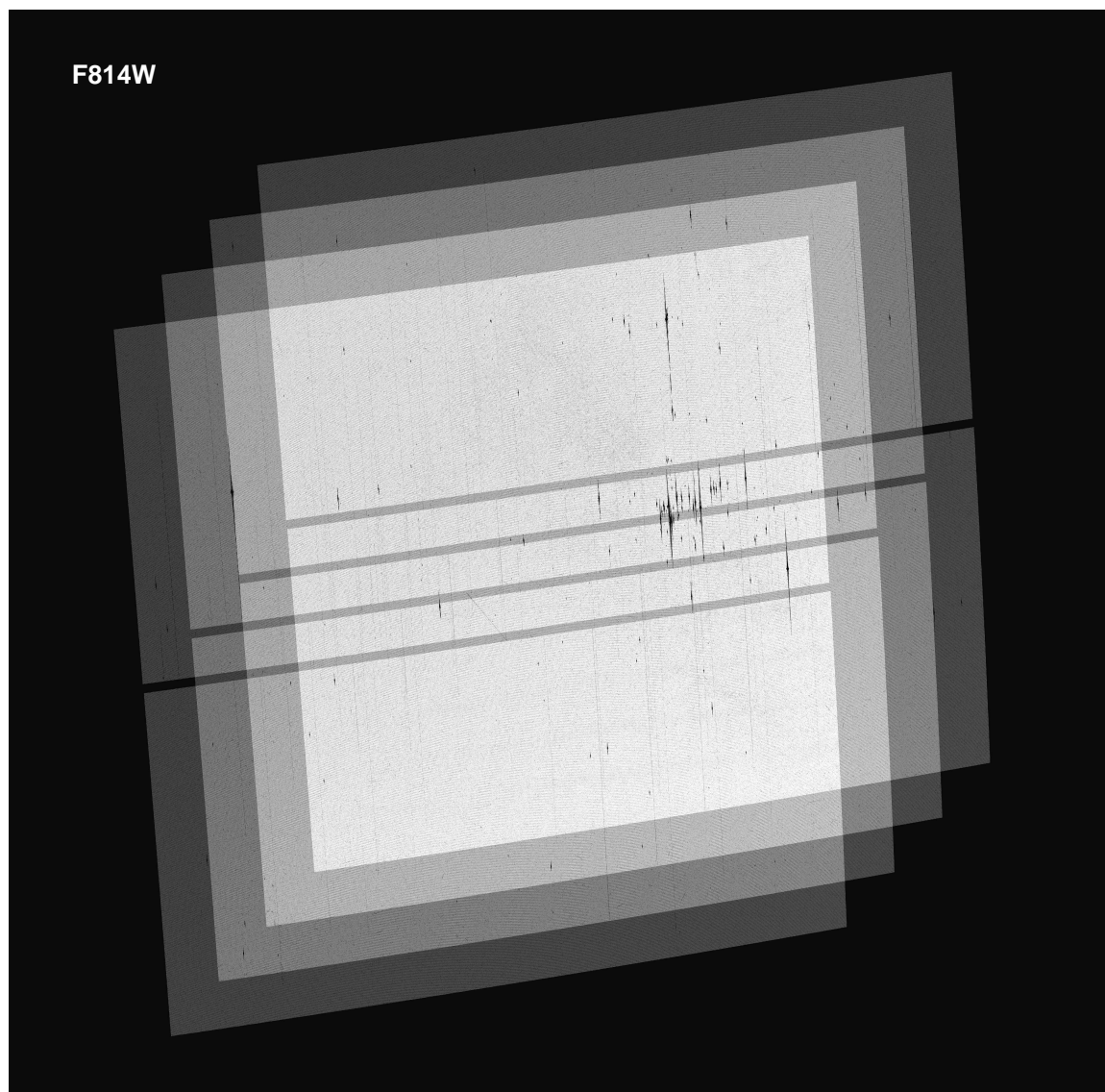


Figure A.0.2: The $F814W$ weighted map for the final drizzled and aligned image.

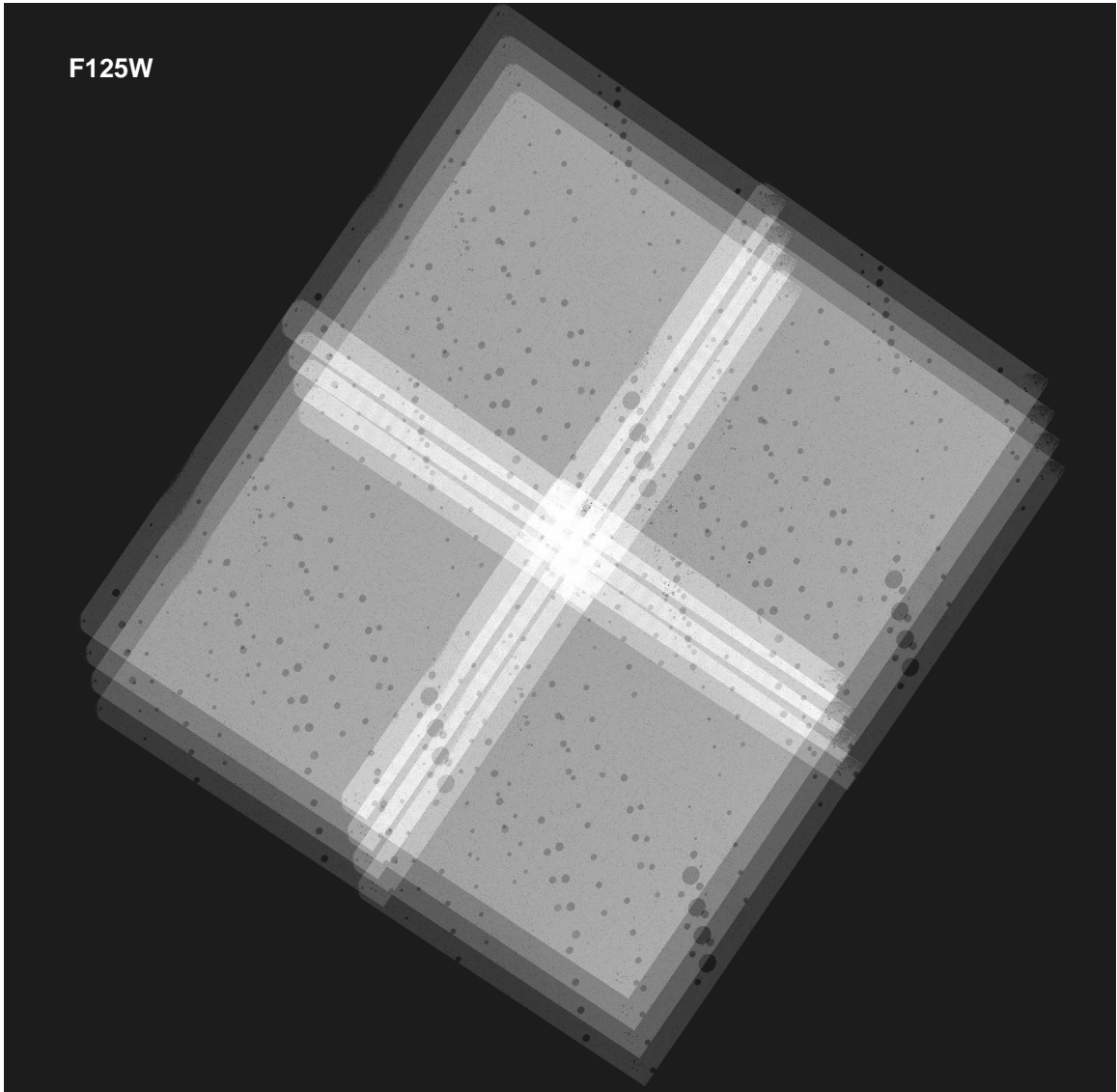


Figure A.0.3: The *F125W* weighted map for the final drizzled and aligned mosaic.

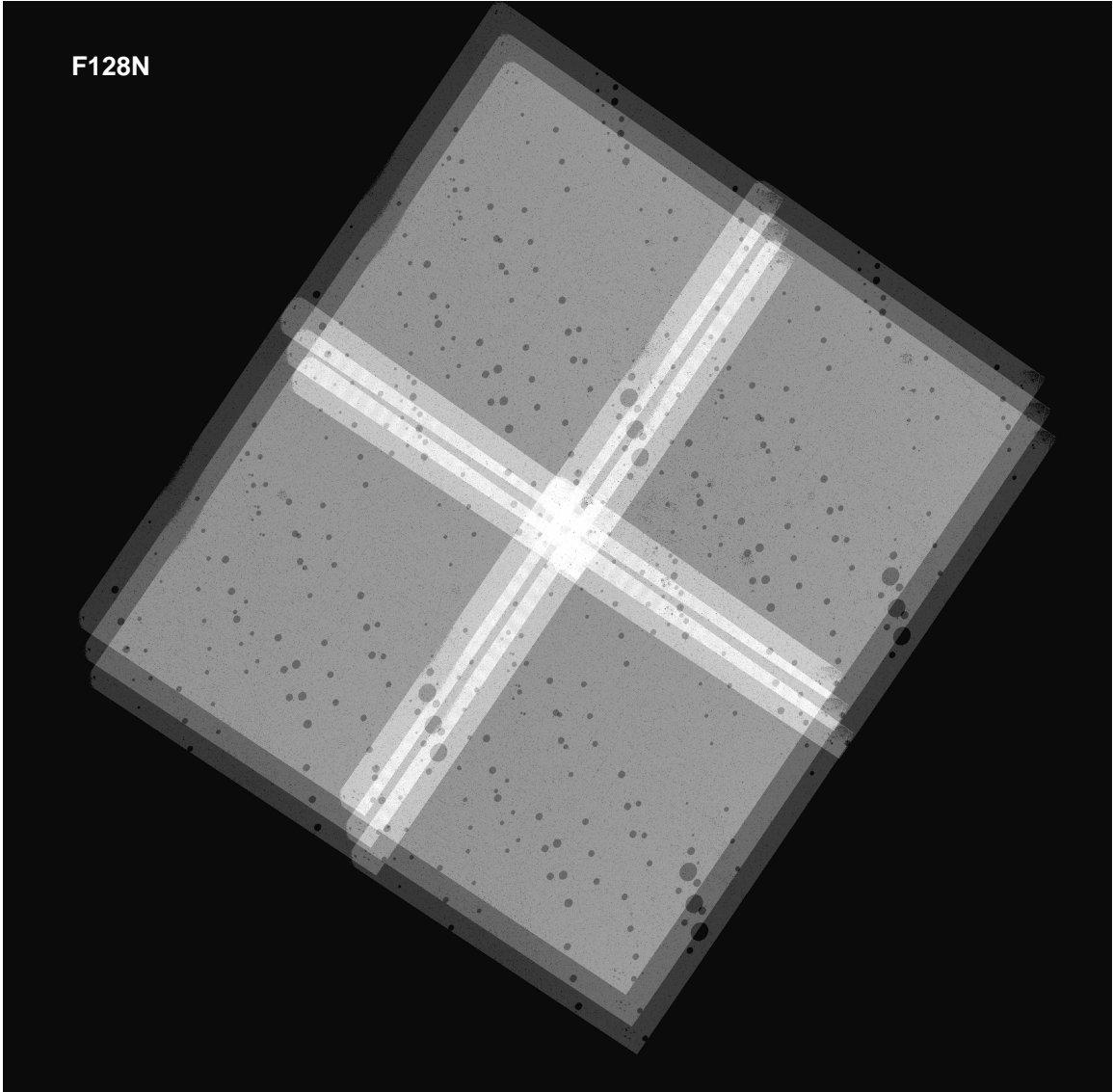


Figure A.0.4: The $F128N$ weighted map for the final drizzled and aligned mosaic.

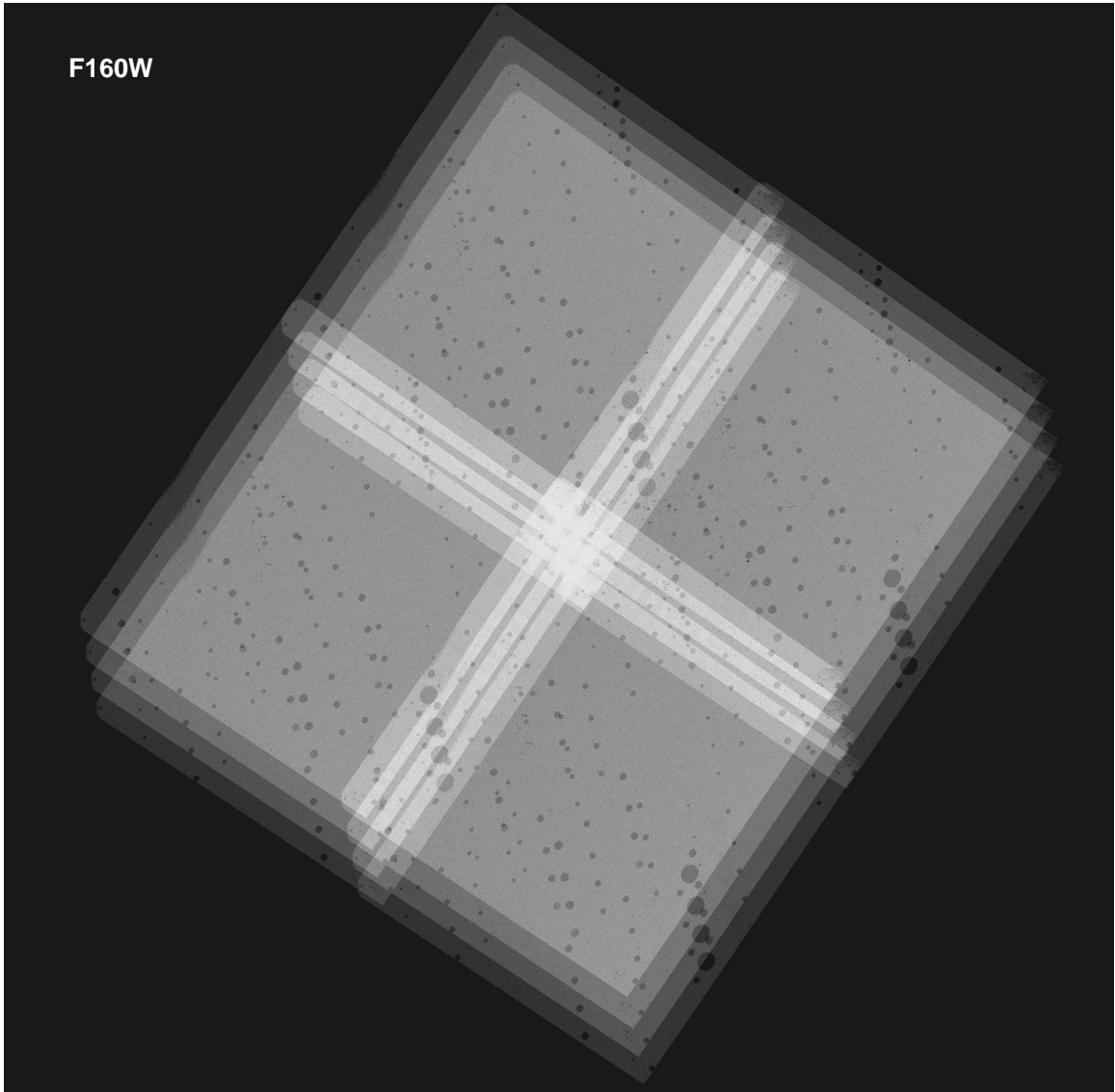


Figure A.0.5: The *F160W* weighted map for the final drizzled and aligned mosaic.

B

The drizzled filter mosaics

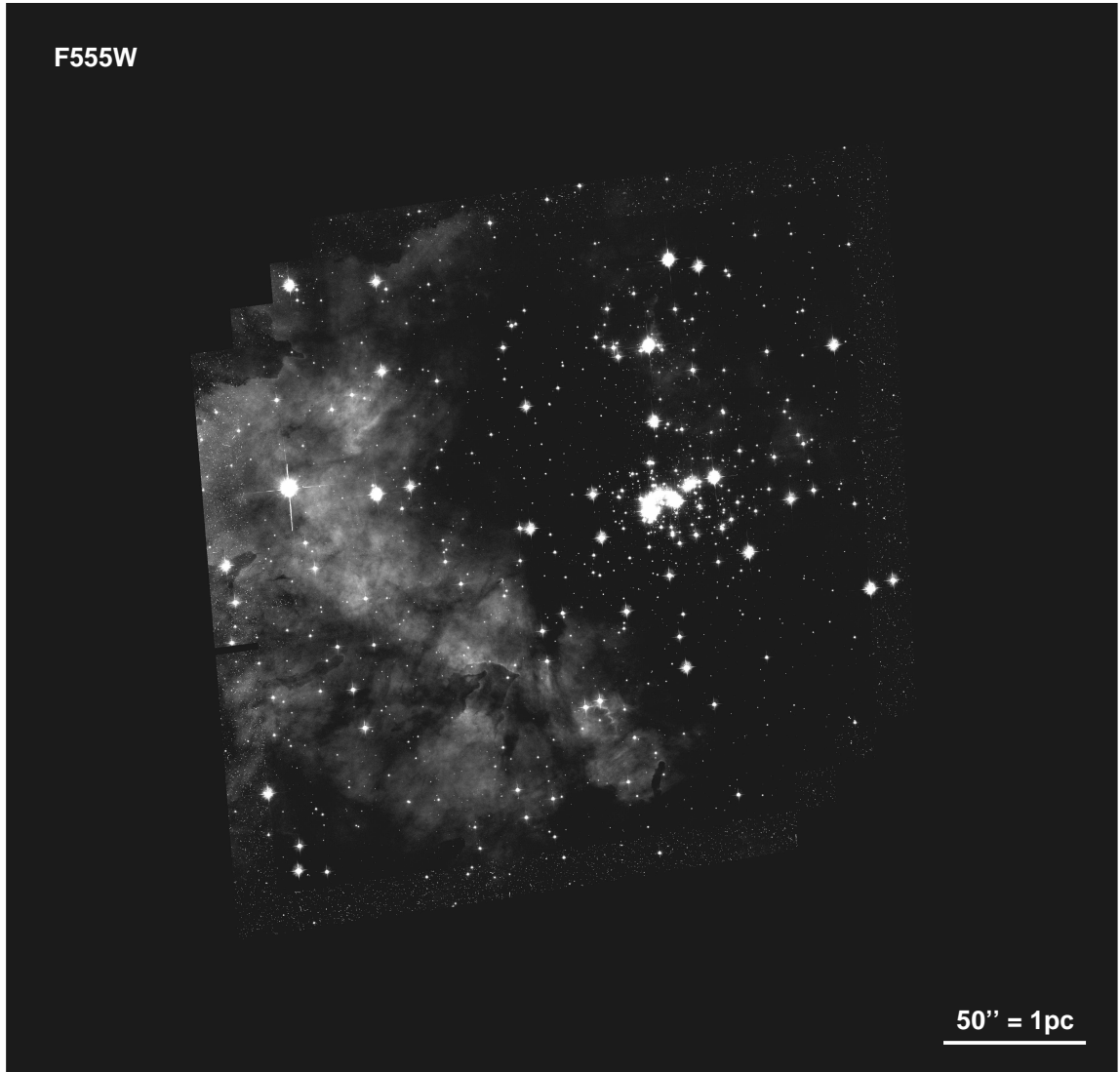


Figure B.0.1: The mosaic of the $F555W$ observation. North is up, East is to the left.

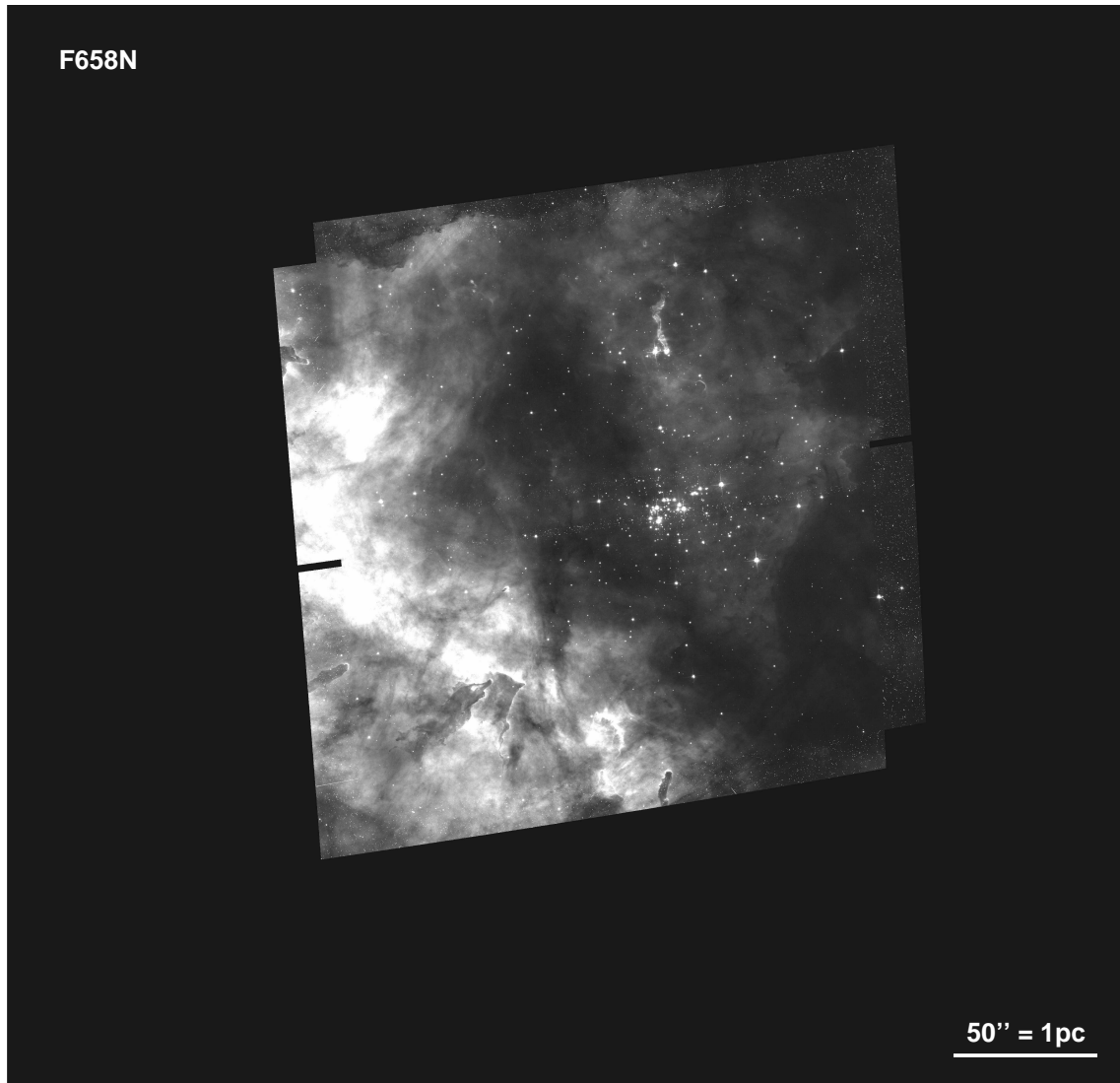


Figure B.0.2: The mosaic of the *F658N* observation. North is up, East is to the left.

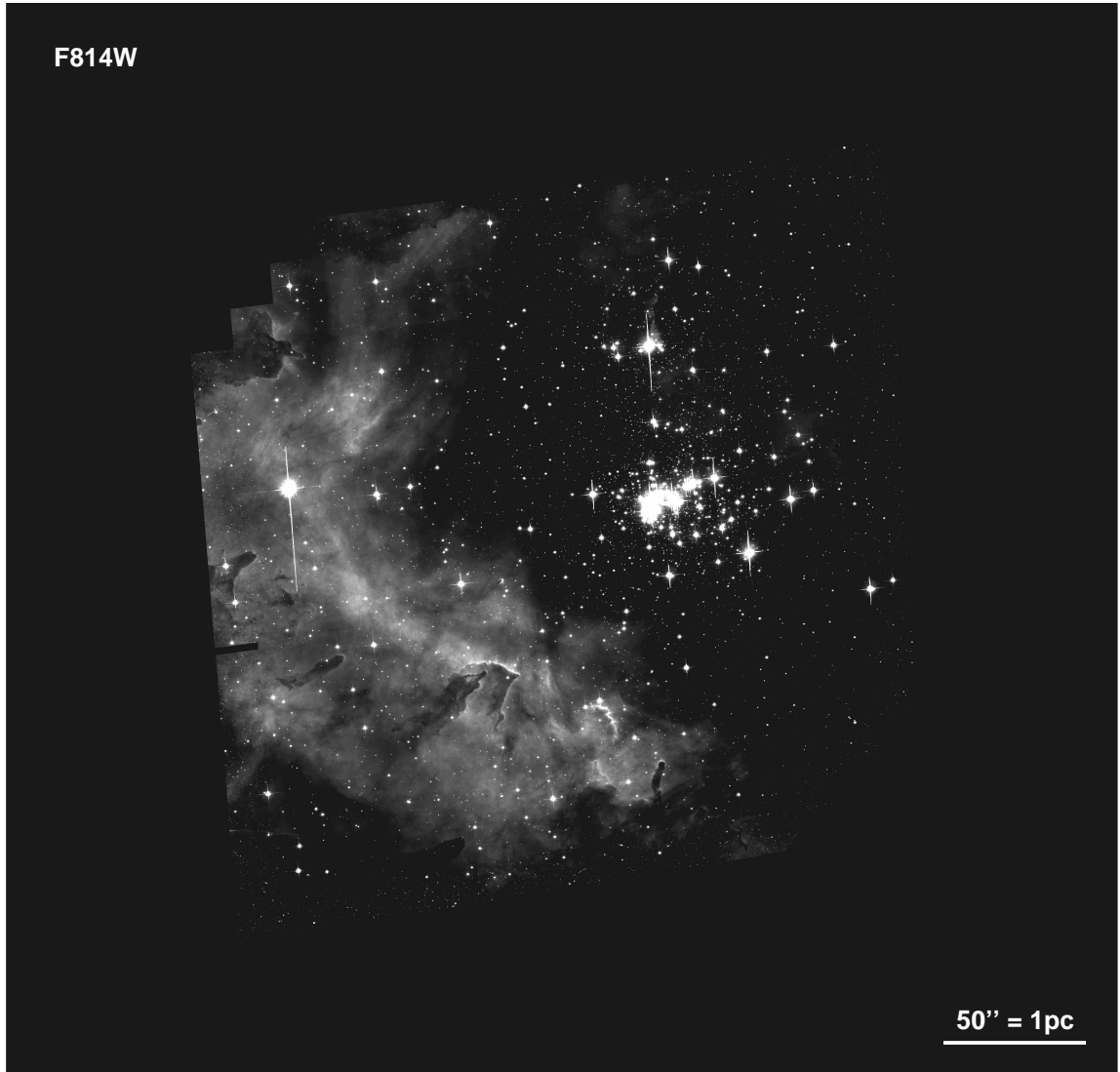


Figure B.0.3: The mosaic of the *F814W* observation. North is up, East is to the left.

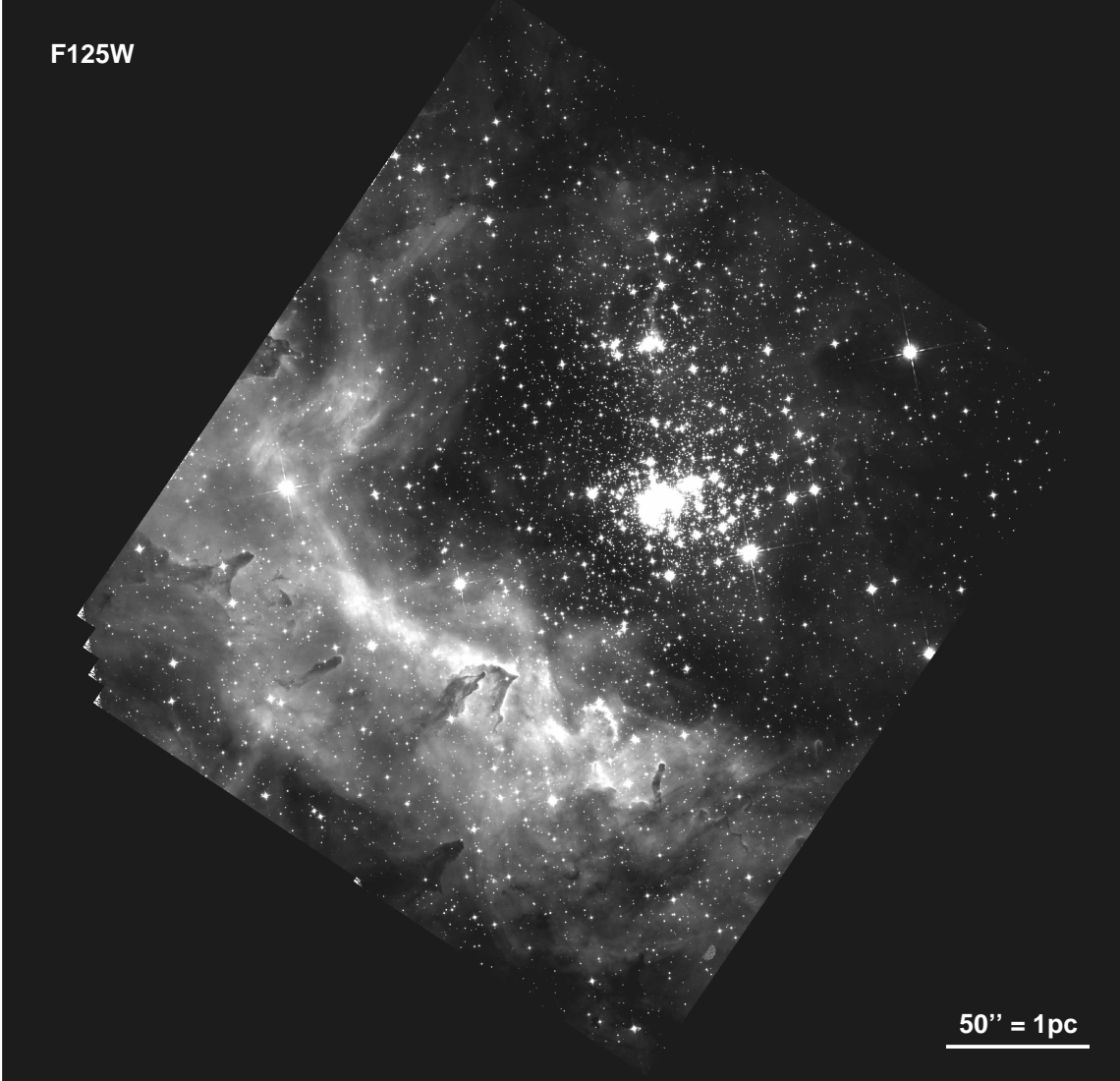


Figure B.0.4: The mosaic of the *F*125*W* observation. North is up, East is to the left.

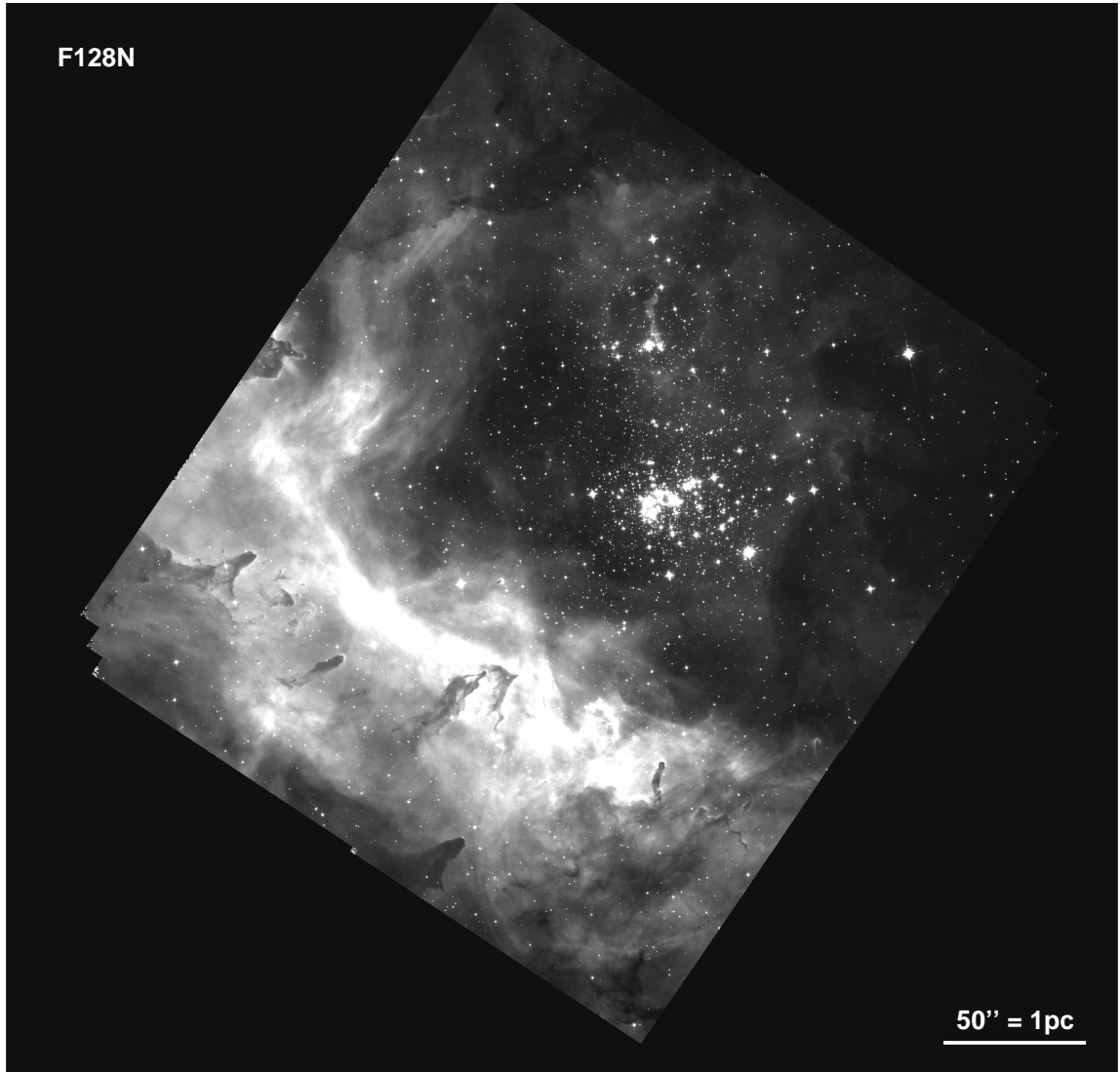


Figure B.0.5: The mosaic of the $F128N$ observation. North is up, East is to the left.

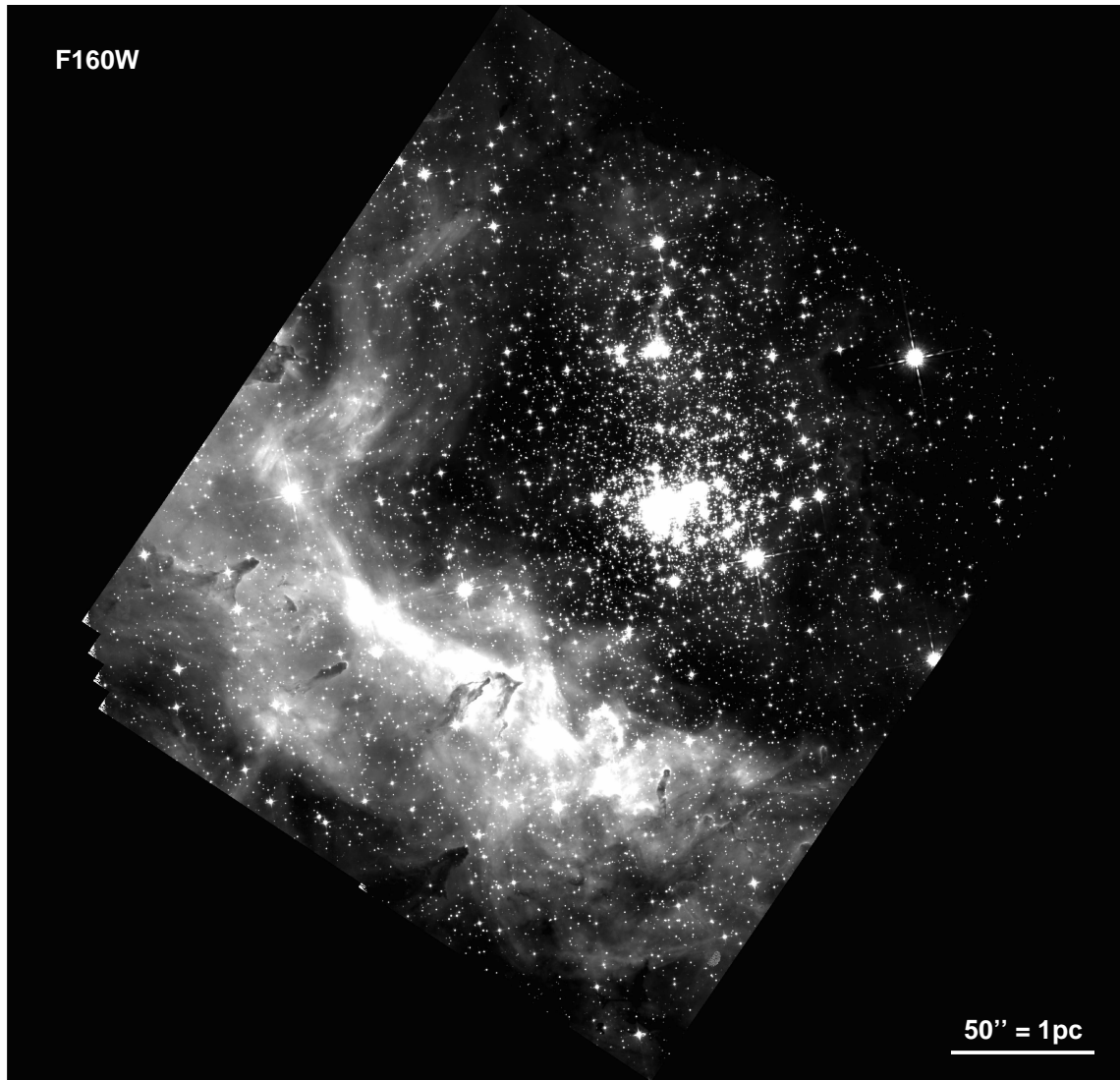


Figure B.0.6: The mosaic of the *F160W* observation. North is up, East is to the left.



Additional completeness maps

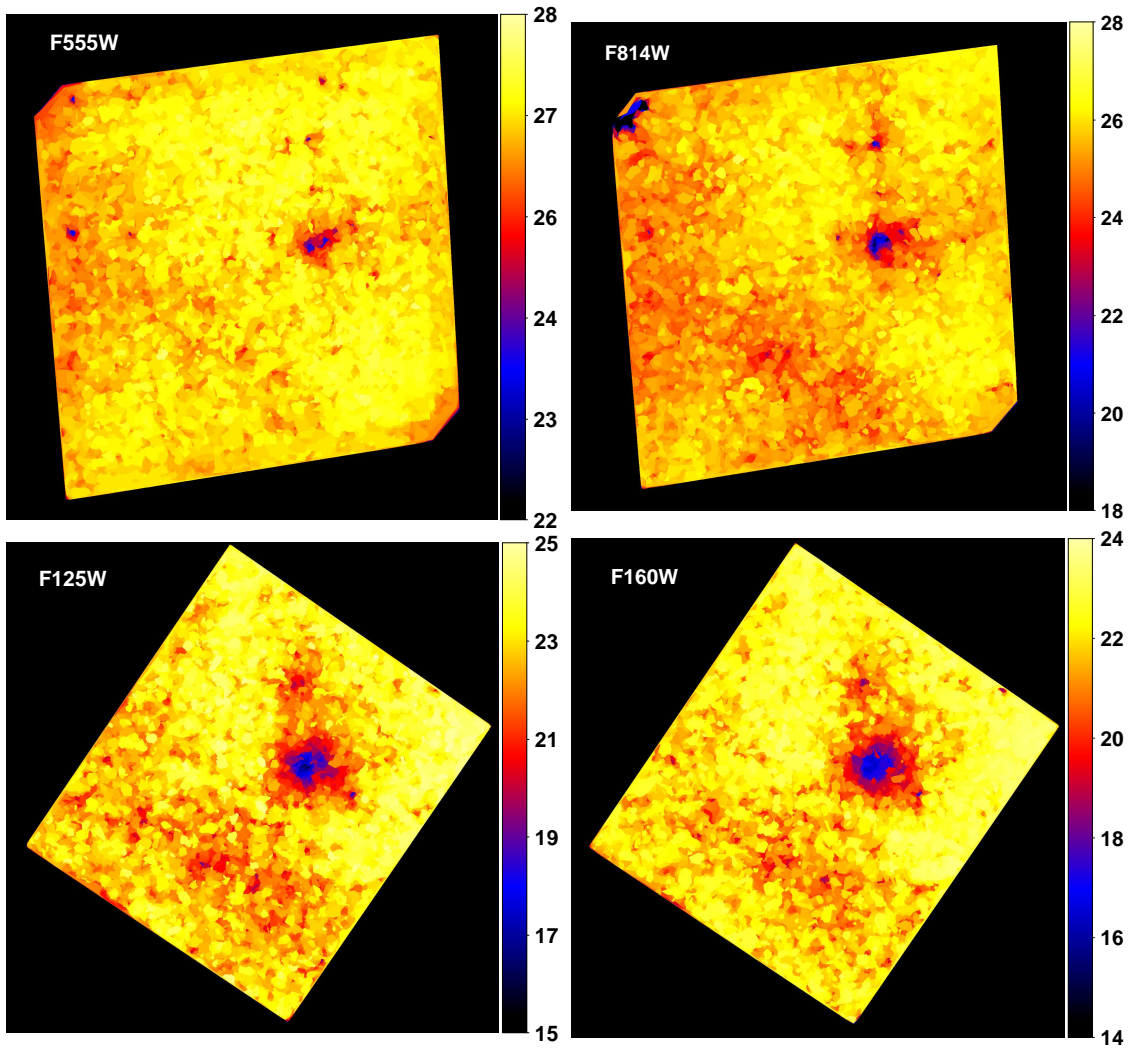


Figure C.0.1: The 25% completeness map for all four wide-band filters. The color bar indicates the magnitude at which such a completeness value is reached. This figure is similar to Fig. 5.3.1

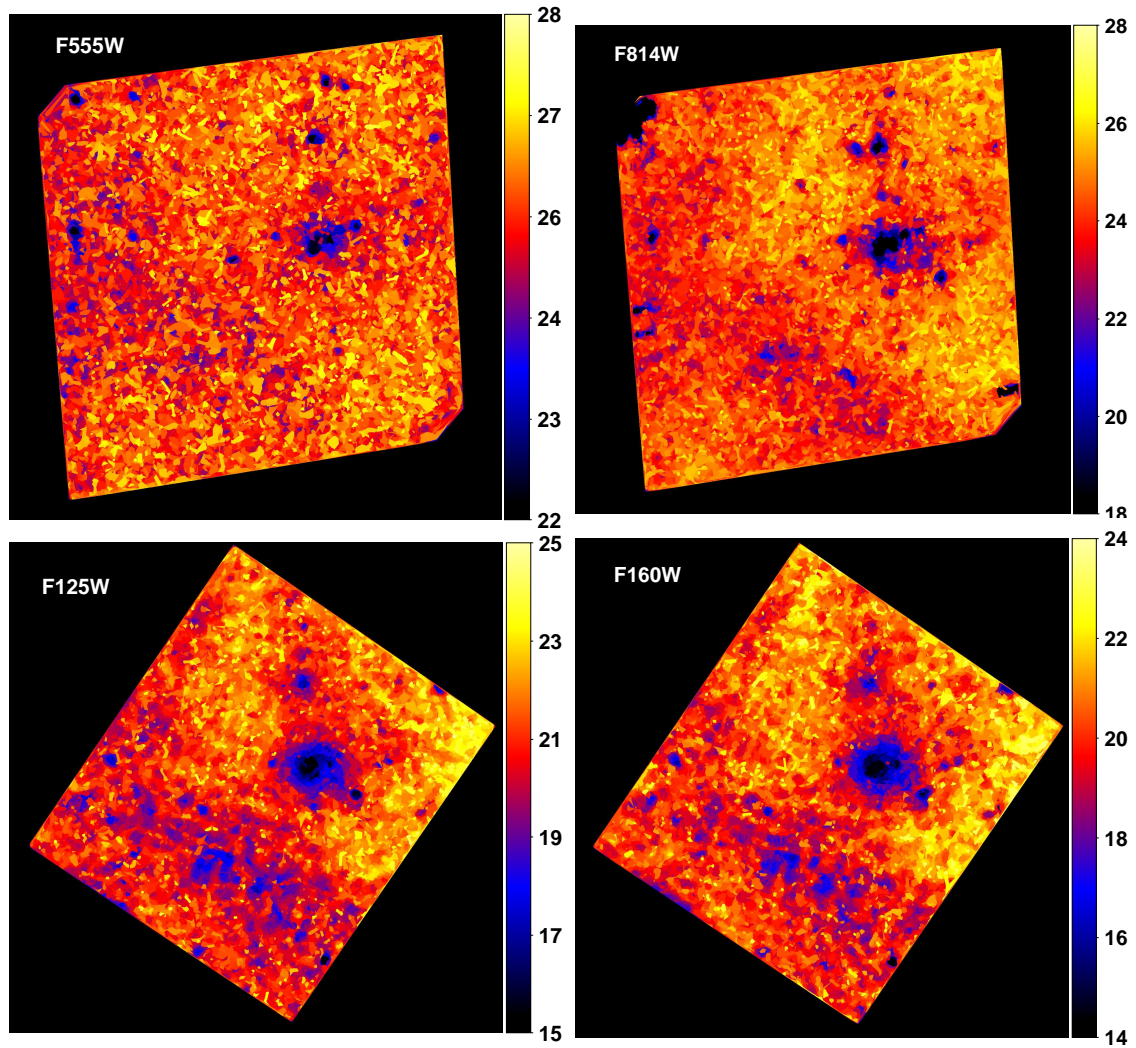


Figure C.0.2: The 75% completeness map for all four wide-band filters. The color bar indicates the magnitude at which such a completeness value is reached. This figure is similar to Fig. 5.3.1

Acknowledgments

I would like to dedicate the final note to my thesis to all the people who have made this PhD in astronomy possible and unforgettable, and who have supported me over the past three years.

Zum Ausklang meiner Arbeit möchte ich mich noch bei Allen bedanken, die mir diesen Doktor der Astronomie ermöglichten und die mich über die letzten drei Jahre unterstützten.

I would like to thank my supervisor, Eva Grebel, for this nice project, her continuous guidance and help over the three years, and the motivation to try new paths and methods. I enjoyed the interesting and sometimes also off-topic talks and discussions we have had. I thank Anna Pasquali for her continuous and outstanding support and encouragement over the past three years and the fruitful scientific and non-scientific discussions, as well as being member of my thesis committee. Many thanks also to Jay Gallagher, who gave interesting thoughts and input on the project and agreed to be part of my thesis committee. Special thanks also to Sabine Reffert, who was so kind to be my second referee.

Special thanks go to Antonella Nota who gave me the opportunity of three outstanding visits at the Space Telescope Science Institute, where I acquired good knowledge about *Hubble* Space Telescope (HST) data reduction and data handling, and where I met a lot of nice and interesting people. Furthermore, I also want to thank Elena Sabbi for patiently answering all my questions regarding data analysis and data reduction and who was always supportive and encouraging. Many thanks to Leonardo Ubeda, who showed me how to reduce HST data and provided me with some of his codes. To Loretta Willers and Alisa Meizlish who always helped me settling in, solved any problems regarding my visit, and gave me a very warm welcome.

Thanks to Christian Fendt for all his efforts in coordinating the International Max Planck Research School (IMPRS), creating a warm and nice environment, planning nice social events such as the summer BBQ, and for his constant support.

I want to thank my office mate, Carolin Wittmann, with whom I had a lot of fun and discussions over the past years and with whom I found support during more stressful times.

Many thanks also to all my friends here in Heidelberg, who made these three years special and with whom I have had a lot of fun. Especially, I would like to thank Reza Moetazedian, Clio Bertelli Motta, Elena Manjavacas, Roxana Chira, María Jesús Jiménez, Sara Rezaei Khoshbakht, Christina Eilers, Richard Teague, Alison Mitchell, Chiara Mazzucchelli, Jakob Herpich, María Claudia (Macla) Ramírez, Fayeze Shabani, and Anna Schauer. I also want to thank my IMPRS generation for the wonderful three years and the nice Thursday evenings.

Special thanks to Hendrik Heinl, Avon Huxor, John Vickers, Veronica Lora, Geneviève Parmentier, Daniel Haydon, Alexander Hygate, Kseniia Sysoliatina, and many more at ARI.

Vielen Dank auch an Helga Ballmann, Martina Buchhaupt, Saskia Mayer, Hildun Pisch-Papendick, Diana Schwalbe und ganz besonders auch an Eleonora Grauer, die immer sehr geduldig mit meinen, oft sehr komplizierten, Dienstreiseabrechnung war.

To all my friends in Baltimore, with whom I had a lot of fun and who made my visits unforgettable. Especially, I would like to thank Camilla Pacifici, Nora Lützgendorf, Lucie Leboulleux, Olivia (Libby) Jones, Annalisa Calamida, Michele Cignoni, Matteo Correnti, Armin Rest, Mamadou N'Diaye, Johan Mazoyer, Brendan Hagan, Allyssa Riley, Varun Bajaj, and Valentina Calvi.

Zu guter Letzt bedanke ich mich ganz herzlich bei meinen Eltern und meiner Schwester, für die jahrelange Unterstützung, sowohl in den letzten drei Jahren, als auch in den Jahren zuvor.

This project was partially funded by the Sonderforschungsbereich 881 (SFB 881, “The Milky Way System”) of the German Research Foundation, particularly via subproject B5.

I thank ESA for the financial support to visit the Space Telescope Science Institute for a productive scientific collaboration.

Based on observations made with the NASA/ESA Hubble Space Telescope, obtained at the Space Telescope Science Institute, which is operated by the Association of Universities for Research in Astronomy, Inc., under NASA contract NAS 5–26555. These observations are associated with program #13038.

References

- Aguirre, J. E., Ginsburg, A. G., Dunham, M. K., Drosback, M. M., Bally, J., Battersby, C., Bradley, E. T., Cyganowski, C., Dowell, D., Evans, II, N. J., Glenn, J., Harvey, P., Rosolowsky, E., Stringfellow, G. S., Walawender, J., and Williams, J. P. (2011). The Bolocam Galactic Plane Survey: Survey Description and Data Reduction. *ApJS*, **192**, 4.
- Aharonian, F., Akhperjanian, A. G., Bazer-Bachi, A. R., Beilicke, M., Benbow, W., Berge, D., Bernlöhr, K., Boisson, C., Bolz, O., Borrel, V., Braun, I., Brion, E., Brown, A. M., Bühler, R., Büsching, I., Boutelier, T., Carrigan, S., Chadwick, P. M., Chounet, L.-M., Coignet, G., Cornils, R., Costamante, L., Degrange, B., Dickinson, H. J., Djannati-Ataï, A., Drury, L. O., Dubus, G., Egberts, K., Emmanoulopoulos, D., Espigat, P., Farnier, C., Feinstein, F., Ferrero, E., Fiasson, A., Fontaine, G., Funk, S., Funk, S., Füßling, M., Gallant, Y. A., Giebels, B., Glicenstein, J. F., Glück, B., Goret, P., Hadjichristidis, C., Hauser, D., Hauser, M., Heinzelmann, G., Henri, G., Hermann, G., Hinton, J. A., Hoffmann, A., Hofmann, W., Holleran, M., Hoppe, S., Horns, D., Jacholkowska, A., de Jager, O. C., Kendziorra, E., Kerschhaggl, M., Khélifi, B., Komin, N., Kosack, K., Lamanna, G., Latham, I. J., Le Gallou, R., Lemièrre, A., Lemoine-Goumard, M., Lohse, T., Martin, J. M., Martineau-Huynh, O., Marcowith, A., Masterson, C., Maurin, G., McComb, T. J. L., Moulin, E., de Naurois, M., Nedbal, D., Nolan, S. J., Noutsos, A., Olive, J.-P., Orford, K. J., Osborne, J. L., Panter, M., Pelletier, G., Petrucci, P.-O., Pita, S., Pühlhofer, G., Punch, M., Ranchon, S., Raubenheimer, B. C., Raue, M., Rayner, S. M., Reimer, A., Reimer, O., Ripken, J., Rob, L., Rolland, L., Rosier-Lees, S., Rowell, G., Sahakian, V., Santangelo, A., Saugé, L., Schlenker, S., Schlickeiser, R., Schröder, R., Schwanke, U., Schwarzburg, S., Schwemmer, S., Shalchi, A., Sol, H., Spangler, D., Spanier, F., Steenkamp, R., Stegmann, C., Superina, G., Tam, P. H., Tavernet, J.-P., Terrier, R., Tluczykont, M., van Eldik, C., Vasileiadis, G., Venter, C., Vialle, J. P., Vincent, P., Völk, H. J., Wagner, S. J., and Ward, M. (2007). Detection of extended very-high-energy γ -ray emission towards the young stellar cluster Westerlund 2. *A&A*, **467**, 1075.
- Allen, D. A. and Hillier, D. J. (1993). The Shape of the Homunculus Nebula around Eta-Carinae. *Proceedings of the Astronomical Society of Australia*, **10**, 338.
- Allison, R. J., Goodwin, S. P., Parker, R. J., Portegies Zwart, S. F., and de Grijs, R. (2010). The early dynamical evolution of cool, clumpy star clusters. *MNRAS*, **407**, 1098.
- Anathpindika, S. V. (2010). Collision between dissimilar clouds: stability of the bow-shock, and the formation of pre-stellar cores. *MNRAS*, **405**, 1431.
- Andersen, M., Zinnecker, H., Moneti, A., McCaughrean, M. J., Brandl, B., Brandner, W., Meylan, G., and Hunter, D. (2009). The Low-Mass Initial Mass Function in the 30 Doradus Starburst Cluster. *ApJ*, **707**, 1347.
- Anderson, K. R., Adams, F. C., and Calvet, N. (2013). Viscous Evolution and Photoevaporation of Circumstellar Disks Due to External Far Ultraviolet Radiation Fields. *ApJ*, **774**, 9.
- Ao, Y., Henkel, C., Menten, K. M., Requena-Torres, M. A., Stanke, T., Mauersberger, R., Aalto, S., Mühle, S., and Mangum, J. (2013). The thermal state of molecular clouds in the Galactic center: evidence for non-photon-driven heating. *A&A*, **550**, A135.
- Appenzeller, I. and Bertout, C. (2013). Inclination effects in T Tauri star spectra. *A&A*, **558**, A83.
- Appenzeller, I., Bertout, C., and Stahl, O. (2005). Edge-on T Tauri stars. *A&A*, **434**, 1005.
- Ascenso, J., Alves, J., Beletsky, Y., and Lago, M. T. V. T. (2007a). Near-IR imaging of Galactic massive clusters: Westerlund 2. *A&A*, **466**, 137.
- Ascenso, J., Alves, J., Vicente, S., and Lago, M. T. V. T. (2007b). NTT and VLT diffraction limited imaging of Trumpler 14: revealing a massive core-halo cluster. *A&A*, **476**, 199.
- Bacon, R., Accardo, M., Adjali, L., Anwand, H., Bauer, S., Biswas, I., Blaizot, J., Boudon, D., Brau-Nogue, S., Brinchmann, J., Caillier, P., Capoani, L., Carollo, C. M., Contini, T., Couderc, P., Daguisé, E., Deiries, S.,

- Delabre, B., Dreizler, S., Dubois, J., Dupieux, M., Dupuy, C., Emsellem, E., Fechner, T., Fleischmann, A., François, M., Gallou, G., Gharsa, T., Glindemann, A., Gojak, D., Guiderdoni, B., Hansali, G., Hahn, T., Jarno, A., Kelz, A., Koehler, C., Kosmalski, J., Laurent, F., Le Floch, M., Lilly, S. J., Lizon, J.-L., Loupiau, M., Manescau, A., Monstein, C., Nicklas, H., Olaya, J.-C., Pares, L., Pasquini, L., Pécontal-Rousset, A., Pelló, R., Petit, C., Popow, E., Reiss, R., Remillieux, A., Renault, E., Roth, M., Rupprecht, G., Serre, D., Schaye, J., Soucail, G., Steinmetz, M., Streicher, O., Stuijk, R., Valentin, H., Vernet, J., Weilbacher, P., Wisotzki, L., and Yerle, N. (2010). The MUSE second-generation VLT instrument. In *Ground-based and Airborne Instrumentation for Astronomy III*, volume 7735 of *Proc. SPIE*, page 773508.
- Banerjee, S. and Kroupa, P. (2014). A Perfect Starburst Cluster made in One Go: The NGC 3603 Young Cluster. *ApJ*, **787**, 158.
- Banerjee, S. and Kroupa, P. (2015). The formation of NGC 3603 young starburst cluster: ‘prompt’ hierarchical assembly or monolithic starburst? *MNRAS*, **447**, 728.
- Baraffe, I., Chabrier, G., Allard, F., and Hauschildt, P. H. (1998). Evolutionary models for solar metallicity low-mass stars: mass-magnitude relationships and color-magnitude diagrams. *A&A*, **337**, 403.
- Baraffe, I., Chabrier, G., Allard, F., and Hauschildt, P. H. (2002). Evolutionary models for low-mass stars and brown dwarfs: Uncertainties and limits at very young ages. *A&A*, **382**, 563.
- Bastian, N., Covey, K. R., and Meyer, M. R. (2010). A Universal Stellar Initial Mass Function? A Critical Look at Variations. *ARA&A*, **48**, 339.
- Bastian, N. and de Mink, S. E. (2009). The effect of stellar rotation on colour-magnitude diagrams: on the apparent presence of multiple populations in intermediate age stellar clusters. *MNRAS*, **398**, L11.
- Bastian, N. and Goodwin, S. P. (2006). Evidence for the strong effect of gas removal on the internal dynamics of young stellar clusters. *MNRAS*, **369**, L9.
- Basu, S. and Mouschovias, T. C. (1994). Magnetic braking, ambipolar diffusion, and the formation of cloud cores and protostars. 1: Axisymmetric solutions. *ApJ*, **432**, 720.
- Bate, M. R., Bonnell, I. A., and Bromm, V. (2002). The formation of close binary systems by dynamical interactions and orbital decay. *MNRAS*, **336**, 705.
- Beccari, G., De Marchi, G., Panagia, N., Valenti, E., Carraro, G., Romaniello, M., Zoccali, M., and Weidner, C. (2015). Mass accretion rates from multiband photometry in the Carina Nebula: the case of Trumpler 14. *A&A*, **574**, A44.
- Beccari, G., Spezzi, L., De Marchi, G., Paresce, F., Young, E., Andersen, M., Panagia, N., Balick, B., Bond, H., Calzetti, D., Carollo, C. M., Disney, M. J., Dopita, M. A., Frogel, J. A., Hall, D. N. B., Holtzman, J. A., Kimble, R. A., McCarthy, P. J., O’Connell, R. W., Saha, A., Silk, J. I., Trauger, J. T., Walker, A. R., Whitmore, B. C., and Windhorst, R. A. (2010). Progressive Star Formation in the Young Galactic Super Star Cluster NGC 3603. *ApJ*, **720**, 1108.
- Belloche, A., Garrod, R. T., Müller, H. S. P., and Menten, K. M. (2014). Detection of a branched alkyl molecule in the interstellar medium: iso-propyl cyanide. *Science*, **345**, 1584.
- Benjamin, R. A., Churchwell, E., Babler, B. L., Bania, T. M., Clemens, D. P., Cohen, M., Dickey, J. M., Indebetouw, R., Jackson, J. M., Kobulnicky, H. A., Lazarian, A., Marston, A. P., Mathis, J. S., Meade, M. R., Seager, S., Stolovy, S. R., Watson, C., Whitney, B. A., Wolff, M. J., and Wolfire, M. G. (2003). GLIMPSE. I. An SIRTf Legacy Project to Map the Inner Galaxy. *PASP*, **115**, 953.
- Binney, J. and Merrifield, M. (1998). *Galactic Astronomy*. Princeton University Press.
- Binney, J. and Tremaine, S. (1987). *Galactic Dynamics*. Princeton University Press.
- Blum, R. D., Schaerer, D., Pasquali, A., Heydari-Malayeri, M., Conti, P. S., and Schmutz, W. (2001). 2 Micron Narrowband Adaptive Optics Imaging in the Arches Cluster. *AJ*, **122**, 1875.
- Bodenheimer, P. H. (2011). *Principles of Star Formation*. Springer-Verlag Berlin Heidelberg.
- Boland, W. and de Jong, T. (1984). Hydrostatic models of molecular clouds. II - Steady state models of spherical clouds. *A&A*, **134**, 87.
- Bolatto, A. D., Simon, J. D., Stanimirović, S., van Loon, J. T., Shah, R. Y., Venn, K., Leroy, A. K., Sandstrom, K., Jackson, J. M., Israel, F. P., Li, A., Staveley-Smith, L., Bot, C., Boulanger, F., and Rubio, M. (2007). The Spitzer Survey of the Small Magellanic Cloud: S³MC Imaging and Photometry in the Mid- and Far-Infrared Wave Bands. *ApJ*, **655**, 212.
- Bonanos, A. Z., Stanek, K. Z., Udalski, A., Wyrzykowski, L., Żebruń, K., Kubiak, M., Szymański, M. K., Szewczyk,

-
- O., Pietrzyński, G., and Soszyński, I. (2004). WR 20a Is an Eclipsing Binary: Accurate Determination of Parameters for an Extremely Massive Wolf-Rayet System. *ApJL*, [611, L33](#).
- Bonnell, I. A. and Bate, M. R. (2002). Accretion in stellar clusters and the collisional formation of massive stars. *MNRAS*, [336, 659](#).
- Bonnell, I. A. and Bate, M. R. (2006). Star formation through gravitational collapse and competitive accretion. *MNRAS*, [370, 488](#).
- Bonnell, I. A., Clarke, C. J., Bate, M. R., and Pringle, J. E. (2001). Accretion in stellar clusters and the initial mass function. *MNRAS*, [324, 573](#).
- Bonnell, I. A. and Davies, M. B. (1998). Mass segregation in young stellar clusters. *MNRAS*, [295, 691](#).
- Bouret, J.-C., Lanz, T., Hillier, D. J., Heap, S. R., Hubeny, I., Lennon, D. J., Smith, L. J., and Evans, C. J. (2003). Quantitative Spectroscopy of O Stars at Low Metallicity: O Dwarfs in NGC 346. *ApJ*, [595, 1182](#).
- Brand, J. and Blitz, L. (1993). The Velocity Field of the Outer Galaxy. *A&A*, [275, 67](#).
- Brandner, W., Grebel, E. K., Barbá, R. H., Walborn, N. R., and Moneti, A. (2001). Hubble Space Telescope NICMOS Detection of a Partially Embedded, Intermediate-Mass, Pre-Main-Sequence Population in the 30 Doradus Nebula. *AJ*, [122, 858](#).
- Bressan, A., Marigo, P., Girardi, L., Nanni, A., and Rubele, S. (2013). Red Giant evolution and specific problems. In *European Physical Journal Web of Conferences*, volume 43, page 03001.
- Bressan, A., Marigo, P., Girardi, L., Salasnich, B., Dal Cero, C., Rubele, S., and Nanni, A. (2012). PARSEC: stellar tracks and isochrones with the PAdova and TRieste Stellar Evolution Code. *MNRAS*, [427, 127](#).
- Briceño, C., Calvet, N., Hernández, J., Vivas, A. K., Hartmann, L., Downes, J. J., and Berlind, P. (2005). The CIDA Variability Survey of Orion OB1. I. The Low-Mass Population of Ori OB1a and 1b. *AJ*, [129, 907](#).
- Briceño, C., Preibisch, T., Sherry, W. H., Mamajek, E. A., Mathieu, R. D., Walter, F. M., and Zinnecker, H. (2007). The Low-Mass Populations in OB Associations. *Protostars and Planets V*, [pages 345–360](#).
- Brodie, J. P. and Strader, J. (2006). Extragalactic Globular Clusters and Galaxy Formation. *ARA&A*, [44, 193](#).
- Caffau, E., Ludwig, H.-G., Steffen, M., Freytag, B., and Bonifacio, P. (2011). Solar Chemical Abundances Determined with a CO5BOLD 3D Model Atmosphere. *SoPh*, [268, 255](#).
- Calvet, N., Hartmann, L., and Strom, S. E. (2000). Evolution of Disk Accretion. *Protostars and Planets IV*, [page 377](#).
- Calzetti, D. (1997). UV opacity in nearby galaxies and application to distant galaxies. In Waller, W. H., editor, *American Institute of Physics Conference Series*, volume 408 of *American Institute of Physics Conference Series*, pages 403–412.
- Calzetti, D., Armus, L., Bohlin, R. C., Kinney, A. L., Koornneef, J., and Storchi-Bergmann, T. (2000). The Dust Content and Opacity of Actively Star-forming Galaxies. *ApJ*, [533, 682](#).
- Calzetti, D., Kinney, A. L., and Storchi-Bergmann, T. (1996). Dust Obscuration in Starburst Galaxies from Near-Infrared Spectroscopy. *ApJ*, [458, 132](#).
- Cardelli, J. A., Clayton, G. C., and Mathis, J. S. (1989). The relationship between infrared, optical, and ultraviolet extinction. *ApJ*, [345, 245](#).
- Carlson, L. R., Sabbi, E., Sirianni, M., Hora, J. L., Nota, A., Meixner, M., Gallagher, III, J. S., Oey, M. S., Pasquali, A., Smith, L. J., Tosi, M., and Waltherbos, R. (2007). Progressive Star Formation in the Young SMC Cluster NGC 602. *ApJL*, [665, L109](#).
- Carraro, G. and Munari, U. (2004). A multicolour CCD photometric study of the open clusters NGC 2866, Pismis 19, Westerlund 2, ESO96-SC04, NGC 5617 and NGC 6204. *MNRAS*, [347, 625](#).
- Carraro, G., Romaniello, M., Ventura, P., and Patat, F. (2004). The star cluster Collinder 232 in the Carina complex and its relation to Trumpler 14/16. *A&A*, [418, 525](#).
- Carraro, G., Turner, D., Majaess, D., and Baume, G. (2013). The distance to the young open cluster Westerlund 2. *A&A*, [555, A50](#).
- Casanova, S., Montmerle, T., Feigelson, E. D., and Andre, P. (1995). ROSAT X-ray sources embedded in the rho Ophiuchi cloud core. *ApJ*, [439, 752](#).
- Castelli, F. and Kurucz, R. L. (2003). New Grids of ATLAS9 Model Atmospheres. In Piskunov, N., Weiss, W. W., and Gray, D. F., editors, *Modelling of Stellar Atmospheres*, volume 210 of *IAU Symposium*, page 20. Astronomical Society of the Pacific.
- Chabrier, G. (2003a). Galactic Stellar and Substellar Initial Mass Function. *PASP*, [115, 763](#).

-
- Chabrier, G. (2003b). The Galactic Disk Mass Function: Reconciliation of the Hubble Space Telescope and Nearby Determinations. *ApJL*, **586**, L133.
- Cheung, A. C., Rank, D. M., Townes, C. H., Thornton, D. D., and Welch, W. J. (1968). Detection of NH₃ Molecules in the Interstellar Medium by Their Microwave Emission. *Physical Review Letters*, **21**, 1701.
- Chiang, E. I. and Goldreich, P. (1999). Spectral Energy Distributions of Passive T Tauri Disks: Inclination. *ApJ*, **519**, 279.
- Choi, J., Dotter, A., Conroy, C., Cantiello, M., Paxton, B., and Johnson, B. D. (2016). Mesa Isochrones and Stellar Tracks (MIST). I. Solar-scaled Models. *ApJ*, **823**, 102.
- Churchwell, E., Whitney, B. A., Babler, B. L., Indebetouw, R., Meade, M. R., Watson, C., Wolff, M. J., Wolfire, M. G., Bania, T. M., Benjamin, R. A., Clemens, D. P., Cohen, M., Devine, K. E., Dickey, J. M., Heitsch, F., Jackson, J. M., Kobulnicky, H. A., Marston, A. P., Mathis, J. S., Mercer, E. P., Stauffer, J. R., and Stolovy, S. R. (2004). RCW 49 at Mid-Infrared Wavelengths: A GLIMPSE from the Spitzer Space Telescope. *ApJS*, **154**, 322.
- Cignoni, M., Sabbi, E., Nota, A., Tosi, M., Degl'Innocenti, S., Moroni, P. G. P., Angeretti, L., Carlson, L. R., Gallagher, J., Meixner, M., Sirianni, M., and Smith, L. J. (2009). Star Formation History in the Small Magellanic Cloud: The Case of NGC 602. *AJ*, **137**, 3668.
- Cignoni, M., Sabbi, E., van der Marel, R. P., Tosi, M., Zaritsky, D., Anderson, J., Lennon, D. J., Aloisi, A., de Marchi, G., Gouliermis, D. A., Grebel, E. K., Smith, L. J., and Zeidler, P. (2015). Hubble Tarantula Treasury Project. II. The Star-formation History of the Starburst Region NGC 2070 in 30 Doradus. *ApJ*, **811**, 76.
- Cignoni, M., Tosi, M., Sabbi, E., Nota, A., Degl'Innocenti, S., Prada Moroni, P. G., and Gallagher, J. S. (2010). Pre-main-sequence Turn-On as a Chronometer for Young Clusters: NGC 346 as a Benchmark. *ApJL*, **712**, L63.
- Cignoni, M., Tosi, M., Sabbi, E., Nota, A., and Gallagher, J. S. (2011). History and Modes of Star Formation in the Most Active Region of the Small Magellanic Cloud, NGC 346. *AJ*, **141**, 31.
- Clark, J. S., Negueruela, I., Crowther, P. A., and Goodwin, S. P. (2005). On the massive stellar population of the super star cluster Westerlund 1. *A&A*, **434**, 949.
- Clarke, C. (2010). The physics and modes of star cluster formation: simulations. *Philosophical Transactions of the Royal Society of London Series A*, **368**, 733.
- Clarke, C. J. (2007). The photoevaporation of discs around young stars in massive clusters. *MNRAS*, **376**, 1350.
- Clemens, D. P., Sanders, D. B., and Scoville, N. Z. (1988). The large-scale distribution of molecular gas in the first Galactic quadrant. *ApJ*, **327**, 139.
- Crowther, P. A., Caballero-Nieves, S. M., Bostroem, K. A., Maíz Apellániz, J., Schneider, F. R. N., Walborn, N. R., Angus, C. R., Brott, I., Bonanos, A., de Koter, A., de Mink, S. E., Evans, C. J., Gräfenor, G., Herrero, A., Howarth, I. D., Langer, N., Lennon, D. J., Puls, J., Sana, H., and Vink, J. S. (2016). The R136 star cluster dissected with Hubble Space Telescope/STIS. I. Far-ultraviolet spectroscopic census and the origin of He II λ 1640 in young star clusters. *MNRAS*, **458**, 624.
- Crowther, P. A., Hadfield, L. J., Clark, J. S., Negueruela, I., and Vacca, W. D. (2006). A census of the Wolf-Rayet content in Westerlund 1 from near-infrared imaging and spectroscopy. *MNRAS*, **372**, 1407.
- Da Rio, N., Gouliermis, D. A., and Gennaro, M. (2010). A New Method for the Assessment of Age and Age Spread of Pre-main-sequence Stars in Young Stellar Associations of the Magellanic Clouds. *ApJ*, **723**, 166.
- Da Rio, N., Robberto, M., Hillenbrand, L. A., Henning, T., and Stassun, K. G. (2012). The Initial Mass Function of the Orion Nebula Cluster across the H-burning Limit. *ApJ*, **748**, 14.
- Da Rio, N., Tan, J. C., and Jaehnig, K. (2014). The Structure, Dynamics, and Star Formation Rate of the Orion Nebula Cluster. *ApJ*, **795**, 55.
- Dahm, S. E. (2008). A Spectroscopic Examination of Accretion Diagnostics for Near Solar Mass Stars in IC 348. *AJ*, **136**, 521.
- Dalcanton, J. J., Williams, B. F., Lang, D., Lauer, T. R., Kalirai, J. S., Seth, A. C., Dolphin, A., Rosenfield, P., Weisz, D. R., Bell, E. F., Bianchi, L. C., Boyer, M. L., Caldwell, N., Dong, H., Dorman, C. E., Gilbert, K. M., Girardi, L., Gogarten, S. M., Gordon, K. D., Guhathakurta, P., Hodge, P. W., Holtzman, J. A., Johnson, L. C., Larsen, S. S., Lewis, A., Melbourne, J. L., Olsen, K. A. G., Rix, H.-W., Rosema, K., Saha, A., Sarajedini, A., Skillman, E. D., and Stanek, K. Z. (2012). The Panchromatic Hubble Andromeda Treasury. *ApJS*, **200**, 18.
- Dale, J. E. (2015). The modelling of feedback in star formation simulations. *NewAR*, **68**, 1.
- Dale, J. E. and Bonnell, I. A. (2008). The effect of stellar winds on the formation of a protocluster. *MNRAS*, **391**, 2.

-
- Dale, J. E., Bonnell, I. A., Clarke, C. J., and Bate, M. R. (2005). Photoionizing feedback in star cluster formation. *MNRAS*, **358**, 291.
- Dale, J. E., Ercolano, B., and Bonnell, I. A. (2012). Ionizing feedback from massive stars in massive clusters - II. Disruption of bound clusters by photoionization. *MNRAS*, **424**, 377.
- Dale, J. E., Ercolano, B., and Bonnell, I. A. (2015). Early evolution of embedded clusters. *MNRAS*, **451**, 987.
- Dame, T. M. (2007). On the Distance and Molecular Environment of Westerlund 2 and HESS J1023-575. *ApJL*, **665**, L163.
- de Jong, T., Boland, W., and Dalgarno, A. (1980). Hydrostatic models of molecular clouds. *A&A*, **91**, 68.
- De Marchi, G., Beccari, G., and Panagia, N. (2013). Photometric Determination of the Mass Accretion Rates of Pre-main-sequence Stars. IV. Recent Star Formation in NGC 602. *ApJ*, **775**, 68.
- De Marchi, G. and Panagia, N. (2015). Star formation in the Local Group as seen by low-mass stars. *ArXiv e-prints*, .
- De Marchi, G., Panagia, N., and Romaniello, M. (2010). Photometric Determination of the Mass Accretion Rates of Pre-main-sequence Stars. I. Method and Application to the SN 1987A Field. *ApJ*, **715**, 1.
- De Marchi, G., Panagia, N., Romaniello, M., Sabbi, E., Sirianni, M., Prada Moroni, P. G., and Degl'Innocenti, S. (2011a). Photometric Determination of the Mass Accretion Rates of Pre-main-sequence Stars. II. NGC 346 in the Small Magellanic Cloud. *ApJ*, **740**, 11.
- De Marchi, G., Paresce, F., Panagia, N., Beccari, G., Spezzi, L., Sirianni, M., Andersen, M., Mutchler, M., Balick, B., Dopita, M. A., Frogel, J. A., Whitmore, B. C., Bond, H., Calzetti, D., Carollo, C. M., Disney, M. J., Hall, D. N. B., Holtzman, J. A., Kimble, R. A., McCarthy, P. J., O'Connell, R. W., Saha, A., Silk, J. I., Trauger, J. T., Walker, A. R., Windhorst, R. A., and Young, E. T. (2011b). Star Formation in 30 Doradus. *ApJ*, **739**, 27.
- Delgado-Donate, E. J., Clarke, C. J., Bate, M. R., and Hodgkin, S. T. (2004). On the properties of young multiple stars. *MNRAS*, **351**, 617.
- Dolphin, A. E. (2000). WFPC2 Stellar Photometry with HSTPHOT. *PASP*, **112**, 1383.
- Dotter, A. (2016). MESA Isochrones and Stellar Tracks (MIST) 0: Methods for the Construction of Stellar Isochrones. *ApJS*, **222**, 8.
- Draine, B. T. (2003). Interstellar Dust Grains. *ARA&A*, **41**, 241.
- Dressel, L. (2012). *Wide Field Camera 3 Instrument Handbook for Cycle 21 v. 5.0*. Baltimore: STScI.
- Drissen, L., Moffat, A. F. J., Walborn, N. R., and Shara, M. M. (1995). The Dense Galactic Starburst NGC 3603. I. HST/FOS Spectroscopy of Individual Stars in the Core and the source of Ionization and Kinetic Energy. *AJ*, **110**, 2235.
- Eddington, A. S. (1916). On the radiative equilibrium of the stars. *MNRAS*, **77**, 16.
- Eggleton, P. (2006). *Evolutionary Processes in Binary and Multiple Stars*. Cambridge University Press.
- Eisenhauer, F., Quirrenbach, A., Zinnecker, H., and Genzel, R. (1998). Stellar Content of the Galactic Starburst Template NGC 3603 from Adaptive Optics Observations. *ApJ*, **498**, 278.
- Elmegreen, B. G. (2000). Star Formation in a Crossing Time. *ApJ*, **530**, 277.
- Elmegreen, B. G. and Efremov, Y. N. (1997). A Universal Formation Mechanism for Open and Globular Clusters in Turbulent Gas. *ApJ*, **480**, 235.
- Elmegreen, B. G. and Lada, C. J. (1977). Sequential formation of subgroups in OB associations. *ApJ*, **214**, 725.
- Elson, R. A. W., Fall, S. M., and Freeman, K. C. (1987). The structure of young star clusters in the Large Magellanic Cloud. *ApJ*, **323**, 54.
- Emerson, J., McPherson, A., and Sutherland, W. (2006). Visible and Infrared Survey Telescope for Astronomy: Progress Report. *The Messenger*, **126**, 41.
- Ercolano, B., Clarke, C. J., and Drake, J. J. (2009). X-Ray Irradiated Protoplanetary Disk Atmospheres. II. Predictions from Models in Hydrostatic Equilibrium. *ApJ*, **699**, 1639.
- Evans, II, N. J., Dunham, M. M., Jørgensen, J. K., Enoch, M. L., Merín, B., van Dishoeck, E. F., Alcalá, J. M., Myers, P. C., Stapelfeldt, K. R., Huard, T. L., Allen, L. E., Harvey, P. M., van Kempen, T., Blake, G. A., Koerner, D. W., Mundy, L. G., Padgett, D. L., and Sargent, A. I. (2009). The Spitzer c2d Legacy Results: Star-Formation Rates and Efficiencies; Evolution and Lifetimes. *ApJS*, **181**, 321.
- Falcón-Barroso, J., Sánchez-Blázquez, P., Vazdekis, A., Ricciardelli, E., Cardiel, N., Cenarro, A. J., Gorgas, J., and Peletier, R. F. (2011). An updated MILES stellar library and stellar population models. *A&A*, **532**, A95.
- Fang, M., van Boekel, R., Wang, W., Carmona, A., Sicilia-Aguilar, A., and Henning, T. (2009). Star and proto-

-
- planetary disk properties in Orion's suburbs. *A&A*, [504](#), [461](#).
- Fazio, G. G., Hora, J. L., Allen, L. E., Ashby, M. L. N., Barmby, P., Deutsch, L. K., Huang, J.-S., Kleiner, S., Marengo, M., Megeath, S. T., Melnick, G. J., Pahre, M. A., Patten, B. M., Polizotti, J., Smith, H. A., Taylor, R. S., Wang, Z., Willner, S. P., Hoffmann, W. F., Pipher, J. L., Forrest, W. J., McMurty, C. W., McCreight, C. R., McKelvey, M. E., McMurray, R. E., Koch, D. G., Moseley, S. H., Arendt, R. G., Mentzell, J. E., Marx, C. T., Losch, P., Mayman, P., Eichhorn, W., Krebs, D., Jhabvala, M., Gezari, D. Y., Fixsen, D. J., Flores, J., Shakoorzadeh, K., Jungo, R., Hakun, C., Workman, L., Karpati, G., Kichak, R., Whitley, R., Mann, S., Tollestrup, E. V., Eisenhardt, P., Stern, D., Gorjian, V., Bhattacharya, B., Carey, S., Nelson, B. O., Glaccum, W. J., Lacy, M., Lowrance, P. J., Laine, S., Reach, W. T., Stauffer, J. A., Surace, J. A., Wilson, G., Wright, E. L., Hoffman, A., Domingo, G., and Cohen, M. (2004). The Infrared Array Camera (IRAC) for the Spitzer Space Telescope. *ApJS*, [154](#), [10](#).
- Feigelson, E. D., Townsley, L. K., Broos, P. S., Busk, H. A., Getman, K. V., King, R. R., Kuhn, M. A., Naylor, T., Povich, M. S., Baddeley, A., Bate, M. R., Indebetouw, R., Luhman, K. L., McCaughrean, M. J., Pittard, J. M., Pudritz, R. E., Sills, A., Song, Y., and Wadsley, J. (2013). Overview of the Massive Young Star-Forming Complex Study in Infrared and X-Ray (MYStIX) Project. *ApJS*, [209](#), [26](#).
- Ferrière, K., Gillard, W., and Jean, P. (2007). Spatial distribution of interstellar gas in the innermost 3 kpc of our galaxy. *A&A*, [467](#), [611](#).
- Fiedler, R. A. and Mouschovias, T. C. (1993). Ambipolar Diffusion and Star Formation: Formation and Contraction of Axisymmetric Cloud Cores. II. Results. *ApJ*, [415](#), [680](#).
- Figer, D. F. (2005). An upper limit to the masses of stars. *Nature*, [434](#), [192](#).
- Figer, D. F., McLean, I. S., and Morris, M. (1999a). Massive Stars in the Quintuplet Cluster. *ApJ*, [514](#), [202](#).
- Figer, D. F., Morris, M., Kim, S. S., and Serabyn, E. (1999b). HST/NICMOS Imaging of the Quintuplet and Arches Clusters. In Falcke, H., Cotera, A., Duschl, W. J., Melia, F., and Rieke, M. J., editors, *The Central Parsecs of the Galaxy*, volume 186 of *Astronomical Society of the Pacific Conference Series*, page 329.
- Figer, D. F., Najarro, F., Gilmore, D., Morris, M., Kim, S. S., Serabyn, E., McLean, I. S., Gilbert, A. M., Graham, J. R., Larkin, J. E., Levenson, N. A., and Teplitz, H. I. (2002). Massive Stars in the Arches Cluster. *ApJ*, [581](#), [258](#).
- Fitzgerald, M. P. (1970). The Intrinsic Colours of Stars and Two-Colour Reddening Lines. *A&A*, [4](#), [234](#).
- Fitzpatrick, E. L. (1999). Correcting for the Effects of Interstellar Extinction. *PASP*, [111](#), [63](#).
- Forbes, D. A. and Bridges, T. (2010). Accreted versus in situ Milky Way globular clusters. *MNRAS*, [404](#), [1203](#).
- Fruchter, A. and Hook, R. N. (1997). Novel image reconstruction method applied to deep Hubble space telescope images. In Tescher, A. G., editor, *Applications of Digital Image Processing XX*, volume 3164 of *Society of Photo-Optical Instrumentation Engineers (SPIE) Conference Series*, pages 120–125.
- Fruchter, A. S. (2010). BetaDrizzle: A Redesign of the MultiDrizzle Package. In *2010 Space Telescope Science Institute Calibration Workshop*, pages 382–387.
- Fujita, Y., Hayashida, K., Takahashi, H., and Takahara, F. (2009). Suzaku Observation of Diffuse X-Ray Emission from the Open Cluster Westerlund 2: a Supernova Remnant? *PASJ*, [61](#), [1229](#).
- Fukui, Y., Ohama, A., Hanaoka, N., Furukawa, N., Torii, K., Dawson, J. R., Mizuno, N., Hasegawa, K., Fukuda, T., Soga, S., Moribe, N., Kuroda, Y., Hayakawa, T., Kawamura, A., Kuwahara, T., Yamamoto, H., Okuda, T., Onishi, T., Maezawa, H., and Mizuno, A. (2014). Molecular Clouds toward the Super Star Cluster NGC 3603 Possible Evidence for a Cloud-Cloud Collision in Triggering the Cluster Formation. *ApJ*, [780](#), [36](#).
- Fukui, Y., Torii, K., Ohama, A., Hasegawa, K., Hattori, Y., Sano, H., Ohashi, S., Fujii, K., Kuwahara, S., Mizuno, N., Dawson, J. R., Yamamoto, H., Tachihara, K., Okuda, T., Onishi, T., and Mizuno, A. (2016). The Two Molecular Clouds in RCW 38: Evidence for the Formation of the Youngest Super Star Cluster in the Milky Way Triggered by Cloud-Cloud Collision. *ApJ*, [820](#), [26](#).
- Furukawa, N., Dawson, J. R., Ohama, A., Kawamura, A., Mizuno, N., Onishi, T., and Fukui, Y. (2009). Molecular Clouds Toward RCW49 and Westerlund 2: Evidence for Cluster Formation Triggered by Cloud-Cloud Collision. *ApJL*, [696](#), [L115](#).
- Furukawa, N., Ohama, A., Fukuda, T., Torii, K., Hayakawa, T., Sano, H., Okuda, T., Yamamoto, H., Moribe, N., Mizuno, A., Maezawa, H., Onishi, T., Kawamura, A., Mizuno, N., Dawson, J. R., Dame, T. M., Yonekura, Y., Aharonian, F., de Oña Wilhelmi, E., Rowell, G. P., Matsumoto, R., Asahina, Y., and Fukui, Y. (2014). The Jet and Arc Molecular Clouds toward Westerlund 2, RCW 49, and HESS J1023-575 ^{12}CO and ^{13}CO ($J = 2-1$ and $J = 1-0$) observations with NANTEN2 and Mopra Telescope. *ApJ*, [781](#), [70](#).

-
- Gascoigne, S. C. B. and Kron, G. E. (1952). Colors and Magnitudes of Some Star Clusters in the Magellanic Clouds. *PASP*, **64**, 196.
- Gennaro, M., Brandner, W., Stolte, A., and Henning, T. (2011). Mass segregation and elongation of the starburst cluster Westerlund 1. *MNRAS*, **412**, 2469.
- Gieles, M., Athanassoula, E., and Portegies Zwart, S. F. (2007). The effect of spiral arm passages on the evolution of stellar clusters. *MNRAS*, **376**, 809.
- Gieles, M. and Portegies Zwart, S. F. (2011). The distinction between star clusters and associations. *MNRAS*, **410**, L6.
- Gieles, M., Portegies Zwart, S. F., Baumgardt, H., Athanassoula, E., Lamers, H. J. G. L. M., Sipior, M., and Leenaarts, J. (2006). Star cluster disruption by giant molecular clouds. *MNRAS*, **371**, 793.
- Ginsburg, A., Bressert, E., Bally, J., and Battersby, C. (2012). There are No Starless Massive Proto-clusters in the First Quadrant of the Galaxy. *ApJL*, **758**, L29.
- Gnedin, O. Y., Lee, H. M., and Ostriker, J. P. (1999). Effects of Tidal Shocks on the Evolution of Globular Clusters. *ApJ*, **522**, 935.
- Gnedin, O. Y. and Ostriker, J. P. (1997). Destruction of the Galactic Globular Cluster System. *ApJ*, **474**, 223.
- Goldsmith, P. F. (2001). Molecular Depletion and Thermal Balance in Dark Cloud Cores. *ApJ*, **557**, 736.
- Goldsmith, P. F. and Langer, W. D. (1978). Molecular cooling and thermal balance of dense interstellar clouds. *ApJ*, **222**, 881.
- Gonzaga, S. and Biretta, J. (2010). in *HST WFPC2 Data Handbook*, v. 5.0, ed. Baltimore: STScI.
- Grabelsky, D. A., Cohen, R. S., Bronfman, L., Thaddeus, P., and May, J. (1987). Molecular clouds in the Carina arm - Large-scale properties of molecular gas and comparison with H I. *ApJ*, **315**, 122.
- Grebel, E. K. (1997). Be star surveys with CCD photometry. II. NGC 1818 and its neighbouring cluster in the Large Magellanic Cloud. *A&A*, **317**, 448.
- Grebel, E. K., Richtler, T., and de Boer, K. S. (1992). Be-Star Surveys with CCD Photometry - Part One - NGC330 and its High Be-Star Content. *A&A*, **254**, L5.
- Grebel, E. K., Roberts, W. J., Will, J.-M., and de Boer, K. S. (1993). Be Stars in young clusters in the Magellanic clouds. *SSRv*, **66**, 65.
- Gullbring, E., Hartmann, L., Briceño, C., and Calvet, N. (1998). Disk Accretion Rates for T Tauri Stars. *ApJ*, **492**, 323.
- Gum, C. S. (1955). A survey of southern HII regions. *MmRAS*, **67**, 155.
- Habe, A. and Ohta, K. (1992). Gravitational instability induced by a cloud-cloud collision - The case of head-on collisions between clouds with different sizes and densities. *PASJ*, **44**, 203.
- Habibi, M., Stolte, A., Brandner, W., Hußmann, B., and Motohara, K. (2013). The Arches cluster out to its tidal radius: dynamical mass segregation and the effect of the extinction law on the stellar mass function. *A&A*, **556**, A26.
- Haghi, H., Zonoozi, A. H., Kroupa, P., Banerjee, S., and Baumgardt, H. (2015). Possible smoking-gun evidence for initial mass segregation in re-virialized post-gas expulsion globular clusters. *MNRAS*, **454**, 3872.
- Harayama, Y., Eisenhauer, F., and Martins, F. (2008). The Initial Mass Function of the Massive Star-forming Region NGC 3603 from Near-Infrared Adaptive Optics Observations. *ApJ*, **675**, 1319.
- Harfst, S., Portegies Zwart, S., and Stolte, A. (2010). Reconstructing the Arches cluster - I. Constraining the initial conditions. *MNRAS*, **409**, 628.
- Hartmann, L., Calvet, N., Gullbring, E., and D'Alessio, P. (1998). Accretion and the Evolution of T Tauri Disks. *ApJ*, **495**, 385.
- Hayashi, C. (1961). Stellar evolution in early phases of gravitational contraction. *PASJ*, **13**.
- Heggie, D. and Hut, P. (2003). Book Review: The gravitational million-body problem - a multidisciplinary approach to star cluster dynamics. Cambridge, Cambridge University Press, XIV+357 pp., 2003, ISBN 0-521-77486-1 (paper), ISBN 0-521-77303-2 (cloth). *Orion: Zeitschrift für Amateur-Astronomie*, **61**, 45.
- Herbig, G. H. (1954). Emission-Line Stars Associated with the Nebulous Cluster NGC 2264. *ApJ*, **119**, 483.
- Herbig, G. H. (1960). The Spectra of Be- and Ae-TYPE Stars Associated with Nebulosity. *ApJS*, **4**, 337.
- Herbig, G. H. (1998). The Young Cluster IC 348. *ApJ*, **497**, 736.
- Hill, E. R., Slee, O. B., and Mills, B. Y. (1958). A Pencil-beam Survey of the Galactic Plane at 3.5 m. *Australian Journal of Physics*, **11**, 530.

-
- Hillenbrand, L. A. (1997). On the Stellar Population and Star-Forming History of the Orion Nebula Cluster. *AJ*, [113](#), [1733](#).
- Hillenbrand, L. A. and Carpenter, J. M. (2000). Constraints on the Stellar/Substellar Mass Function in the Inner Orion Nebula Cluster. *ApJ*, [540](#), [236](#).
- Hillenbrand, L. A. and Hartmann, L. W. (1998). A Preliminary Study of the Orion Nebula Cluster Structure and Dynamics. *ApJ*, [492](#), [540](#).
- Hillenbrand, L. A., Massey, P., Strom, S. E., and Merrill, K. M. (1993). NGC 6611: A cluster caught in the act. *AJ*, [106](#), [1906](#).
- Hills, J. G. (1980). The effect of mass loss on the dynamical evolution of a stellar system - Analytic approximations. *ApJ*, [235](#), [986](#).
- Hind, J. R. (1864). Note on the Variable Nebula in Taurus. *MNRAS*, [24](#), [65](#).
- Hodge, P. W. (1961). Studies of the Large Magellanic Cloud. V. The Young Populous Clusters. *ApJ*, [133](#), [413](#).
- Hopkins, P. F., Cox, T. J., Hernquist, L., Narayanan, D., Hayward, C. C., and Murray, N. (2013). Star formation in galaxy mergers with realistic models of stellar feedback and the interstellar medium. *MNRAS*, [430](#), [1901](#).
- Hunter, D. A., Shaya, E. J., Holtzman, J. A., Light, R. M., O'Neil, Jr., E. J., and Lynds, R. (1995). The Intermediate Stellar Mass Population in R136 Determined from Hubble Space Telescope Planetary Camera 2 Images. *ApJ*, [448](#), [179](#).
- Hur, H., Park, B.-G., Sung, H., Bessell, M. S., Lim, B., Chun, M.-Y., and Sohn, S. T. (2015). Reddening, distance, and stellar content of the young open cluster Westerlund 2. *MNRAS*, [446](#), [3797](#).
- Hur, H., Sung, H., and Bessell, M. S. (2012). Distance and the Initial Mass Function of Young Open Clusters in the η Carina Nebula: Tr 14 and Tr 16. *AJ*, [143](#), [41](#).
- Hußmann, B., Stolte, A., Brandner, W., Gennaro, M., and Liermann, A. (2012). The present-day mass function of the Quintuplet cluster based on proper motion membership. *A&A*, [540](#), [A57](#).
- Jeans, J. H. (1928). *Astronomy and cosmogony*. Cambridge University Press.
- Johnson, H. L. and Morgan, W. W. (1953). Fundamental stellar photometry for standards of spectral type on the revised system of the Yerkes spectral atlas. *ApJ*, [117](#), [313](#).
- Johnson, K. E., Leroy, A. K., Indebetouw, R., Brogan, C. L., Whitmore, B. C., Hibbard, J., Sheth, K., and Evans, A. S. (2015). The Physical Conditions in a Pre-super Star Cluster Molecular Cloud in the Antennae Galaxies. *ApJ*, [806](#), [35](#).
- Jones, B. F. and Walker, M. F. (1988). Proper motions and variabilities of stars near the Orion Nebula. *AJ*, [95](#), [1755](#).
- Joy, A. H. (1945). T Tauri Variable Stars. *ApJ*, [102](#), [168](#).
- Kamann, S., Husser, T.-O., Brinchmann, J., Emsellem, E., Weilbacher, P. M., Wisotzki, L., Wendt, M., Krajnović, D., Roth, M. M., Bacon, R., and Dreizler, S. (2016). MUSE crowded field 3D spectroscopy of over 12 000 stars in the globular cluster NGC 6397. II. Probing the internal dynamics and the presence of a central black hole. *A&A*, [588](#), [A149](#).
- Kamann, S., Wisotzki, L., and Roth, M. M. (2013). Resolving stellar populations with crowded field 3D spectroscopy. *A&A*, [549](#), [A71](#).
- Kennicutt, Jr., R. C. (1991). *Properties of Giant H II Regions*, page 349. the Cambridge University Press.
- King, I. (1962). The structure of star clusters. I. an empirical density law. *AJ*, [67](#), [471](#).
- King, I. R. (1966). The structure of star clusters. IV. Photoelectric surface photometry in nine globular clusters. *AJ*, [71](#), [276](#).
- Kissler-Patig, M., Pirard, J.-F., Casali, M., Moorwood, A., Ageorges, N., Alves de Oliveira, C., Baksai, P., Bedin, L. R., Bendek, E., Biereichel, P., Delabre, B., Dorn, R., Esteves, R., Finger, G., Gojak, D., Huster, G., Jung, Y., Kiekebush, M., Klein, B., Koch, F., Lizon, J.-L., Mehrgan, L., Petr-Gotzens, M., Pritchard, J., Selman, F., and Stegmeier, J. (2008). HAWK-I: the high-acuity wide-field K-band imager for the ESO Very Large Telescope. *A&A*, [491](#), [941](#).
- Kroupa, P. (1995). The dynamical properties of stellar systems in the Galactic disc. *MNRAS*, [277](#).
- Kroupa, P. (2001). On the variation of the initial mass function. *MNRAS*, [322](#), [231](#).
- Kroupa, P. (2004). Massive stars: their birth sites and distribution. *NewAR*, [48](#), [47](#).
- Kruijssen, J. M. D. (2012). On the fraction of star formation occurring in bound stellar clusters. *MNRAS*, [426](#), [3008](#).

-
- Kruijssen, J. M. D. (2014). A Galactic-Scale Origin for Stellar Clustering. In Stamatellos, D., Goodwin, S., and Ward-Thompson, D., editors, *The Labyrinth of Star Formation*, volume 36 of *Astrophysics and Space Science Proceedings*, page 437.
- Kruijssen, J. M. D. (2015). Are globular clusters the natural outcome of regular high-redshift star formation? *ArXiv e-prints*, .
- Kruijssen, J. M. D. and Longmore, S. N. (2013). Comparing molecular gas across cosmic time-scales: the Milky Way as both a typical spiral galaxy and a high-redshift galaxy analogue. *MNRAS*, **435**, 2598.
- Kruijssen, J. M. D., Pelupessy, F. I., Lamers, H. J. G. L. M., Portegies Zwart, S. F., and Icke, V. (2011). Modelling the formation and evolution of star cluster populations in galaxy simulations. *MNRAS*, **414**, 1339.
- Krumholz, M. R., Klein, R. I., McKee, C. F., Offner, S. S. R., and Cunningham, A. J. (2009). The Formation of Massive Star Systems by Accretion. *Science*, **323**, 754.
- Kudritzki, R. P. (2002). Line-driven Winds, Ionizing Fluxes, and Ultraviolet Spectra of Hot Stars at Extremely Low Metallicity. I. Very Massive O Stars. *ApJ*, **577**, 389.
- Kuhn, M. A., Feigelson, E. D., Getman, K. V., Baddeley, A. J., Broos, P. S., Sills, A., Bate, M. R., Povich, M. S., Luhman, K. L., Busk, H. A., Naylor, T., and King, R. R. (2014). The Spatial Structure of Young Stellar Clusters. I. Subclusters. *ApJ*, **787**, 107.
- Kuhn, M. A., Getman, K. V., and Feigelson, E. D. (2015). The Spatial Structure of Young Stellar Clusters. II. Total Young Stellar Populations. *ApJ*, **802**, 60.
- Kurosawa, R., Harries, T. J., and Symington, N. H. (2006). On the formation of H α line emission around classical T Tauri stars. *MNRAS*, **370**, 580.
- Kurosawa, R. and Romanova, M. M. (2012). Line formation in the inner winds of classical T Tauri stars: testing the conical-shell wind solution. *MNRAS*, **426**, 2901.
- Lada, C. J. (2005). Star Formation in the Galaxy: An Observational Overview. *Progress of Theoretical Physics Supplement*, **158**, 1.
- Lada, C. J. and Lada, E. A. (2003). Embedded Clusters in Molecular Clouds. *ARA&A*, **41**, 57.
- Lada, C. J., Margulis, M., and Dearborn, D. (1984). The formation and early dynamical evolution of bound stellar systems. *ApJ*, **285**, 141.
- Lada, C. J. and Wilking, B. A. (1984). The nature of the embedded population in the Rho Ophiuchi dark cloud - Mid-infrared observations. *ApJ*, **287**, 610.
- Lada, E. A., Depoy, D. L., Evans, II, N. J., and Gatley, I. (1991). A 2.2 micron survey in the L1630 molecular cloud. *ApJ*, **371**, 171.
- Laidler et al. (2005). *Synphot Users's Guide*, volume Version 5.0. Baltimore: STScI.
- Lang, C. C., Goss, W. M., and Rodríguez, L. F. (2001). Very Large Array Detection of the Ionized Stellar Winds Arising from Massive Stars in the Galactic Center Arches Cluster. *ApJL*, **551**, L143.
- Larson, R. B. (1981). Turbulence and star formation in molecular clouds. *MNRAS*, **194**, 809.
- Lee, E. J., Murray, N., and Rahman, M. (2012). Milky Way Star-forming Complexes and the Turbulent Motion of the Galaxy's Molecular Gas. *ApJ*, **752**, 146.
- Liermann, A., Hamann, W.-R., and Oskinova, L. M. (2009). The Quintuplet cluster. I. A K-band spectral catalog of stellar sources. *A&A*, **494**, 1137.
- Liermann, A., Hamann, W.-R., and Oskinova, L. M. (2012). The Quintuplet cluster. III. Hertzsprung-Russell diagram and cluster age. *A&A*, **540**, A14.
- Liermann, A., Hamann, W.-R., and Oskinova, L. M. (2014). The Quintuplet cluster. III. Hertzsprung-Russell diagram and cluster age (Corrigendum). *A&A*, **563**, C2.
- Liermann, A., Hamann, W.-R., Oskinova, L. M., Todt, H., and Butler, K. (2010). The Quintuplet cluster. II. Analysis of the WN stars. *A&A*, **524**, A82.
- Lim, B., Chun, M.-Y., Sung, H., Park, B.-G., Lee, J.-J., Sohn, S. T., Hur, H., and Bessell, M. S. (2013). The Starburst Cluster Westerlund 1: The Initial Mass Function and Mass Segregation. *AJ*, **145**, 46.
- Lizano, S. and Shu, F. H. (1989). Molecular cloud cores and bimodal star formation. *ApJ*, **342**, 834.
- Longmore, S. N., Kruijssen, J. M. D., Bally, J., Ott, J., Testi, L., Rathborne, J., Bastian, N., Bressert, E., Molinari, S., Battersby, C., and Walsh, A. J. (2013). Candidate super star cluster progenitor gas clouds possibly triggered by close passage to Sgr A*. *MNRAS*, **433**, L15.
- Longmore, S. N., Kruijssen, J. M. D., Bastian, N., Bally, J., Rathborne, J., Testi, L., Stolte, A., Dale, J., Bressert,

-
- E., and Alves, J. (2014). The Formation and Early Evolution of Young Massive Clusters. *Protostars and Planets VI*, pages 291–314.
- Lynden-Bell, D. and Pringle, J. E. (1974). The evolution of viscous discs and the origin of the nebular variables. *MNRAS*, 168, 603.
- Mackey, A. D. and Gilmore, G. F. (2003). Surface brightness profiles and structural parameters for 53 rich stellar clusters in the Large Magellanic Cloud. *MNRAS*, 338, 85.
- Maíz-Apellániz, J. (2002). The Size Distribution of Massive Young Clusters. In Geisler, D. P., Grebel, E. K., and Minniti, D., editors, *Extragalactic Star Clusters*, volume 207 of *IAU Symposium*, page 697.
- Maíz Apellániz, J. (2013). Do we need a new family of optical-NIR extinction laws? In Guirado, J. C., Lara, L. M., Quilis, V., and Gorgas, J., editors, *Highlights of Spanish Astrophysics VII*, page 583. Spanish Astronomical Society.
- Massey, P. (2003). MASSIVE STARS IN THE LOCAL GROUP: Implications for Stellar Evolution and Star Formation. *ARA&A*, 41, 15.
- Massey, P., Lang, C. C., Degioia-Eastwood, K., and Garmany, C. D. (1995). Massive stars in the field and associations of the magellanic clouds: The upper mass limit, the initial mass function, and a critical test of main-sequence stellar evolutionary theory. *ApJ*, 438, 188.
- Massey, P., Parker, J. W., and Garmany, C. D. (1989). The stellar content of NGC 346 - A plethora of O stars in the SMC. *AJ*, 98, 1305.
- Mathis, J. S. (1990). Interstellar dust and extinction. In Blitz, L., editor, *The Evolution of the Interstellar Medium*, volume 12 of *Astronomical Society of the Pacific Conference Series*, pages 63–77.
- Mathis, J. S. and Wallenhorst, S. G. (1981). The size distribution of interstellar particles. III - Peculiar extinctions and normal infrared extinction. *ApJ*, 244, 483.
- McKee, C. F. (1999). The Dynamical Structure and Evolution of Giant Molecular Clouds. In Lada, C. J. and Kylafis, N. D., editors, *NATO Advanced Science Institutes (ASI) Series C*, volume 540 of *NATO Advanced Science Institutes (ASI) Series C*, page 29.
- McLeod, A. F., Dale, J. E., Ginsburg, A., Ercolano, B., Gritschneider, M., Ramsay, S., and Testi, L. (2015). The Pillars of Creation revisited with MUSE: gas kinematics and high-mass stellar feedback traced by optical spectroscopy. *MNRAS*, 450, 1057.
- McLeod, A. F., Gritschneider, M., Dale, J. E., Ginsburg, A., Klaassen, P. D., Mottram, J. C., Preibisch, T., Ramsay, S., Reiter, M., and Testi, L. (2016). Connecting the dots: a correlation between ionizing radiation and cloud mass-loss rate traced by optical integral field spectroscopy. *MNRAS*, 462, 3537.
- McMillan, S. L. W., Vesperini, E., and Portegies Zwart, S. F. (2007). A Dynamical Origin for Early Mass Segregation in Young Star Clusters. *ApJL*, 655, L45.
- McNamara, D. H., Madsen, J. B., Barnes, J., and Ericksen, B. F. (2000). The Distance to the Galactic Center. *PASP*, 112, 202.
- Mengel, S. and Tacconi-Garman, L. E. (2009). Westerlund 1: bound or unbound? *Ap&SS*, 324, 321.
- Mizuno, A. and Fukui, Y. (2004). Physical properties of molecular clouds as revealed by NANTEN CO survey: from the galactic center to the galactic warp. In Clemens, D., Shah, R., and Brainerd, T., editors, *Milky Way Surveys: The Structure and Evolution of our Galaxy*, volume 317 of *Astronomical Society of the Pacific Conference Series*, page 59.
- Moekkel, N. and Bonnell, I. A. (2009). Does subcluster merging accelerate mass segregation in local clusters? *MNRAS*, 400, 657.
- Moffat, A. F. J., Shara, M. M., and Potter, M. (1991a). New Wolf-Rayet stars in Galactic open clusters - Sher 1 and the giant H II region core Westerlund 2. *AJ*, 102, 642.
- Moffat, A. F. J., Shara, M. M., and Potter, M. (1991b). New Wolf-Rayet stars in Galactic open clusters - Sher 1 and the giant H II region core Westerlund 2. *AJ*, 102, 642.
- Mohr-Smith, M., Drew, J. E., Barentsen, G., Wright, N. J., Napiwotzki, R., Corradi, R. L. M., Eislöffel, J., Groot, P., Kalari, V., Parker, Q. A., Raddi, R., Sale, S. E., Unruh, Y. C., Vink, J. S., and Wesson, R. (2015). New OB star candidates in the Carina Arm around Westerlund 2 from VPHAS+. *MNRAS*, 450, 3855.
- Molinari, S., Bally, J., Glover, S., Moore, T., Noreiga-Crespo, A., Plume, R., Testi, L., Vázquez-Semadeni, E., Zavagno, A., Bernard, J.-P., and Martin, P. (2014). The Milky Way as a Star Formation Engine. *Protostars and Planets VI*, pages 125–148.

-
- Morris, M. and Serabyn, E. (1996). The Galactic Center Environment. *ARA&A*, **34**, 645.
- Muench, A., Getman, K., Hillenbrand, L., and Preibisch, T. (2008). *Star Formation in the Orion Nebula I: Stellar Content*, page 483. Astronomical Society of the Pacific.
- Muno, M. P., Law, C., Clark, J. S., Dougherty, S. M., de Grijs, R., Portegies Zwart, S., and Yusef-Zadeh, F. (2006). Diffuse, Nonthermal X-Ray Emission from the Galactic Star Cluster Westerlund 1. *ApJ*, **650**, 203.
- Muzerolle, J., Briceño, C., Calvet, N., Hartmann, L., Hillenbrand, L., and Gullbring, E. (2000). Detection of Disk Accretion at the Substellar Limit. *ApJL*, **545**, L141.
- Muzerolle, J., Calvet, N., and Hartmann, L. (2001). Emission-Line Diagnostics of T Tauri Magnetospheric Accretion. II. Improved Model Tests and Insights into Accretion Physics. *ApJ*, **550**, 944.
- Muzerolle, J., Flaherty, K., Balog, Z., Furlan, E., Smith, P. S., Allen, L., Calvet, N., D'Alessio, P., Megeath, S. T., Muench, A., Rieke, G. H., and Sherry, W. H. (2009). Evidence for Dynamical Changes in a Transitional Protoplanetary Disk with Mid-Infrared Variability. *ApJL*, **704**, L15.
- Muzerolle, J., Hartmann, L., and Calvet, N. (1998a). A Brgamma Probe of Disk Accretion in T Tauri Stars and Embedded Young Stellar Objects. *AJ*, **116**, 2965.
- Muzerolle, J., Hartmann, L., and Calvet, N. (1998b). Emission-Line Diagnostics of T Tauri Magnetospheric Accretion. I. Line Profile Observations. *AJ*, **116**, 455.
- Nagata, T., Woodward, C. E., Shure, M., Pipher, J. L., and Okuda, H. (1990). AFGL 2004 - an infrared quintuplet near the Galactic center. *ApJ*, **351**, 83.
- Najarro, F., Figer, D. F., Hillier, D. J., Geballe, T. R., and Kudritzki, R. P. (2009). Metallicity in the Galactic Center: The Quintuplet Cluster. *ApJ*, **691**, 1816.
- Nakano, T. (1984). Contraction of magnetic interstellar clouds. *FChPh*, **9**, 139.
- Negueruela, I., Clark, J. S., and Ritchie, B. W. (2010). The population of OB supergiants in the starburst cluster Westerlund 1. *A&A*, **516**, A78.
- Nigra, L., Gallagher, J. S., Smith, L. J., Stanimirović, S., Nota, A., and Sabbi, E. (2008). NGC 602 Environment, Kinematics and Origins. *PASP*, **120**, 972.
- Nota, A., Sirianni, M., Sabbi, E., Tosi, M., Clampin, M., Gallagher, J., Meixner, M., Oey, M. S., Pasquali, A., Smith, L. J., Waltherbos, R., and Mack, J. (2006). Discovery of a Population of Pre-Main-Sequence Stars in NGC 346 from Deep Hubble Space Telescope ACS Images. *ApJL*, **640**, L29.
- O'Dell, C. R., Muench, A., Smith, N., and Zapata, L. (2008). *Star Formation in the Orion Nebula II: Gas, Dust, Proplyds and Outflows*, page 544. Astronomical Society of the Pacific.
- Ohama, A., Dawson, J. R., Furukawa, N., Kawamura, A., Moribe, N., Yamamoto, H., Okuda, T., Mizuno, N., Onishi, T., Maezawa, H., Minamidani, T., Mizuno, A., and Fukui, Y. (2010). Temperature and Density Distribution in the Molecular Gas Toward Westerlund 2: Further Evidence for Physical Association. *ApJ*, **709**, 975.
- Osterbrock, D. E. and Bochkarev, N. G. (1989). Book-Review - Astrophysics of Gaseous Nebulae and Active Galactic Nuclei. *Soviet Ast.*, **33**, 694.
- Ostriker, J. P., Spitzer, Jr., L., and Chevalier, R. A. (1972). On the Evolution of Globular Clusters. *ApJL*, **176**, L51.
- Panagia, N., Romaniello, M., Scuderi, S., and Kirshner, R. P. (2000). Young Stellar Populations around SN 1987A. *ApJ*, **539**, 197.
- Pang, X., Grebel, E. K., Allison, R. J., Goodwin, S. P., Altmann, M., Harbeck, D., Moffat, A. F. J., and Drissen, L. (2013). On the Origin of Mass Segregation in NGC 3603. *ApJ*, **764**, 73.
- Pang, X., Pasquali, A., and Grebel, E. K. (2011). A Two-dimensional Map of the Color Excess in NGC 3603. *AJ*, **142**, 132.
- Panuzzo, P., Bressan, A., Granato, G. L., Silva, L., and Danese, L. (2003). Dust and nebular emission. I. Models for normal galaxies. *A&A*, **409**, 99.
- Parker, R. J. and Goodwin, S. P. (2015). Comparisons between different techniques for measuring mass segregation. *MNRAS*, **449**, 3381.
- Parker, R. J., Wright, N. J., Goodwin, S. P., and Meyer, M. R. (2014). Dynamical evolution of star-forming regions. *MNRAS*, **438**, 620.
- Pellegrini, E. W., Baldwin, J. A., and Ferland, G. J. (2011). Structure and Feedback in 30 Doradus. II. Structure and Chemical Abundances. *ApJ*, **738**, 34.

-
- Peng, E. W., Jordán, A., Côté, P., Takamiya, M., West, M. J., Blakeslee, J. P., Chen, C.-W., Ferrarese, L., Mei, S., Tonry, J. L., and West, A. A. (2008). The ACS Virgo Cluster Survey. XV. The Formation Efficiencies of Globular Clusters in Early-Type Galaxies: The Effects of Mass and Environment. *ApJ*, **681**, 197.
- Piatti, A. E., Bica, E., and Claria, J. J. (1998). Fundamental parameters of the highly reddened young open clusters Westerlund 1 and 2. *A&AS*, **127**, 423.
- Pickles, A. J. (1998). A Stellar Spectral Flux Library: 1150-25000 Å. *PASP*, **110**, 863.
- Pilbratt, G. L., Riedinger, J. R., Passvogel, T., Crone, G., Doyle, D., Gageur, U., Heras, A. M., Jewell, C., Metcalfe, L., Ott, S., and Schmidt, M. (2010). Herschel Space Observatory. An ESA facility for far-infrared and submillimetre astronomy. *A&A*, **518**, L1.
- Pirard, J.-F., Kissler-Patig, M., Moorwood, A., Biereichel, P., Delabre, B., Dorn, R., Finger, G., Gojak, D., Huster, G., Jung, Y., Koch, F., Le Louarn, M., Lizon, J.-L., Mehrgan, L., Pozna, E., Silber, A., Sokar, B., and Stegmeier, J. (2004). HAWK-I: A new wide-field 1- to 2.5- μ m imager for the VLT. In Moorwood, A. F. M. and Iye, M., editors, *Ground-based Instrumentation for Astronomy*, volume 5492 of *Proc. SPIE*, pages 1763–1772.
- Plummer, H. C. (1911). On the problem of distribution in globular star clusters. *MNRAS*, **71**, 460.
- Portegies Zwart, S. F., McMillan, S. L. W., and Gieles, M. (2010). Young Massive Star Clusters. *ARA&A*, **48**, 431.
- Povich, M. S., Benjamin, R. A., Whitney, B. A., Babler, B. L., Indebetouw, R., Meade, M. R., and Churchwell, E. (2008). Interstellar Weather Vanes: GLIMPSE Mid-Infrared Stellar Wind Bow Shocks in M17 and RCW 49. *ApJ*, **689**, 242.
- Preibisch, T. (2012). The reliability of age measurements for Young Stellar Objects from Hertzsprung-Russell or color-magnitude diagrams. *Research in Astronomy and Astrophysics*, **12**, 1.
- Preibisch, T., Brown, A. G. A., Bridges, T., Guenther, E., and Zinnecker, H. (2002). Exploring the Full Stellar Population of the Upper Scorpius OB Association. *AJ*, **124**, 404.
- Preibisch, T., Zeidler, P., Ratzka, T., Roccatagliata, V., and Petr-Gotzens, M. G. (2014). The VISTA Carina Nebula Survey . I. Introduction and source catalog. *A&A*, **572**, A116.
- Preibisch, T., Zinnecker, H., and Herbig, G. H. (1996). ROSAT X-ray observations of the young cluster IC 348. *A&A*, **310**, 456.
- Price, D. J. and Bate, M. R. (2009). Inefficient star formation: the combined effects of magnetic fields and radiative feedback. *MNRAS*, **398**, 33.
- Rauw, G., Crowther, P. A., De Becker, M., Gosset, E., Nazé, Y., Sana, H., van der Hucht, K. A., Vreux, J.-M., and Williams, P. M. (2005). The spectrum of the very massive binary system WR 20a (WN6ha + WN6ha): Fundamental parameters and wind interactions. *A&A*, **432**, 985.
- Rauw, G., De Becker, M., Nazé, Y., Crowther, P. A., Gosset, E., Sana, H., van der Hucht, K. A., Vreux, J.-M., and Williams, P. M. (2004). WR 20a: A massive cornerstone binary system comprising two extreme early-type stars. *A&A*, **420**, L9.
- Rauw, G., Manfroid, J., Gosset, E., Nazé, Y., Sana, H., De Becker, M., Foellmi, C., and Moffat, A. F. J. (2007). Early-type stars in the core of the young open cluster Westerlund 2. *A&A*, **463**, 981.
- Rauw, G., Sana, H., and Nazé, Y. (2011). A spectroscopic investigation of early-type stars in the young open cluster Westerlund 2. *A&A*, **535**, A40.
- Rieke, G. H. (2009). History of infrared telescopes and astronomy. *Experimental Astronomy*, **25**, 125.
- Robin, A. C., Reylé, C., Derrière, S., and Picaud, S. (2003). A synthetic view on structure and evolution of the Milky Way. *A&A*, **409**, 523.
- Rodgers, A. W., Campbell, C. T., and Whiteoak, J. B. (1960). A catalogue of H α -emission regions in the southern Milky Way. *MNRAS*, **121**, 103.
- Roman-Lopes, A., Barba, R. H., and Morrell, N. I. (2011). Two O2 If*/WN6 stars possibly ejected from the massive young Galactic cluster Westerlund 2. *MNRAS*, **416**, 501.
- Romaniello, M., Panagia, N., Scuderi, S., and Kirshner, R. P. (2002). Accurate Stellar Population Studies from Multiband Photometric Observations. *AJ*, **123**, 915.
- Romaniello, M., Panagia, N., Scuderi, S., and SINS Collaboration (1998). HST Study of the Stellar Populations around SN 1987A. In Richtler, T. and Braun, J. M., editors, *Magellanic Clouds and Other Dwarf Galaxies*, page 197. Shaker Verlag.
- Sabbi, E., Anderson, J., Lennon, D. J., van der Marel, R. P., Aloisi, A., Boyer, M. L., Cignoni, M., de Marchi, G., de Mink, S. E., Evans, C. J., Gallagher, III, J. S., Gordon, K., Gouliermis, D. A., Grebel, E. K., Koekemoer,

-
- A. M., Larsen, S. S., Panagia, N., Ryon, J. E., Smith, L. J., Tosi, M., and Zaritsky, D. (2013). Hubble Tarantula Treasury Project: Unraveling Tarantula's Web. I. Observational Overview and First Results. *AJ*, **146**, 53.
- Sabbi, E., Lennon, D. J., Anderson, J., Cignoni, M., van der Marel, R. P., Zaritsky, D., De Marchi, G., Panagia, N., Gouliermis, D. A., Grebel, E. K., Gallagher, III, J. S., Smith, L. J., Sana, H., Aloisi, A., Tosi, M., Evans, C. J., Arab, H., Boyer, M., de Mink, S. E., Gordon, K., Koekemoer, A. M., Larsen, S. S., Ryon, J. E., and Zeidler, P. (2016). Hubble Tarantula Treasury Project. III. Photometric Catalog and Resulting Constraints on the Progression of Star Formation in the 30 Doradus Region. *ApJS*, **222**, 11.
- Sabbi, E., Lennon, D. J., Gieles, M., de Mink, S. E., Walborn, N. R., Anderson, J., Bellini, A., Panagia, N., van der Marel, R., and Maíz Apellániz, J. (2012). A Double Cluster at the Core of 30 Doradus. *ApJL*, **754**, L37.
- Sabbi, E., Sirianni, M., Nota, A., Tosi, M., Gallagher, J., Meixner, M., Oey, M. S., Walterbos, R., Pasquali, A., Smith, L. J., and Angeretti, L. (2007). Past and Present Star Formation in the SMC: NGC 346 and its Neighborhood. *AJ*, **133**, 44.
- Sabbi, E., Sirianni, M., Nota, A., Tosi, M., Gallagher, J., Smith, L. J., Angeretti, L., Meixner, M., Oey, M. S., Walterbos, R., and Pasquali, A. (2008). The Stellar Mass Distribution in the Giant Star Forming Region NGC 346. *AJ*, **135**, 173.
- Sagar, R., Miakutin, V. I., Piskunov, A. E., and Duzhnevskaja, O. B. (1988). A study of the spatial stellar mass distribution in some young open clusters. *MNRAS*, **234**, 831.
- Salpeter, E. E. (1955). The Luminosity Function and Stellar Evolution. *ApJ*, **121**, 161.
- Sana, H., Momany, Y., Gieles, M., Carraro, G., Beletsky, Y., Ivanov, V. D., de Silva, G., and James, G. (2010). A MAD view of Trumpler 14. *A&A*, **515**, A26.
- Sánchez-Blázquez, P., Peletier, R. F., Jiménez-Vicente, J., Cardiel, N., Cenarro, A. J., Falcón-Barroso, J., Gorgas, J., Selam, S., and Vazdekis, A. (2006). Medium-resolution Isaac Newton Telescope library of empirical spectra. *MNRAS*, **371**, 703.
- Scalo, J. M. (1986). The stellar initial mass function. *FCPh*, **11**, 1.
- Schnurr, O., Casoli, J., Chené, A.-N., Moffat, A. F. J., and St-Louis, N. (2008). The very massive binary NGC 3603-A1. *MNRAS*, **389**, L38.
- Scholz, A., Coffey, J., Brandeker, A., and Jayawardhana, R. (2007). Rotation and Activity of Pre-Main-Sequence Stars. *ApJ*, **662**, 1254.
- Seale, J. P., Looney, L. W., Wong, T., Ott, J., Klein, U., and Pineda, J. L. (2012). The Life and Death of Dense Molecular Clumps in the Large Magellanic Cloud. *ApJ*, **751**, 42.
- Shetty, R., Beaumont, C. N., Burton, M. G., Kelly, B. C., and Klessen, R. S. (2012). The linewidth-size relationship in the dense interstellar medium of the Central Molecular Zone. *MNRAS*, **425**, 720.
- Shin, J. and Kim, S. S. (2016). Low-end mass function of the Quintuplet cluster. *MNRAS*, **460**, 1854.
- Sicilia-Aguilar, A., Hartmann, L. W., Fűrész, G., Henning, T., Dullemond, C., and Brandner, W. (2006). High-Resolution Spectroscopy in Tr 37: Gas Accretion Evolution in Evolved Dusty Disks. *AJ*, **132**, 2135.
- Sicilia-Aguilar, A., Hartmann, L. W., Szentgyorgyi, A. H., Fabricant, D. G., Fűrész, G., Roll, J., Conroy, M. A., Calvet, N., Tokarz, S., and Hernández, J. (2005). Accretion, Kinematics, and Rotation in the Orion Nebula Cluster: Initial Results from Hectochelle. *AJ*, **129**, 363.
- Siess, L., Dufour, E., and Forestini, M. (2000). An internet server for pre-main sequence tracks of low- and intermediate-mass stars. *A&A*, **358**, 593.
- Sirianni, M., Jee, M. J., Benítez, N., Blakeslee, J. P., Martel, A. R., Meurer, G., Clampin, M., De Marchi, G., Ford, H. C., Gilliland, R., Hartig, G. F., Illingworth, G. D., Mack, J., and McCann, W. J. (2005). The Photometric Performance and Calibration of the Hubble Space Telescope Advanced Camera for Surveys. *PASP*, **117**, 1049.
- Skrutskie, M. F., Cutri, R. M., Stiening, R., Weinberg, M. D., Schneider, S., Carpenter, J. M., Beichman, C., Capps, R., Chester, T., Elias, J., Huchra, J., Liebert, J., Lonsdale, C., Monet, D. G., Price, S., Seitzer, P., Jarrett, T., Kirkpatrick, J. D., Gizis, J. E., Howard, E., Evans, T., Fowler, J., Fullmer, L., Hurt, R., Light, R., Kopan, E. L., Marsh, K. A., McCallon, H. L., Tam, R., Van Dyk, S., and Wheelock, S. (2006). The Two Micron All Sky Survey (2MASS). *AJ*, **131**, 1163.
- Slesnick, C. L., Hillenbrand, L. A., and Carpenter, J. M. (2004). The Spectroscopically Determined Substellar Mass Function of the Orion Nebula Cluster. *ApJ*, **610**, 1045.
- Slesnick, C. L., Hillenbrand, L. A., and Carpenter, J. M. (2008). A Large-Area Search for Low-Mass Objects in Upper Scorpius. II. Age and Mass Distributions. *ApJ*, **688**, 377.

-
- Smith, K. W., Lewis, G. F., Bonnell, I. A., Bunclark, P. S., and Emerson, J. P. (1999). Rapid variations of T Tauri spectral features: clues to the morphology of the inner regions. *MNRAS*, **304**, 367.
- Smith, L. F., Shara, M. M., and Moffat, A. F. J. (1996). A three-dimensional classification for WN stars. *MNRAS*, **281**, 163.
- Smith, N. (2002). Near-infrared and optical emission-line structure of the Keyhole Nebula in NGC 3372. *MNRAS*, **331**, 7.
- Smith, N. (2006). A census of the Carina Nebula - I. Cumulative energy input from massive stars. *MNRAS*, **367**, 763.
- Smith, N. and Brooks, K. J. (2008). *The Carina Nebula: A Laboratory for Feedback and Triggered Star Formation*, volume 8, page 138. Astronomical Society of the Pacific.
- Snyder, L. E., Buhl, D., Zuckerman, B., and Palmer, P. (1969). Microwave Detection of Interstellar Formaldehyde. *Physical Review Letters*, **22**, 679.
- Sparke, L. S. and Gallagher, III, J. S. (2007). *Galaxies in the Universe: An Introduction*. Cambridge University Press.
- Spezzi, L., de Marchi, G., Panagia, N., Sicilia-Aguilar, A., and Ercolano, B. (2012). Photometric determination of the mass accretion rates of pre-mainsequence stars - III. Results in the Large Magellanic Cloud. *MNRAS*, **421**, 78.
- Spitzer, L. (1978). *Physical processes in the interstellar medium*. Wiley-VCH.
- Spitzer, L. (1987). *Dynamical evolution of globular clusters*. Princeton University Press.
- Spitzer, Jr., L. (1958). Distribution of Galactic Clusters. *ApJ*, **127**, 17.
- Spitzer, Jr., L. (1969). Equipartition and the Formation of Compact Nuclei in Spherical Stellar Systems. *ApJL*, **158**, L139.
- Stahler, S. W. and Palla, F. (2005). *The Formation of Stars*. Wiley-VCH.
- Stolte, A., Brandner, W., Brandl, B., and Zinnecker, H. (2006). The Secrets of the Nearest Starburst Cluster. II. The Present-Day Mass Function in NGC 3603. *AJ*, **132**, 253.
- Stolte, A., Brandner, W., Brandl, B., Zinnecker, H., and Grebel, E. K. (2004). The Secrets of the Nearest Starburst Cluster. I. Very Large Telescope/ISAAC Photometry of NGC 3603. *AJ*, **128**, 765.
- Stolte, A., Brandner, W., Grebel, E. K., Lenzen, R., and Lagrange, A.-M. (2005). The Arches Cluster: Evidence for a Truncated Mass Function? *ApJL*, **628**, L113.
- Stolte, A., Grebel, E. K., Brandner, W., and Figer, D. F. (2002). The mass function of the Arches cluster from Gemini adaptive optics data. *A&A*, **394**, 459.
- Stolte, A., Hußmann, B., Olczak, C., Brandner, W., Habibi, M., Ghez, A. M., Morris, M. R., Lu, J. R., Clarkson, W. I., and Anderson, J. (2015). Circumstellar discs in Galactic centre clusters: Disc-bearing B-type stars in the Quintuplet and Arches clusters. *A&A*, **578**, A4.
- Stolte, A., Morris, M. R., Ghez, A. M., Do, T., Lu, J. R., Wright, S. A., Ballard, C., Mills, E., and Matthews, K. (2010). Disks in the Arches Cluster - Survival in a Starburst Environment. *ApJ*, **718**, 810.
- Subramaniam, A., Mathew, B., Bhatt, B. C., and Ramya, S. (2006). NGC 7419: a young open cluster with a number of very young intermediate mass pre-MS stars. *MNRAS*, **370**, 743.
- Sung, H. and Bessell, M. S. (2004). The Initial Mass Function and Stellar Content of NGC 3603. *AJ*, **127**, 1014.
- Takahira, K., Tasker, E. J., and Habe, A. (2014). Do Cloud-Cloud Collisions Trigger High-mass Star Formation? I. Small Cloud Collisions. *ApJ*, **792**, 63.
- Tarrab, I. (1982). The initial mass function for young open clusters. *A&A*, **109**, 285.
- Theuns, T. (1991). *Hydrodynamics of encounters between star clusters and molecular clouds*. KNUDSEN.
- Tobin, J. J., Hartmann, L., Furesz, G., Mateo, M., and Megeath, S. T. (2009). Kinematics of the Orion Nebula Cluster: Velocity Substructure and Spectroscopic Binaries. *ApJ*, **697**, 1103.
- Tobin, J. J., Hartmann, L., and Loinard, L. (2010). The Inner Envelope and Disk of L1527 Revealed: Gemini L-band-scattered Light Imaging. *ApJL*, **722**, L12.
- Tomisaka, K., Ikeuchi, S., and Nakamura, T. (1990). The equilibria and evolutions of magnetized, rotating, isothermal clouds. IV - Quasi-static evolution. *ApJ*, **362**, 202.
- Trumpler, R. J. (1931). The Distance of the Orion Nebula. *PASP*, **43**, 255.
- Ubeda et al. (2012). *Advanced Camera for Surveys Instrument Handbook for Cycle 21 v. 12.0*. Baltimore: STScI.
- Underhill, A. B., Doazan, V., Lesh, J. R., Aizenman, M. L., and Thomas, R. N. (1982). B stars with and without

-
- emission lines. Monograph Series on Nonthermal Phenomena in Stellar Atmospheres. *NASA Special Publication*, 456.
- van der Hucht, K. A. (2001). The VIIth catalogue of galactic Wolf-Rayet stars. *NewAR*, 45, 135.
- Vargas Álvarez, C. A., Kobulnicky, H. A., Bradley, D. R., Kannappan, S. J., Norris, M. A., Cool, R. J., and Miller, B. P. (2013). The Distance to the Massive Galactic Cluster Westerlund 2 from a Spectroscopic and HST Photometric Study. *AJ*, 145, 125.
- Vesperini, E., McMillan, S. L. W., and Portegies Zwart, S. (2009). Effects of Primordial Mass Segregation on the Dynamical Evolution of Star Clusters. *ApJ*, 698, 615.
- Voggel, K., Hilker, M., Baumgardt, H., Collins, M. L. M., Grebel, E. K., Husemann, B., Richtler, T., and Frank, M. J. (2016). Probing the boundary between star clusters and dwarf galaxies: A MUSE view on the dynamics of Crater/Laevens I. *MNRAS*, 460, 3384.
- Walborn, N. R. (1995). The Stellar Content of the Carina Nebula (Invited Paper). In Niemela, V., Morrell, N., and Feinstein, A., editors, *Revista Mexicana de Astronomia y Astrofisica Conference Series*, volume 2 of *Revista Mexicana de Astronomia y Astrofisica Conference Series*, page 51.
- Walborn, N. R., Barbá, R. H., Brandner, W., Rubio, M., Grebel, E. K., and Probst, R. G. (1999). Some Characteristics of Current Star Formation in the 30 Doradus Nebula Revealed by HST/NICMOS. *AJ*, 117, 225.
- Walborn, N. R. and Blades, J. C. (1986). An O3 star in the Small Magellanic Cloud H II region NGC 346. *ApJL*, 304, L17.
- Walborn, N. R. and Blades, J. C. (1997). Spectral Classification of the 30 Doradus Stellar Populations. *ApJS*, 112, 457.
- Walborn, N. R. and Fitzpatrick, E. L. (1990). Contemporary optical spectral classification of the OB stars - A digital atlas. *PASP*, 102, 379.
- Walker, D. L., Longmore, S. N., Bastian, N., Kruijssen, J. M. D., Rathborne, J. M., Galván-Madrid, R., and Liu, H. B. (2016). Comparing young massive clusters and their progenitor clouds in the Milky Way. *MNRAS*, 457, 4536.
- Walter, F. M., Vrba, F. J., Mathieu, R. D., Brown, A., and Myers, P. C. (1994). X-ray sources in regions of star formation. 5: The low mass stars of the Upper Scorpius association. *AJ*, 107, 692.
- Weidner, C. and Kroupa, P. (2004). Evidence for a fundamental stellar upper mass limit from clustered star formation. *MNRAS*, 348, 187.
- Weisz, D. R., Johnson, L. C., Foreman-Mackey, D., Dolphin, A. E., Beerman, L. C., Williams, B. F., Dalcanton, J. J., Rix, H.-W., Hogg, D. W., Fouesneau, M., Johnson, B. D., Bell, E. F., Boyer, M. L., Gouliermis, D., Guhathakurta, P., Kalirai, J. S., Lewis, A. R., Seth, A. C., and Skillman, E. D. (2015). The High-mass Stellar Initial Mass Function in M31 Clusters. *ApJ*, 806, 198.
- Werner, M. W., Roellig, T. L., Low, F. J., Rieke, G. H., Rieke, M., Hoffmann, W. F., Young, E., Houck, J. R., Brandl, B., Fazio, G. G., Hora, J. L., Gehrz, R. D., Helou, G., Soifer, B. T., Stauffer, J., Keene, J., Eisenhardt, P., Gallagher, D., Gautier, T. N., Irace, W., Lawrence, C. R., Simmons, L., Van Cleve, J. E., Jura, M., Wright, E. L., and Cruikshank, D. P. (2004). The Spitzer Space Telescope Mission. *ApJS*, 154, 1.
- Westerlund, B. (1961). On the identification of a radio source in Carina. *Arkiv for Astronomi*, 2, 419.
- Westmoquette, M. S., Bastian, N., Smith, L. J., Seth, A. C., Gallagher, III, J. S., O'Connell, R. W., Ryon, J. E., Silich, S., Mayya, Y. D., Muñoz-Tuñón, C., and Rosa González, D. (2014). An Optical-Near-IR Study of a Triplet of Super Star Clusters in the Starburst Core of M82. *ApJ*, 789, 94.
- Whitmore, B. C., Chandar, R., Schweizer, F., Rothberg, B., Leitherer, C., Rieke, M., Rieke, G., Blair, W. P., Mengel, S., and Alonso-Herrero, A. (2010). The Antennae Galaxies (NGC 4038/4039) Revisited: Advanced Camera for Surveys and NICMOS Observations of a Prototypical Merger. *AJ*, 140, 75.
- Whitney, B. A., Indebetouw, R., Babler, B. L., Meade, M. R., Watson, C., Wolff, M. J., Wolfire, M. G., Clemens, D. P., Bania, T. M., Benjamin, R. A., Cohen, M., Devine, K. E., Dickey, J. M., Heitsch, F., Jackson, J. M., Kobulnicky, H. A., Marston, A. P., Mathis, J. S., Mercer, E. P., Stauffer, J. R., Stolovy, S. R., and Churchwell, E. (2004). A GLIMPSE of Star Formation in the Giant H II Region RCW 49. *ApJS*, 154, 315.
- Wuchterl, G. and Tscharnuter, W. M. (2003). From clouds to stars. Protostellar collapse and the evolution to the pre-main sequence I. Equations and evolution in the Hertzsprung-Russell diagram. *A&A*, 398, 1081.
- Zeidler, P., Grebel, E. K., Nota, A., Sabbi, E., Pasquali, A., Tosi, M., Bonanos, A. Z., and Christian, C. (2016a). A High-resolution Multiband Survey of Westerlund 2 with the Hubble Space Telescope. II. Mass Accretion in

-
- the Pre-main-sequence Population. *AJ*, [152](#), [84](#).
- Zeidler, P., Nota, A., Grebel, E. K., Sabbi, E., Pasquali, A., Tosi, M., and Christian, C. (2016b). A High-resolution Multiband Survey of Westerlund 2 with the Hubble Space Telescope. III. The present-day stellar mass function. *AJ*, *submitted*.
- Zeidler, P., Preibisch, T., Ratzka, T., Roccatagliata, V., and Petr-Gotzens, M. G. (2016c). The VISTA Carina Nebula Survey. II. Spatial distribution of the infrared-excess-selected young stellar population. *A&A*, [585](#), [A49](#).
- Zeidler, P., Sabbi, E., Nota, A., Grebel, E. K., Tosi, M., Bonanos, A. Z., Pasquali, A., Christian, C., de Mink, S. E., and Ubeda, L. (2015). A High-resolution Multiband Survey of Westerlund 2 with the Hubble Space Telescope. I. Is the Massive Star Cluster Double? *AJ*, [150](#), [78](#).
- Zinnecker, H. and Yorke, H. W. (2007). Toward Understanding Massive Star Formation. *ARA&A*, [45](#), [481](#).